Effect of State Feedback Coupling on the Design of Voltage Source Inverters for Standalone Applications

Doctoral Dissertation
Doctoral Program in Electronics Engineering (29th Cycle)

Effect of State Feedback Coupling on the Design of Voltage Source Inverters for Standalone Applications

By

Federico de Bosio

******

Supervisor(s):
Prof. Michele Pastorelli, Supervisor
Dr. Maurizio Fantino, Co-Supervisor

Doctoral Examination Committee:
Prof. Jesus Doval-Gandoy, Referee, University of Vigo - ES
Prof. Rosario Miceli, Referee, University of Palermo - IT
Prof. Olivier Terzo, Referee, Istituto Superiore Mario Boella - IT
Prof. Andrea Cavagnino, Referee, Politecnico di Torino - IT
Prof. Gianmario Pellegrino, Referee, Politecnico di Torino - IT

Politecnico di Torino
2017

Declaration

I hereby declare that, the contents and organization of this dissertation constitute my own original work and does not compromise in any way the rights of third parties, including those relating to the security of personal data.

Federico de Bosio

2017

* This dissertation is presented in partial fulfillment of the requirements for **Ph.D. degree** in the Graduate School of Politecnico di Torino (ScuDo).

I would like to dedicate this thesis to my loving parents

Acknowledgment

During my Ph.D. studies I had the pleasure and opportunity to work with many researchers involved in the field of power electronics. I would like to express my gratitude to my collaborator in research Prof. Luiz Antonio de Souza Ribeiro, for his advices and idea during and after my stay abroad in Denmark. We shared very good moments together. I also had the opportunity to collaborate with Francisco Daniel Freijedo, who contributed as collaborator in research for several research activities. It was a pleasure to be invited as PhD visiting researcher at Aalborg University, Denmark by Prof. Josep Maria Guerrero.

I would like to thank my supervisor Prof. Michele Pastorelli and co-supervisor Dr. Maurizio Fantino for their flexibility and availability demonstrated during the three years of Doctorate. A special thank goes to Istituto Superiore Mario Boella for its financial support.

Finally, the constant support of my family, girlfriend and friends allow me to successfully conclude this PhD, overcoming many difficulties along the path.

Abstract

This Ph.D. thesis aims at investigating the effect of state feedback cross-coupling decoupling of the capacitor voltage on the dynamics performance of Voltage Source Inverters for standalone microgrids/Uninterruptible Power Supply systems. Computation and PWM delays are the main factors which limit the achievable bandwidth of current regulators in digital implementations. In particular, the performance of state feedback decoupling is degraded because of these delays.

Two decoupling techniques aimed at improving the transient response of voltage and current regulators are investigated, named nonideal and ideal capacitor voltage decoupling respectively. In particular, the latter solution consists in leading the capacitor voltage on the state feedback decoupling path in order to compensate for system delays. Practical implementation issues are discussed with reference to both the decoupling techniques. Moreover, different resonant regulators structures for the inner current loop are analysed and compared to investigate which is the most suitable for standalone microgrid applications.

A design methodology for the voltage loop, which considers the closed loop transfer functions developed for the inner current loop, is also provided. Proportional resonant voltage controllers tuned at specific harmonic frequencies are designed according to the Nyquist criterion taking into account application requirements. For this purpose, a mathematical expression based on root locus analysis is proposed to find the minimum value of the resonant gain at the fundamental frequency.

The exact model of the output LC filter of a three-phase inverter is derived in the z-domain. The devised formulation allows the comparison of two techniques based on a lead compensator and Smith predictor structure. These solutions permit the bandwidth

of the current regulator to be widened while still achieving good dynamic performance. As a consequence, the voltage regulator can be designed for a wide bandwidth and even mitigates odd harmonics arising with unbalance loads supply. Discrete-time domain implementation issues of an anti-wind up scheme are discussed as well, highlighting the limitations of some discretization methods.

Experimental tests performed in accordance to Uninterruptible Power Supply standards verify the theoretical analysis.

Sommario

La presente tesi di dottorato si propone di indagare l'effetto del disaccoppiamento della tensione capacitiva e della corrente induttiva sulle prestazioni dinamiche di convertitori elettronici controllati in tensione nel campo applicativo delle microreti e gruppi statici di continuità in isola. I ritardi di attuazione imputabili al calcolo computazionale e aggiornamento delle variabili campionate rappresentano i principali fattori che limitano l’ampiezza di banda dei regolatori in campo digitale. Nello specifico, le prestazioni dinamiche dovute al disaccoppiamento delle variabili di stato controllate sono deteriorate a causa di questi ritardi.

Due tecniche di disaccoppiamento volte a migliorare la risposta dinamica transitoria di regolatori di tensione e corrente sono analizzate, denominate disaccoppiamento della tensione capacitiva non ideale ed ideale, rispettivamente. In particolare, quest'ultima soluzione consiste nel progettare un compensatore di anticipi sul ramo di retroazione di disaccoppiamento per compensare i ritardi di sistema. Sono a proposito discussi i conseguenti problemi d’implementazione con riferimento alle diverse tecniche di disaccoppiamento.

Nel seguito, sono analizzate diverse strutture di controllori proporzionali risonanti per il regolatore di corrente e confrontate in modo da identificare la struttura più adatta per applicazioni di microreti in isola.

E’ anche analizzata una metodologia di progettazione del regolatore di tensione, che considera le funzioni di trasferimento ad anello chiuso sviluppate per l'anello interno di corrente. I regolatori di tensione basati su controllori proporzionali risonanti a specifiche frequenze armoniche sono progettati secondo il criterio di Nyquist, tenendo in

considerazione le esigenze applicative. A questo scopo, una formulazione matematica basata sul luogo delle radici si propone di trovare il valore minimo del guadagno integrale del controllore risonante alla frequenza fondamentale.

Il modello esatto del filtro di uscita LC di un convertitore trifase è derivato nel dominio del discreto dalle equazioni differenziali del sistema fisico analizzato. La formulazione permette di confrontare due tecniche basate su una struttura di compensazione di anticipi e a predittore di Smith, impiegate per aumentare l'ampiezza di banda del regolatore di corrente, pur garantendo buone prestazioni dinamiche. In questo modo, il regolatore di tensione può essere progettato per un'ampiezza di banda maggiore e quindi mitigare armoniche dispari derivanti dall'alimentazione di carichi squilibrati. Problemi d'implementazione nel campo del discreto di un sistema anti-wind up sono altresì discussi, evidenziando i limiti di alcuni metodi di discretizzazione.

Prove sperimentali effettuate in conformità alle norme riguardanti i gruppi di continuità statici verificano l'analisi teorica.

Contents

List of Figures

List of Tables

List of Abbreviations and Acronyms

AC	Alternating current
A/D	Analog-to-Digital
ANC	Adaptive Noise Cancelling
BEM	Balanced Envelopes Modulation
D/A	Digital-to-Analog
DC	Direct current
DG	Distributed Generator
div	Division
FE	Forward Euler
FFT	Fast Fourier Transform
FPGA	Field Programmable Gate Array
FR	Frequency response
FSS	Finite Settling Step
HC	Harmonic compensator
HD	Harmonic distortion
IEC	International Electrotechnical Commission
I/O	Input-Output
IGBT	Insulated Gate Bipolar Transistor
IIR	Infinite Impulse Response
MLP	Multi-Layer Perception
NN	Neural Network
NSD	New System Dynamics
ODE	Ordinary Differential Equation
P	Proportional
PCC	Point of Common Coupling
PI	Proportional integral
PR	Proportional resonant
PWM	Pulse Width Modulation
SVPWM	Space Vector Pulse Width Modulation
VPR	Complex Vector PR
VSI	Voltage Source Inverter
THD	Total Harmonic Distortion
UF	Unbalance Factor
UPS	Uninterruptible Power Supply
ZOH	Zero-Order Hold

ZPM	Zero-Pole Matching

Nomenclature

Roman Letters

A	State Feedback Matrix
B	Input Coupling Matrix
C	Controller transfer function
$\bar{C}$	Strictly proper transfer function
C_f	Filter capacitor [F]
CL	Closed loop transfer function
C_n	Rated capacitance [F]
C_{NL}	Capacitor of the nonlinear load [F]
C_∞	Direct feedthrough transfer function
d	Direct axis of the synchronous reference frame
D	Disturbance Input Matrix
d_p	Primary input
dq	Synchronous reference frame
E	Input transfer function in the Laplace domain
f_{bw}	Bandwidth [Hz]
f_{grid}	Grid frequency [Hz]
f_{ref}	Reference frequency [Hz]
f_s	Sampling frequency [Hz]
f_{sw}	Switching frequency [Hz]
G_{dec}	Decoupling transfer function
G_i	Current regulator transfer function
G_{lead}	Phase-lead compensator transfer function
G_{LPF}	Low-pass filter transfer function
G_p	Plant transfer function
G_P	Active power transfer function
G_{PWM}	Transfer Function related to computation and PWM delays
G_Q	Reactive power transfer function
G_v	Voltage regulator transfer function
h	Harmonic order
i_a	Armature current [A]

I_a	Laplace of i_a [A]
$\mathbf{i}_{\alpha\beta}$	$= i_\alpha + j i_\beta$. Complex vector of a generic current in the stationary reference frame [A]
$\mathbf{i}_{dq}$	$= i_d + j i_q$. Complex vector of a generic current in the synchronous reference frame [A]
I_F	Forward current [A]
I_{FSM}	Not repetitive forward current [A]
i_L	Inductor current [A]
I_L	Laplace or Z-transform of i_L [A]
$\mathbf{i}_{L\alpha\beta}$	$= i_{L\alpha} + j i_{L\beta}$. Complex vector of i_L in the stationary reference frame [A]
$\mathbf{I}_{L\alpha\beta}$	Laplace or Z-transform of $\mathbf{i}_{L\alpha\beta}$ [A]
i_o	Output current in the natural reference frame [A]
I_o	Output current in the Laplace domain [A]
$\mathbf{i}_{o\alpha\beta}$	$= i_{o\alpha} + j i_{o\beta}$. Complex vector of i_o in the stationary reference frame [A]
$\mathbf{I}_{o\alpha\beta}$	Laplace or Z-transform of $\mathbf{i}_{o\alpha\beta}$ [A]
i_p	Phase current [A]
I_r	Rated line current rms value [A]
$\mathbf{i}_{sdq}$	Stator current in the synchronous reference frame [V]
J	Inertia [kg m^2]
k_E	Speed Constant [V/rad/s]
k_i	Integral gain
k_{iI}	Integral gain of the current loop
k_{iP}	Integral gain for active power droop control
k_L	Lead compensator gain
k_p	Proportional gain
k_{pI}	Proportional gain of the current loop
k_{pP}	Proportional gain for active power droop control
k_{pQ}	Proportional gain for reactive power droop control
k_{pV}	Proportional gain of the voltage loop
k_T	Torque Constant [Nm/rad/s]
L	Load inductance [H]
L_e	Self-inductance [H]
L_f	Filter inductance [H]
L_{NL}	Inductance of the nonlinear load [H]

L_{vr}	Virtual impedance inductance [H]
M	Manipulated Input
m_c	Common Mode Modulation Index
M_{ID}	Transfer Function of repetitive controller
m_p	Differential Modulation Index
M_p	Overshoot
N	Samples per period
n_o	Noise
n_p	Differential modulation phase-neutral index
OL	Open Loop Transfer Function
p	Generic pole
P	Active power [W]
P^+	Fundamental positive sequence component of active power [W]
P_c	Controller pole
P_{max}	Maximum power [W]
P_p	Plant pole
$P_{r,inv}$	Rated inverter active power [W]
q	Quadrature axis of the synchronous reference frame
Q	Reactive power [Var]
Q_{max}	Maximum reactive power [Var]
Q^+	Fundamental positive sequence component of reactive power [Var]
R	Inductor equivalent series resistance [Ω]
R_1	Ideal PR transfer function in the Laplace domain
R_2	Complex vector PR transfer function in the Laplace domain
R_{ESR}	Equivalent series resistance of the capacitance [Ω]
R_{is}	Internal series resistance [Ω]
R_l	Linear load resistance [Ω]
R_{NL}	Resistance of the nonlinear load [Ω]
R_s	Stator resistance [Ω]
R_{TH}	Slope resistance [Ω]
R_{vr}	Virtual impedance resistance [Ω]
s	Laplace domain variable
S	Apparent power [VA]
S_{3f}	Three-phase apparent power [VA]
s_g	Signal
S_p	Pulse
t	Time variable [s]

$\tan\delta_0$	Dielectric dissipation factor [s]
T_d	Computation and PWM delays [s]
T_{em}	Electromagnetic torque [Nm]
T_L	Load torque [Nm]
t_p	Peak time [s]
T_s	Sampling period [s]
T_{VJ}	Junction temperature [°]
$t_{s,2\%}$	Settling time [s]
$\hat{u}$	Output of C_∞
U_{CFF}	Command Feed Forward controller
U_d	Vector of Disturbance
U_{DID}	Disturbance Input Decoupling controller
U_m	Vector of Manipulated Inputs
U_{SFB}	State Feedback controller
U_{SFBD}	State Feedback cross-coupling Decoupling controller
v_a	Armature voltage [V]
V_a	Laplace of v_a [V]
$\boldsymbol{v}_{bemf}$	Back-emf voltage [V]
$\boldsymbol{V}_{bemf}$	Laplace of $\boldsymbol{v}_{bemf}$ [V]
$\boldsymbol{v}_{bemfdq}$	Back-emf voltage in the synchronous reference frame [V]
v_c	Capacitor voltage [V]
V_c	Laplace or Z-transform of v_c [V]
$\mathbf{v}_{c\alpha\beta}$	$= v_{c\alpha} + jv_{c\beta}$. Complex vector of v_c in the stationary reference frame [V]
$\mathbf{V}_{c\alpha\beta}$	Laplace or Z-transform of $\mathbf{v}_{c\alpha\beta}$ [V]
$\boldsymbol{v}_{dc}$	DC bus voltage [V]
v_{dev}	Voltage deviation [V]
$\mathbf{v}_{dq}$	Voltage in the synchronous reference frame [V]
V_F	Forward voltage drop [V]
$\mathbf{V}_{i\alpha\beta}$	Input applied voltage in the synchronous reference frame [V]
V_n	Rated voltage [V]
v_{NM}	Phase voltage between the neutrals N and M [V]
v_{pM}	Phase voltage with respect to intermediate DC bus neutral M [V]
v_{pN}	Phase voltage respect to load neutral N [V]
$V_{r,l}$	Line voltage rms value [V]
V_{rms}	Rms voltage [V]
V_{RRM}	Maximum repetitive reverse blocking voltage [V]

V_s	Not recurrent surge voltage [V]
$\mathbf{v}_{sdq}$	Stator voltage in the synchronous reference frame [V]
V_{TH}	Threshold voltage [V]
x	Reference Input
X	State Vector
$\dot{X}$	Derivative of State Vector
y	Output of the adaptive filter
Y	Output transfer function in the Laplace domain
Z	Impedance in the Laplace domain [Ω]
Z_c	Controller zero

Greek Letters

α	Alpha axis of the stationary reference frame
αβ	Stationary reference frame
β	Beta axis of the stationary reference frame
Δf	Frequency deviation [Hz]
Δf_{max}	Maximum frequency deviation [Hz]
Δk_{iI}	Integral gain value of the current loop deviation
ΔV_{max}	Maximum voltage deviation [Hz]
ε	Error
η	Sensitivity function
θ_m	Mechanical angle [rad]
Θ_m	Laplace of θ_m [rad]
ʒ	Damping ratio
σ	Real part of the poles
σL_s	Short-circuit stator inductance [H]
τ	Time constant
τ_z	Zero time constant
τ_p	Pole time constant
τ_P	Plant time constant
φ	Phase leading angle [°]
ϕ	Generic output
ω_{bw}	Bandwidth [rad/s]
ω_c	Cut-off frequency of nonideal PR [rad/s]
ω_d	Imaginary part of the poles
ω_e	Frequency in the synchronous reference frame [rad/s]
ω_m	Mechanical speed [rad/s]

ω_n	Natural frequency [rad/s]
ω_o	Fundamental frequency [rad/s]

List of Subscripts

s	Stator
p	Physical
a	Active
crit	Critical
0	Reference
min	Minimum
max	Maximum

List of Superscripts

$\sim$	Estimated
$*$	Reference
$1\pm$	Positive/negative sequence at fundamental
$3\pm$	Positive/negative sequence at the 3^{rd} harmonic
$5\pm$	Positive/negative sequence at the 5^{th} harmonic
$7\pm$	Positive/negative sequence at the 7^{th} harmonic

List of Publications

Journal papers

[1] **F. de Bosio**, L. A. de S. Ribeiro, F. D. Freijedo, M. Pastorelli, and J. M. Guerrero, "Effect of state feedback coupling and system delays on the transient performance of stand-alone VSI with LC output filter", *IEEE Trans. Ind. Electron.*, vol. 63, no. 8, pp. 4909-4918, 2016

[2] **F. de Bosio**, L. A. de S. Ribeiro, F. D. Freijedo, M. Pastorelli, and J. M. Guerrero, "Discrete-Time Domain Modelling of Voltage Source Inverters in Standalone Applications: Enhancement of Regulators Performance by Means of Smith Predictor", *IEEE Trans. Power Electron.*, vol. 32, no. 10, pp. 8100-8114, 2017

[3] **F. de Bosio** and V. Verda, "Thermoeconomic analysis of a Compressed Air Energy Storage (CAES) system integrated with a wind power plant in the framework of the IPEX Market", *Applied Energy*, vol. 152, pp. 173-182, 2015

[4] C. Li, **F. de Bosio**, S. K. Chaudhary, J. C. Vasquez, J. M. Guerrero, "Economic Dispatch for Operation Cost Minimization under Real Time Pricing in Droop Controlled DC Microgrid", *IEEE Trans. Emerg. Sel. Topics Power Electron.*, vol. 5, no. 1, pp. 587-595, 2017

Magazine papers

[5] **F. de Bosio**, M. Pastorelli, and M. Fantino, "Sistemi di accumulo: tipologie e applicazioni", *Rivista AEIT*, vol.10, 2014

International conference papers

[6] **F. de Bosio**, M. Pastorelli, A. Mazza, G. Chicco, G. Bracco, E. Giorcelli, G. Mattiazzo, and M. Raffero, "Sea-wave power converter modeling for fault conditions analysis", in *Conf. Proc. IEEE PowerTech*, Eindhoven, NL, Jun./Jul. 2015

[7] **F. de Bosio**, M. Pastorelli, L. A. de S. Ribeiro, M. S. Lima, F. D. Freijedo, and J. M. Guerrero, "Current control loop design and analysis based on resonant regulators for microgrid applications", in *Conf. Proc. IEEE Ind. Electron. Soc. (IECON)*, Yokohama, JP, Nov. 2015, pp. 5322-5327

[8] **F. de Bosio**, L. A. de S. Ribeiro, M. S. Lima, F. D. Freijedo, J. M. Guerrero, and M. Pastorelli, "Inner current loop analysis and design based on resonant regulators for isolated microgrid applications", in *Proc. IEEE Braz./South. Power Electron. Conf.(COBEP/SPEC)*, Fortaleza, BR, Nov. 2015

[9] C. Li, **F. de Bosio**, S. K. Chaudhary, J. C. Vasquez, and J. M. Guerrero, "Operation Cost Minimization of Droop-Controlled DC Microgrids Based on Real-Time Pricing and Optimal Power Flow", in *Conf. Proc. IEEE Ind. Electron. Soc. (IECON)*, Yokohama, JP, Nov. 2015, pp. 3905-3909

[10] E. Riva Sanseverino, N. Q. Nguyen, M. L. Di Silvestre, G. Zizzo, **F. de Bosio**, and Q. Tran, "Frequency constrained optimal Power Flow based on Glow-worm Swarm Optimization in Islanded Microgrids", in *Conf. IEEE AEIT Int. Annu.*, Naples, IT, Oct. 2015

[11] G. Chicco**, F. de Bosio**, M. Pastorelli, and M. Fantino, "Clustering-based Performance Assessment of Thermal Energy Management in Buildings", in *IEEE Int. Telecom. Energy Conf. (INTELEC)*, Osaka, JP, Oct. 2015

[12] M. Pastorelli, G. Mutani, and **F. de Bosio**, "A model for the evaluation of thermal and electric energy consumptions in residential buildings", in *Proc. IEEE Int. Conf. on Ren. Energy Res. And Appl. (ICRERA)*, Palermo, IT, Nov. 2015, pp. 1399-1404

[13] M. Martino, M. Pastorelli, and **F. de Bosio**, "Towards Smart Energy Users by Adopting an Innovative Billing System", *Optimisation of Community Scale Renewables*, Turin, IT, Sep. 2015

[14] **F. de Bosio**, L. A. de S. Ribeiro, F. D. Freijedo, J. M. Guerrero, and M. Pastorelli, "Effect of state feedback coupling on the transient performance of voltage source inverters with LC filter", in *Conf. Proc. IEEE Power Electron. and Appl. (EPE)*, Karlsruhe, DEU, Sep. 2016

[15] **F. de Bosio**, L. A. de S. Ribeiro, F. D. Freijedo, and J. M. Guerrero, "Implementation issues on the design of current loops based on resonant regulators for isolated microgrids", in *Conf. Proc. IEEE Power Electron. and Appl. (EPE)*, Karlsruhe, DEU, Sep. 2016

[16] **F. de Bosio**, L. A. de S. Ribeiro, M. Savaghebi, J. Vasquez, and J. M. Guerrero, "Control Design of VSIs to Enhance Transient Performance in Microgrids", in *Conf. Proc. IEEE Power Electron. and Appl. (EPE)*, Karlsruhe, DEU, Sep. 2016

[17] R. Tisseur, **F. de Bosio**, G. Chicco, M. Fantino, and M. Pastorelli, "Ant Colony for Storage Optimization", in *Proc. IEEE Int. Univ. Power Eng. Conf. (UPEC)*, Coimbra, PT, Sep. 2016

[18] **F. de Bosio**, A. C. Luna, L. A. de S. Ribeiro, M. Graells, O. R. Saavedra, and J. M. Guerrero, "Analysis and Improvement of the Energy Management of an Isolated Microgrid in Lencois Island based on a Linear Optimization Approach", in *Conf. Proc. IEEE Energy Conv. Congr. and Exp. (ECCE)*, Milwaukee, USA, Sep. 2016

[19] **F. de Bosio**, L. A. de S. Ribeiro, F. D. Freijedo, J. M. Guerrero, and M. Pastorelli, "Enhancement of Current and Voltage Controllers Performance by Means of Lead Compensation and Anti-Windup for Islanded Microgrids", in *Conf. Proc. IEEE Energy Conv. Congr. and Exp. (ECCE)*, Milwaukee, USA, Sep. 2016

[20] **F. de Bosio**, L. A. de S. Ribeiro, F. D. Freijedo, J. M. Guerrero, and M. Pastorelli, “Voltage and Current Regulators Design of Power Converters in Islanded Microgrids based on State Feedback Decoupling”, in *Conf. Proc. IEEE Energy Conv. Congr. and Exp. (ECCE)*, Milwaukee, USA, Sep. 2016

[21] **F. de Bosio**, L. A. de S. Ribeiro, F. D. Freijedo, M. Pastorelli, and J. M. Guerrero, “State Feedback Decoupling with In-Loop Lead Compensator in Stand-Alone VSIs”, in *Conf. Proc. IEEE Ind. Electron. Soc. (IECON)*, Florence, IT, Nov. 2016

[22] **F. de Bosio**, L. A. de S. Ribeiro, F. D. Freijedo, J. M. Guerrero, and M. Pastorelli, “Enhanced current and voltage regulators for stand-alone applications”, in *IEEE Int. Telecom. Energy Conf. (INTELEC)*, Austin, Texas, USA, Oct. 2016

[23] **F. de Bosio**, V. Verda, M. C. Masoero, and M. Pastorelli, “Unit cost of electrical energy of a hybrid CAES-wind power plant by means of exergoeconomic analysis”, in *Conf. Smart Int. and Green Energy (SINERGREEN)*, Rome, IT, May 2016

Chapter I

1. Introduction and Background

1.1 Framework and Scope of the Research

Part of the work described in this chapter has been previously published in [1], [2], [7], [8], [14], [15], [16], [19], [20], [21], [22].

According to the European 20-20-20 plan, the use of renewable energy resources will be increased by 20% of total energy consumption by 2020, mostly via decentralized power generators [24]. In general, there will be an increase in energy demand as the world population is expected to grow by 19.8% in twenty years compared to the level of 2010 [25]. Not only renewables, but also traditional fossil-based energy sources are expected to grow in order to meet these challenging goals. The spread diffusion of these resources requires new ways to monitor and control the energy flows. Instead of a large network with few power stations, a diffusion of several local energy communities is expected to be a viable solution for a more sustainable energy management. The microgrid concept permits the management of these communities: local power networks can be controlled and operated independently of the larger power grid by means of distributed generators units.

Renewable and fossil-based energy sources are usually interfaced via power converters and controlled in closed loop with the innermost loops being the current and the voltage regulators in standalone applications, i.e. not grid connected. With the increasing share of energy resources, even more demanding dynamic performance are required to voltage and current regulators intended for standalone applications. In this context, the transient response of voltage and current regulators plays an important role in modern applications of power electronics. The general power converter

employed is the Voltage Source Inverter (VSI) operating in voltage or current control mode. Inaccurate design of the inner loops degrades significantly the performance of the overall control system, potentially interfering with outer loops characterized by slower dynamics. This is the case in ac and dc droop-controlled microgrids [26], [27], [28], possibly with hierarchical control based on secondary and tertiary control [29], [30], [31] and variable speed drives [32], [33]. Thus, effective control of voltage and current is mandatory to succeed in implementing the desired feature of each application. According to [34], four general requirements are usually imposed on any current or voltage regulator: i) to achieve zero steady-state error; ii) to accurately track the commanded reference and reject any disturbance; iii) to widen the closed loop control bandwidth as much as possible to achieve fast transient response; iv) to reduce the total harmonic distortion by compensating for low order harmonics. Mandatory requirements specifically for ac power supply/Uninterruptible Power Supply (UPS) systems, which are characterized by a high level of similarity with the system architecture addressed, are fault and peak current protection as well [35].

A possible implementation of the regulators for the inner loops is based on proportional resonant (PR) controllers in the $\alpha\beta$-stationary reference frame. Their features are equivalent to two proportional integral (PIs) controllers implemented in two synchronous reference frames [36], one for the positive sequence and the other for the negative sequence component of the signal. However, PR controllers are easier to implement being the controlled states on α- and β-axis naturally decoupled. In the synchronous reference frame a decoupling technique is often needed since the states on *d*- and *q*-axis are not independent [37]. Another advantage is the less number of transformations required to reach the $\alpha\beta$-stationary reference frame, which makes PR controllers an attractive solution in low-cost digital signal processor units because of their low computational burden [38]. Furthermore, PR controllers can be directly used in single-phase power converters applications without the need of further modifications [39], [40], [41].

Substantial research activities have been made in the design of regulators for systems with a strong electromotive force, e.g. grid connected, and motor drives applications. However, design issues for standalone applications have not been so far discussed in depth. In this scenario, the coupling between the inductor current and capacitor voltage significantly degrades the system performance. Moreover, the effect of computation and pulse-width modulated (PWM) delays on the achievable bandwidth when voltage decoupling is performed has not been addressed in depth so far.

The main research activities presented in this thesis are related to the abovementioned issues associated to standalone systems and provide feasible solutions to overcome them. The following aspects are investigated:

- A systematic design methodology to mitigate the effect of computation and PWM delays which are not compensated for on the decoupling path with voltage decoupling is provided. Specifically, a low-pass filter cascaded with a lead compensator on the state feedback decoupling path is proposed for further improvements. It is important to note that even without the one sample delay introduced by computation, the sample-and-hold effect is still present and limits the achievable bandwidth, thus reducing the benefits introduced by the decoupling.

- The influence of state feedback voltage decoupling on the performance of different proportional resonant regulators structures is investigated. Discretization issues related to their implementation, sensitivity to frequency and integral gains variations are the main aspects analysed to assess their behaviour.

- A model in the discrete-time domain which takes into account the coupling of the capacitor voltage with the inductor current, even if voltage decoupling is performed, is derived analytically. This model is shown to better represent the physical system being addressed. The effect of widening the inner current loop bandwidth by means of two proposed techniques based on a lead compensator structure and Smith Predictor is investigated.

- A design methodology for the voltage loop, which considers the closed loop transfer functions derived for the inner current loop, is provided. Its effect is reflected in the Nyquist trajectories calculated for the voltage loop, and hence affects the selection of the controller gains. Furthermore, a criterion to select the minimum value of the resonant gain at the fundamental frequency is proposed, which leads to an easy mathematical formulation for practical design. Moreover, discretization issues of an anti-wind up scheme for the voltage regulator are analysed.

- The theoretical analysis is validated experimentally with reference to the dynamic output characteristics imposed by the standard IEC 62040-3 for UPS systems. The laboratory tests performed consider different testing conditions, e.g. supply of balanced/unbalanced linear/nonlinear loads with/without resonant regulators tuned at specific frequencies.

1.2 Literature Review

The state of the art is analysed, with special focus on (but not limited to) the relevant findings related to standalone applications. Substantial research activities have been

made in the design of regulators for systems with a strong electromotive force, e.g. grid connected [40], [42], [43], [44], [45], [46], [47], and motor drives applications [48], [49], [50], [51]. However, design issues for standalone applications have not been so far discussed in depth.

In this context, some significant works related to the control of VSIs, either grid-connected or in standalone mode, are revised. Subsequently, relevant works on PR controllers are introduced identifying their main contribution. Finally, works related to direct discrete-time implementation techniques are analysed.

In [35] a comprehensive review of linear and nonlinear current regulators is assessed. PIs and state feedback controllers, along with predictive techniques are discussed. With regard to nonlinear regulators, bang-bang and predictive controllers with on-line optimization are reviewed.

In [52] an analytical method to determine the best possible gains of linear ac current controllers is derived, taking into account computation and PWM delays. These latter, along with the dc bus voltage and the plant series inductance, limit mainly the proportional gain value. Back-emf feedforward has been identified as a possible solution to reduce the level of disturbance input injection into the control loop.

In [53] different multi-loop control approaches using alternative feedback control variables are investigated. However, the PWM modulator is replaced by a unit gain transfer function since the design for VSIs operating in standalone/grid-connected mode has been made for low-frequency control analysis. A similar analysis is addressed in [54], [55], [56] comparing the use of the inductor and capacitor current as controlled state variables in terms of disturbance rejection properties.

In [57] a delay prediction and feedback strategy of computation delay is proposed to widen the bandwidth of a grid-connected power converter. This approach allows the bandwidth to be widened while preserving an enough damped closed loop response.

In [58] a fast acting current control scheme to regulate the load current during all energizing conditions of multiple load transformers powered by a UPS system has been proposed. The system, extremely valid from an architecture point of view, is highly dependent on the values of controller gains both for current and voltage loops. Moreover, the control structure is not the usual considered based on cascaded controllers and no effect of delays is considered.

For what concerns the PR controllers, the following works and related contributions are revised.

In [59] the PR controllers theory is briefly revised highlighting the main benefits introduced by applying this kind of controller. In particular, the possibility of implementing selective harmonic compensation is one of the main features of this controller.

In [60] a frequency-domain analysis of different resonant current regulators for active power filters is performed, taking into account computation and PWM delays. System delays are proved to limit stability for high order harmonic compensation.

In [61] a methodology to assess the transient response of PR current regulators is proposed, aimed at achieving fast and enough damped closed loop responses during transient conditions in grid-connected applications. It is shown how the controller gains have to be chosen as a compromise between command tracking and disturbance rejection performance.

In [62] two types of resonant controllers intended for grid-connected applications are compared. The main outcome relies on the possibility to summarize these controllers in a more general structure.

The benefits introduced by a direct discrete-time domain design approach are discussed with reference to the following papers.

In [63] a direct discrete-time design approach for current regulators is proposed, leading to the derivation of a small-signal *z*-domain model.

In [64] observers for the capacitor current and disturbance are proposed to achieve a fast and robust current loop, respectively. Capacitor voltage feedforward is performed and the capacitor current is used as a controlled state.

In [65] the effect of computation and PWM delays, rounding and truncation errors and flux imbalance in the output transformer are analysed to design an online UPS system.

In [66] the design of a multi-loop predictive voltage controller is addressed. The feedforward of the capacitor current and a load current estimator are implemented.

In general, for what concerns state feedback decoupling, this control action has often been used for decoupling the cross-coupling caused by the implementation of current controllers in the synchronous reference frame [34], for decoupling the back-emf effect in dc [67] and ac drives [68] (resulting in a current control strategy independent of the speed), and for decoupling current and voltage states in dc-dc converters [69] and UPS systems [70]. Nevertheless, because the system delays have not been taken into account, the resulting model used to design and analyse the inner current loop becomes simply the model of an RL load.

As a general comment it must be noted that, in the present literature, the effect and modelling of the delays for islanded systems have not been fully analysed. When voltage decoupling is performed, the influence of not compensating for computation and PWM delays on the state feedback decoupling path is not taken into account. In fact, in previous works, the decoupling of the controlled states neglects the effect of computation and PWM delays when performed. This is equivalent to considering the decoupling as ideal. Nevertheless, system delays degrade the performance of state

feedback decoupling. This effect cannot be ignored, since implies a reduction in the achievable bandwidth.

1.3 Major Results

The contribution provided by this thesis can be summarized in the following key points:

- Detailed modelling and analysis of the effect of computation and PWM delays when state feedback voltage decoupling is performed. The analysis is firstly performed in the continuous-time domain, followed by a more precise derivation in the discrete-time domain. A lead-lag filter on the decoupling path allows the voltage decoupling to be more effective and the system less dependent on the load.

- Comparison of different PR regulators structure with respect to the requirements imposed to the controllers in microgrids applications. Specifically, discretization issues, sensitivity to frequency and integral gain variations of three PR controllers are investigated. Complex Vector PR controller shows the lowest sensitivity to integral and frequency deviations. The structure with two integrators and forward and backward Euler as discretization methods show reduced performance (steady-state error is observed) as the resonant frequency of the regulator is increased.

- Comparison and evaluation of the dynamic performance of the inner control loops with respect to the use of a lead compensator on the forward path or a Smith predictor structure. The Smith predictor shows the fastest response to changes in the reference inductor current allowing the current loop bandwidth to be widened. As the current regulator bandwidth is widened, the voltage loop dynamics can be enhanced.

- As the voltage loop can be widened, an anti-wind up scheme is even more important during demanding transients. Discretization issues of an anti-wind up scheme based on inverse state feedback dynamics are analysed, providing feasible solutions to overcome them.

- The design of the voltage loop is based on the Nyquist criterion, which is usually applied for current loop design purposes. Moreover, an easy mathematical criterion to set the fundamental integral gain is provided.

1.4 Thesis Structure and Related Publications

The thesis is organized as follows.

In **Chapter 1** the state of the art related to standalone applications is discussed. The scope of the research and its significance is introduced.

In **Chapter 2** some basic concepts related to VSIs are briefly reviewed. Additionally, an overview of the main current loop control structures is presented. Moreover, a short review of IEC 62040-3 standard for UPS systems is provided. The main issues useful to perform the experimental tests aimed at validating the theoretical analysis are presented. Finally, three active control actions to achieve better performance of current and voltage regulators are presented. Specifically, state-feedback cross-coupling decoupling, disturbance input decoupling and command feedforward are revised.

In **Chapter 3** the influence of system delay modelling on the design of the current regulator in the continuous-time domain is investigated. The inner loop current control with and without state feedback voltage decoupling is analyzed. Several resonant controllers' structures for the current loop are investigated by means of root locus and frequency response analysis, highlighting the issues arising when different discretization methods are used for digital implementation. With reference to a proportional controller, a feasible solution to compensate for computation and PWM delays on the state feedback decoupling path is derived. Subsequently, a PR voltage controller design is proposed for the voltage loop. Detailed design and tuning are provided according to the Nyquist criterion. The theoretical solution is supported by experimental results, according to the IEC 62040-3 standard for UPS systems.

In **Chapter 4** the direct discrete-time modelling of the current and voltage regulators is investigated. To this extent, the exact model of an LC filter in the *z*-domain is derived. The complete mathematical derivation is reported in the Appendix. Two techniques based respectively on a lead compensator and Smith predictor structure are implemented via direct pole placement and compared to achieve a wider current loop bandwidth. The same criterion presented in Chapter 3 is used to design the voltage regulator. Laboratory tests are performed to verify the compliance with the IEC 62040-3 standards.

In **Chapter 5** the main conclusions are discussed with reference to the results previously presented and future research activities are suggested.

The main results discussed and presented in this thesis have also been published in two JCR-indexed journal papers [1], [2] and nine conference papers [7], [8], [14], [15], [16], [19], [20], [21], [22].

Chapter II

2 Voltage Source Inverter Concepts

2.1 Voltage Source Inverter in Standalone Mode

Part of the work described in this chapter (mainly part of paragraph 2.2.1.2) has been previously published in [7].

In isolated microgrids the VSI is typically equipped with an LC filter at its output. This topology is also employed in UPS systems [54], [71], [72]. In general, the VSI it operates in voltage control mode with the capacitor voltage and inductor currents being the controlled states. In some cases the capacitor current is used as controlled state to improve the disturbance rejection [53], [54].

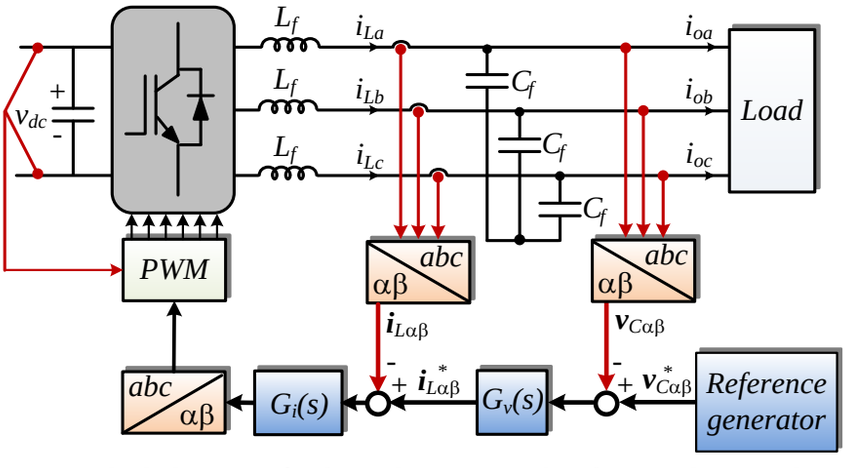

Fig. 2.1. Block diagram of a three phase VSI with voltage and current loops

In Fig. 2.1 the block diagram including a three-phase three-leg inverter with its inner loops is presented. The purpose of the inner current loop is to track the commands from the outer voltage loop and to ensure fast dynamic disturbance rejection within its bandwidth. Whenever the current regulator is unable to perform properly these tasks, the system performance degrades.

The system architecture described above is a general architecture recognized to be valid to investigate UPS systems. For this reason it has been adopted as reference

architecture for this thesis and will be extensively explained with additional details in the following paragraphs.

It can be noted in Fig. 2.1 the use of the transformation matrix, proposed by Edith Clarke, which is applied to move from three-phase quantities in the natural reference frame to two-phase quantities in the αβ-stationary reference frame [73], [74]. This transformation matrix, which preserves the magnitude of a three-phase signal, is as follows

$$[T] = \frac{2}{3}\begin{bmatrix} 1 & -\frac{1}{2} & -\frac{1}{2} \\ 0 & \frac{\sqrt{3}}{2} & -\frac{\sqrt{3}}{2} \\ \frac{1}{2} & \frac{1}{2} & \frac{1}{2} \end{bmatrix}$$

This matrix is also orthogonal, i.e. $[T]^{-1} = [T]^{t}$. As a consequence, given a three-phase signal $\boldsymbol{x}_{abc}$, this is transformed in the stationary reference frame as

$$\begin{bmatrix} x_\alpha \\ x_\beta \\ x_o \end{bmatrix} = [T] \begin{bmatrix} x_a \\ x_b \\ x_c \end{bmatrix}$$

A graphical representation of the generic vector $\boldsymbol{x}_{\alpha\beta} = x_\alpha + jx_\beta$ in the stationary reference frame is reported in Fig. 2.2.

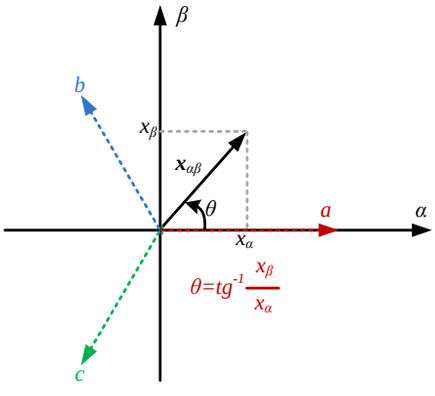

Fig. 2.2. Graphical representation of a generic vector $\boldsymbol{x}_{\boldsymbol{\alpha\beta}}$

On the other hand, the transformation matrix which preserves the power is

$$[T_p] = \sqrt{\frac{2}{3}}\begin{bmatrix} 1 & -\frac{1}{2} & -\frac{1}{2} \\ 0 & \frac{\sqrt{3}}{2} & -\frac{\sqrt{3}}{2} \\ \frac{1}{\sqrt{2}} & \frac{1}{\sqrt{2}} & \frac{1}{\sqrt{2}} \end{bmatrix}$$

The transformed signals appear as two sinusoidal functions phase-shifted by 90 electrical degrees, having a magnitude $\sqrt{3}/\sqrt{2}$ higher than the original value in the natural reference frame, as can be seen in Fig. 2.3.

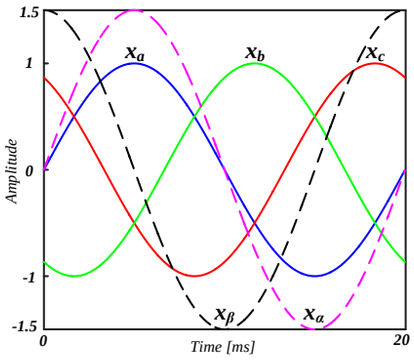

Fig. 2.3. Two-phase components in the αβ-stationary reference frame obtained from a symmetrical three-phase signal of direct sequence

A further transformation is based on the rotational matrix. The two-phase signals in the *αβ*-stationary reference frame are thus transformed in a rotating frame, referred to as *dq*-synchronous reference frame. The correspondent vector representing the signal rotates with angular speed *ω*, at the same velocity of the rotating frame. In other terms, ac variables are 'rotated' into a frame synchronous to the fundamental output frequency. For this reason the signals appear as constant values, i.e. dc quantities. The following transformation is applied

$$\begin{bmatrix} x_d \\ x_q \end{bmatrix} = \begin{bmatrix} cos\theta & sin\theta \\ -sin\theta & cos\theta \end{bmatrix} \begin{bmatrix} x_\alpha \\ x_\beta \end{bmatrix}$$

A graphical representation of the corresponding transformation is shown in Fig. 2.4.

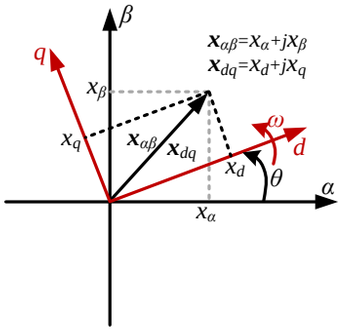

Fig. 2.4. Graphical representation of a generic vector $\boldsymbol{x_{dq}}$.

2.1.1 Computation and PWM Delays

Nowadays the implementation of regulators for medium power level hard-switches converters is usually performed in the discrete-time domain. Compared to analog controllers, digital implementation of the regulators are convenient as they allow the implementation of complex control functions, low number of control components, high reliability, adaptability and programmability, high immunity to components' aging, negligible offsets and thermal drifts [75], [76], [77], [78]. On the other hand, digital regulators have the well-known drawback represented by limitation in the attainable control bandwidth, mainly due to computation and PWM delays [52]. Other causes of minor concern can be identified in the quantization of signals and coefficients, particularly in case of fixed-point arithmetic with small word length, and time delay in the Analog-to-Digital (A/D) conversion process [76], [63], [79], [80], [81].

Although many authors proposed different modulation strategies, two main techniques can be identified, named *naturally sampled PWM* and *regular sampled PWM*. Specifically, *naturally sampled PWM*, usually employed in analog controllers, allows the comparison of a reference sinusoidal signal with a high-frequency saw tooth or triangular carrier [82], [83]. Nowadays, up-to-date digital devices as Field Programmable Gate Arrays (FPGAs) allow accurate implementation of *naturally sampled PWM* techniques [84], [85]. On the other hand, in a fully-digital implementation, *regular sampled PWM* is usually used. This technique refers to the switching at the intersection between a regularly sampled reference waveform and a high-frequency carrier [82]. This implies the low-frequency reference waveform is sampled and held constant during each carrier interval. Among *regular sampled PWM* techniques, two main control schemes can be implemented, referred to as *symmetrical/single update* and *asymmetrical/double update* sampling. With reference to Fig. 2.5(a), for a triangular symmetrical carrier and *regular sampled PWM* with symmetrical sampling, a phase delay respect to the continuous reference waveform is introduced by the modulator because of the sampling process. This is usually approximated as half of the carrier interval [86]. Moreover, an execution time delay occurs between the sampling instant and the application of the pulse signal, which is equal to one sampling period [86]. This delay is usually referred to as computation delay. One of the reasons is to synchronize the sampling instants of the measured current (voltage) with the positive/negative peaks of the triangular carrier. This technique, referred to as synchronous sampling, allows the sampling of the average value of the current (voltage), since at the positive/negative peaks of the carrier the ripple component is null. This avoids the use of low-pass filters which would introduce additional delays in the system. To summarize, computation and PWM delays provide

globally a system delay of one-and-a-half the modulation period in case of *regular sampled PWM* with symmetrical sampling and symmetrical triangular waveform as carrier.

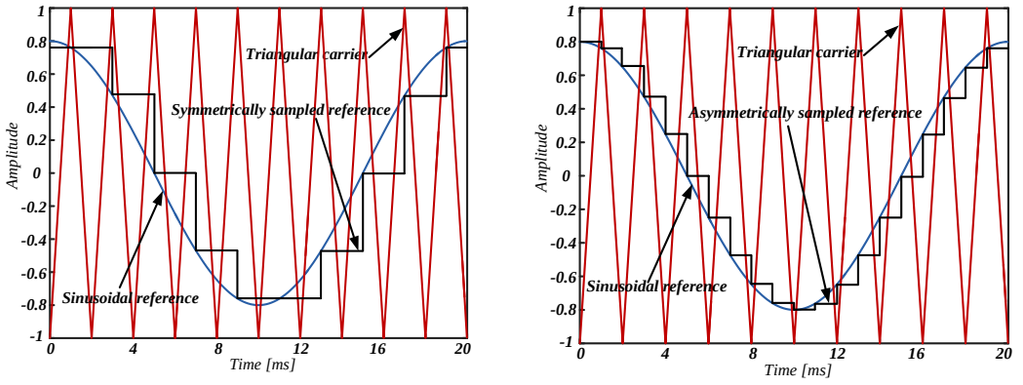

Fig. 2.5. Regular sampled PWM with: (a) symmetrical sampling (single update) and with triangular carrier (sampling at positive peaks); (b) asymmetrical sampling (double update) and with triangular carrier (sampling at positive and negative peaks)

On the other hand, in case of triangular symmetrical carrier and *regular sampled PWM* with asymmetrical sampling, the modulating waveform is sampled every half carrier-cycle instant, corresponding to the positive and negative peaks of the triangular wave [87] [see Fig. 2.5(b)]. This implies the computation delay is halved compared to symmetrical sampling. As a consequence, also the PWM delay is halved, leading to a phase delay of one quarter the carrier interval. Finally, computation and PWM delays account only for three-over-four the sampling period.

2.1.2 Space-Vector Pulse-Width Modulation

Starting from the basic *regular sampled PWM* technique, different modulation schemes have been proposed in literature. Among PWM techniques for three-phase power converters, the well-known Space-Vector pulse-width modulation (SVPWM) allows the time instants of the null vector to be varied, introducing an additional degree of freedom. This technique allows the extension of the linear modulation region by almost 15 percent compared to traditional PWM techniques based on sinusoidal modulation. This permits the achievement of the maximum modulation index and the minimization of the output voltage distortion. It is important to note that this technique is equivalent to a PWM scheme based on third harmonic injection as well as to balancing of the negative and positive envelopes of the modulating waveform (Balanced Envelopes Modulation - BEM). With reference to a three-phase three-wire power converter supplying a three-phase star-connected balanced and symmetric load, as the one shown in Fig. 2.6, the following relation among the phase currents is verified

$$\sum_{p=1}^{3} i_p = 0 \rightarrow i_1 + i_2 + i_3 = 0, \tag{2.1}$$

which means the zero current component is null and only two degrees of freedom are available on the phase currents. In other words, the remaining current is equal to the sum of the other two with negative sign.

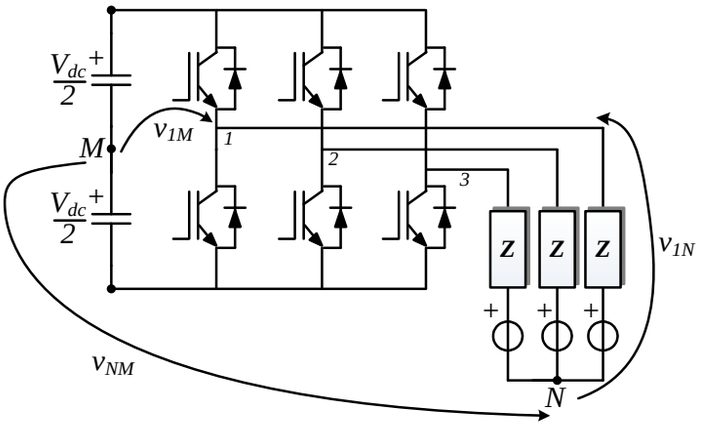

Fig. 2.6. Three-phase three-wire VSI with IGBTs supplying a balanced and symmetric three-phase star-connected load

With reference to Fig. 2.6, the relationship per-phase between the voltages is

$$v_{pM} = v_{pN} + v_{NM} \tag{2.2}$$

This implies

$$\sum_{p=1}^{3} v_{pM} = \sum_{p=1}^{3} v_{pN} + 3v_{NM} \rightarrow$$

$$v_{NM} = \frac{1}{3}\sum_{p=1}^{3} v_{pM} \tag{2.3}$$

being $\sum_{p=1}^{3} v_{pN} = 0$ as a consequence of supplying a three-phase balanced and symmetric load. By normalizing the voltages with respect to $V_{dc}/2$, the differential modulation index m_p, the common mode modulation index m_c and the differential modulation phase-neutral index n_p are defined

$$m_p = \frac{v_{pM}}{\frac{V_{dc}}{2}} \rightarrow \boldsymbol{m}_p = \frac{\sum_{p=1}^{3} v_{pM}}{\frac{V_{dc}}{2}} \tag{2.4}$$

$$m_c = \frac{v_{NM}}{\frac{V_{dc}}{2}} \rightarrow m_c = \frac{1}{3}\sum_{p=1}^{3} m_p \tag{2.5}$$

$$n_p = \frac{v_{pN}}{\frac{V_{dc}}{2}} \rightarrow \boldsymbol{n}_p = \frac{\sum_{p=1}^{3} v_{pN}}{\frac{V_{dc}}{2}} \tag{2.6}$$

Bold character is used to denote vectors. The relationship between the modulation indexes is thus

$$\boldsymbol{n}_p = \boldsymbol{m}_p - m_c \begin{bmatrix} 1 \\ 1 \\ 1 \end{bmatrix} \tag{2.7}$$

From (2.5) and (2.7) it follows

$$\begin{cases} n_1 = \frac{2}{3} m_1 - \frac{m_2 + m_3}{3} \\ n_2 = \frac{2}{3} m_2 - \frac{m_1 + m_3}{3} \\ n_3 = \frac{2}{3} m_3 - \frac{m_1 + m_2}{3} \end{cases} \tag{2.8}$$

To determine the position of the i-th component of $\boldsymbol{n}_p$ it is necessary to determine the three components of $\boldsymbol{m}_p$. The power converter can thus assume eight different states depending on $\boldsymbol{m}_p$ combination. The eight possible switches combinations are shown in Fig. 2.7 and the representation in polar form is reported in Fig. 2.8.

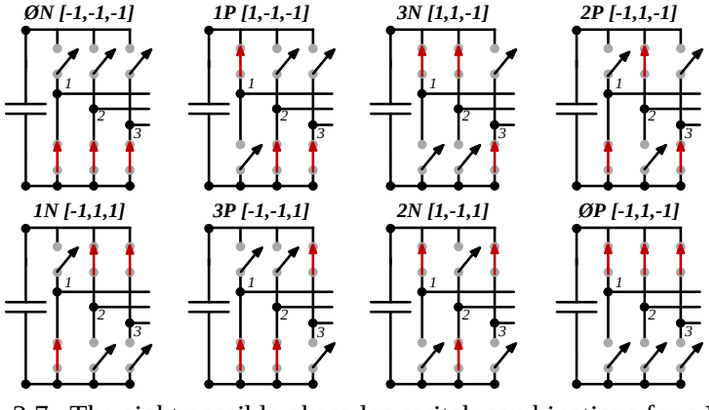

Fig. 2.7. The eight possible phase leg switch combinations for a VSI

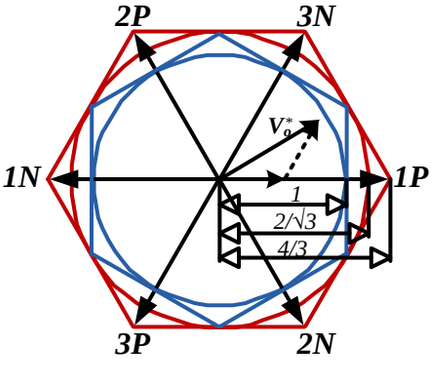

Fig. 2.8. Location of eight possible stationary voltage vectors, hexagons and circles limits

The outer boundary limit is represented by the biggest hexagon, which allows $n_p = 4/3$. However, the maximum n_p which is not dependent on the angle of the sector and preserves the amplitude is described by the red circle, which provides $n_p = 2/\sqrt{3}$. This corresponds to an extension of the linear modulation region by 15%. In case the average value of m_c is set to zero by the modulation scheme, the modulation region is reduced. A smaller hexagon rotated by $\pi/6$ with respect to the outer one is achieved. The correspondent inscribed circle limits n_p to unity.

2.2 Loop Control Structures

The main current control techniques are briefly reviewed in the following. A possible classification can be made according to the nature of the regulator, recognizing linear and nonlinear controller structures [35]. Specifically, linear control schemes include Proportional Integral (PI) and Proportional Resonant (PR) state feedback controllers, predictive and Finite Settling Step (FSS) techniques with constant switching frequency. On the other hand, nonlinear techniques comprise bang-bang (hysteresis, delta modulation) controller, repetitive controller and Adaptive Noise Cancelling (ANC) techniques along with Neural Networks (NN) and fuzzy-logic based controllers.

2.2.1 Linear Control Methods

2.2.1.1 PI state feedback controller

Among linear controllers, PI controller is probably the most employed for current control in industrial applications. The transfer function of a conventional PI controller is

$$C(s) = k_p + \frac{k_i}{s} \tag{2.9}$$

being k_p the proportional gain and k_i the gain of the integral term. The value of k_p mainly determines the controller bandwidth. This controller allows zero-steady error to be achieved as dc signals are regulated, due to the infinite gain at low frequencies provided by the pole of the integral term. For this reason, three-phase signals are usually transformed in the *dq*-rotating reference frame to appear as a vector of constant dc values [74], [88], [89]. The transformed signals can thus be controlled with zero steady-state error by PI compensators. However, the transformation to the synchronous reference frame can lead to some unwanted coupled effect between the *d*- and *q*-axis [90], [91], [92], [93]. Depending on the application, this interaction can be neglected or affect system dynamics.

The PI controller is also employed in the stationary reference frame [57], [35], [34], [94]. However, since it has to regulate ac signals, it suffers from steady-state error [95]. As an attempt to further reduce this error, the bandwidth of the regulator can be increased [57].

Another implementation is the use of three PI controllers in the natural reference frame, which suffers from significant steady-state amplitude and phase errors [96], [97], [98].

2.2.1.2 PR state feedback controller

PR controllers are used to control ac signals on the basis of the internal model principle [99]. This principle states the controlled output can track a class of reference commands without steady-state error if the model of the reference is included in the stable closed loop system [100]. In fact, the transfer function of the resonant term of an ideal PR controller at fundamental frequency ω_o is

$$G(s) = \frac{s}{s^2 + \omega_o^2}$$

This transfer function is the Laplace transform of the following sinusoidal function

$$L\{\cos(\omega_o t)\} = \frac{s}{s^2 + \omega_o^2}$$

The implementation based on the co-sinusoidal function is preferred since it provides a zero in the origin, thus giving 90° phase advance.

The implementation of the PR regulators is usually performed in the *αβ*-stationary reference frame [101], [59], [102], [103], [60], [104], [61], [96], [105], [106], [107], [108]. Nevertheless some implementation of these controllers in the synchronous reference frame can be found in literature [109]. The design of the gains for a PR controller can be made starting from the design of a PI regulator employed in the *dq*-

synchronous reference frame, since PR regulators are just implementations of two PI controllers, one for the positive and the other for the negative sequence of the signal in the stationary reference frame [110], [111], [112].

For the simple case of a PI controller and an RL load the complex vector block diagram is shown in Fig. 2.9. As shown in [113], the nature of the controller zero and plant pole are different, one real (k_i/k_p) and the other complex ($-R/L - j\omega_e$). This mismatch is a function of the synchronous frequency and, for a given bandwidth, it results in closed loop dominant poles close to imaginary axis that produce overshoot in the response. As also shown in Fig. 2.9 this behaviour can be overcome by decoupling the cross-coupling due to the synchronous reference frame implementation.

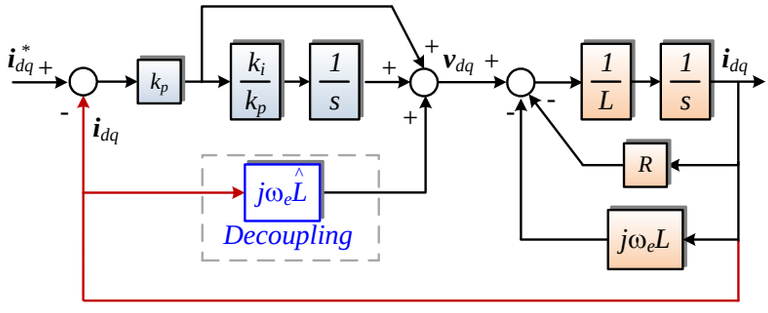

Fig. 2.9. Closed loop complex vector block diagram of an RL load with a synchronous frame PI controller, shown in the synchronous reference frame ($\boldsymbol{\omega_e}$)

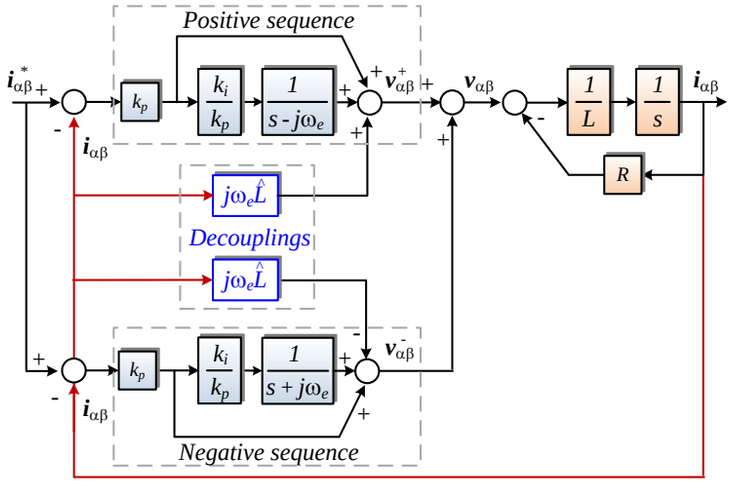

(a)

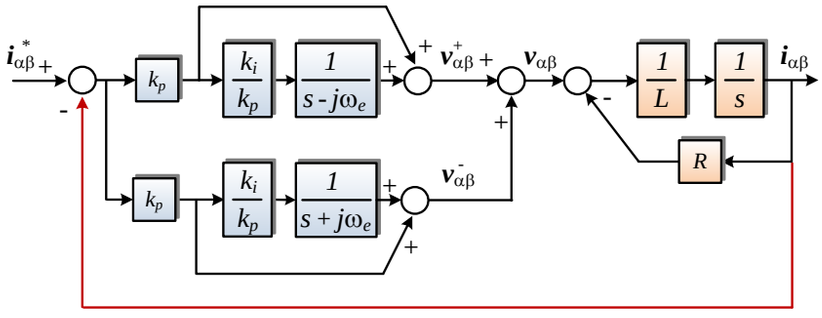

(b)

Fig. 2.10. PR regulator with an RL load: (a) explicitly showing the decoupling; (b) resulting regulator

The PR regulator is the implementation of two of these controllers in the stationary reference frame, as shown in Fig. 2.10(a). As can be seen in Fig. 2.10(b), the cross-coupling decoupling of the positive sequence regulator cancels the decoupling of the negative sequence regulator. Therefore, the problem that is present in the synchronous frame PI when there is no decoupling is also present in the PR regulator no matter if a decoupling is done.

The complex vector root locus for two different synchronous frequencies, with the current regulator tuned to cancel the pole plant ($k_i/k_p = R/L$), is shown in Fig. 2.11. At low resonant frequencies [see Fig. 2.11(a)], the controller zero Z_c (a complex number) approximately interacts more with the controller pole P_c (also a complex number), both being close to the plant poles P_p. As the controller bandwidth increases the closer the zero and closed loop poles will be. This allows the response of the system to be dominated by the fastest closed loop pole. Furthermore, less oscillation is expected since the closed loop poles are moving away from the imaginary axis.

As the resonant frequency increases (for the same bandwidth) the resulting slower closed loop roots become closer to the imaginary axis and away from the zero. Therefore, more oscillation is expected. The results become worse as the resonant frequency increases, and the regulator bandwidth decreases. This can be a serious problem when harmonic compensators are used since these regulators are supposed to work at high resonant frequencies, and, in general, have low bandwidth.

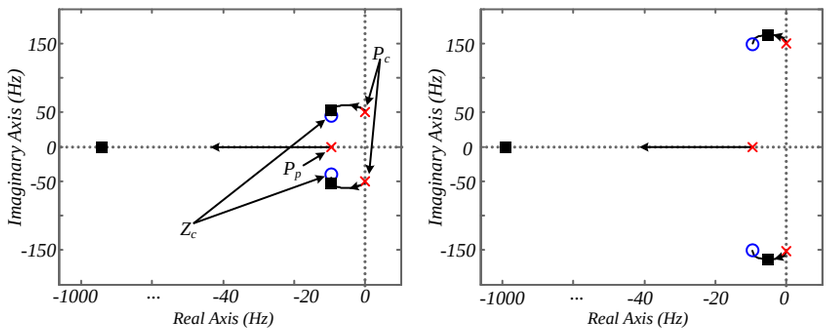

(a) (b)

Fig. 2.11. Complex vector root locus of RL load with PR regulator: x – open loop poles; ■ closed loop poles; **o** – zeros (a) at the fundamental resonant frequency (50 Hz); (b) at the resonant frequency of 150 Hz

2.2.1.3 Predictive techniques and deadbeat controller

Predictive techniques allow the estimation at the beginning of each sampling period of the current error vector based on the actual error and load parameters [35], [114], [115], [116], [117], [118]. In this way, the voltage vector to be generated by a PWM scheme during the next modulation period is determined, so as to minimize the forecast error [35].

As an example, the model of an induction motor in the rotating reference frame is considered

$$\boldsymbol{v}_{sdq}(t) = R_s \boldsymbol{i}_{sdq}(t) + \sigma L_s \frac{d\boldsymbol{i}_{sdq}(t)}{dt} + \boldsymbol{v}_{bemfdq}(t), \tag{2.10}$$

where $\boldsymbol{v}_{\mathrm{sdq}}(\mathrm{t})$ and $\boldsymbol{i}_{\mathrm{sdq}}(\mathrm{t})$ are the stator voltage and current respectively, R_s is the stator resistance, σL_s the short-circuit inductance and $\boldsymbol{v}_{bemfdq}(\mathrm{t})$ the back-emf. Neglecting the resistance (approximately true in big machines), an approximation for the trajectory of the current vector is

$$\frac{d\boldsymbol{i}_{sdq}(t)}{dt} \cong \frac{1}{\sigma L_s}\left[\boldsymbol{v}_{sdq}(t) - \boldsymbol{v}_{bemfdq}(t)\right]. \tag{2.11}$$

If the sampling time T_s is sufficiently small, then the following approximation is true

$$\frac{d\boldsymbol{i}_{sdq}(t)}{dt} \cong \frac{\boldsymbol{i}_{sdq}(T_s) - \boldsymbol{i}_{sdq}(0)}{T_s}. \tag{2.12}$$

Substituting (2.12) in (2.11), it leads to

$$\boldsymbol{i}_{sdq}(T_s) - \boldsymbol{i}_{sdq}(0) \cong \frac{T_s}{\sigma L_s}\left[\boldsymbol{v}_{sdq}(0) - \boldsymbol{v}_{bemfdq}(0)\right]. \tag{2.13}$$

Suppose the desired value of the current vector $\boldsymbol{i}^*_{sdq}(T_s)$ is known at the beginning of the sampling time. Since is desirable to force the current error to zero in the interval $[0, T_s]$, then at the end of the interval it is expected that

$$\boldsymbol{i}_{sdq}(T_s) = \boldsymbol{i}^*_{sdq}(T_s). \tag{2.14}$$

Therefore, the voltage vector that should be applied at the beginning of the sampling interval to drive the error to zero at the end of the interval is

$$\boldsymbol{v}^*_{sdq}(0) = \frac{\widetilde{\sigma L_s}}{T_s}\left[\boldsymbol{i}^*_{sdq}(T_s) - \boldsymbol{i}_{sdq}(0)\right] + \tilde{\boldsymbol{v}}_{bemfdq}(0), \tag{2.15}$$

where $\widetilde{\sigma L_s}$ and $\tilde{\boldsymbol{v}}_{bemfdq}(0)$ are the estimated values of σL_s and $\boldsymbol{v}_{bemfdq}(0)$, respectively. It is considered that the current vector reference is known at the beginning of the sampling period. The main drawback of predictive controllers is the parameter estimation dependence.

Among predictive techniques, deadbeat controller has gain popularity since allows the fastest tracking performance. On the other hand, it suffers of poor disturbance rejection, model uncertainties, parameters mismatch and noise on sensed variables [66], [119], [120], [121], [122], [123], [124]. For these reasons, several works have been done to mitigate these drawbacks [125], [126], [127], [128]. Deadbeat controller belongs to a class of controllers known as Finite Settling Step (FSS) controllers [129]. These latter allow the commanded reference, given a feasible command trajectory, to be achieved in a finite number of steps. Since there is no counterpart in the continuous-time domain, the design of this controller typology is performed directly in the discrete-time domain. With reference to Fig. 2.12, this corresponds to place the dominant poles of the system in the centre of the unit circle in the *z*-domain. In this sense, deadbeat represents the boundary between two stable regions in the unit circle, with the one on the left characterized by oscillations at half the sampling frequency. This behaviour is highly undesirable for control purposes in the power electronics field.

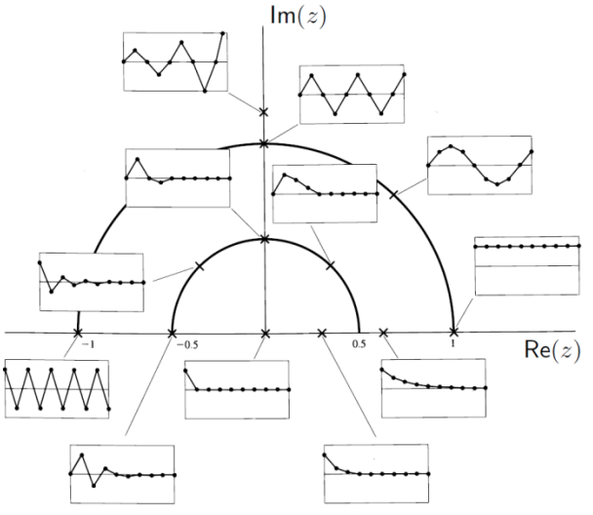

Fig. 2.12. Z-domain decay for different pole placement **[130]**

2.2.2 Nonlinear Control Methods

2.2.2.1 Hysteresis control

One of the simplest control structures to implement is hysteresis control. The error signal is regulated within lower and upper bounds based on a defined hysteresis band, as can be seen in Fig. 2.13.

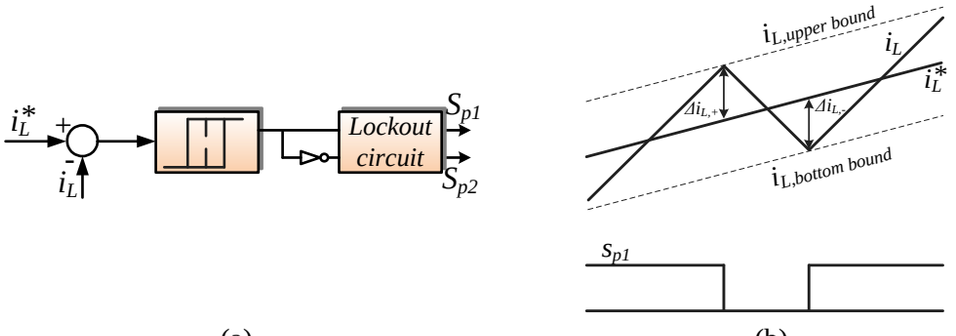

(a) (b)

Fig. 2.13 Hysteresis control: (a) block diagram representation; (b) inductor current behaviour with boundaries and correspondent pulses

When the measured current becomes greater (lower) than the current reference by the hysteresis band, the inverter leg is switched to the negative (positive) direction. In this way the current ripple is specified by the hysteresis band and the inverter switching frequency varies over a fundamental cycle [131]. To overcome this limitation, variable hysteresis band switching techniques have been proposed [132], [133], [134], [135], [136], [137], [138].

2.2.2.2 Sliding mode controller and delta modulation

Sliding mode techniques are based on changes of the controller structure in order to compensate for physical plant parameters variation and disturbance occurrences. A special case of this kind of controllers is represented by the delta modulation. This latter does not allow PWM since commutations occur only at fixed times [139], [140], [141], [142]. In [143], delta modulation is used to minimize the integral of the output voltage error, irrespective of AC voltage variations. However, distorted line currents are achieved. In [139], delta modulation is applied to control the switch of a buck converter. Since the excursion of the integral of the sampled voltage respect to a fixed value of comparison is determined by sampling frequency, delta modulators exhibit subharmonics [144].

2.2.2.3 Repetitive controller

Repetitive controllers represent a special application of the Internal Model Principle [145]. The aim of a repetitive control is to reject the effect of arbitrary periodic disturbances or to track a periodic reference input [146]. By means of this technique the system learns how to carry out a repetitive (periodic) task [145]. The concept of repetitive control was firstly introduced by Inoue *et al.* [147]. Subsequently this technique has been applied for different applications related to control of power converters [148], [149], [150], [151], [100]. For digital implementation of repetitive controllers in its simplest structure, a discrete periodic signals generator can take the form

$$M_{ID} = \frac{1}{1 - z^{-N}}.$$

N are the samples per period such that $T = NT_s$, being T_s the sampling interval. As M_{ID} is placed in a stabilized closed loop system, a commanded periodic reference with known period T can be tracked at sampling instants. However, the arbitrary phase shift introduced by M_{ID} can lead to unwanted stability robustness issues.

2.2.2.4 Adaptive Noise Cancelling

A technique widely used in Signal Processing is Adaptive Noise Cancelling (ANC) [152], [153]. With reference to Fig. 2.14, a primary input (d) comprising the signal (s) and superimposed noise (n_0) is compared with a noisy reference input (x), which is adaptively filtered (y) according to the error (ε) between the two inputs. The aim is to eliminate the noise on the primary input obtaining as output a filtered signal $\varepsilon = s$

[154], [112]. It should be noted that ε represents also the parameter used for adaptive filtering of the reference input.

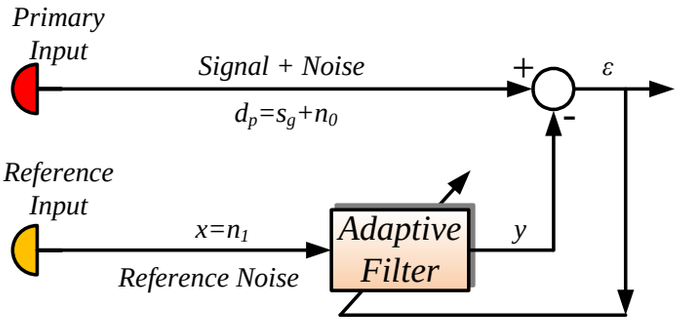

Fig. 2.14. Adaptive Noise Cancelling principle

2.2.2.5 Neural Network and fuzzy-logic based controllers

Neural Network (NN) has been proposed as an alternative to conventional state feedback controllers [155], [156], [157], [158]. This kind of controller has the capability to learn from previous experience via ad-hoc training functions, e.g. the sigmoid or the linear type. In practice, parallel processing structures composed by several units, connected by weighted signals, reproduce nonlinear relationships learned from examples [159]. Once the NN structure has been trained, it can provide the correct outputs even for arbitrary inputs not included in the previous set of training functions. An NN structure usually comprises an input and output layer with hidden layers in between, as can be seen in Fig. 2.15 for the case of Multi-Layer Perception (MLP) NN algorithm.

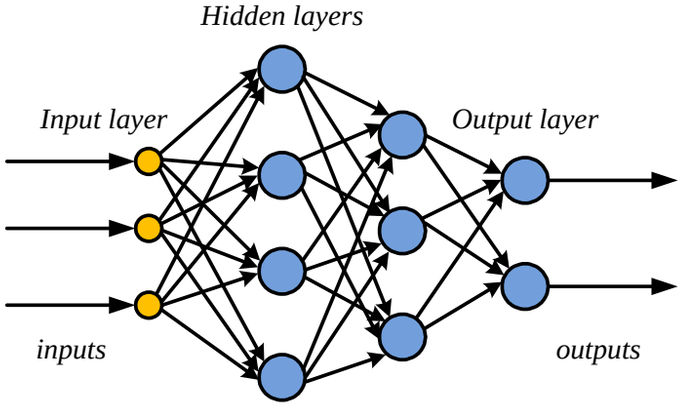

Fig. 2.15. Multi-Layer Perception structure with input units, hidden layers and output layer

Fuzzy-logic represents another interesting tool in dealing with uncertainties and nonlinearities in control systems. Usually inputs are not perfectly known but only defined within a certain range. A set of user-defined fuzzy rules transforms fuzzy

inputs in outputs. In this sense, fuzzy logic can be considered a technique for mapping as NN techniques. However, unlike NN, fuzzy-logic explains the input-output relationship [159]. In the field of power electronics this technique has been widely investigated and applied for current control [160], [161], [162], [163].

2.3 Active Control Actions

The general State Equation used to represent control systems is

$$\dot{X} = AX + BU_m + DU_d, \tag{2.16}$$

where X is the State Vector, A is the State Feedback Matrix, B is the Input Coupling Matrix, D is the Disturbance Input Matrix, U_m is the vector of the Manipulated Inputs from the controller to the physical system and U_d is the vector of Disturbance. Moreover

$$U_m = U_{SFB} + U_{SFBD} + U_{DID} + U_{CFF}, \tag{2.17}$$

where U_{SFB}, U_{SFBD}, U_{DID} and U_{CFF} are the manipulated inputs associated to State Feedback, State Feedback cross-coupling Decoupling, Disturbance Input Decoupling and Command Feed Forward controllers. In the following paragraphs an explanation of these control actions is provided.

2.3.1 State Feedback Cross-Coupling Decoupling

In control systems the controlled states and manipulated inputs are usually cross-coupled. Once the physical system is represented via a block diagram, a clear identification of the states naturally coupled is needed. Accordingly, it is possible to decouple these variables via an active state feedback control action. This method is referred to as state feedback cross-coupling decoupling. In the following some examples are provided to explain the benefits introduced by applying cross-coupling decoupling.

Let us consider the model of a DC motor, e.g. a permanent magnet dc servo motor drive, as the one shown in Fig. 2.16.

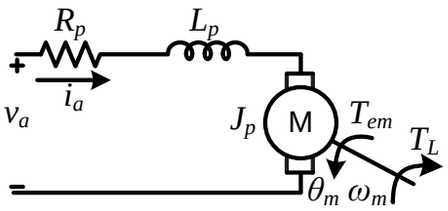

Fig. 2.16. Physical system modelling of a dc permanent magnet servo drive

The ordinary differential equations of the system, neglecting the damping term, are

$$\begin{cases} L_p \dfrac{di_a(t)}{dt} = v_a(t) - v_{bemf}(t) - i_a(t)R_p \\ J_p \dfrac{d\omega_m(t)}{dt} = T_{em}(t) - T_L(t), \end{cases} \tag{2.18}$$

The subscript p is used to refer to as *physical* variables/parameters. L_p and J_p are the motor inductance and inertia respectively. $T_{em}(t) = k_T i_a(t)$ is the electromagnetic torque, where k_T $[V/rad/s]$ is the DC motor torque constant between $T_{em}(t)$ and the armature current $i_a(t)$. The back-electromagnetic voltage is $v_{bemf}(t) = k_{ep}\omega_m(t)$, where k_{ep} $[Nm/rad/s]$ is the speed constant between the motor speed ω_m and $v_{bemf}(t)$.

The armature current and motor speed can be selected as controlled states variables. The armature voltage $v_a(t)$ represents a manipulated input to the physical system. On the other hand, the load torque $T_L(t)$ is a disturbance to the system.

From the system of equations in (2.18) it is possible to derive the correspondent block diagram in the Laplace domain, shown in Fig. 2.17.

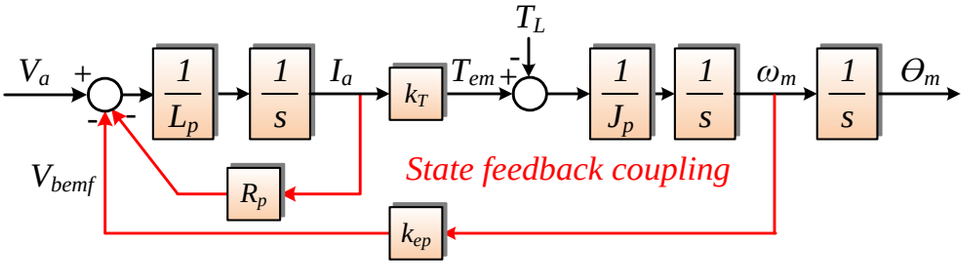

Fig. 2.17. Simplified block diagram of the closed loop system of a DC permanent magnet servo drive neglecting system delays and damping

From Fig. 2.17 two state feedback cross-coupled paths can be identified. In particular, I_a affects the physical system via the motor armature resistance R_p. Similarly, V_{bemf} (or ω_m) and I_a are coupled. In fact, as V_{bemf} changes, since it is fed back to the first summing junction, it affects the direct path which comes next, i.e. I_a.

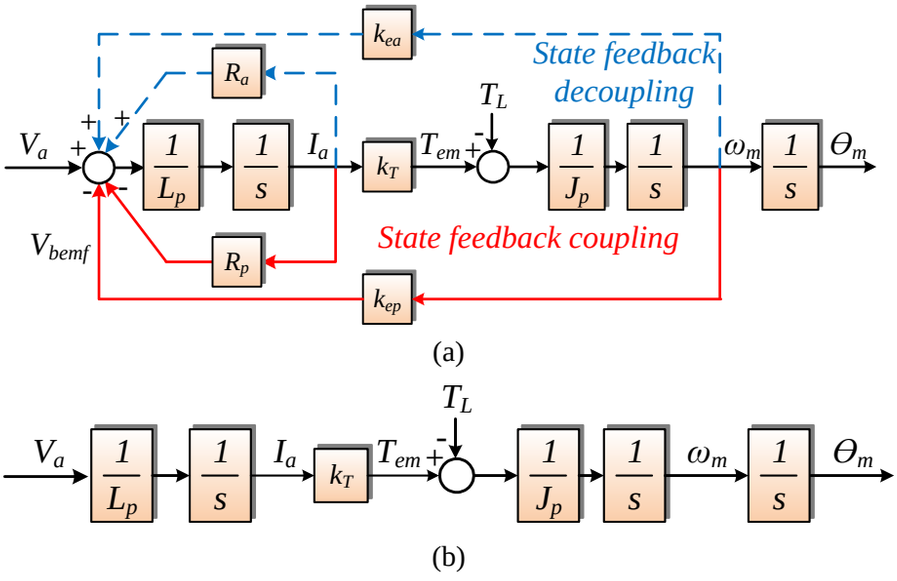

(a)

(b)

Fig. 2.18. Simplified block diagram of the closed loop system of a DC permanent magnet servo drive neglecting system delays and damping: (a) state feedback cross-coupling decoupling with R_a and k_{ea}; (b) resulting closed-loop system after decoupling control actions with $R_a = R_p$ and $k_{ea} = k_{ep}$

For the above reasons two decoupling techniques can be applied:

- Introduce an additional state feedback path with gain $R_a = R_p$, where the subscript a is used to refer to as *active* variables/parameters, since are not physically present in the system but added via active control actions. This control action allows to decouple the effect of I_a on the physical system;
- To decouple the effect of V_{bemf}, an additional state feedback path is introduced with gain $k_{ea} = k_{ep}$.

The above mentioned state feedback cross-coupling decoupling active actions are shown in the block diagram of Fig. 2.18(a). Since the transfer function associated to the modulator is approximated by a unit gain and computation and PWM delays are neglected, the system in Fig. 2.18(a) is equivalent to the system in Fig. 2.18(b), which represents an inductive load.

The effect of state feedback decoupling is to improve the command tracking performances, sometimes decreasing the disturbance rejection properties of the system. It has also implications in the dynamic performance providing better dynamics during transients thanks to the added virtual damping to the system.

The benefits introduced by state feedback decoupling will be extensively analysed since this active control action is applied to study the main physical system investigated in this thesis.

2.3.2 Disturbance Input Decoupling

Another possible active control action consists in decoupling the disturbance to the physical system, i.e. referred to as Disturbance Input Decoupling (DID) [69]. In fact, in some cases, it is possible to measure the disturbance to the physical system or reconstruct it via other control techniques, e.g. observers [164], [165], [166].

In order to effectively decouple the disturbance, the following relationship is considered, starting from (2.16)

$$BU_{mDID} + DU_d \cong 0 \rightarrow$$

$$U_{mDID} \cong -\tilde{B}^{-1} DU_d \tag{2.19}$$

Being the superscript $\sim$, denoting estimated values.

However, for digital implementations, the following model in the discrete-time domain must be considered to design the transfer function associated to DID, i.e. $G_{DID}(z)$.

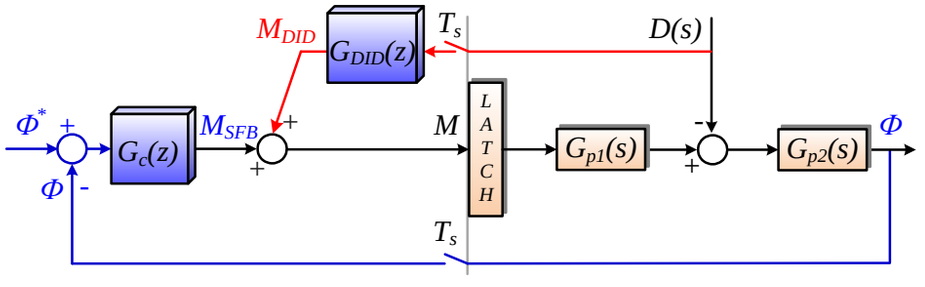

Fig. 2.19. Model with Disturbance Input Decoupling

As shown in Fig. 2.19, the physical plant is split in two transfer function in the continuous-time domain, named $G_{p1}(s)$ and $G_{p2}(s)$. The manipulated input to the physical system is referred to with M. This is obtained as the sum of the output from the state feedback controller (M_{SFB}) and the output of $G_{DID}(z)$. The latch interface holds the output of the digital controller over a sample period. The variables fed back from the physical system in the continuous-time domain are sampled at the sample rate T_s and converted from Analog to Digital format. $D(s)$ represents the disturbance to the physical system. Accordingly

$$\boldsymbol{Z}\{\boldsymbol{L}\{\text{Latch}\}D(s)G_{p2}(s)\} - D(z)G_{DID}(z)NSD(z) = 0 \tag{2.20}$$

Where $NSD(z) = \boldsymbol{Z}\{\boldsymbol{L}\{\text{Latch}\}G_{p1}(s)G_{p2}(s)\}$ is referred to as New System Dynamics. Consequently

$$G_{DID}(z) = \frac{\boldsymbol{Z}\{\boldsymbol{L}\{\text{Latch}\}G_{p2}(s)\}}{\boldsymbol{Z}\{\boldsymbol{L}\{\text{Latch}\}G_{p1}(s)G_{p2}(s)\}} = \frac{\boldsymbol{Z}\{\boldsymbol{L}\{\text{Latch}\}D(s)G_{p2}(s)\}}{D(z)NSD(z)} \tag{2.21}$$

In this case the disturbance must be known a priori, which is practically unfeasible. Another possibility is to model $D(s)$ as to enter the physical system via a latch interface, as can be seen in Fig. 2.20. In this case, the aim is to make the disturbance input response at the sample instant equal to zero. This is reasonable unless the disturbance is faster respect to the sample rate. In this scenario (2.20) becomes

$$D(z)\boldsymbol{Z}\{\boldsymbol{L}\{\text{Latch}\}G_{p2}(s)\} - D(z)G_{DID}(z)NSD(z) = 0 \tag{2.22}$$

Consequently

$$G_{DID}(z) = \frac{\boldsymbol{Z}\{\boldsymbol{L}\{\text{Latch}\}G_{p2}(s)\}}{\boldsymbol{Z}\{\boldsymbol{L}\{\text{Latch}\}G_{p1}(s)G_{p2}(s)\}} = \frac{\boldsymbol{Z}\{\boldsymbol{L}\{\text{Latch}\}G_{p2}(s)\}}{NSD(z)} \tag{2.23}$$

In this case the disturbance must not be known a priori, but only at the sampling instant.

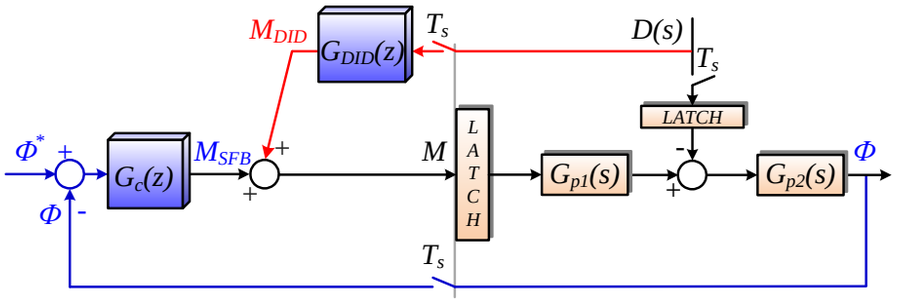

Fig. 2.20. Model with Disturbance Input Decoupling latched

The main reason to perform DID is to increase the disturbance rejection properties of the system, in proportion to the DID the system is able to perform.

2.3.3 Command Feedforward

Another possible active control action is Command Feedforward. In literature, this term is sometimes used to refer erroneously to state feedback cross-coupling decoupling. In fact, as State Feedback cross-coupling Decoupling, Command Feedforward is used for decoupling purposes. However, it is used to improve command tracking performance without affecting intrinsic dynamics.

It is based on knowing in advance the commanded reference trajectories, which are fed in open loop via an appropriate transfer function after the state feedback controller. With reference to (2.16)

$$U_{CFF} = \tilde{B}^{-1}\left[\dot{X}^* - \widetilde{AX}^*\right] \tag{2.24}$$

For a digital implementation, the Command Feedforward active control action is represented in Fig. 2.21. Given an arbitrary trajectory $\emptyset^*$ to follow, this is fed forward to the closed loop such that the tracking error is held to zero. In this way, the manipulated input from the state feedback controller M_{SFB} is adjusted before being applied to the physical system (M) through the latch interface.

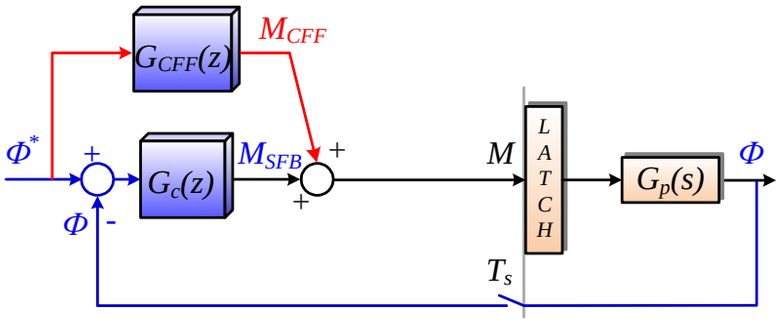

Fig. 2.21. Generic model to illustrate Command Feedforward principle

Accordingly, the following expressions can be derived to compute $G_{CFF}(z)$

$$NSD(z) = \frac{\emptyset(z)}{M(z)} \rightarrow M_{CFF} = \emptyset^*(z)\, N\tilde{S}D^{-1}$$

Being $N\tilde{S}D$ the estimated NSD. As a consequence

$$G_{CFF}(z) = N\tilde{S}D^{-1}$$

2.4 Standards for UPS Systems

In this Section the standard of reference to assess the dynamic performance of power converters in standalone microgrids/UPS systems supplying linear and nonlinear loads is described, highlighting the main relevant aspects. The standard of reference is the IEC 62040-3 normative [167], which sets the *method of specifying the performance and test requirements* for UPS systems. Specifically, it defines a UPS system as a *combination of converters, switches and energy storage devices (such as batteries), constituting a power system for maintaining continuity of load power in case of input power failure*. In this thesis the system addressed does not include energy storage devices, except for the DC source. The analysis is performed as "starting" from the DC link.

In normal mode of operation a UPS should be compatible with public low-voltage supplies. Among the main requirements, *the THD of voltage should be lower than 8% with a maximum level of individual harmonics according to the compatibility levels for individual harmonic voltages in low-voltage* networks, as imposed by IEC 61000-

2-2, reported in Table 2.1. Even though the UPS operates off-grid, this standard can be considered for further evaluations of harmonic distortion in the output supplied voltage.

Table 2.1 Compatibility levels for individual harmonic voltages in low voltage networks (rms values as percent of rms value of the fundamental component) - IEC 61000-2-2 standard

Odd harmonics non-multiple of 3		**Odd harmonics multiple of 3**		**Even harmonics**	
Harmonic order [h]	Harmonic voltage [%]	Harmonic order [h]	Harmonic voltage [%]	Harmonic order [h]	Harmonic voltage [%]
5	6	3	5	2	2
7	5	9	1.5	4	1
11	3.5	15	0.3	6	0.5
13	3	21	0.2	8	0.5
17≤n≤ 49	X_1[1]	21≤n≤ 45	0.2	10≤n≤ 50	X_2[2]

The lab-test experiments are performed to verify *the THD of voltage while supplying rated steady-state linear and nonlinear loads*, as specified in IEC 62040-3 — Annex E. Moreover, the HD of specific low-order harmonics multiples of the fundamental frequency are computed. *The output voltage transient deviation and recovery time for a step change in load current for both linear and nonlinear loads* are verified as well, in compliance with the standards specified in IEC 62040-3—Annex E.

The reference linear load R_l is resistive, such that

$$R_l = \frac{V_{r,l}^2}{P_{r,inv}}$$

Being $V_{r,l}$ the rms value of the line voltage (phase-to-phase) at inverter output in rated conditions, while $P_{r,inv}$ is the rated active power of the inverter. In this work, $V_{r,l} = \sqrt{3}\,220\ V$ and $P_{r,inv} = 2200\ W$ (unit power factor), which gives $R_l = 66\ \Omega$. A value of $R_l = 68\ \Omega$ has been set to perform the tests.

A diode bridge rectifier with an LC output filter supplying a resistive load is used as nonlinear load. The load resistance of the diode bridge rectifier is set such that the load rms current is equal to that supplying the reference linear load. With reference to a three-phase three-wire symmetrical system

$$S_{3f} = \sqrt{3} V_{r,l} I_r$$

[1] $X_1 = 2.27x(17/n)-0.27$
[2] $X_2 = 0.25x(10/n)+0.25$

with I_r being the rms value of the rated line current and S_{3f} the apparent power. With the values previously introduced $I_r \cong 3.3\ A$. It should be noted that this value slightly varies depending on the harmonic output voltage components, which are compensated by PR controllers tuned at specific low-order harmonics.

Depending on the load supplied, i.e. linear or nonlinear, the instantaneous voltage variation to a full step load change from open circuit to rated load shall comply with the limits imposed by the normative. With reference to Fig. 2.22, the voltage deviation from a reference value is mapped within an envelope which sets the acceptable voltage deviation boundaries, depending on the load supplied and the time occurrence during transient. In the following, the dynamic output performance in case of linear and nonlinear loads supply is verified according to similar curves imposed by the normative.

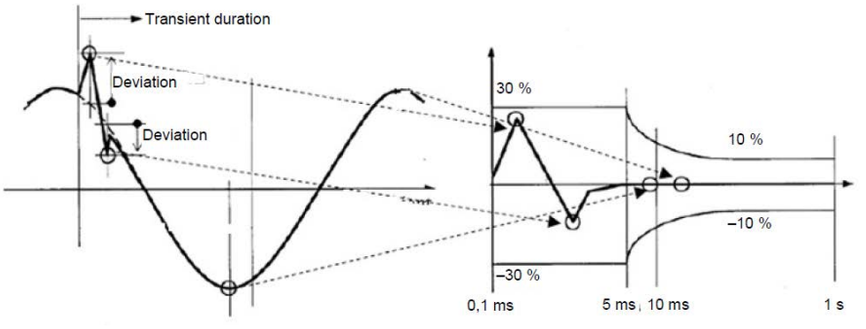

Fig. 2.22. Instantaneous voltage variation in compliance with the dynamic output performance imposed to critical loads. [Picture from IEC 62040-3 standard]

Chapter III

3 Physical System Modelling in the Continuous-Time Domain

3.1 Continuous-Time Domain Modelling

Part of the work described in this chapter has been previously published in [1], [7], [8], [14], [15], [16], [20], [21].

With reference to the block diagram of a three-phase VSI with voltage and current loops represented in Fig. 2.1, the simplified block diagram of the closed loop system is shown in Fig. 3.1.

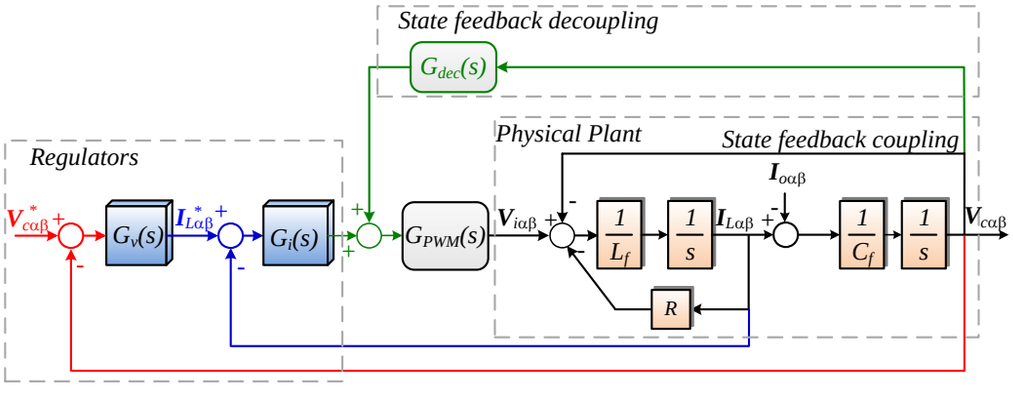

Fig. 3.1. Simplified block diagram of the closed loop system

$\boldsymbol{V}^*_{c\alpha\beta}$ and $\boldsymbol{I}^*_{L\alpha\beta}$ are the reference capacitor voltage and current vectors, $\boldsymbol{I}_{o\alpha\beta}$ is the output current vector, which acts as a disturbance to the system, and $\boldsymbol{V}_{i\alpha\beta}$ is the input voltage applied to the LC filter. $G_i(s)$ and $G_v(s)$ represent the current and voltage regulators transfer functions, $G_{PWM}(s)$ is the transfer function related to computation and PWM delays, whereas $G_{dec}(s)$ is the transfer function related to the decoupling of the controlled states. L_f and R are the filter inductor and its equivalent series resistance (ESR) respectively, while C_f is the filter capacitor. With reference to Fig. 2.1, the capacitor $C_f = 3C$ is the equivalent capacitance of a Y connection configuration.

The design of voltage and current regulators is based on serial tuning, with the innermost loop the first to be designed according to the desirable bandwidth and system damping [168]. In the next section the design of current regulators is discussed, with respect to voltage decoupling and the reduction in the achievable bandwidth whenever the computation and PWM delays are not compensated for on the decoupling path.

The differential equations describing the system in a single-phase representation are

$$\begin{cases} L_f \dfrac{di_L(t)}{dt} = v_i(t) - v_c(t) - i_L(t)R \\ C_f \dfrac{dv_c(t)}{dt} = i_L(t) - i_o(t). \end{cases} \tag{3.1}$$

The ESR of C_f is not considered in the model, since its effect appears far above the frequency range of concern [54], it is usually small and has little effect in dynamics. In the Laplacian domain

$$\begin{cases} sL_f I_L(s) = V_i(s) - V_c(s) - I_L(s)R \\ sC_f V_c(s) = I_L(s) - I_o(s). \end{cases} \tag{3.2}$$

Since

$$V_i(s) = [I_L^*(s) - I_L(s)]G_i(s)G_{PWM}(s). \tag{3.3}$$

Substituting the first equation of (3.2) in (3.3) leads to

$$sL_f I_L(s) = [I_L^*(s) - I_L(s)]G_i(s)G_{PWM}(s) - V_c(s) - I_L(s)R. \tag{3.4}$$

The equations are transformed to the $\alpha\beta$-stationary reference frame as

$$\begin{cases} sL_f \boldsymbol{I}_{L\alpha\beta}(s) = [\boldsymbol{I}_{L\alpha\beta}^*(s) - \boldsymbol{I}_{L\alpha\beta}(s)]\, G_i(s)G_{PWM}(s) - \boldsymbol{V}_{c\alpha\beta}(s) - \boldsymbol{I}_{L\alpha\beta}(s)R \\ sC_f \boldsymbol{V}_{c\alpha\beta}(s) = \boldsymbol{I}_{L\alpha\beta}(s) - \boldsymbol{I}_{o\alpha\beta}(s). \end{cases} \tag{3.5}$$

Where

$$\begin{cases} \boldsymbol{I}_{L\alpha\beta}(s) = I_{L\alpha}(s) + jI_{L\beta}(s) \\ \boldsymbol{I}_{o\alpha\beta}(s) = I_{o\alpha}(s) + jI_{o\beta}(s). \end{cases} \tag{3.6}$$

$$\boldsymbol{V}_{c\alpha\beta}(s) = V_{c\alpha}(s) + jV_{c\beta}(s). \tag{3.7}$$

3.2 Inner Current Loop Design

To design the inner current loop the block diagram of Fig. 3.2 is considered. The output current $\boldsymbol{I}_{o\alpha\beta}$ is related to $\boldsymbol{V}_{c\alpha\beta}$ through a generic load impedance $\boldsymbol{Z}(s)$.

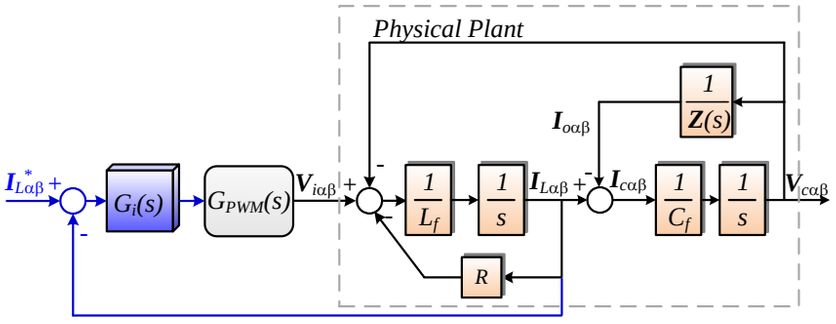

Fig. 3.2 Block diagram for the inner current loop

The design of the coefficients at the fundamental frequency of a PR controller, employed for the control of alternating quantities in the $\alpha\beta$-stationary reference frame, can be made starting from the design of a PI controller employed in the dq-rotating reference frame, as previously explained in Section 2.2.1.2. The link between the two controllers is represented by the rotational matrix.

The physical parameters of the inverter-side filter and the operation features of the inverter used in this work are given in Table 3.1. The grid frequency is $f_{grid} = 50\ Hz$.

Table 3.1 System Parameters

Parameter	Value
Switching frequency	$f_{sw} = 10\ kHz$
Filter inductance	$L_f = 1.8\ mH$
Filter capacitor	$C_f = 27\ \mu F$
Inductor ESR	$R = 0.1\ \Omega$
Linear load	$R_l = 68\ \Omega$
Nonlinear load	$C_{NL} = 235\ \mu F$ $R_{NL} = 155\ \Omega$ $L_{NL} = 0.084\ mH$

The proportional gain k_{pI} value is chosen to provide an inner current loop bandwidth of $\boldsymbol{f_{bw} = 1\ kHz}$ (1/10 of f_{sw}). However, it is possible to change this value to analyse its effect on the closed loop response. **Firstly, the design is based on neglecting the effect of capacitor voltage state cross-coupling**. It can be considered as a disturbance to the inner current loop. Therefore

$$k_{pI} = 2\pi f_{bw} L_f = \omega_{bw} L_f \rightarrow \quad k_{pI} \cong 11.31. \tag{3.8}$$

It must be remarked that the gain calculated in this design does not take into account the computation and PWM delays. These effects will be taken into account later, and the regulators gains shown here are just to have a reference value. The integral term of the PR controller k_{iI} does not change the bandwidth, but has an

influence in the gain and phase at 50 Hz. Higher values of k_{iI} reduce the magnitude and phase error at 50 Hz. A zero-pole cancellation approach can be used for its design

$$k_{pI} + \frac{k_{iI}}{s} = \frac{sk_{pI} + k_{iI}}{s} = \frac{k_p\left(s + \frac{k_{iI}}{k_{pI}}\right)}{s}. \tag{3.9}$$

According to the physical values of the inverter-side filter, the relationship between k_{pI} and k_{iI} is

$$\frac{k_{iI}}{k_{pI}} = \frac{R}{L_f} \rightarrow k_{iI} = \frac{R}{L_f} k_{pI}. \tag{3.10}$$

Therefore

$$k_{iI} \cong 628.$$

This is a reference value and will be changed in the design to show its effect on the inner current closed loop frequency response. The closed loop transfer function to analyse the behaviour of the inner loop is derived based on

$$\left[\boldsymbol{I}^*_{L\alpha\beta}(s) - \boldsymbol{I}_{L\alpha\beta}(s)\right] G_i(s) G_{PWM}(s) = \boldsymbol{V}_{i\alpha\beta}(s). \tag{3.11}$$

$$\boldsymbol{I}_{L\alpha\beta}(s) = \left[\boldsymbol{V}_{i\alpha\beta}(s) - \boldsymbol{V}_{c\alpha\beta}(s)\right] \frac{1}{sL_f + R}. \tag{3.12}$$

$$\boldsymbol{V}_{c\alpha\beta}(s) = \left[\boldsymbol{I}_{L\alpha\beta}(s) - \boldsymbol{I}_{o\alpha\beta}(s)\right] \frac{1}{C_f s}. \tag{3.13}$$

Rearranging (3.12) and substituting in (3.11), leads to

$$\boldsymbol{I}_{L\alpha\beta}(s)\left(sL_f + R\right) + \boldsymbol{V}_{c\alpha\beta}(s) = \boldsymbol{V}_{i\alpha\beta}(s)(s) \rightarrow$$

$$\boldsymbol{I}_{L\alpha\beta}(s)\left(sL_f + R\right) + \boldsymbol{V}_{c\alpha\beta}(s) = \left[\boldsymbol{I}^*_{L\alpha\beta}(s) - \boldsymbol{I}_{L\alpha\beta}(s)\right] G_i(s) G_{PWM}(s). \tag{3.14}$$

Substituting (3.13) in (3.14) and rearranging

$$\boldsymbol{I}_{L\alpha\beta}(s)\left(sL_f + R\right) + \left[\boldsymbol{I}_{L\alpha\beta}(s) - \boldsymbol{I}_{o\alpha\beta}(s)\right] \frac{1}{C_f s} = G_i(s) G_{PWM}(s) \boldsymbol{I}^*_{L\alpha\beta}(s) - G_i(s) G_{PWM}(s) \boldsymbol{I}_{L\alpha\beta}(s) \rightarrow$$

$$\boldsymbol{I}_{L\alpha\beta}(s)\left(sL_f + R\right) + \boldsymbol{I}_{L\alpha\beta}(s) \frac{1}{sC_f} + G_i(s) G_{PWM}(s) \boldsymbol{I}_{L\alpha\beta}(s) = G_i(s) G_{PWM}(s) \boldsymbol{I}^*_{L\alpha\beta}(s) + \boldsymbol{I}_{o\alpha\beta}(s) \frac{1}{C_f s} \rightarrow$$

$$\left[\left(sL_f + R\right) C_f s + G_i(s) G_{PWM}(s) C_f s + 1\right] \boldsymbol{I}_{L\alpha\beta}(s) = G_i(s) G_{PWM}(s) C_f s \boldsymbol{I}^*_{L\alpha\beta}(s) + \boldsymbol{I}_{o\alpha\beta}(s) \rightarrow$$

$$\boldsymbol{I}_{L\alpha\beta}(s) = \frac{G_i(s)G_{PWM}(s)C_f s}{L_f C_f s^2 + RC_f s + G_i(s)G_{PWM}(s)C_f s + 1}\boldsymbol{I}^*_{L\alpha\beta}(s) + \frac{1}{L_f C_f s^2 + RC_f s + G_i(s)G_{PWM}(s)C_f s + 1}\boldsymbol{I}_{o\alpha\beta}(s)\,. \tag{3.15}$$

This transfer function can be analysed in two ways: i) by looking just at the tracking features of the controller and analyse the effect of $\boldsymbol{V}_{c\alpha\beta}(s)$ [or $\boldsymbol{I}_{o\alpha\beta}(s)$] as a disturbance (disturbance rejection properties). For this case, neglecting $\boldsymbol{V}_{c\alpha\beta}(s)$ [or $\boldsymbol{I}_{o\alpha\beta}(s)$] results in the analysis of the tracking performance, and neglecting $\boldsymbol{I}^*_{L\alpha\beta}(s)$ results in the analysis of the disturbance rejection; ii) by including the effect of $\boldsymbol{I}_{o\alpha\beta}(s)$ as a function of the output voltage and load impedance. For this case, it is possible to have in just one transfer function the steady-state features of the tracking and disturbance. However, the resulting frequency response is load dependent. To take into account this effect, the following model can be employed

$$\boldsymbol{I}_{o\alpha\beta}(s) = \frac{\boldsymbol{V}_{c\alpha\beta}(s)}{\boldsymbol{Z}(s)}\,. \tag{3.16}$$

By substituting (3.16) in (3.13) and rearranging

$$\boldsymbol{I}_{o\alpha\beta}(s) = \frac{\boldsymbol{I}_{L\alpha\beta}(s) - \boldsymbol{I}_{o\alpha\beta}(s)}{\boldsymbol{Z}(s)C_f s} \rightarrow$$

$$\boldsymbol{Z}(s)C_f s\boldsymbol{I}_{o\alpha\beta}(s) + \boldsymbol{I}_{o\alpha\beta}(s) = \boldsymbol{I}_{L\alpha\beta}(s) \rightarrow$$

$$\left[\boldsymbol{Z}(s)C_f s + 1\right]\boldsymbol{I}_{o\alpha\beta}(s) = \boldsymbol{I}_{L\alpha\beta}(s) \rightarrow$$

$$\boldsymbol{I}_{o\alpha\beta}(s) = \frac{1}{\boldsymbol{Z}(s)C_f s + 1}\boldsymbol{I}_{L\alpha\beta}(s)\,. \tag{3.17}$$

Consequently, substituting (3.17) in (3.15)

$$\boldsymbol{I}_{L\alpha\beta}(s) = \frac{G_i(s)G_{PWM}(s)C_f s}{L_f C_f s^2 + RC_f s + G_i(s)G_{PWM}(s)C_f s + 1}\boldsymbol{I}^*_{L\alpha\beta}(s) + \frac{1}{\left[L_f C_f s^2 + RCs + G_i(s)G_{PWM}(s)C_f s + 1\right]}\frac{1}{\left[\boldsymbol{Z}(s)C_f s + 1\right]}\boldsymbol{I}_{L\alpha\beta}(s) \rightarrow$$

$$\boldsymbol{I}_{L\alpha\beta}(s)\left\{1-\frac{1}{\left[L_fC_fs^2+RC_fs+G_i(s)G_{PWM}(s)C_fs+1\right]\left[\boldsymbol{Z}(s)C_fs+1\right]}\right\}$$
$$=\frac{G_i(s)G_{PWM}(s)Cs}{L_fC_fs^2+RC_fs+G_i(s)G_{PWM}(s)C_fs+1}\boldsymbol{I}^*_{L\alpha\beta}(s)\rightarrow$$

$$\boldsymbol{I}_{L\alpha\beta}(s)\left\{\frac{\left[L_fC_fs^2+RC_fs+G_i(s)G_{PWM}(s)C_fs+1\right]\left[\boldsymbol{Z}(s)C_fs+1\right]-1}{\left[(L_fC_fs^2+RC_fs+G_i(s)G_{PWM}(s)C_fs+1)\right]\left[\boldsymbol{Z}(s)C_fs+1\right]}\right\}$$
$$=\frac{G_i(s)G_{PWM}(s)C_fs}{L_fC_fs^2+RC_fs+G_i(s)G_{PWM}(s)C_fs+1}\boldsymbol{I}^*_{L\alpha\beta}(s)\rightarrow$$

$$\boldsymbol{I}_{L\alpha\beta}(s)=\frac{G_i(s)G_{PWM}(s)C_fs\left[\boldsymbol{Z}(s)C_fs+1\right]}{\left[L_fC_fs^2+RC_fs+G_i(s)G_{PWM}(s)C_fs+1\right]\left[\boldsymbol{Z}(s)C_fs+1\right]-1}\boldsymbol{I}^*_{L\alpha\beta}(s)\rightarrow$$

$$\boldsymbol{I}_{L\alpha\beta}(s)=\frac{\boldsymbol{Z}(s)C_f^2sG_i(s)G_{PWM}(s)+G_i(s)G_{PWM}(s)C_f}{a_{den_1}s^2+b_{den_1}s+c_{den_1}}\boldsymbol{I}^*_{L\alpha\beta}(s), \tag{3.18}$$

being

$$a_{den_1}=\boldsymbol{Z}(s)L_fC_f^2,$$

$$b_{den_1}=\boldsymbol{Z}(s)RC_f^2+Z(s)C_f^2G_i(s)G_{PWM}(s)+L_fC_f,$$

$$c_{den_1}=\boldsymbol{Z}(s)C_f+RC_f+G_i(s)G_{PWM}(s)C_f.$$

The two transfer functions in (3.15) and (3.18) include the effect of the output voltage on the current loop. One way to eliminate this effect is performing a voltage cross-coupling decoupling. If the output voltage is measured, it is possible to decouple its effect on the inner current loop as shown in Fig. 3.3.

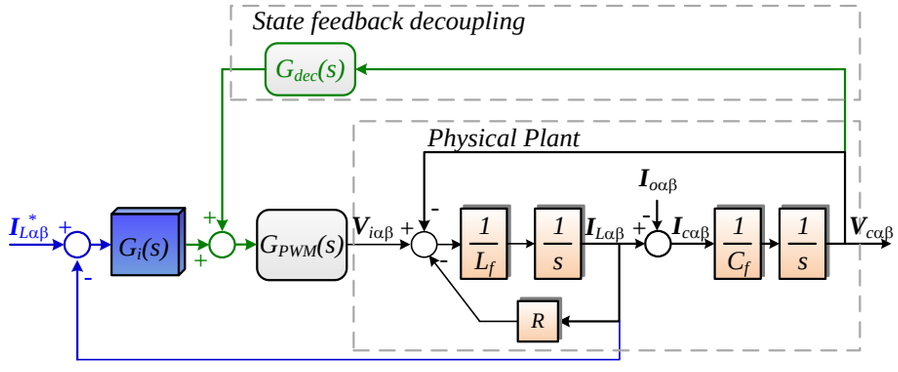

Fig. 3.3 Block diagram of the inner current loop with output voltage cross-coupling decoupling

For the system presented in Fig. 3.3, the following transfer function can be derived

$$\boldsymbol{V}_{i\alpha\beta}(s) = G_i(s)G_{PWM}(s)\left[\boldsymbol{I}^*_{L\alpha\beta}(s) - \boldsymbol{I}_{L\alpha\beta}(s)\right] + G_{dec}(s)G_{PWM}(s)\boldsymbol{V}_{c\alpha\beta}(s). \quad (3.19)$$

Therefore

$$\boldsymbol{I}_{L\alpha\beta}(s) = \left[\boldsymbol{V}_{i\alpha\beta}(s) - \boldsymbol{V}_{c\alpha\beta}(s)\right]\frac{1}{sL_f + R} \rightarrow$$

$$\left(L_f s + R\right)\boldsymbol{I}_{L\alpha\beta}(s) = \boldsymbol{V}_{i\alpha\beta}(s) - \boldsymbol{V}_{c\alpha\beta}(s) \rightarrow$$

$$\begin{aligned}\left(L_f s + R\right)&\boldsymbol{I}_{L\alpha\beta}(s)\\ &= G_i(s)G_{PWM}(s)\left[\boldsymbol{I}^*_{L\alpha\beta}(s) - \boldsymbol{I}_{L\alpha\beta}(s)\right] + G_{dec}(s)G_{PWM}(s)\boldsymbol{V}_{c\alpha\beta}(s)\\ &- \boldsymbol{V}_{c\alpha\beta}(s) \rightarrow\end{aligned}$$

$$\begin{aligned}\left(L_f s + R\right)&\boldsymbol{I}_{L\alpha\beta}(s)\\ &= G_i(s)G_{PWM}(s)\boldsymbol{I}^*_{L\alpha\beta}(s) - G_i(s)G_{PWM}(s)\boldsymbol{I}_{L\alpha\beta}(s)\\ &+ [G_{dec}(s)G_{PWM}(s) - 1]\boldsymbol{V}_{c\alpha\beta}(s).\end{aligned} \quad (3.20)$$

Substituting (3.13) in (3.20) leads to

$$\begin{aligned}\left[L_f s + R + G_i(s)G_{PWM}(s)\right]&\boldsymbol{I}_{L\alpha\beta}(s)\\ &= G_i(s)G_{PWM}(s)\boldsymbol{I}^*_{L\alpha\beta}(s)\\ &+ [G_{dec}(s)G_{PWM}(s) - 1]\frac{\left[\boldsymbol{I}_{L\alpha\beta}(s) - \boldsymbol{I}_{o\alpha\beta}(s)\right]}{C_f s} \rightarrow\end{aligned}$$

$$\begin{aligned}C_f s\left[L_f s + R + G_i(s)G_{PWM}(s)\right]&\boldsymbol{I}_{L\alpha\beta}(s)\\ &= G_i(s)G_{PWM}(s)Cs\boldsymbol{I}^*_{L\alpha\beta}(s) + [G_{dec}(s)G_{PWM}(s) - 1]\boldsymbol{I}_{L\alpha\beta}(s)\\ &- [G_{dec}(s)G_{PWM}(s) - 1]\boldsymbol{I}_{o\alpha\beta}(s) \rightarrow\end{aligned}$$

$$\begin{aligned}\left\{L_f C_f s^2 + RCs + G_i(s)G_{PWM}(s)Cs - [G_{dec}(s)G_{PWM}(s) - 1]\right\}&\boldsymbol{I}_{L\alpha\beta}(s)\\ &= G_i(s)G_{PWM}(s)Cs\boldsymbol{I}^*_{L\alpha\beta}(s) - [G_{dec}(s)G_{PWM}(s) - 1]\boldsymbol{I}_{o\alpha\beta}(s) \rightarrow\end{aligned}$$

$$\begin{aligned}&\boldsymbol{I}_{L\alpha\beta}(s)\\ &= \frac{G_i(s)G_{PWM}(s)C_f s}{L_f C_f s^2 + RCs + G_i(s)G_{PWM}(s)Cs - [G_{dec}(s)G_{PWM}(s) - 1]}\boldsymbol{I}^*_{L\alpha\beta}(s)\\ &- \frac{G_{dec}(s)G_{PWM}(s) - 1}{L_f C_f s^2 + RC_f s + G_i(s)G_{PWM}(s)C_f s - [G_{dec}(s)G_{PWM}(s) - 1]}\boldsymbol{I}_{o\alpha\beta}(s).\end{aligned} \quad (3.21)$$

By considering *ideal voltage cross-coupling decoupling* (this corresponds to design $G_{dec}(s) = G_{PWM}(s)^{-1}$), the closed loop transfer function for the inner current loop is

$$\boldsymbol{I}_{L\alpha\beta}(s) = \frac{G_i(s)G_{PWM}(s)}{L_f s + R + G_i(s)G_{PWM}(s)} \boldsymbol{I}^*_{L\alpha\beta}(s). \tag{3.22}$$

By observing this transfer function, it is possible to conclude that the output current does not affect anymore the inner current loop. This results in an easier design of the controller, with better dynamics, and with a dynamic behaviour that is not load sensitive.

To analyse the dynamic properties of the above transfer function it is necessary to choose the regulator topology (and its design), and to choose the appropriate model of the delay. In the next sections these topics will be addressed.

3.3 System Delay Modelling

The first thing to consider in the analysis is what model should be used for the computation and PWM delays. The physical delay has the form of an exponential decay ($e^{-T_d s}$). There are at least two first-order expressions based on rational transfer functions that are usually used to approximate the delay (options based on the first order Padé approximation) [37]

$$e^{-T_d s} \approx \frac{1}{1 + T_d s}. \tag{3.23}$$

$$e^{-T_d s} \approx \frac{1 - (T_d/2)s}{1 + (T_d/2)s}. \tag{3.24}$$

By considering $T_d = 1.5T_s$ and $T_s = 100\ \mu s$ ($f_s = 10\ kHz$), the frequency response of $e^{-T_d s}$, (3.23), and (3.24) are shown in Fig. 3.4. From this plot, it is clear that the approximation to be used depends on the frequency range to analyse, and this is coupled to the bandwidth chosen for the regulators. For the approximation using a first order lag, i.e. (3.23), the match is very good until approximately 300 Hz ($f_s/30$). On the other hand, for the approximation using a zero in the right half plane, i.e. (3.24), the match is satisfactory until 1 kHz ($f_s/10$). Therefore, if the inner loop is designed to have a wide bandwidth or the regulator is supposed to control harmonics, the expression (3.24) is the approximation to be used. To employ an inadequate approximation can lead to wrong design as it is shown later in this thesis.

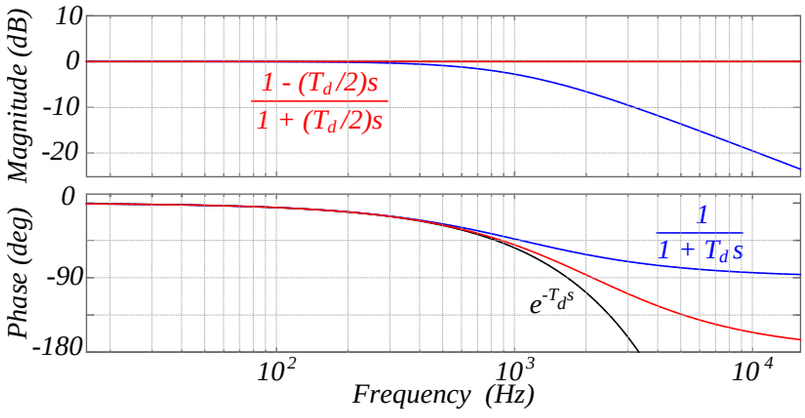

Fig. 3.4 Frequency response of the delay (exponential) and its approximations (first order lag and fist order Padé approximations) - $\boldsymbol{T_d = 1.5T_s = 150\ \mu s}$

3.4 Regulators Topologies

The analysis of the inner current loop is performed considering the following regulators:

1) P controller:

$$G_i(s) = k_{pI}$$

2) Nonideal PR controller ($\omega_o = 2\pi 50\ rad/s,\ \omega_c = 5\ rad/s$)

$$G_i(s) = k_{pI} + \frac{2k_{iI}\omega_c s}{s^2 + 2\omega_c s + \omega_o^2}$$

3) Ideal PR controller ($\omega_o = 2\pi 50\ rad/s$)

$$G_i(s) = k_{pI} + \frac{k_{iI} s}{s^2 + \omega_o^2}$$

4) Complex Vector PR controller (VPR) ($\omega_o = 2\pi 50\ rad/s$)

$$G_i(s) = \frac{k_{pI} s^2 + k_{iI} s}{s^2 + \omega_o^2}$$

In the next sections the effect of state feedback voltage decoupling on the performance of these regulators structures is investigated.

3.4.1 P Regulator

3.4.1.1 P controller without voltage decoupling

As a benchmark for comparison, the P controller is used. Also, a bandwidth for the inner current loop equal to 1 kHz is considered. The design of the gain depends on the delay model used and whether voltage decoupling is performed. The first case analysed is without voltage decoupling, i.e. $G_{dec}(s) = 0$, and neglecting computation and PWM delays, i.e. $G_{PWM}(s) = 1$. Neglecting $\boldsymbol{I}_{o\alpha\beta}(s)$ in (3.21) results in the analysis of the tracking performance, leading to

$$\boldsymbol{I}_{L\alpha\beta}(s) = \frac{G_i(s)C_f s}{L_f C_f^2 s^2 + \left(RC_f + G_i(s)C_f\right)s + 1}\boldsymbol{I}^*_{L\alpha\beta}(s). \tag{3.25}$$

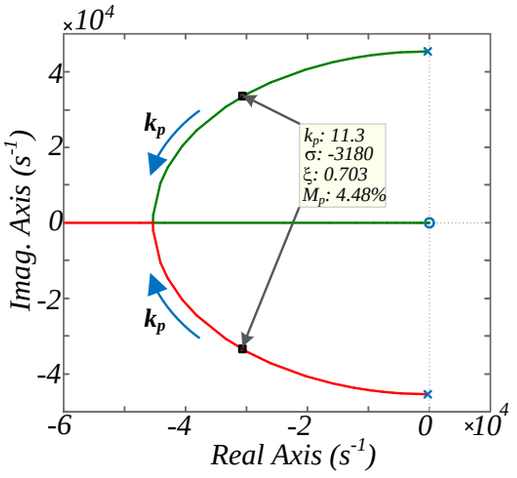

Fig. 3.5 Root locus for the inner current loop with **P regulator, without voltage decoupling and neglecting system delays**: x – open loop poles; ■ closed loop poles for $\boldsymbol{k_{pI} = 11.32}$; o – zeros

It can be noticed from the root locus in Fig. 3.5 that as the gain is increased, higher damping is achieved. This is in contrast with the results obtained if system delays are included for analysis.

The second case analysed is without voltage decoupling and using the model for the delay in (3.23). The block diagram used to tune the system is shown in Fig. 3.6.

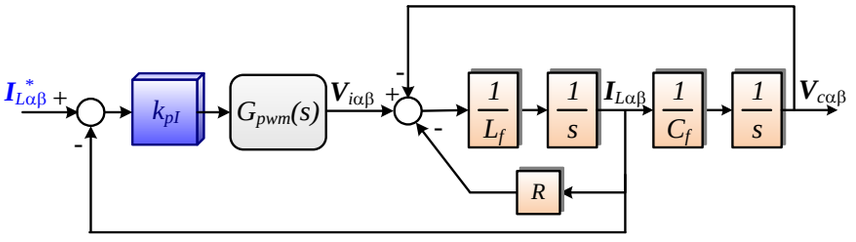

(a)

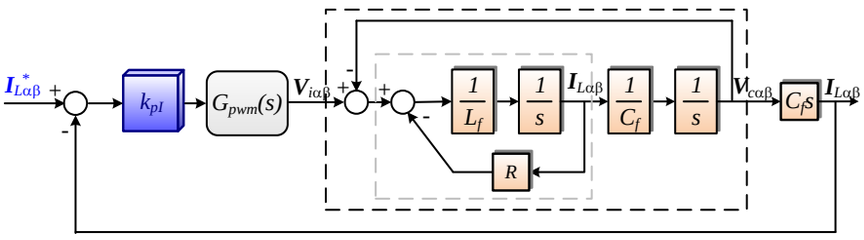

(b)

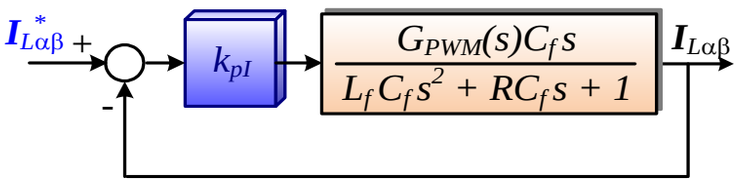

(c)

Fig. 3.6 Block diagram used for tuning the inner current loop without voltage decoupling: (a) simplification neglecting the output current; (b) block diagram manipulation of (a); (c) resulting open loop transfer function from (b)

The root locus of this system with the open and closed loop poles is shown in Fig. 3.7. The open loop poles are complex conjugate due to the coupling of the capacitor voltage.

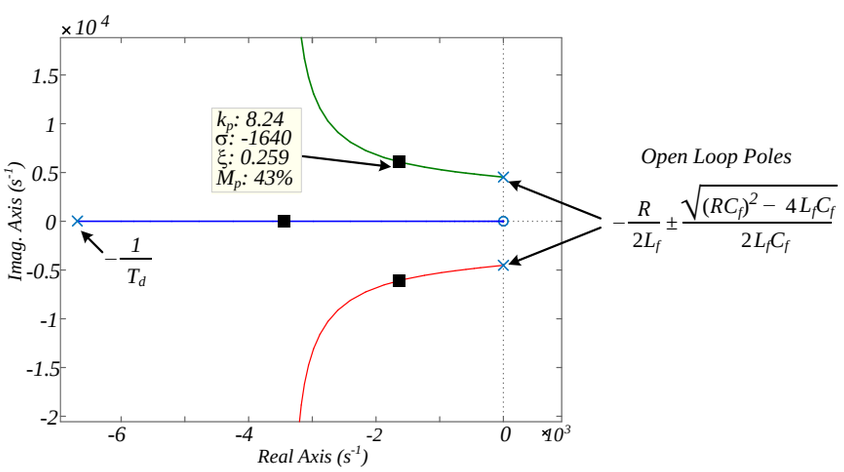

Fig. 3.7 Root locus for the inner current loop with **P regulator and without voltage decoupling**: x – open loop poles; ■ closed loop poles for $\boldsymbol{k_{pI} = 8.24}$; o - zeros; $\boldsymbol{G_{PWM}(s) = 1/(1 + T_d s)}$

It must be noted that no matter the bandwidth of the system is, the closed loop system will always have low damping. For the chosen bandwidth of 1 kHz the regulator gain is approximately $\boldsymbol{k_{pI} = 8.12}$.

Fig. 3.8 shows the eigenvalue and zero migration as a function of the load. It shows that the system has a faster and lower damping behaviour as the load increases.

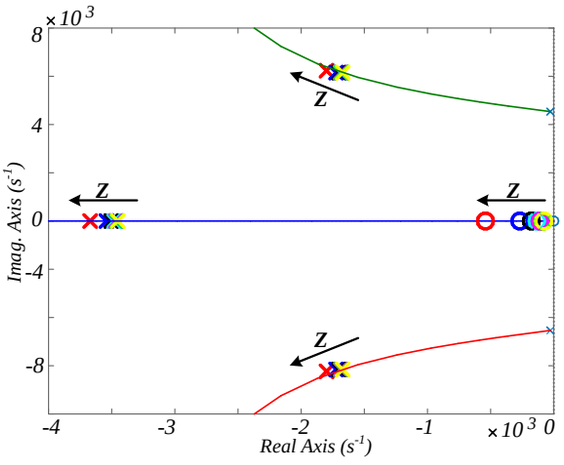

Fig. 3.8 Closed loop eigenvalue migration as a function of the load: arrows indicate increasing of the load impedance: x – closed loop poles; o – zeros; $\boldsymbol{G_{PWM}(s) = 1/(1 + T_d s)}$

The frequency response as a function of the load impedance is shown in Fig. 3.9. The arrow indicates increase in the load impedance, from short circuit (command tracking performance only) to open circuit conditions. For any value of the impedance the system shows a low gain for a broad frequency range including fundamental frequency (50 Hz), which means the commanded reference is not properly tracked resulting in very high steady-state error. That is why in some research work the use of resonant regulators is suggested for this loop [26].

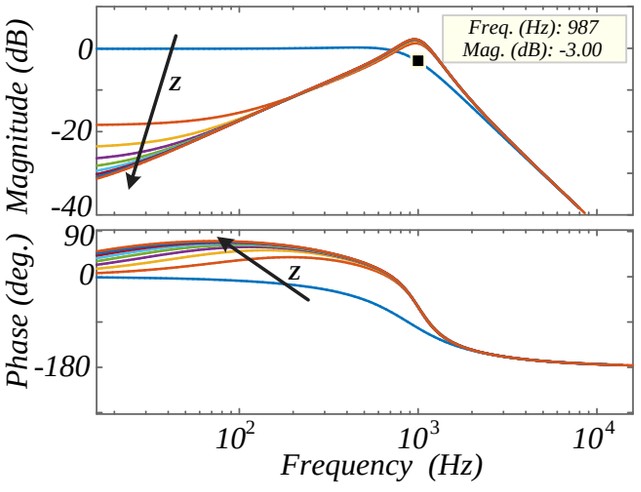

Fig. 3.9 Closed loop frequency response for the inner current loop with **P regulator without voltage decoupling**: effect of the load – arrows indicate increasing in the load impedance (from short circuit until open circuit); $\boldsymbol{G_{PWM}(s) = 1/(1 + T_d s)}$

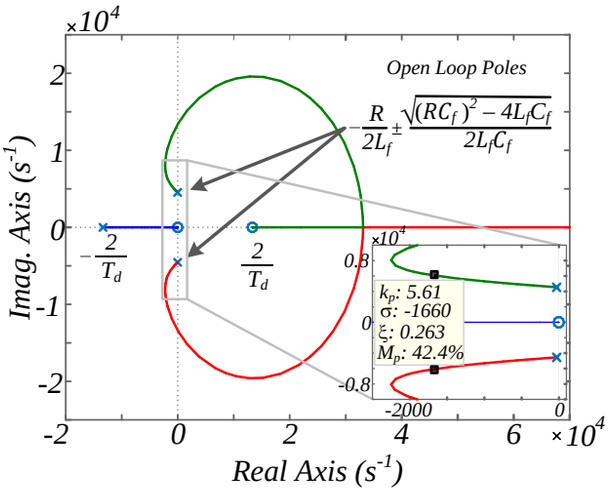

Fig. 3.10 Root locus for the inner current loop with **P regulator and without voltage decoupling**: x – open loop poles; ■ closed-loop poles for $\boldsymbol{k_{pI} = 5.61}$; o – zeros; $\boldsymbol{G_{PWM}(s) = (1 - T_d s/2)/(1 + T_d s/2)}$

However, as it will be shown later, using some resonant structures without voltage decoupling can lead to instability, independently of the regulator gains. Furthermore, at short circuit, the system behaves as an RL load. At this condition, it can be seen that the system bandwidth is approximately 1 kHz, as designed. However, it is difficult to assess the bandwidth of the system because the gain at low frequency is changing, and it is not possible to have a specific value for it at low frequencies.

By considering the delay model in (3.24), the root locus of the system is presented in Fig. 3.10. This root locus shows that due to the right half plane zero (non-minimal phase zero) the system can become unstable for certain gain values. This explains why the real system becomes unstable when the gain is increased above a certain value. This behaviour cannot be predicted when the model in (3.23) is used as approximation for computation and PWM delays.

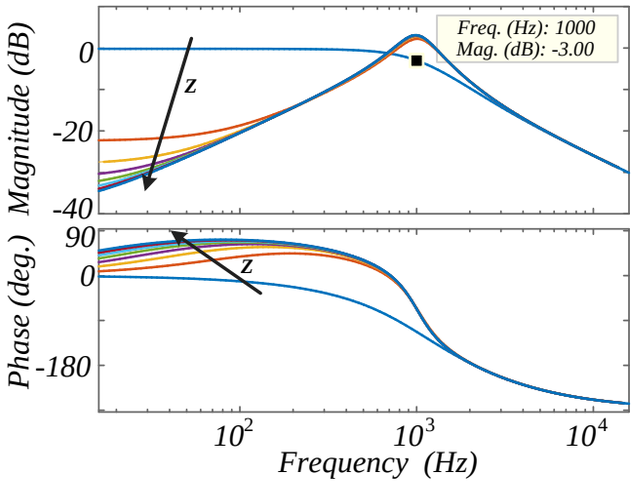

Fig. 3.11 Closed loop frequency response for the inner current loop with **P regulator and without voltage decoupling**: effect of the load – arrows indicate increasing in the load impedance (from short circuit until open circuit); $\boldsymbol{G_{PWM}(s) = (1 - T_d s/2)/(1 + T_d s/2)}$

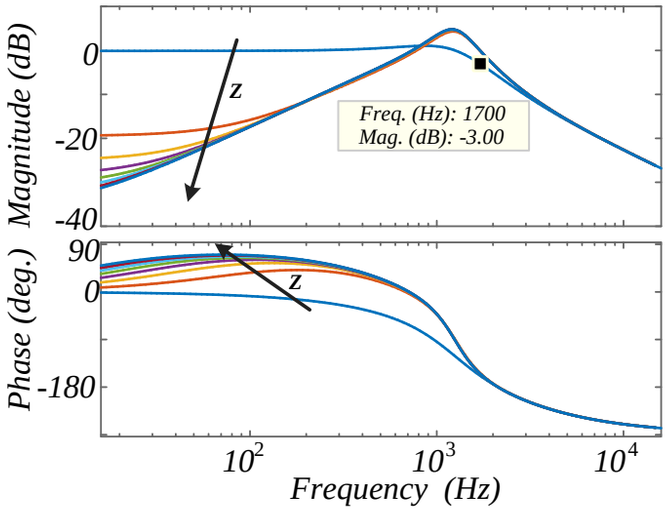

Fig. 3.12 Closed loop frequency response for the inner current loop with **P regulator and without voltage decoupling**: effect of the load – arrows indicate increasing in the load impedance (from short circuit until open circuit); $\boldsymbol{G_{PWM}(s) = (1 - T_d s/2)/(1 + T_d s/2)}$

Another important consideration is as follows: to have the same bandwidth as for the case when $G_{PWM}(s) = 1/(1 + T_d s)$, implies that the gain value should be $\boldsymbol{k_{pI} = 5.61}$. This is shown in the frequency response of Fig. 3.11. If the gain value is kept equal to $k_{pI} = 8.24$, the resulted bandwidth is approximately 1.7 kHz, as can be seen in Fig. 3.12.

The main outcomes of this analysis are here summarized:

- The capacitor coupling produces load dependent dynamics;

- Even with a P regulator the resulting closed loop system has a very low damping;
- The P regulator is unable to produce zero steady-state error at 50 Hz;
- The delay model affects the understanding of the system behaviour and the design of the regulator. Table 3.2 summarizes the gain values as a function of the delay model used to design the system for a bandwidth of approximately 1 kHz. There is a difference between the design with and without delay that can reach approximately 50%, depending on the delay model used.

Table 3.2 Designed regulator parameter as a function of the delay model to have 1 kHz bandwidth without state feedback voltage decoupling

Delay Model	Value
$\boldsymbol{G_{PWM}(s) = 1}$ (no delay)	$k_{pI} = 11.31$
$\boldsymbol{G_{PWM}(s) = 1/[1 + T_d s]}$	$k_{pI} = 8.24$
$\boldsymbol{G_{PWM}(s) = [1 - (T_d/2)s]/[1 + (T_d/2)s]}$	$k_{pI} = 5.61$

3.4.1.2 P controller with ideal voltage decoupling

If it were possible to exactly decouple (cancel) the capacitor coupling as shown in Fig. 3.3, the simplified model presented in Fig. 3.13 could be used to analyse the dynamic behaviour of the inner current loop.

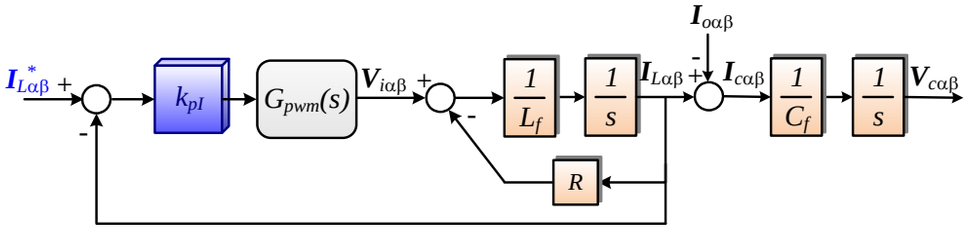

Fig. 3.13 Simplified block diagram of the inner current loop with ideal voltage decoupling

In this case, *ideal voltage decoupling* is achieved. As can be seen, the load does not have influence on the inner current loop anymore. The corresponding closed loop transfer function has been previously derived [see (3.22)], to which corresponds the following open loop transfer function, with gain k_{pI}

$$OL(s) = k_{pI}\frac{G_{PWM}(s)}{L_f s + R}. \tag{3.26}$$

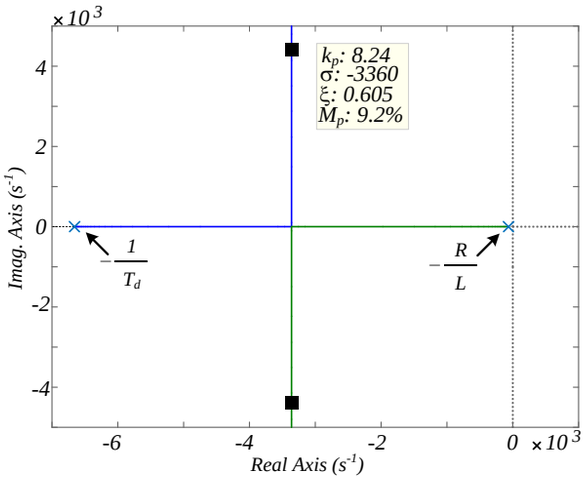

Fig. 3.14 Root locus for the inner current loop with **P regulator and with ideal voltage decoupling**: x – open loop poles; ■ closed loop poles for $\boldsymbol{k_{pI} = 8.24}$; o – zeros; $\boldsymbol{G_{PWM}(s) = 1/(1 + T_d s)}$

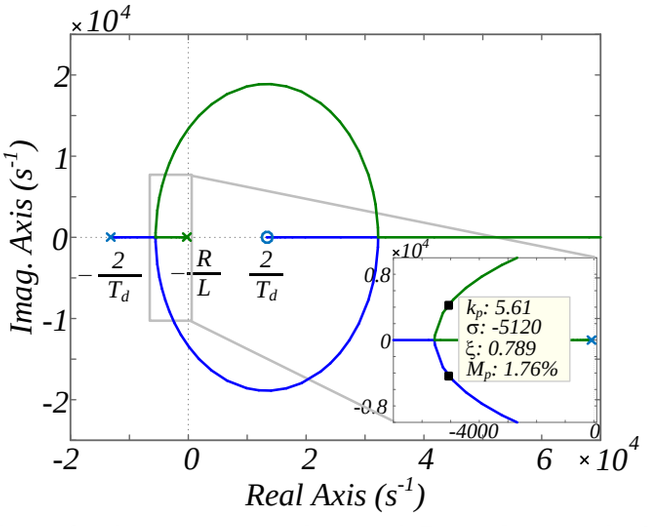

Fig. 3.15 Root locus for the inner current loop with **P regulator and with ideal voltage decoupling**: x – open loop poles; ■ closed-loop poles for $\boldsymbol{k_{pI} = 5.61}$; o – zeros; $\boldsymbol{G_{PWM}(s) = (1 - T_d s/2)/(1 + T_d s/2)}$

For this system, the root loci for the two delay models are presented in Fig. 3.14 and Fig. 3.15. As can be seen, due to the cross-coupling decoupling, the open loop poles are real. Therefore, the tuning is much easier and the resulting closed loop systems present a damping much higher than for the case without decoupling, for the same bandwidth of 1 kHz. Furthermore, for the delay model with the zero on the right half-plane, the system will be stable for values of $k_{pI} < (2L_f + RT_d)/T_d$. With reference to the plant values in Table 3.1, the system is stable for $k_{pI} < 24.1$.

With reference to the root locus in Fig. 3.16, the gain has been slightly increased to $k_{pI} = 6.42$, to which corresponds the damping factor $\xi = 0.707$. The correspondent bandwidth increases to about 1.2 kHz.

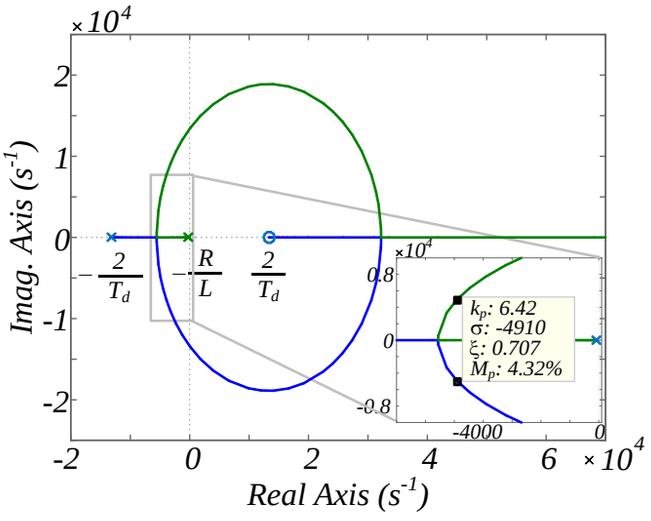

Fig. 3.16 Root locus for the inner current loop with **P regulator and with ideal voltage decoupling**: x – open loop poles; ■ closed-loop poles for $\boldsymbol{k_{pI} = 6.42}$; o – zeros; $\boldsymbol{G_{PWM}(s) = (1 - T_d s/2)/(1 + T_d s/2)}$

Fig. 3.17 and Fig. 3.18 show the frequency response of the closed loop system for the P regulator with ideal voltage decoupling using the two delay models. The system is not anymore load dependent, and except for the different gains ($k_{pI} = 8.28$ in Fig. 3.17 and $k_{pI} = 6.42$ in Fig. 3.18) the system has approximately the same behaviour with the expected bandwidth.

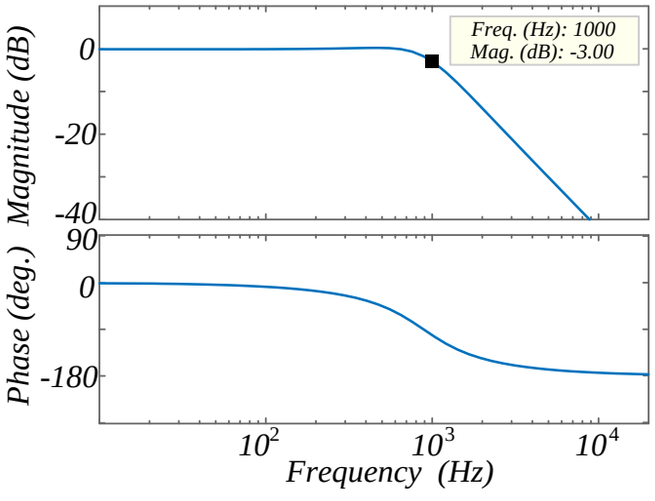

Fig. 3.17 Closed loop frequency response for the inner current loop with **P regulator with voltage decoupling** for $\boldsymbol{k_{pI} = 8.28}$: $\boldsymbol{G_{PWM}(s) = 1/(1 + T_d s)}$

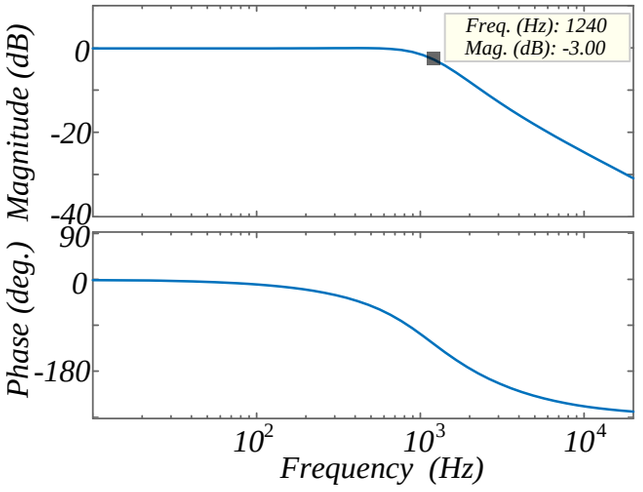

Fig. 3.18 Closed loop freq. response for the inner current loop with **P regulator with voltage decoupling** for $\boldsymbol{k_{pI} = 6.42}$: $\boldsymbol{G_{PWM}(s) = (1 - T_d s/2)/(1 + T_d s/2)}$

From now on, all the analysis will be presented only for the delay model $G_{PWM}(s) = [1 - (T_d/2)s]/[1 + (T_d/2)s]$. This model is adopted to simulate the system and represents better the dynamic properties observed during the simulations. It must be noted that if the bandwidth of the regulators and frequency range of interesting is low, there is no significant difference of using one or other model.

Looking again at the open loop transfer function in (3.26)

$$OL(s) = k_{pI}\frac{G_{PWM}(s)}{L_f s + R} \rightarrow$$

$$OL(s) = k_{pI}\frac{[1 - (T_d/2)s]}{[L_f s + R][1 + (T_d/2)s]} \rightarrow$$

$$OL(s) = k_{pI}\frac{2 - T_d s}{L_f T_d s^2 + (2L_f + RT_d)s + 2R} \rightarrow$$

The correspondent closed loop transfer function is

$$CL(s) = \frac{-\frac{k_{pI}}{L_f}s + \frac{2k_{pI}}{L_f T_d}}{s^2 + \left(\frac{2L_f + RT_d - T_d k_{pI}}{L_f T_d}\right)s + \left(\frac{2R + 2k_{pI}}{L_f T_d}\right)} \rightarrow$$

$$\boldsymbol{I}_{L\alpha\beta}(s) = \frac{-\frac{k_{pI}}{L_f}s + \frac{2k_{pI}}{L_f T_d}}{s^2 + \left(\frac{2L_f + RT_d - T_d k_{pI}}{L_f T_d}\right)s + \left(\frac{2R + 2k_{pI}}{L_f T_d}\right)} \boldsymbol{I}^*_{L\alpha\beta}(s). \quad (3.27)$$

Being a canonical 2nd order system of the form

$$G(s) = \frac{\omega_n^2}{s^2 + 2\zeta\omega_n s + \omega_n^2}. \quad (3.28)$$

We can approximately apply the following relationships to the settling time, peak time, and overshoot, respectively

$$t_{s,2\%} = 4\tau \approx \frac{4}{\sigma}$$

$$t_p = \frac{\pi}{\omega_d}$$

$$M_p = e^{-\zeta\pi/\sqrt{1-\zeta^2}}$$

The main outcomes of this analysis are:

- The capacitor voltage decoupling produces load independent dynamics with good dynamic properties**;**
- The resulted system with a proportional regulator (for the same bandwidth) has a much higher damping than the case without voltage decoupling**;**
- The delay model affects the design of the regulator**;**
- The P regulator with voltage decoupling can produce almost zero steady-state error for this system. It must be remarked that the reason for producing this error is because the equivalent series resistance of the inductor is very small for this system (0.1 **Ω**). The bigger this value is the bigger will be the steady-state error**;**
- It is possible to use just a P regulator in the inner current loop when there is an outer voltage loop as is the case with isolated microgrids/UPS systems.

3.4.1.3 P controller with nonideal voltage decoupling

The results presented in the previous section consider the decoupling as ideal. Unfortunately, unless a lead compensator is designed to compensate for all the delays in the system (computation, PWM and measurement) the decoupling will be nonideal. In practice, the decoupling should be done using a system as shown in Fig. 3.3. $G_{dec}(s)$ must be designed to compensate for the delays (lead compensator). To see the effect

of $G_{dec}(s)$ on the system, the transfer function previously derived [see (3.21)] must be analysed, taking into account the load dependency [see (3.17)], leading to

$$\boldsymbol{I}_{L\alpha\beta}(s) = \frac{G_i(s)G_{PWM}(s)C_f s}{L_f C_f s^2 + RC_f\, s + G_i(s)G_{PWM}(s)C_f s + 1 - G_{dec}(s)G_{PWM}(s)}\boldsymbol{I}^*_{L\alpha\beta}(s) - \frac{G_{dec}(s)G_{PWM}(s) - 1}{L_f C_f s^2 + RC_f s + G_i(s)G_{PWM}(s)C_f s + 1 - G_{dec}(s)G_{PWM}(s)}\frac{1}{\boldsymbol{Z}(s)C_f s + 1}\boldsymbol{I}^*_{L\alpha\beta}(s) \rightarrow$$

$$\boldsymbol{I}_{L\alpha\beta}(s)\left\{\frac{\left[L_f C_f s^2 + RC_f s + G_i(s)G_{PWM}(s)C_f s + 1 - G_{dec}(s)G_{PWM}(s)\right]\left[\boldsymbol{Z}(s)C_f s + 1\right] + \left[G_{dec}(s)G_{PWM}(s) - 1\right]}{\left[L_f C_f s^2 + RC_f s + G_i(s)G_{PWM}(s)C_f s + 1 - G_{dec}(s)G_{PWM}(s)\right]\left[\boldsymbol{Z}(s)C_f s + 1\right]}\right\}$$

$$= \frac{G_i(s)G_{PWM}(s)C_f s}{L_f C_f s^2 + RC_f s + G_i(s)G_{PWM}(s)C_f s + 1 - G_{dec}(s)G_{PWM}(s)}\boldsymbol{I}^*_{L\alpha\beta}(s) \rightarrow$$

$$\boldsymbol{I}_{L\alpha\beta}(s) = \frac{\boldsymbol{Z}(s)C_f^2 G_i(s)G_{PWM}(s)s + C_f G_i(s)G_{PWM}(s)}{a_{den_1}s^2 + b_{den_1}s + c_{den_2}}\boldsymbol{I}^*_{L\alpha\beta}(s), \tag{3.29}$$

where

$$c_{den_2} = \boldsymbol{Z}(s)C_f + RC_f + G_i(s)G_{PWM}(s)C_f - \boldsymbol{Z}(s)C_f G_{dec}(s)G_{PWM}(s).$$

By considering *ideal voltage decoupling* [this corresponds to design $G_{dec}(s) = G_{PWM}(s)^{-1}$], the closed loop transfer function is

$$\boldsymbol{I}_{L\alpha\beta}(s) = \frac{\boldsymbol{Z}(s)C_f^2 G_i(s)G_{PWM}(s)s + C_f G_i(s)G_{PWM}(s)}{a_{den_1}s^2 + b_{den_1}s + c_{den_3}}\boldsymbol{I}^*_{L\alpha\beta}(s), \tag{3.30}$$

being, as previously defined,

$$a_{den_1} = \boldsymbol{Z}(s)L_f C_f^2,$$

$$b_{den_1} = \boldsymbol{Z}(s)RC_f^2 + Z(s)C_f^2 G_i(s)G_{PWM}(s) + L_f C_f.$$

Moreover

$$c_{den_3} = RC_f + G_i(s)G_{PWM}(s)C_f.$$

If the load is neglected [($\boldsymbol{Z}(s) = 0$) in the above expression], the same expression as for *ideal voltage decoupling* is derived [see (3.22)].

Although the impedance $\boldsymbol{Z}(s)$ appears in the derived transfer function, the closed loop bode plot, step response and root locus of the system does not change as the impedance varies. This confirms the load independence of the system when *ideal voltage decoupling* is performed.

From the practical point of view, care must be taken to design $G_{dec}(s)$ such that it compensates for the delay introduced by $G_{PWM}(s)$. In fact, *ideal voltage decoupling*

corresponds to design $G_{dec}(s) = G_{PWM}(s)^{-1}$, which results in an unstable transfer function if the approximation for $G_{PWM}(s)$ with the non-minimum phase zero is used or it is not practically feasible if the other approximation is employed since a derivative term should be used on the decoupling path. Unfortunately, a pure time delay does not have a realizable inverse [145]. Therefore, the analysis considering *ideal voltage decoupling* is just to understanding the best performance that could be achieved if that possibility could be implemented.

3.4.1.4 P controller with nonideal voltage decoupling with unit transfer function

If the decoupling is performed utilizing a decoupling transfer function approximated by a unit gain $G_{dec}(s) = 1$, the system closed loop transfer function, with explicit dependence on the load, will be

$$\boldsymbol{I}_{L\alpha\beta}(s) = \frac{\boldsymbol{Z}(s)C_f^2 G_i(s)G_{PWM}(s)s + C_f G_i(s)G_{PWM}(s)}{a_{den_1}s^2 + b_{den_1}s + c_{den_4}}\boldsymbol{I}^*_{L\alpha\beta}(s), \tag{3.31}$$

being

$$c_{den_4} = RC_f + G_i(s)G_{PWM}(s)C_f + \boldsymbol{Z}(s)C_f - \boldsymbol{Z}(s)C_f G_{PWM}(s).$$

In this case, the decoupling is nonideal and the computation and PWM delays on the state feedback decoupling path are not compensated. This design approach is named *nonideal voltage decoupling with unit transfer function*, or simply *nonideal voltage decoupling*.

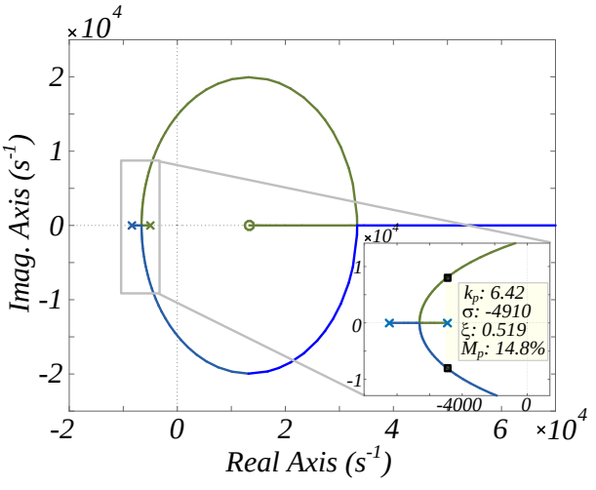

Fig. 3.19 Root locus for the inner current loop with **P regulator and nonideal voltage decoupling** - $\boldsymbol{G_{dec}(s) = 1}$: x – open loop poles; ■ closed loop poles for $\boldsymbol{k_{pI} = 6.42}$; o – zeros

The system is different from the case with *ideal voltage decoupling* since the inner loop is affected by the output current. With *nonideal voltage decoupling with unit transfer function*, the value of the gain to achieve 1 kHz bandwidth is approximately $\boldsymbol{k_{pI} = 6.42}$. For this case the root locus is shown in Fig. 3.19. Compared to *ideal voltage decoupling* (see Fig. 3.16) the damping of the system degrades with higher overshoot for the same proportional gain (see Fig. 3.19). However, the damping is still much higher than without voltage decoupling (see Fig. 3.10).

The resulting closed loop frequency response is presented in Fig. 3.20.

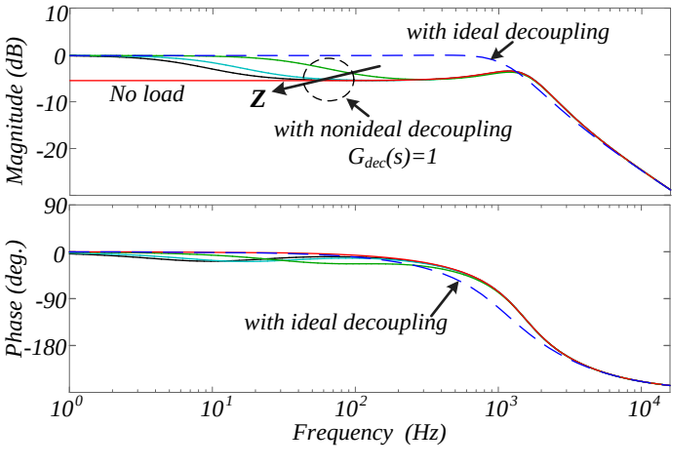

Fig. 3.20 Closed loop frequency response for the inner current loop with P regulator and with *nonideal* ($\boldsymbol{G_{dec}(s) = 1}$) and *ideal voltage decoupling* – arrows indicate decreasing in load (from rated resistive load until no-load)

Due to the nonideal voltage decoupling the system is still load dependent, but to a lesser extent than without decoupling. The achievable bandwidth is considerably reduced and limited by the computation and PWM delays, which are not compensated for on the state feedback decoupling path. However, it should be noted that the decoupling provides approximately 0 dB closed loop gain at low frequency components, as expected from a closed loop system.

3.4.1.5 P controller with nonideal voltage decoupling with lead-lag compensator

To overcome the limitation introduced by modelling $G_{dec}(s) = G_{PWM}(s)^{-1}$, a possible solution could be to design $G_{dec}(s)$ as a first order phase-lead compensator with the form

$$G_{lead}(s) = \frac{1 + \tau_z s}{1 + \tau_p s},$$

with $\tau_p < \tau_z$ determining the frequency range where positive phase is added to the system. The signal should be advanced in phase to compensate for the lag of $G_{PWM}(s)$ at each frequency. As can be seen in the phase diagram of Fig. 3.4, the lag increases significantly with the increase in frequency. If $G_{dec}(s) = G_{lead}(s)$ is designed to compensate for the delay at fundamental frequency, the closed loop transfer function is almost load independent (see Fig. 3.21), as if *ideal voltage decoupling* were performed.

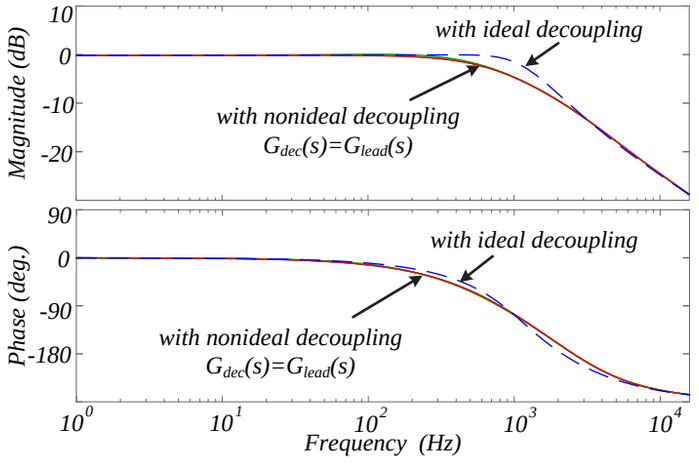

Fig. 3.21 Closed loop frequency response for the inner current loop with P regulator and with *nonideal* ($\boldsymbol{G_{dec}(s) = G_{lead}(s)}$) and *ideal voltage decoupling*

However, for practical implementations, a low-pass filter $G_{LPF}(s)$ cascaded with $G_{lead}(s)$ is used in order to avoid the amplification of high frequency components and noise affecting the measured voltage signal. Thus, the signal is advanced only in a specific frequency range. In the following analysis this implementation is referred to as *nonideal voltage decoupling with lead-lag compensator*. $G_{LPF}(s)$ introduces an additional lag which $G_{lead}(s)$ should compensate for. Accordingly, the frequency response of the system (see Fig. 3.22) degrades compared to the frequency response in Fig. 3.21. Nevertheless, this implementation provides better characteristics than the one that does not compensate for the delay (see Fig. 3.20). In fact, higher values at low frequency and lower load dependency than with *nonideal voltage decoupling with unit transfer function* can be observed.

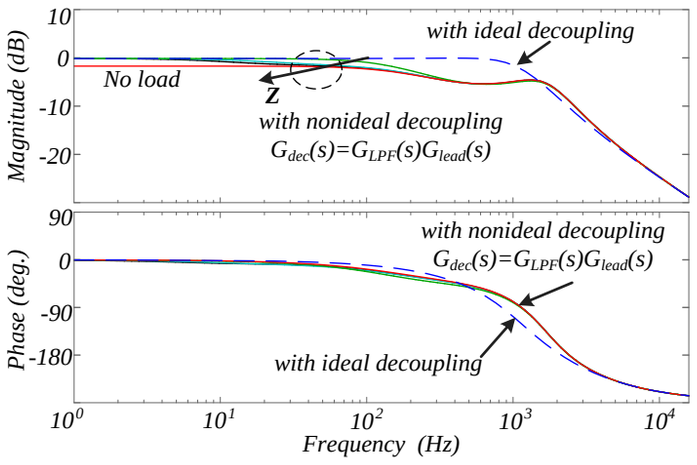

Fig. 3.22 Closed loop frequency response for the inner current loop with P regulator and with *nonideal* ($\boldsymbol{G_{dec}(s) = G_{LPF}(s)G_{lead}(s)}$) and *ideal voltage decoupling* – arrows indicate decreasing in load (from rated resistive load until no-load)

3.4.2 Nonideal PR Regulator

3.4.2.1 Nonideal PR controller without voltage decoupling

For each PR regulator analysed, the integrator gain k_{iI} was changed from 11 to 511 to see its effect on the closed loop frequency response. The variation range was chosen based on the values around the one that produces ideally zero-pole cancelation ($k_{iI} = 311$). The effect of the load is neglected by considering a very high value of load impedance in the design (no load condition). For each case, the proportional gain was tuned for a 1 kHz bandwidth.

The root locus of the system for $k_{iI}/k_{pI} = R/L_f$ and *without voltage decoupling* is shown in Fig. 3.23(a) and Fig. 3.23(b). By comparison with the case of the P regulator (see Fig. 3.10) there are two more complex conjugate poles and zeros. Those are the dominant poles close to the origin as shown in Fig. 3.23(b).

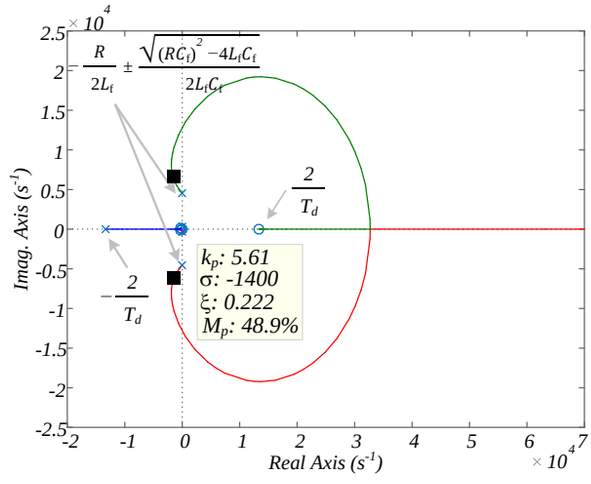

(a)

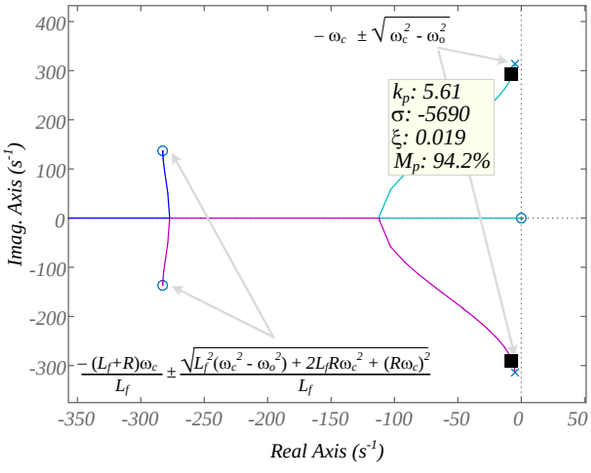

(b)

Fig. 3.23 (a) Root locus for the inner current loop with **nonideal PR regulator without voltage decoupling**: x – open loop poles**;** o – zeros**;** $G_{PWM}(s) = (1 - T_d s/2)/(1 + T_d s/2)$**;** (b) Zoom in the region close to the origin: closed loop poles for $\boldsymbol{k_{pI} = 5.61; k_{iI} = 5.61R/L_f}$

Fig. 3.24 shows the closed loop frequency response of nonideal PR controller *without voltage decoupling*. From this plot, it can be observed that:

- The controller is unable to produce zero steady-state error at the desired resonant frequency (50 Hz), mainly because of the phase that is not zero degree at that frequency**;**
- The smaller the integrator gain (k_{iI}) the bigger will be the error at 50 Hz**;**
- Changes in the resonant frequency (reference of the regulator), while the resonant gain ω_o is kept constant at the tuned resonant frequency, can have a significant impact in the steady-state error, especially if the parameter ω_c is small.

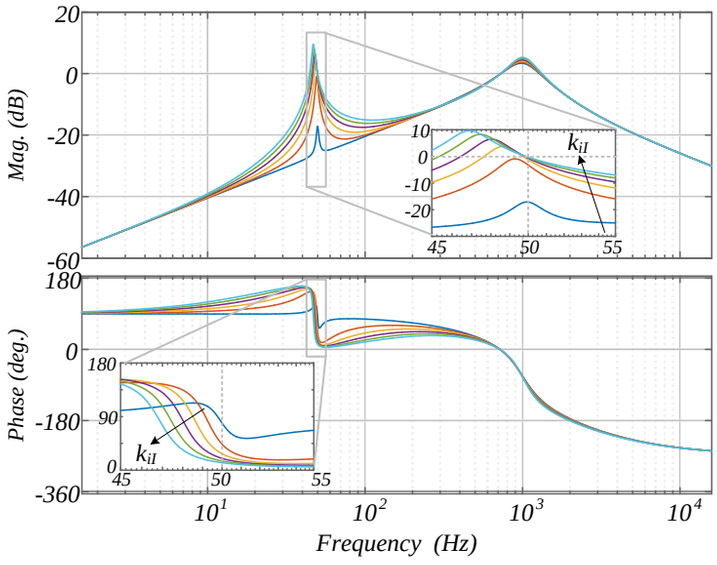

Fig. 3.24 Closed loop frequency response for the inner current loop with **nonideal PR regulator without voltage decoupling**: $\boldsymbol{k_{pI} = 5.61}$; $\boldsymbol{k_{iI} = 11 - 511}$ (arrows indicate increasing of $\boldsymbol{k_{iI}}$)

3.4.2.2 Nonideal PR controller with ideal voltage decoupling

By ideally decoupling the capacitor voltage, as previously described, results in the root locus of Fig. 3.25. For this case it was considered that $k_{iI}/k_{pI} = R/L_f$.

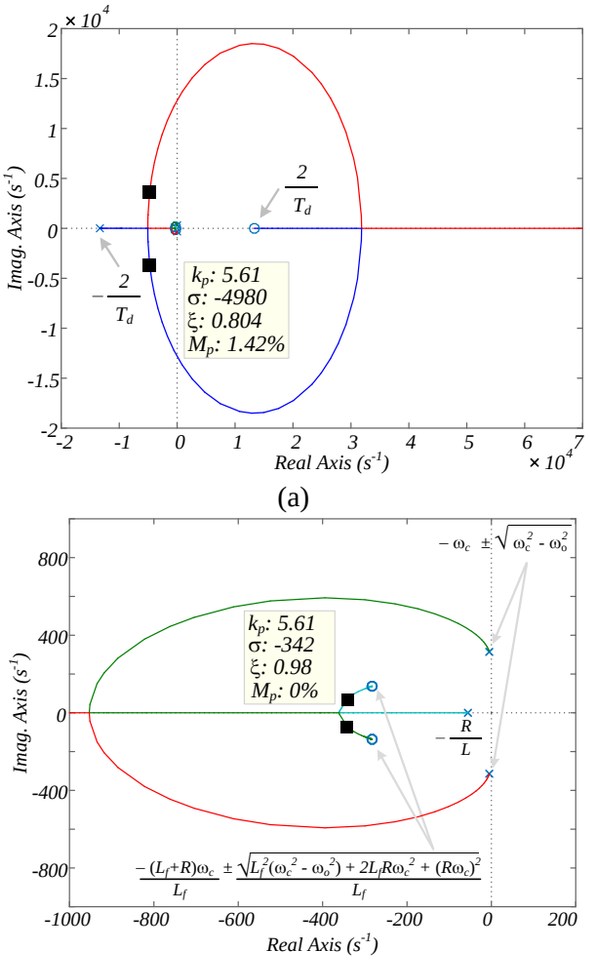

Fig. 3.25 (a) Root locus for the inner current loop with **nonideal PR regulator with ideal voltage decoupling**: x – open loop poles**;** o – zeros**;** $G_{PWM}(s) = (1 - T_d s/2)/(1 + T_d s/2)$**;** (b) Zoom in the region close to origin**;** ■ closed loop poles for $\boldsymbol{k_{pI} = 5.61}$; $\boldsymbol{k_{iI} = 5.61R/L_f}$

As expected from the previous discussion on the P regulator, it is possible to achieve closed loop dynamics with bigger damping than for the case *without voltage decoupling* (for 1 kHz bandwidth).

By using the above design, the closed loop frequency response as a function of k_{iI} is shown in Fig. 3.26. From this plot, it can be observed that:

- The controller is **almost able** to produce zero steady-state error at the desired resonant frequency (50 Hz)**;**
- The smaller the integrator gain (k_{iI}) the bigger will be the error at 50 Hz. However, the error is very small and is fundamentally in the phase, much smaller than the case without voltage decoupling**;**

- The system frequency response has low sensitivity to frequency variations around the resonant frequency. However, the smaller the integrator gain (k_{iI}) the bigger will be the sensitivity around 50 Hz**;**
- The corrective effect of the nonideal PR regulator around the resonant frequency is just 2%**;**
- Changes in the fundamental frequency have little impact on the steady-state error.

In general, it can be said that the effect of voltage cross-coupling decoupling is more important than the use of a PR regulator.

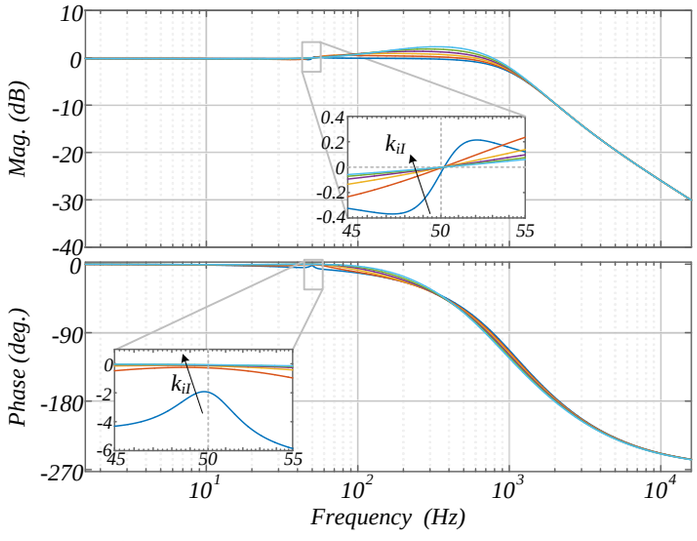

Fig. 3.26 Closed loop frequency response for the inner current loop with **nonideal PR regulator with ideal voltage decoupling**: $\boldsymbol{k_{pI} = 5.61}$; $\boldsymbol{k_{iI} = 11 - 511}$ (arrows indicate increasing of $\boldsymbol{k_{iI}}$)

3.4.2.3 Nonideal PR controller with nonideal voltage decoupling

When *nonideal voltage decoupling* is performed ($G_{dec}(s) = 1$) the resulting root locus becomes as shown in Fig. 3.27. For this case (as it was previously explained for the P regulator), the system is different and the analysis must be done again. With *nonideal voltage decoupling* and using the same gain as for the case of a P regulator ($k_{pI} = 5.61$) it is still possible to achieve a closed loop system with good damping ($\zeta = 0.562$ @ 1 kHz).

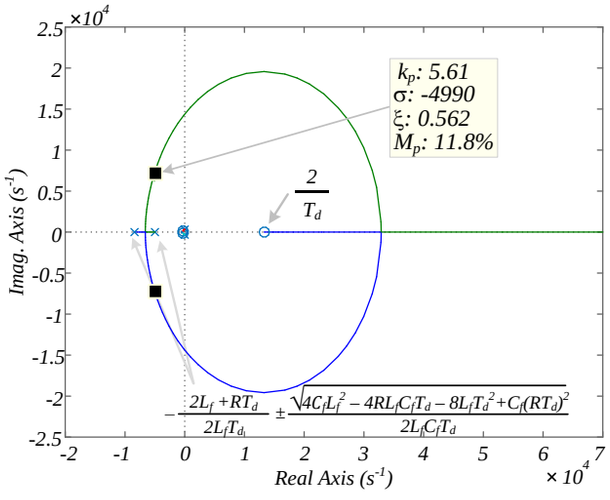

(a)

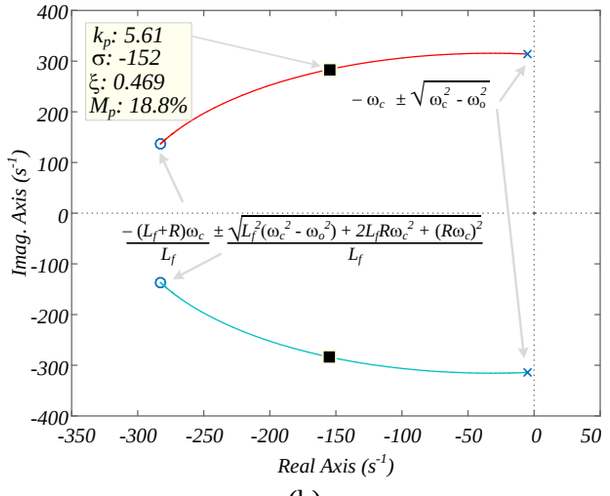

(b)

Fig. 3.27 (a) Root locus for the inner current loop with **nonideal PR regulator with nonideal voltage decoupling** – $\boldsymbol{G_{dec}(s) = 1}$: x – open loop poles; o – zeros; $\boldsymbol{G_{PWM}(s) = (1 - T_d s/2)/(1 + T_d s/2)}$; (b) Zoom in the region close to origin; ■ closed loop poles for $\boldsymbol{k_{pI} = 5.61}$; $\boldsymbol{k_{iI} = 5.61R/L_f}$

3.4.3 Ideal PR Regulator

3.4.3.1 Ideal PR controller without voltage decoupling

When the ideal PR is used, the root locus of the system *without voltage decoupling* for $k_{iI}/k_{pI} = R/L_f$ is shown in Fig. 3.28. By comparison with the case of the P regulator (see Fig. 3.10) there are two more complex conjugate poles and zeros. Those are the dominant poles close to the origin as shown in Fig. 3.28(b). By comparison with the nonideal PR [see Fig. 3.23(b)] the open loop poles for this case are on the imaginary

axis with approximately the same imaginary part of the zeros. As a result, by closing the loop fundamentally the imaginary part does not change. There is almost no damping and 100% of overshoot. Being the dominant poles very close to the imaginary axis, high settling time is expected.

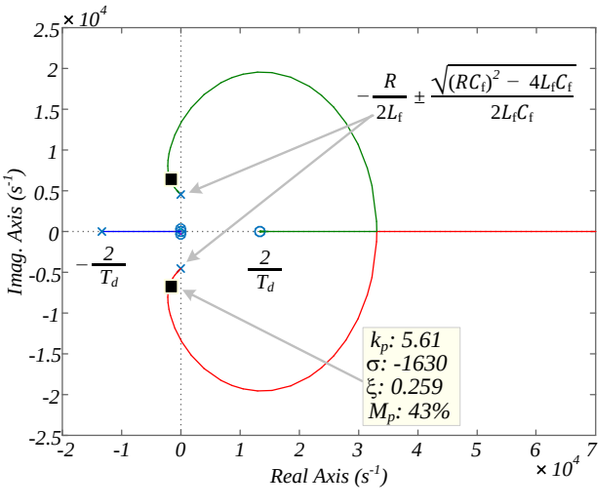

(a)

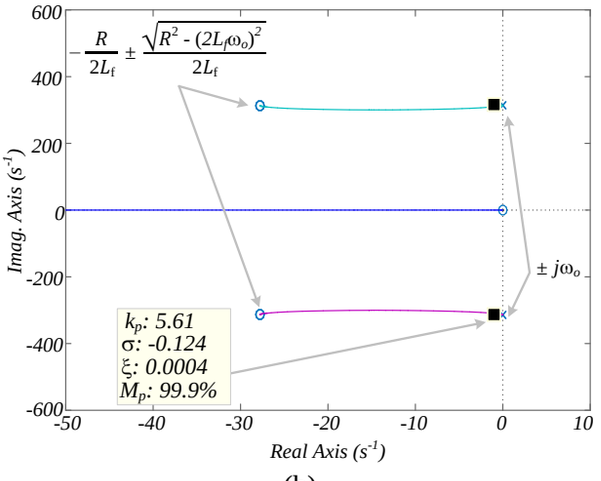

(b)

Fig. 3.28 (a) Root locus of the inner current loop with **ideal PR regulator without voltage decoupling**: x – open loop poles; o – zeros; ■ closed loop poles for $\boldsymbol{k_{pI} = 5.61}$; $\boldsymbol{k_{iI} = 5.61R/L_f}$; $\boldsymbol{G_{PWM}(s) = (1 - T_d s/2)/(1 + T_d s/2)}$; (b) zoom in the region close to origin

Fig. 3.29 shows the closed loop frequency response for the system with the ideal PR controller *without voltage decoupling* for the same bandwidth and variation of k_{iI}. From this plot, it can be observed that:

- The controller is **able** to produce zero steady-state error at the desired resonant frequency (50 Hz)**;**

- The system frequency response is **very sensitive to frequency variations** (reference of the regulator), around the fundamental frequency. Small changes in frequency (reference of the regulator), while the resonant gain ω_o is kept constant at the tuned resonant frequency, can result in very high steady-state error**;**
- The smaller the integrator gain (k_{iI}) the bigger the sensitivity to frequency variations around the resonant frequency (50 Hz) will be.

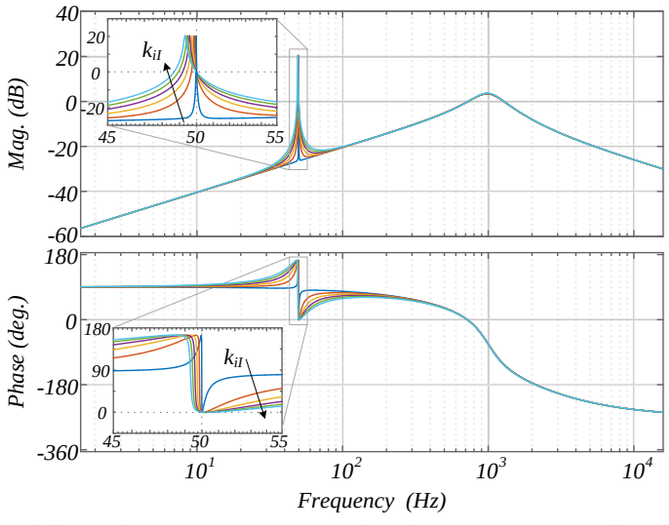

Fig. 3.29 Closed loop frequency response for the inner current loop with **ideal PR regulator without voltage decoupling**: $\boldsymbol{k_{pI} = 5.61}$; $\boldsymbol{k_{iI} = 11 - 511}$ (arrows indicate increasing of $\boldsymbol{k_{iI}}$)

3.4.3.2 Ideal PR controller with ideal voltage decoupling

By ideally decoupling the capacitor voltage the root locus in Fig. 3.30 can be observed. For this case it was considered that $k_{iI}/k_{pI} = R/L_f$. Differently from the nonideal PR the closed loop poles dynamics at the resonant frequency have poor damping, although they are almost cancelled by the zeros. However, if the regulator bandwidth is smaller the zeros and poles are more separated which can result in spikes close to that frequency. Comparing these results with those obtained *without voltage decoupling*, the settling time is expected to decrease being the dominant closed loop poles further from the imaginary axis.

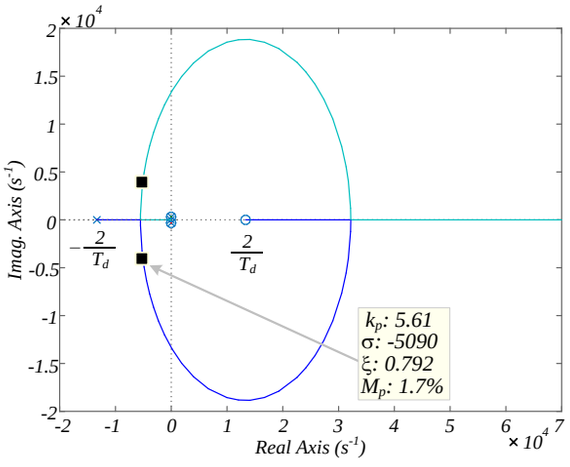

(a)

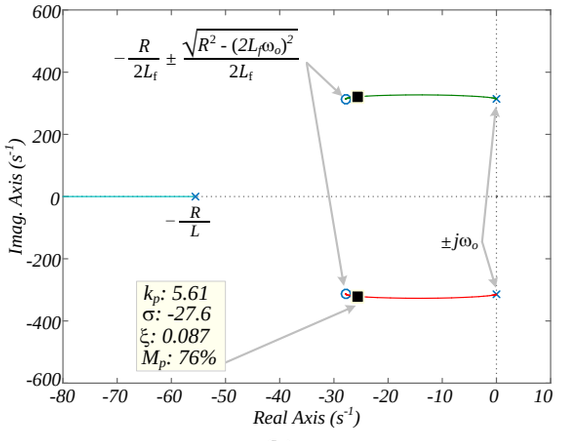

(b)

Fig. 3.30 (a) Root locus of the inner current loop with **ideal PR regulator with ideal voltage decoupling**: x – open loop poles; o – zeros; ■ closed loop poles for $\boldsymbol{k_{pI} = 5.61}$; $\boldsymbol{k_{iI} = 5.61R/L}$; $\boldsymbol{G_{PWM}(s) = (1 - T_d s/2)/(1 + T_d s/2)}$; (b) zoom in the region close to origin

Fig. 3.31 shows the closed loop frequency response for the inner current loop using ideal PR regulator with *ideal voltage decoupling*. It can be observed that:

- The controller is **able** to produce zero steady-state error at the desired resonant frequency (50 Hz)**;**
- The system frequency response has low sensitivity to frequency variations around the resonant frequency. However, the smaller the integrator gain (k_{iI}) the bigger will be the sensitivity around 50 Hz. Furthermore, this sensitivity is bigger than in the case of nonideal PR controller**;**
- The corrective effect of the ideal PR controller around the resonant frequency is just 2%**;**

In synthesis it can be said that the effect of voltage cross-coupling decoupling is more important than the use of the PR controller.

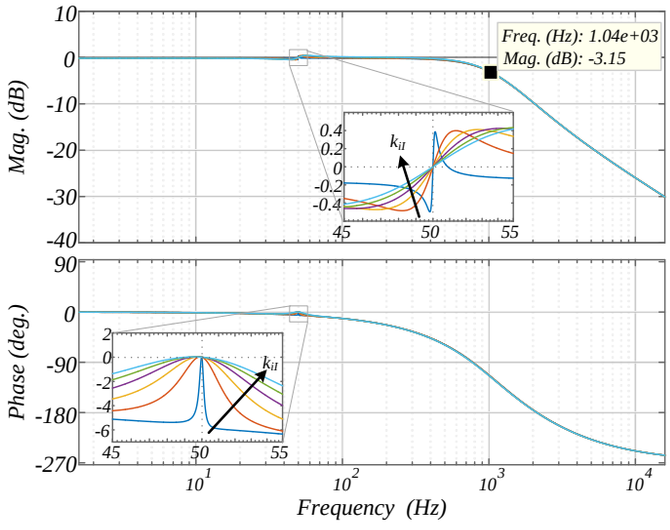

Fig. 3.31 Closed loop frequency response for the inner current loop with **ideal PR regulator with ideal voltage decoupling**: $\boldsymbol{k_{pI} = 5.61}$; $\boldsymbol{k_{iI} = 11 - 511}$ (arrows indicate increasing of $\boldsymbol{k_{iI}}$)

3.4.3.3 Ideal PR controller with nonideal voltage decoupling

When *nonideal voltage decoupling* is performed the resulted root locus becomes as presented in Fig. 3.32. It must be noted that it is still possible to achieve closed loop system dynamics with good damping ($\boldsymbol{\zeta = 0.562}$ @ 1 kHz), as can be seen in Fig. 3.32(a). However, the dominant closed loop poles show low damping and high overshoot [see Fig. 3.32(b)].

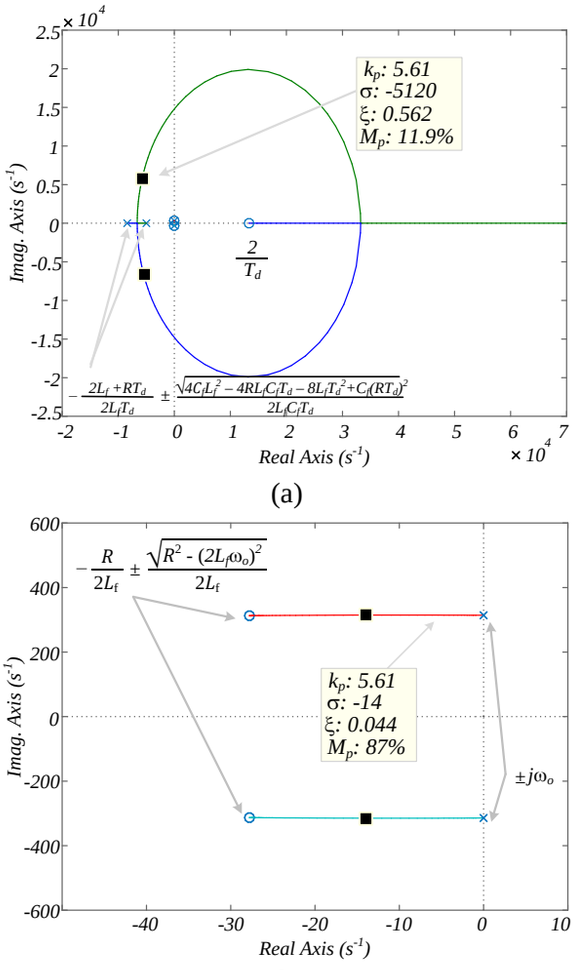

Fig. 3.32 (a) Root locus of the inner current loop **with ideal PR regulator with nonideal voltage decoupling** – $\boldsymbol{G_{dec}(s) = 1}$: x – open loop poles; o – zeros; ■ closed loop poles for $\boldsymbol{k_{pI} = 5.61}$; $\boldsymbol{k_{iI} = 5.61R/L_f}$; $\boldsymbol{G_{PWM}(s) = (1 - T_d s/2)/(1 + T_d s/2)}$; (b) zoom in the region close to origin

3.4.4 VPR Regulator

3.4.5 VPR controller without voltage decoupling

When the complex vector PR is used, the root locus of the system *without voltage decoupling* for $k_{iI}/k_{pI} = R/L_f$ is shown in Fig. 3.33. The root locus close to the origin [see Fig. 3.33(b)] shows that the system with this regulator is unstable for any value of k_{pI} or k_{iI}.

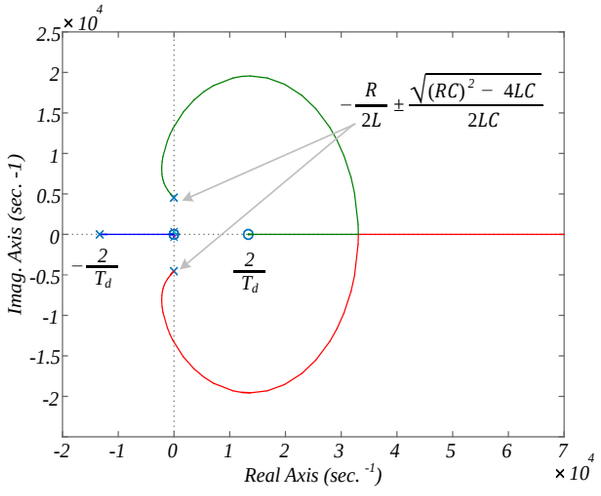

(a)

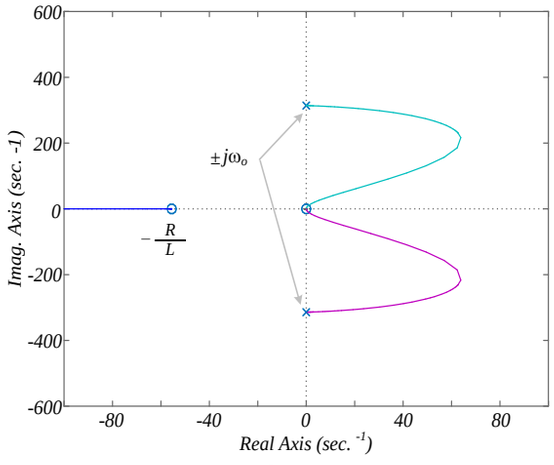

(b)

Fig. 3.33 (a) Root locus of the inner current loop with **complex vector PR regulator without voltage decoupling**: x – open loop poles; o – zeros; $\boldsymbol{k_{iI}/k_{pI} = R/L_f}$; $\boldsymbol{G_{PWM}(s) = (1 - T_d s/2)/(1 + T_d s/2)}$; (b) zoom in the region close to origin

Although the system is unstable, it is worth to look at its frequency response, as shown in Fig. 3.34, for the same gains and zero locations as the previous resonant regulators. It can be observed that:

- If the system were stable, the controller would be able to produce zero steady–state error at the desired resonant frequency (50 Hz)**;**
- The system response has low sensitivity to frequency variations around the resonant frequency. This feature is well suited for systems whose frequency changes**;**
- Changes in the integrator gain (k_{iI}) has almost no influence in the frequency response around the resonant frequency. At least in the range observed. This feature is basically due to closer zeros and poles design of this controller.

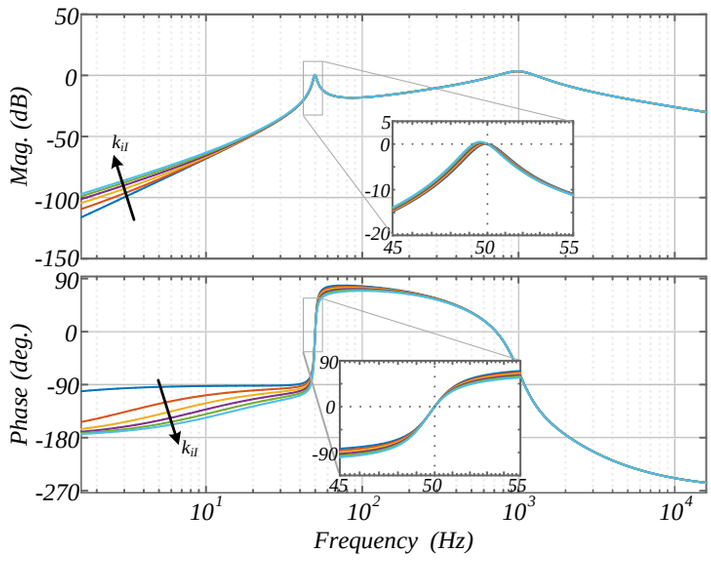

Fig. 3.34 Closed loop frequency response for the inner current loop with **complex vector PR regulator without voltage decoupling**: $\boldsymbol{k_{pI} = 5.61}$; $\boldsymbol{k_{iI} = 11 - 311}$ (arrows indicate increasing of $\boldsymbol{k_{iI}}$)

3.4.5.1 VPR controller with ideal voltage decoupling

When the complex vector PR is used with *ideal voltage decoupling*, the root locus of the system for $k_{iI}/k_{pI} = R/L_f$ is shown in Fig. 3.35. The root locus close to the origin [see Fig. 3.35(b)] shows that:

- the design produces ideal zero-pole cancelation**;**
- the dominant pole is real resulting in a dynamic behaviour without overshoot.

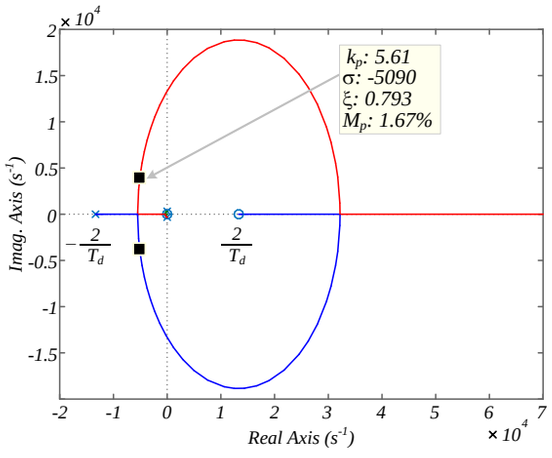

(a)

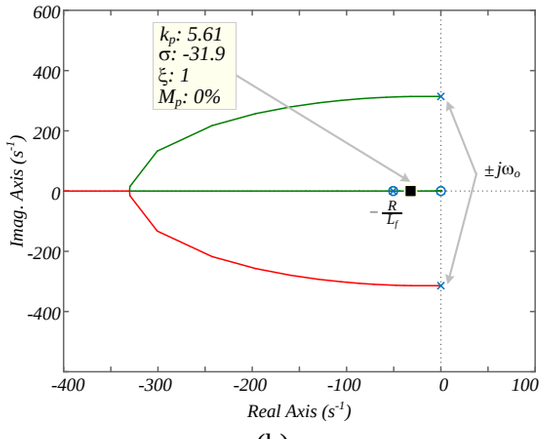

(b)

Fig. 3.35 (a) Root locus of the inner current loop with **complex vector PR regulator with ideal voltage decoupling**: x – open loop poles; o – zeros; $\boldsymbol{k_{iI}/k_{pI} = R/L_f}$; $\boldsymbol{G_{PWM}(s) = (1 - T_d s/2)/(1 + T_d s/2)}$; (b) zoom in the region close to origin

Fig. 3.36 shows the closed loop frequency response of Complex VPR controller with *ideal voltage decoupling*. It can be observed that:

- The controller is **able** to produce zero steady state error at the desired resonant frequency (50 Hz)**;**
- The system frequency response has low sensitivity to frequency variations around the resonant. Indeed, this sensitivity is smaller than in the cases of ideal and non-ideal PR controllers**;**
- The system frequency response has low sensitivity to the integrator gain (k_{iI}) variation**;**

It can be said that the effect of voltage cross-coupling decoupling is more important than the use of a Complex Vector PR controller.

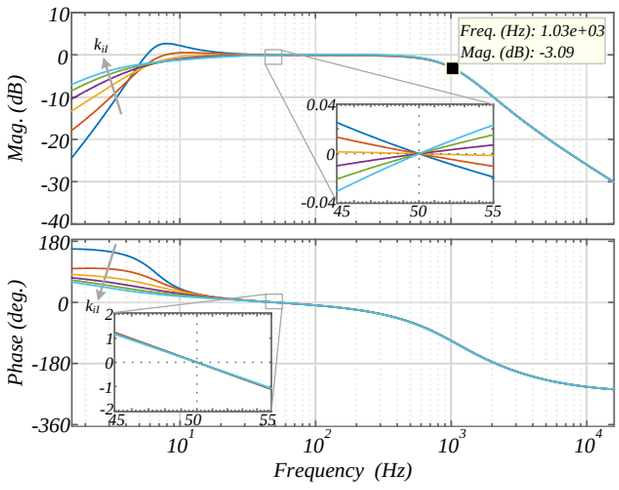

Fig. 3.36 Closed loop frequency response for the inner current loop with **complex vector PR regulator with ideal voltage decoupling**: $\boldsymbol{k_{pI} = 5.61}$; $\boldsymbol{k_{iI} = 11 - 311}$ (arrows indicate increasing of $\boldsymbol{k_{iI}}$)

3.4.5.2 VPR controller with nonideal voltage decoupling

As nonideal voltage decoupling is considered for the complex vector PR regulator, the system performance degrades as shown in Fig. 3.37. The root locus close to the origin [see Fig. 3.37(b)] shows that the closed loop poles are complex conjugate with low overshoot.

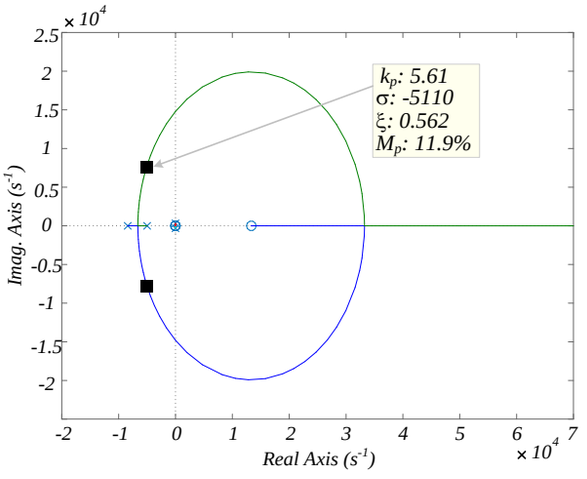

(a)

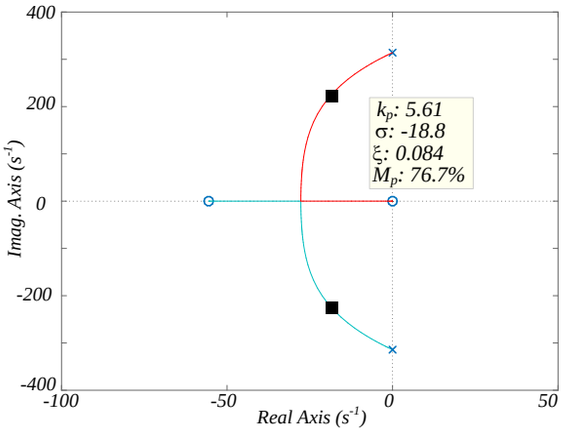

(b)

Fig. 3.37 (a) Root locus of the inner current loop with **complex vector PR regulator with nonideal voltage decoupling**: x – open loop poles; o – zeros; $\boldsymbol{k_{iI}/k_{pI} = R/L_f}$; $\boldsymbol{G_{PWM}(s) = (1 - T_d s/2)/(1 + T_d s/2)}$; (b) zoom in the region close to origin

The main outcomes related to nonideal PR, ideal PR and Complex Vector PR controllers are summarized in Table 3.3, whether state feedback cross-coupling decoupling is performed.

Table 3.3 Sensitivity of Proportional Resonant controllers to integral gain values and frequency deviations

	w/o voltage decoupling		**with voltage decoupling**	
Controller	Sensitivity to Δk_{iI}	Sensitivity to Δf	Sensitivity to Δk_{iI}	Sensitivity to Δf
NonIdeal PR	HIGH	MEDIUM	MEDIUM	MEDIUM
Ideal PR	HIGH	HIGH	MEDIUM	HIGH
VPR	UNSTABLE	UNSTABLE	LOW	LOW

3.5 Discretization Issues

In real time applications, in general all the regulators are implemented in the discrete-time domain. Therefore, it is important to verify the effect of the discretization method adopted in the performance of each regulator. The most used implementation of PR regulators is the structure that uses two integrators. The implementation in the s-domain is shown in Fig. 3.38(a) for the ideal PR, and in Fig. 3.38(b) for the case of complex vector PR. Similar structures can be derived for the nonideal PR regulator. As can be seen in these graphs the resonant frequency gain (ω_o^2) appears as an explicit gain outside the integrators structure. This is an interesting feature in applications where there is frequency adaptation and this gain changes. For example, Fig. 3.39(a) and Fig. 3.39(b) show the discrete-time implementation of the ideal PR and complex vector PR, respectively.

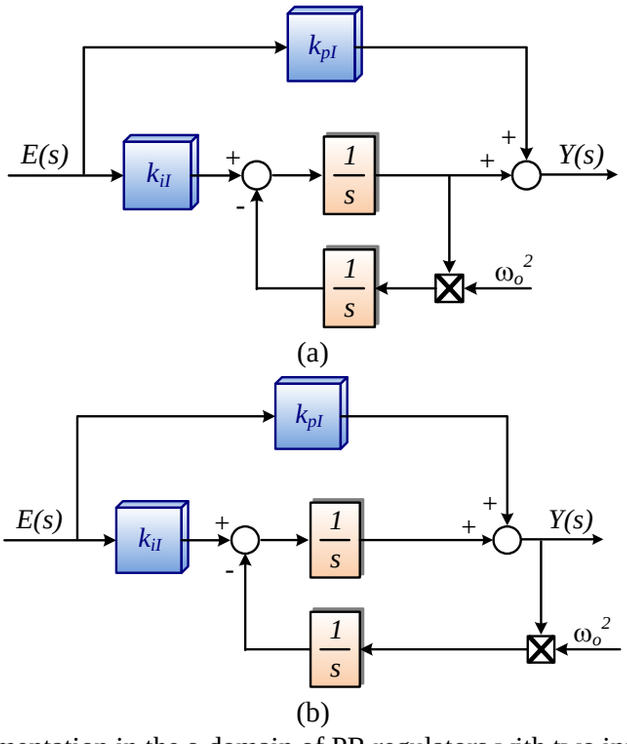

Fig. 3.38 Implementation in the s-domain of PR regulators with two integrator structure: (a) ideal PR; (b) complex vector PR

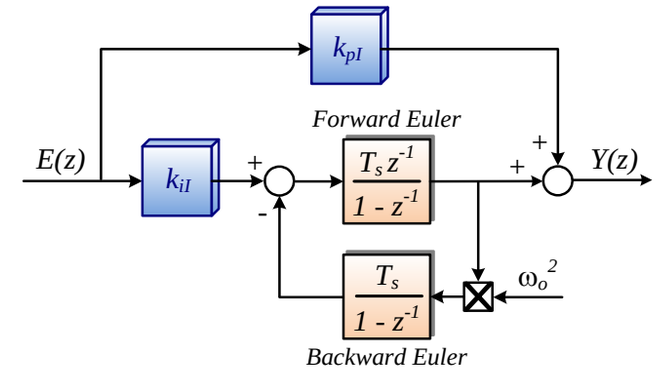

(a)

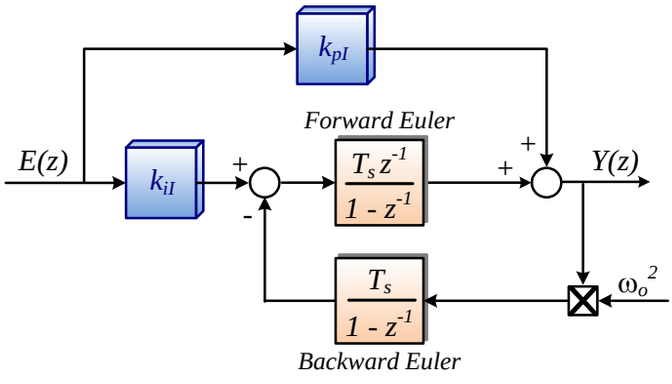

(b)

Fig. 3.39 Implementation in the z-domain of PR regulators with two integrator structure: (a) ideal PR; (b) complex vector PR

As can be seen the reason to use this implementation is that there is no need to perform on-line calculations of the discrete-time version of the regulator gains. Furthermore, the use of the backward Euler discretization method for the second integrator is needed to avoid algebraic loops.

Several possibilities can be used for the method that discretizes the PR regulators, e.g. impulse invariant, Tustin with frequency prewarping, etc. The use of these methods implies the discretization of the resonant part of the regulator. For the case of the ideal PR, the transfer function for any harmonic of the fundamental resonant frequency is

$$G_i(s) = \frac{Y(s)}{E(s)} = k_{pI} + k_{iI,h} R_{1,h}(s), \tag{3.32}$$

where $R_{1,h}(s) = s/(s^2 + h^2\omega_o^2)$. In this transfer function, h is the number that represents each harmonic of the fundamental resonant frequency (ω_o). For the case of the complex vector PR, the transfer function is

$$G_i(s) = k_{pI,h} R_{2,h}(s) + k_{iI,h} R_{1,h}(s), \tag{3.33}$$

where $R_{2,h}(s) = s^2/(s^2 + h^2\omega_o^2)$. The discrete version of each term ($R_{1,h}(s)$ and $R_{2,h}(s)$) using impulse invariant and Tustin with frequency prewarping are presented in Table 3.4. As can be seen the main drawback of using these implementations is the requirement of online computation of the regulators gains in case frequency adaptation is performed.

Table 3.4. Z-Domain transfer functions of $\boldsymbol{R_{1,h}(s)}$ and $\boldsymbol{R_{2,h}(s)}$ using the Impulse Invariant and Tustin with Prewarping methods

Resonant Term	Impulse Invariant	Tustin with Frequency Prewarping
$\boldsymbol{R_{1,h}(s)}$	$R_{1,h}(z) = T_s \dfrac{1 - z^{-1}\cos(h\omega_o T_s)}{1 - 2z^{-1}\cos(h\omega_o T_{sw}) + z^{-2}}$	$R_{1,h}(z) = \dfrac{\sin(h\omega_o T_s)}{2h\omega_o} \dfrac{1 - z^{-2}}{1 - 2z^{-1}\cos(h\omega_o T_s) + z^{-2}}$
$\boldsymbol{R_{2,h}(s)}$	$R_{2,h}(z) = -h\omega_o T_s \dfrac{z^{-1}\sin(h\omega_o T_s)}{1 - 2z^{-1}\cos(h\omega_o T_s) + z^{-2}}$	$R_{2,h}(z) = \cos^2\left(\dfrac{h\omega_o T_s}{2}\right) \dfrac{1 - 2z^{-1} + z^{-2}}{1 - 2z^{-1}\cos(h\omega_o T_s) + z^{-2}}$

To analyse the effect of the discretization methods on the closed loop frequency response, the closed loop frequency response in the *s*-domain is compared to the closed loop frequency response in the *z*-domain. For the *z*-domain, the transfer functions of the regulators are discretized using the forward and backward Euler method, the impulse invariant, and Tustin with frequency prewarping. The derivation of the correspondent difference equations are reported in Appendix - Section A.

For each plot presented in the next paragraphs, it is shown the frequency region around the resonant frequency of interest. For each resonant controller the design is based on the zero-pole cancelation approach and the proportional gain is tuned to give a 50 Hz bandwidth for each harmonic regulator. Fig. 3.40, Fig. 3.41, Fig. 3.42, and Fig. 3.43 show the comparison at fundamental frequency, and at the 5th, 7th, and 11th harmonics of the fundamental, respectively. For each plot the discretization methods used are impulse invariant and forward and backward Euler with the structure with two integrators.

As can be seen in Fig. 3.40 at low and fundamental frequencies there is no difference between the continuous and discrete-time frequency response, no matter the discretization method used. However, as the frequency increases as shown in Fig. 3.41, Fig. 3.42, and Fig. 3.43 the discrete-time frequency response using the structure with two integrators does not represents adequately the continuous-time behaviour. There is a shift in the frequency response around the resonant frequency and the regulator does not produce anymore the desired feature of zero steady-state error (0 dB, 0^o) at the designed resonant frequency. Furthermore, the bigger the resonant frequency the bigger will be the shift in the frequency response.

As a conclusion, the discretization method plays an important role in the performance of the resonant regulators. However, if a wrong discretization method is used, the PR regulator does not produce the desired effect.

As a final remark, although it is not shown in the figures, the discretization using Tustin with frequency prewarping produces similar results as the impulse invariant method.

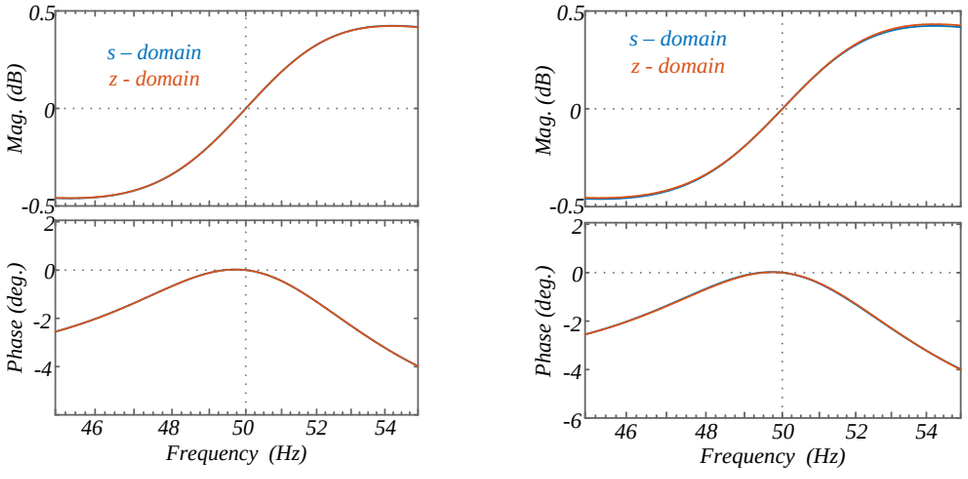

Fig. 3.40 Comparison of the continuous and discrete-time closed loop frequency response of the inner current loop with ideal PR regulator and with voltage decoupling at fundamental frequency: (a) structure with two integrators - Forward and backward Euler method; (b) impulse invariant method

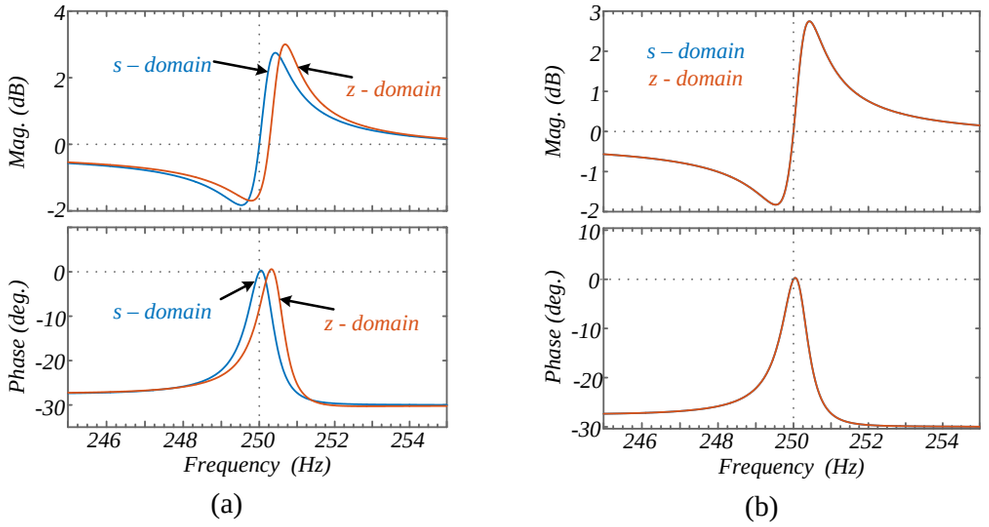

Fig. 3.41 Comparison of the continuous and discrete-time closed loop frequency response of the inner current loop with ideal PR regulator and with voltage decoupling at 5th harmonic of the fundamental frequency: (a) structure with two integrators - Forward and backward Euler method; (b) impulse invariant method

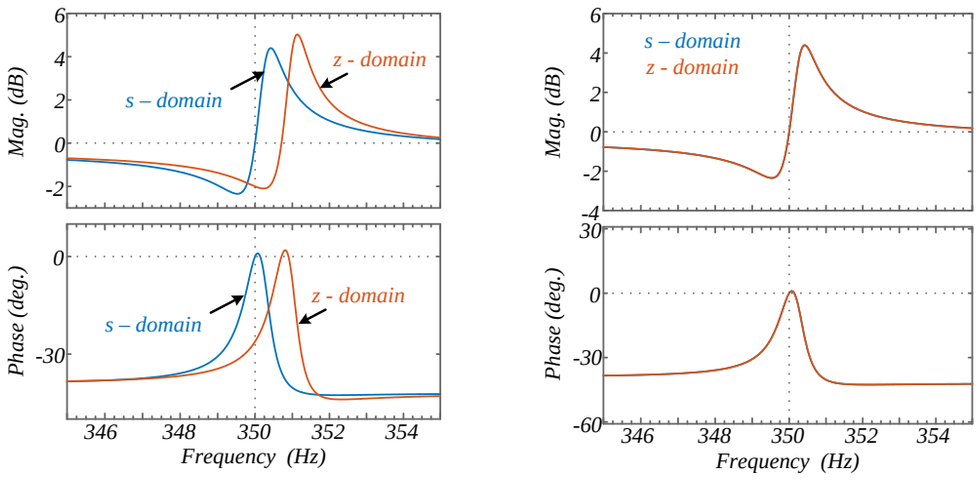

Fig. 3.42 Comparison of the continuous and discrete-time closed loop frequency response of the inner current loop with ideal PR regulator and with voltage decoupling at 7th harmonic of the fundamental frequency: (a) structure with two integrators - Forward and backward Euler method; (b) impulse invariant method

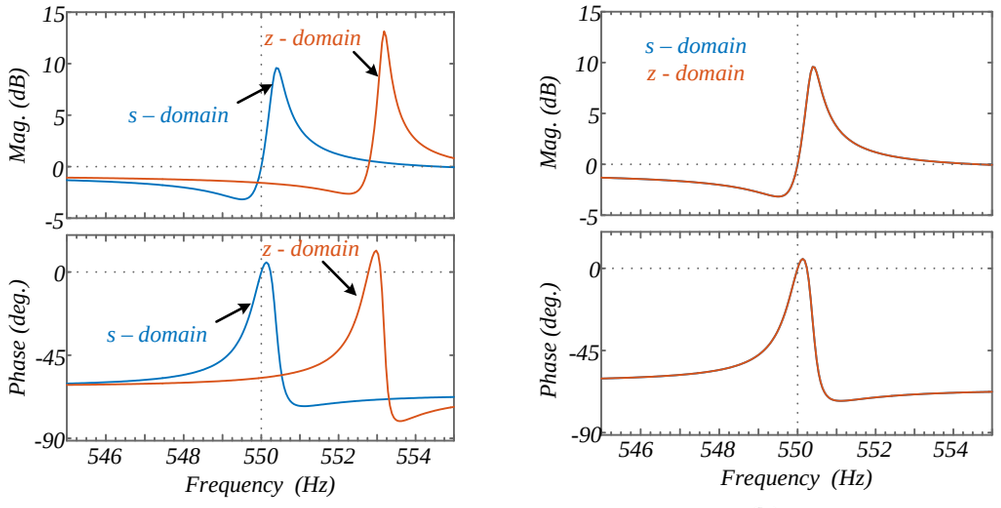

Fig. 3.43 Comparison of the continuous and discrete-time closed loop frequency response of the inner current loop with ideal PR regulator and with voltage decoupling at 11th harmonic of the fundamental frequency: (a) structure with two integrators - Forward and backward Euler method; (b) impulse invariant method

3.6 Voltage Regulator Design

A PR structure is chosen as regulator for the voltage loop [169]. The addition of resonant filters provides a good steady-state tracking of the fundamental component and mitigates the main harmonics associated to nonlinear loads. The gains of the system are selected to provide also a good dynamic response when the system is tested

according to the requirements imposed by the normative for UPS systems. The voltage regulator is based on PR controllers with a lead compensator structure as

$$G_v = k_{pV} + \sum_{h=1,5,7} k_{iV,h} \frac{s\cos(\varphi_h) - h\omega_1 \sin(\varphi_h)}{s^2 + (h\omega_1)^2}, \tag{3.34}$$

where h refers to the harmonic order to be compensated. The proportional gain k_{pV} determines the bandwidth of the voltage regulator, and is designed for around 150 Hz. The phase-leading angles at each harmonic frequency φ_h are set such that the trajectories of the open loop system on the Nyquist diagram, with the PR regulators at the fundamental frequency, 5th and 7th harmonics, guarantee a sensitivity peak $1/\eta$ lower than a threshold value [170]. In this work this threshold has been set to $\eta = 0.5$ at no-load condition. After calculating the phase-leading angles, the resonant gain at the fundamental frequency $k_{iV,1}$ is selected in order to achieve a fast response to changes in the fundamental component. Equation (3.35) can be rewritten just for the resonant controller at fundamental frequency, leading to the second-order system

$$G_v(s) = k_{pV} \frac{s^2 + \frac{k_{iV,1}}{k_{pV}}\cos(\varphi_1)s + \left[\omega_1^2 - \frac{k_{iV,1}}{k_{pV}}\omega_1 \sin(\varphi_1)\right]}{s^2 + \omega_1^2}. \tag{3.35}$$

According to Evans root locus theory, the open loop poles move towards the open loop zeros when the loop is closed. For this reason, the pair of zeros of the PR controller is moved as far as possible from the right half plane. This corresponds to place them on the same location, such that the pair of poles of $G_v(s)$ is coincident. As a consequence $k_{iV,1}$ can be designed according to

$$k_{iV,1} \geq K \frac{2k_{pV}\text{ʒ}_{crit}\omega_1}{\cos(\varphi_1)}, \tag{3.36}$$

where the lower bound of the inequality refers to $K = 1$, with the damping factor $\text{ʒ}_{crit} = 1$, and small phase-leading angles at the fundamental frequency. For the phase-leading angle at the fundamental frequency $\varphi_1 = 3.3°$, the gain is $k_{iV,1} = 31.47$. The upper bound is set by $k_{iV,1}$ values which do not significantly degrade the relative stability of the closed loop system [32].

The harmonic resonant gains are selected to have reduced transient oscillations [61], as well as to fulfil the requirements set by the UPS standards (see Table 3.5).

Table 3.5 Voltage Regulator Control Parameters

Parameter		**Value**	
Proportional gain		$k_{pV} = 0.05$	
Integral gains and lead angles	@50Hz	$k_{iV,1} = 31.47$	$\varphi_1 = 3.3°$
	@250Hz	$k_{iV,5} = 15$	$\varphi_5 = 37°$
	@350Hz	$k_{iV,7} = 15$	$\varphi_7 = 44°$

In Fig. 3.44 the Nyquist diagram of the system in Fig. 3.1 with the parameters of Table 3.1 is shown. The inverse of the sensitivity peak, i.e. η, is higher than 0.5 at no-load condition and 0.4 at rated load ($Z = 68\,\Omega$), respectively, with all the harmonic compensators activated.

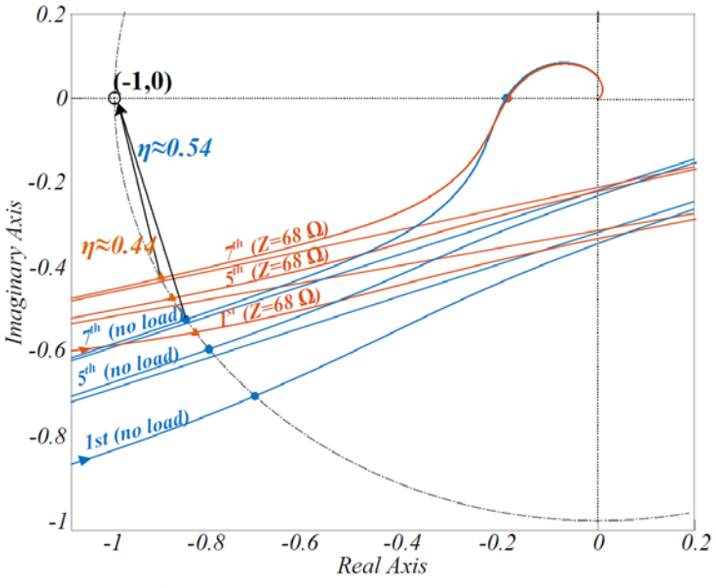

Fig. 3.44 Nyquist diagram of the system at no-load and rated load ($\mathbf{Z = 68}\,\Omega$) conditions

3.7 Experimental Results

3.7.1 Experimental Setup

To verify the theoretical analysis developed in previous sections, a laboratory test bed has been set up based on a 2.2 kVA Danfoss VLT® AutomationDrive power converter with IGBTs, driven by dSpace DS1006 platform. An Analog-to-Digital (A/D) DS2004 board is used to digitalize the analog signals sensed via LEM current and voltage transducers. A 16-bit high resolution Digital-to-Analog (D/A) conversion board DS2102 is used to monitor the signals with an oscilloscope. A photo of the experimental setup is shown in Fig. 3.45.

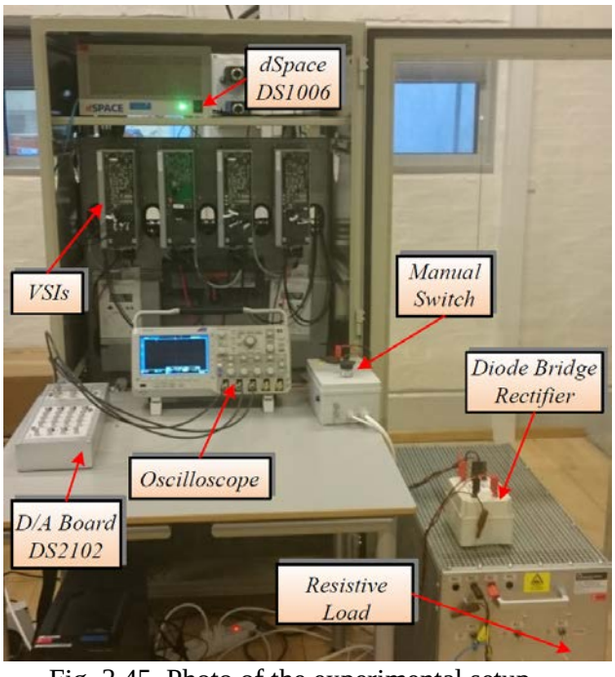

Fig. 3.45 Photo of the experimental setup

The measurement board comprises a ±15 V Tracopower TMS 10215 switched-mode power supply (see Fig. 3.46). The voltage transducer LV 25-P ($I_{PN} = 10\ mA$ and $V_{PN} = 10 \div 500\ V$) is a wide bandwidth closed-loop LEM sensor. The magnetic field generated by a current passing through the transducer is sensed. Voltage is measured starting from a current proportional to the measured voltage, which is set by an external resistor. The current transducer LA 55-P is a closed-loop LEM sensor ($I_{PN} = 50\ A$) with a 200 kHz bandwidth.

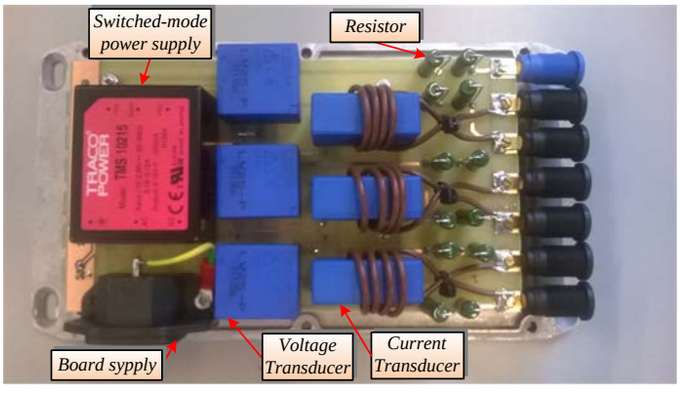

Fig. 3.46 Measurement board

(a) (b)

Fig. 3.47 DC source power supply: (a) single module; (b) stack of four modules

The DS1006 Processor Board is used for real-time implementation of software algorithms for power converter control. It is based on a quad-core processor with 2.8 GHz clock frequency. A 32-bit I/O bus for modular I/O configuration is used for connection to I/O boards. An RS232 interface with standard UART is used for serial interface allowing transfer rates of up to 115.2 kbaud.

The input rectifier section of the Danfoss power module along with the DC link capacitance has been replaced by an 80 kW bidirectional DC power supply. It consists of four modules 20 kW each based on Regatron technology (TopCon TC.GSS), as can be seen in Fig. 3.47.

The linear resistive load allows the setting of different resistance values (see Fig. 3.48). In particular, the switches on the front-end allow the selection of 57 Ω, 115 Ω, 230 Ω or 450 Ω. A proper combination of these values permits the desired value of resistive load per each phase to be achieved.

Fig. 3.48 Resistive load

The schematic of the nonlinear load used to perform the laboratory test is shown in Fig. 3.49. It consists of a three-phase diode bridge rectifier with LC output filter. The main parameters of the diode bridge rectifier FUO 22-16N are highlighted in Table 3.6. It consists of six diodes with DCB base plate. The forward current I_F and the maximum not repetitive forward current I_{FSM}, i.e. the surge overload current, are provided in graphical form, as can be seen in Fig. 3.50.

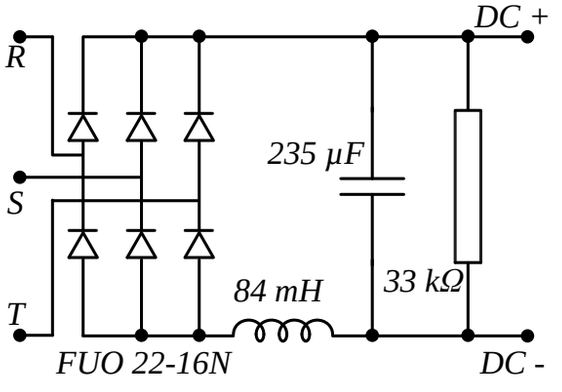

Fig. 3.49 Schematic of the nonlinear load (diode-bridge rectifier with capacitive output)

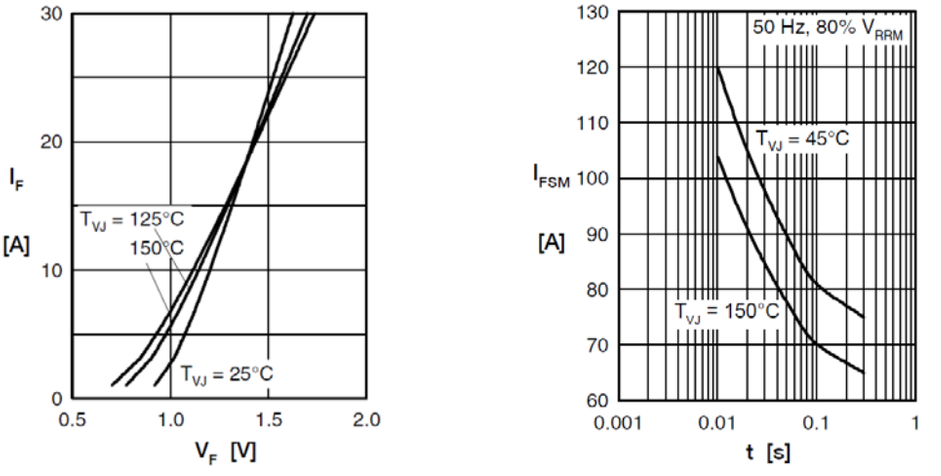

(a) (b)

Fig. 3.50 Characteristic curves of FUO 22-16N: (a) forward voltage - forward current for two different junction temperatures**;** (b) Not repetitive forward current

Table 3.6 FUO 22-16N specification from Datasheet

Symbol	Definition	Value
$\boldsymbol{V_{RRM}}$ $\boldsymbol{[V]}$ @ $\boldsymbol{T_{VJ}}$ = $\boldsymbol{25\ °C}$	Max. repetitive reverse blocking voltage	1600 V
$\boldsymbol{V_F}$ $\boldsymbol{[V]}$ @ $\boldsymbol{T_{VJ}}$ = $\boldsymbol{25\ °C}$	Forward voltage drop	1.20 V
$\boldsymbol{V_{TH}}$ $\boldsymbol{[V]}$ @ $\boldsymbol{T_{VJ}}$ = $\boldsymbol{175\ °C}$	Threshold voltage	0.81 V
$\boldsymbol{R_{TH}}$ $\boldsymbol{[V]}$ @ $\boldsymbol{T_{VJ}}$ = $\boldsymbol{175\ °C}$	Slope resistance	31 mΩ

With reference to the output inverter-side LC filter, the three-phase capacitors belong to E62-3ph family provided by Electronicon manufacturer. They are designed for demanding conditions, like the ones required in UPS applications. They are film capacitors connected internally in a delta configuration with low series resistances. The main parameters are summarized in Table 3.7.

Table 3.7 E62-3ph capacitors from Datasheet

Symbol	Definition	Value
$\boldsymbol{C_n}$ $\boldsymbol{[\mu F]}$	Rated capacitance	3 x 9 ±5%
$\boldsymbol{R_{is}}$ $\boldsymbol{[m\Omega]}$	Internal series resistance	3 x 1.8
$\boldsymbol{L_e}$ $\boldsymbol{[nH]}$	Self-inductance	100
$\boldsymbol{tan\delta_0}$	Dielectric dissipation factor	$2 \cdot 10^{-4}$
$\boldsymbol{V_n}$ $\boldsymbol{[V]}$	Rated voltage (peak value)	750 V AC
$\boldsymbol{V_{rms}}$ $\boldsymbol{[V]}$	Rms voltage	530 V
$\boldsymbol{V_s}$	Non recurrent surge voltage	1610 V

To evaluate the ESR of the capacitance R_{ESR} the following formula is applied

$$R_{ESR} = R_s + \frac{tan\delta_0}{2\pi f C_n}$$

At $f = 50\ Hz$, it results $R_{ESR} \cong R_s$.

The oscilloscope used to record the data belongs to MSO2000B series of Tektronix. Among the main features, it is characterized by a 200 MHz bandwidth, 4 analog and 16 digital channels, 1 GS/s maximum sample rate, a time-base range from 4 ns/div to 100 s/div, and FFT analysis for simplified waveform analysis.

3.7.2 Current Loop Only

3.7.2.1 PR regulators

By means of the test bed, four aspects are investigated: 1) discretization issues**;** 2) sensitivity to frequency variation in the reference of the regulator**;** 3) effect of voltage decoupling**;** 4) effect of the integrator gain value.

Regarding the discretization issues, the following methods are analysed: 1) structure with two integrators using forward and backward Euler discretization methods**;** 2) impulse invariant**;** 3) Tustin with frequency prewarping. As expected from the simulation results all methods perform well, producing zero steady-state error, at low frequency levels. For high frequency levels the performance begins to degrade for the structure with two integrators, as can be seen in Fig. 3.51, where a reference sinusoidal current at 250 Hz (5^{th} harmonic of the fundamental current) is imposed to the regulator. The results are shown for the case without voltage decoupling [see Fig. 3.51(a)] and with voltage decoupling [see Fig. 3.51(b)]. The data have been plotted in Matlab after have been recorded in dSpace ControlDesk scopes. It can be observed that:

- The regulator does not produce zero steady-state error, whether or not voltage decoupling is performed**;**
- the error is bigger when the capacitor voltage is not decoupled [see Fig. 3.51(a)].

If the implementation is based on the discretization of the regulator transfer function as shown in Table 3.4, the regulator performance is not affected by the discretization method (impulse invariant or Tustin with frequency prewarping). It must be noted that the frequency range for which this conclusion is valid is up to 1/10 of the switching frequency. Above this value, any regulator will have degraded performance. As an example, Fig. 3.52 shows the steady-state currents and error when the regulator

is implemented using impulse invariant as discretization method at the same conditions of Fig. 3.51. It is clear that the regulator produces zero steady-state error whether or not voltage decoupling is performed. This is the expected result from the theoretical analysis. Furthermore, although it is not shown, the same conclusions can be drawn for the cases of nonideal and complex vector PR regulators.

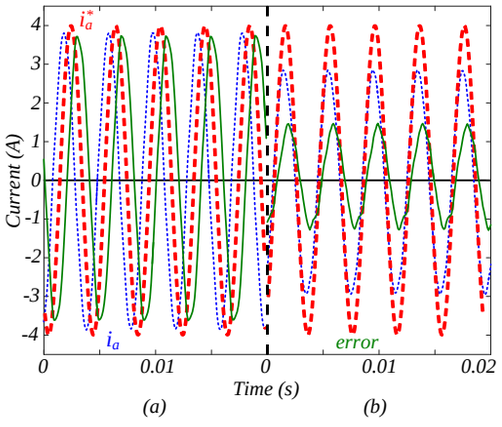

Fig. 3.51 Steady-state currents and error for ideal PR when implemented with two integrators using forward and backward Euler as discretization method - 5th harmonic reference tracking: (a) without voltage decoupling; (b) with voltage decoupling

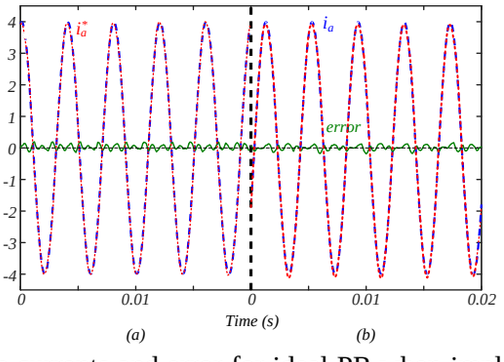

Fig. 3.52 Steady-state currents and error for ideal PR when implemented with impulse invariant as discretization method - 5th harmonic reference tracking: (a) without voltage decoupling; (b) with voltage decoupling

The bigger the reference frequency, the bigger will be the effect of the discretization method on the performance of the regulator. Fig. 3.53 shows the experimental results when a reference sinusoidal current at 550 Hz (11th harmonic of fundamental current) is imposed to the regulator. Again, the results are shown for the case without voltage decoupling [Fig. 3.53(a)] and with voltage decoupling [Fig. 3.53(b)]. It can be observed that:

- the regulator does not produce zero steady-state error, whether or not voltage decoupling is performed. Actually, by the size of the error the regulator is not

working anymore. As expected, the error is much higher than for the 5th harmonic tracking shown in Fig. 3.51;

- the effect of voltage decoupling is negligible. The phase error at that frequency is not corrected by the resonant regulator [see Fig. 3.43(a)].

The result of tracking an 11th harmonic sinusoidal reference with the regulator discretized using impulse invariant as discretization method is shown in Fig. 3.54. It shows that even at high frequencies this discretization method does not degrade the performance of the regulator.

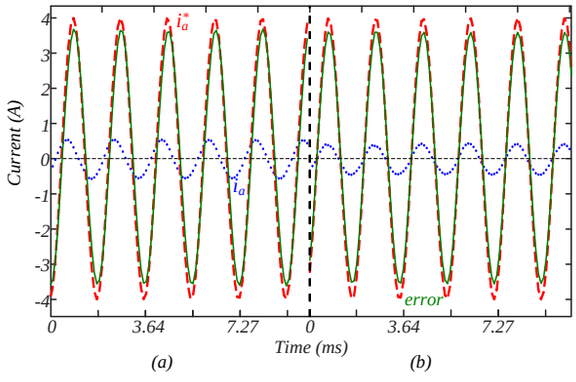

Fig. 3.53 Steady-state currents and error for ideal PR when implemented with two integrators using forward and backward Euler as discretization method - 11th harmonic reference tracking: (a) without voltage decoupling; (b) with voltage decoupling

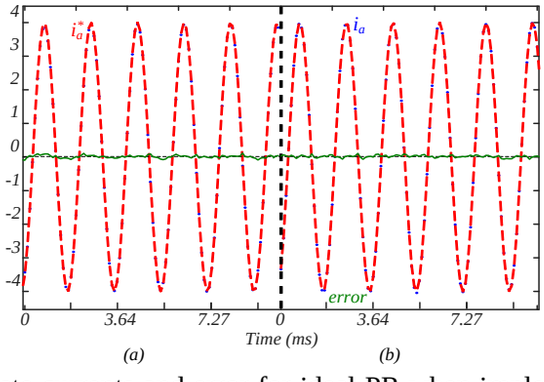

Fig. 3.54 Steady-state currents and error for ideal PR when implemented with impulse invariant as discretization method - 11th harmonic reference tracking: (a) without voltage decoupling; (b) with voltage decoupling

The sensitivity to frequency variations is analysed by changing the reference frequency while the resonant gain is kept constant at the previous defined resonant frequency. To avoid any influence of the discretization in this analysis, the regulators are discretized using impulse invariant method. For example, in the results shown in Fig. 3.55 and Fig. 3.56 the regulator reference frequency is made equal to 49 Hz while

the resonant gain is kept equal to $\omega_o = 2\pi 50\, rad/s$. It is clear that the effect of voltage decoupling has a significant impact on the performance of the closed loop system, reducing significantly the error. Comparing both figures it can be concluded that the zero steady-state error with voltage decoupling depends on the value of k_{iI}. This means that the sensitivity to frequency variations is a function of the integrator gain: for values around the one that produces zero/pole cancelation ($k_{iI} = 311$) the sensitivity is small (see Fig. 3.55).

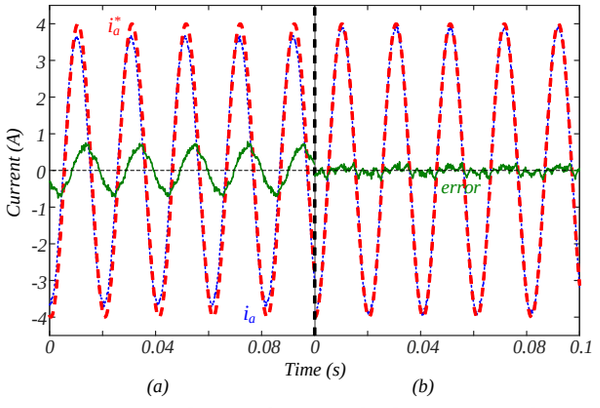

Fig. 3.55 Steady-state currents and error for nonideal PR: (a) without voltage decoupling; (b) with voltage decoupling - $\boldsymbol{f_{ref} = 49\ Hz}$, $\boldsymbol{k_{iI} = 311}$

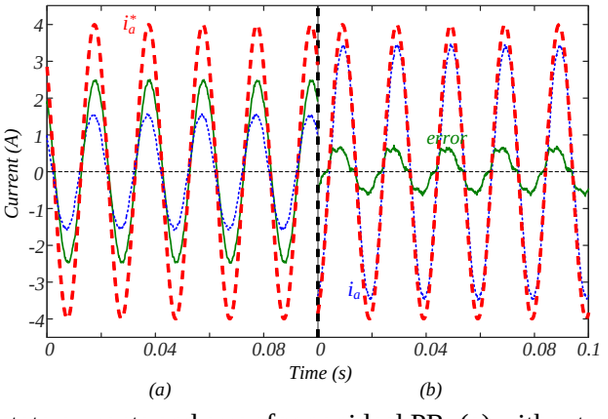

Fig. 3.56 Steady-state currents and error for nonideal PR: (a) without voltage decoupling; (b) with voltage decoupling - $\boldsymbol{f_{ref} = 49\ Hz}$, $\boldsymbol{k_{iI} = 11}$

The same frequency sensitivity analysis is made for the ideal PR regulator. Again, the discretization method is impulse invariant. Fig. 3.57 and Fig. 3.58 show the results for the cases with $k_{iI} = 311$ and $k_{iI} = 11$, respectively. By comparing Fig. 3.57 with Fig. 3.55, and Fig. 3.56 with Fig. 3.58 it can be concluded that the ideal PR regulator is more sensitive to frequency variations than the nonideal PR. Furthermore, the smaller is the integrator gain, the bigger is the sensitivity. As a result, a bigger steady-

state error occurs at low integrator gains. This is already predicted by the simulation frequency response analysis.

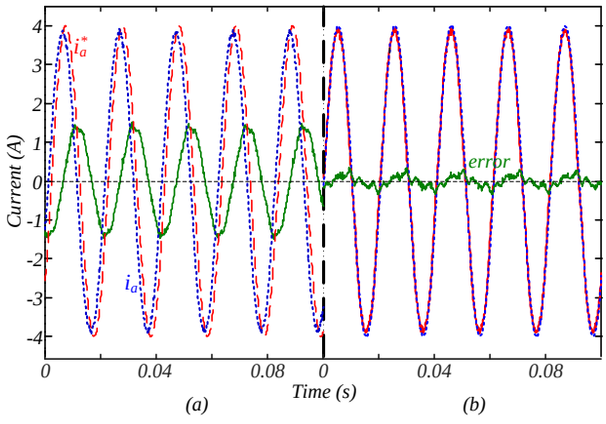

Fig. 3.57 Steady-state currents and error for ideal PR: (a) without voltage decoupling; (b) with voltage decoupling - $\boldsymbol{f_{ref} = 49\ Hz}$, $\boldsymbol{k_{il} = 311}$

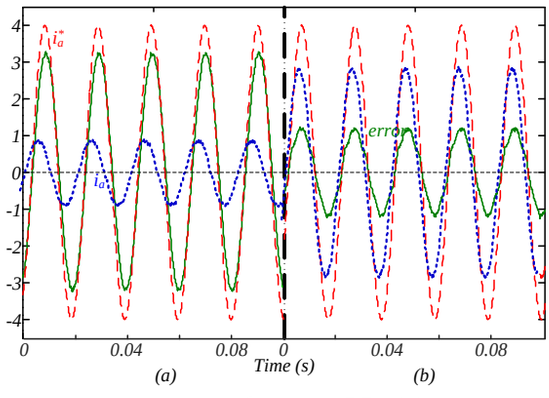

Fig. 3.58 Steady-state currents and error for ideal PR: (a) without voltage decoupling; (b) with voltage decoupling - $\boldsymbol{f_{ref} = 49\ Hz}$, $\boldsymbol{k_{il} = 11}$

For bigger frequency variations, the error increases, as can be seen in Fig. 3.59 (compared to Fig. 3.57). In this figure the reference frequency is changed to 47.5 Hz while the resonant gain is kept equal to $\omega_o = 2\pi 50\ rad/s$.

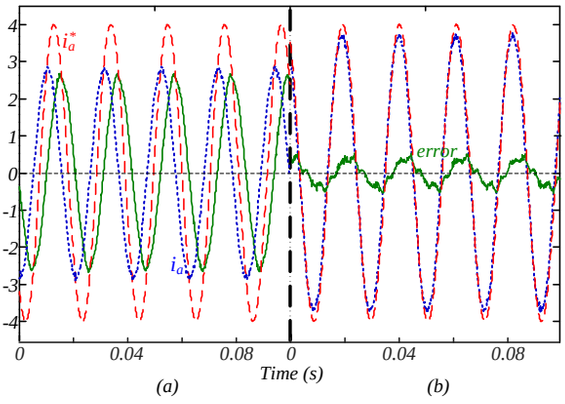

Fig. 3.59 Steady-state currents and error for ideal PR: (a) without voltage decoupling; (b) with voltage decoupling - $\boldsymbol{f_{ref} = 47.5\ Hz}$, $\boldsymbol{k_{il} = 311}$

The same frequency sensitivity analysis is made for the complex vector PR regulator. Again, the discretization method used is impulse invariant to avoid its influence on the analysis.

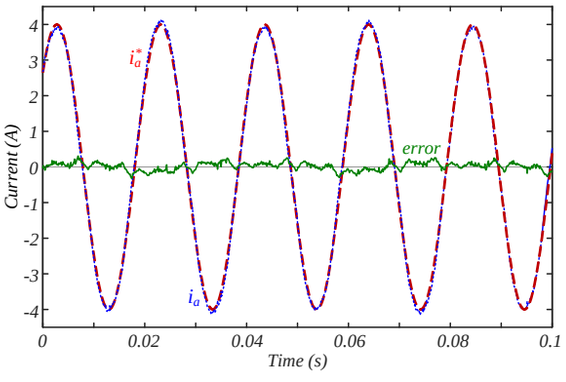

Fig. 3.60 Steady-state currents and error for complex vector PR: with voltage decoupling - $\boldsymbol{f_{ref} = 49\ Hz}$, $\boldsymbol{k_{il} = 311}$

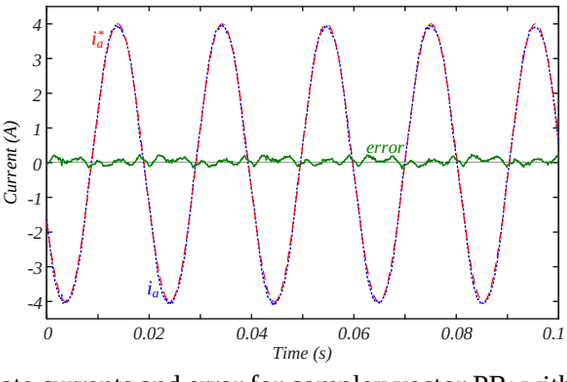

Fig. 3.61 Steady-state currents and error for complex vector PR: with voltage decoupling - $\boldsymbol{f_{ref} = 49\ Hz}$, $\boldsymbol{k_{il} = 11}$

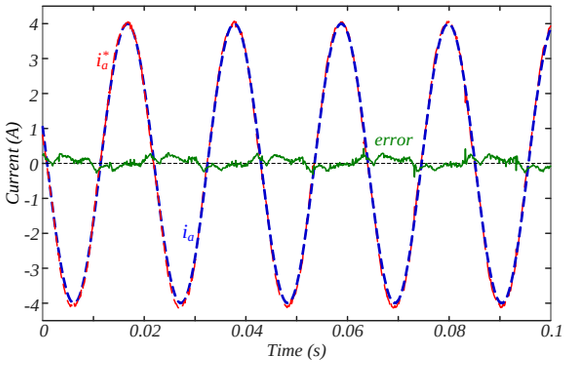

Fig. 3.62 Steady-state currents and error for complex vector PR: with voltage decoupling - $\boldsymbol{f_{ref} = 47.5\ Hz, k_{iI} = 311}$

Fig. 3.60 and Fig. 3.61 show the experimental results for the cases with $k_{iI} = 311$ and $k_{iI} = 11$, respectively. As expected from frequency response analysis, this controller produces zero steady-state error even for small values of k_{iI}, and frequency variations. It is the one that has the lowest sensitivity to frequency and integrator gain variations. This can be clearly observed in Fig. 3.62 where the reference frequency is equal to 47.5 Hz.

3.7.2.2 Proportional controller

Regarding the dynamic of the current loop only, a step response of the inductor current is performed using the test bed. The current regulator control parameters are reported in Table 3.8.

Table 3.8 Current regulator control parameters

Parameter	Value
Proportional gain w/o decoupling	$k_{pI} = 5.61$
Proportional gain with decoupling	$k_{pI} = 6.42$

In order to achieve approximately zero steady-state error with different control structures and voltage decoupling, the reference is multiplied by a constant, which is equivalent to multiply by a gain the closed loop transfer function of the inductor current. It should be noted that the dynamics of the system with the current loop only, i.e. voltage loop disabled and current reference generated manually, is not affected by this gain.

If voltage decoupling is not performed, due to the low gain at low frequencies, a high reference current must be provided to achieve the rated value (see the frequency response analysis in Fig. 3.11). However, it is not possible to achieve the rated current since the converter protection activates, due to the high initial current. Thus, in order to

obtain step response captures without voltage decoupling a lower reference current has to be provided.

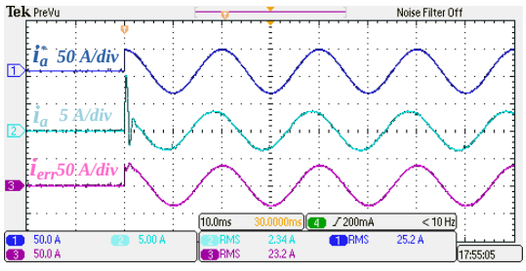

(a)

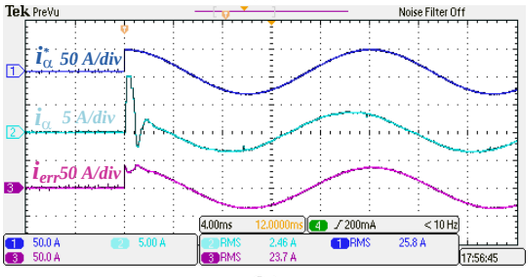

(b)

Fig. 3.63 Step response of the reference current without voltage decoupling: (a) (1) reference; (2) real; (3) inductor current error - (α-axis), timescale 10 ms/div; (b) (1) reference; (2) real; (3) inductor current error - (α-axis), timescale 4 ms/div

In Fig. 3.63 it can be seen the current during the transient is higher than the steady-state value because of low damping, as expected from the theoretical analysis. It should be noted the different scales for the reference (50 A/div) and real inductor current in α-axis (5 A/div). This test proves that the current loop is not working properly, since the reference is not tracked.

With reference to voltage decoupling with $G_{dec}(s) = 1$ the response is much more damped and the steady-state error is almost zero, even if just a P controller is used (see Fig. 3.64).

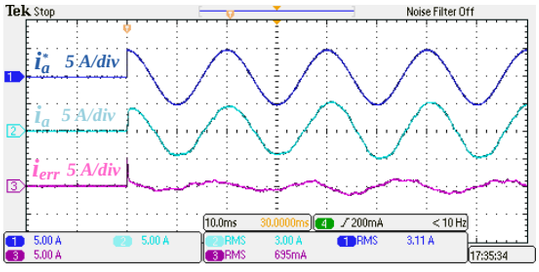

(a)

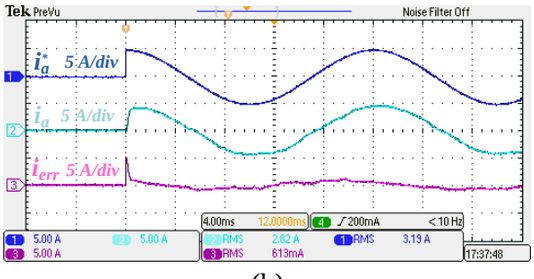

(b)

Fig. 3.64 Step response of the reference current with voltage decoupling and $\boldsymbol{G_{dec}(s) = 1}$: (1) reference; (2) real; (3) inductor current error - (α-axis), timescale 10 ms/div; (b) (1) reference; (2) real; (3) inductor current error - (α-axis), timescale 4 ms/div

The response to a step change in the inductor current is similarly more damped with a lower steady-state error in case $G_{dec}(s) = G_{LPF}(s)G_{lead}(s)$ and a P controller are used (see Fig. 3.65).

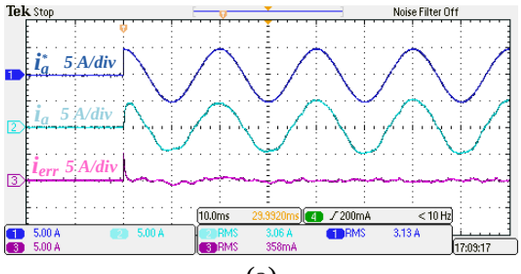

(a)

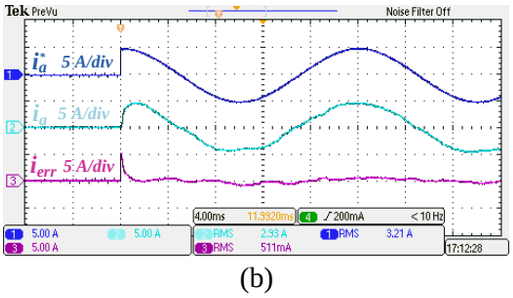

(b)

Fig. 3.65 Step response of the reference current with voltage decoupling and $\boldsymbol{G_{dec}(s) = G_{LPF}(s)G_{lead}(s)}$: (1) reference; (2) real; (3) inductor current error - (α-axis), timescale 10 ms/div; (b) (1) reference; (2) real; (3) inductor current error - (α-axis), timescale 4 ms/div

In this case, $G_{LPF}(s)$ is designed as a first order IIR Butterworth low-pass filter with a bandwidth of 400 Hz and a sampling frequency of 10 kHz. The lag introduced at fundamental frequency is 7.09°. $G_{lead}(s)$ is designed to compensate for the lag at fundamental frequency introduced by $G_{LPF}(j\omega_1)$ and $G_{PWM}(j\omega_1)$. The discrete-time implementation of the low-pass filter is

$$G_{LPF}(z) = K\frac{a_1 + a_2 z^{-1}}{b_1 + b_2 z^{-1}}, \tag{3.37}$$

where $K = 0.1122$, $a_1 = a_2 = 1$, $b_1 = 1$, $b_2 = -0.7757$.

The lead compensator is designed with the form

$$G_{lead}(s) = \frac{1 + \tau_z s}{1 + \tau_p s}, \tag{3.38}$$

being $\tau_z = 1.8433 \times 10^{-4}$ and $\tau_p = 3.4354 \times 10^{-5}$. Subsequently the filter is discretized with the Tustin method in order to get the discrete-time implementation.

It can be stated that a simple P controller can be used in the current loop only if voltage decoupling is performed, even if this decoupling is not ideal. Thanks to the capacitor voltage decoupling, the controller tracks the fundamental component with fast transient response.

To verify the behaviour of the inner current loop under overload, a step load change more than four times the rated load is performed. The load impedance changes from 68 Ω to 16 Ω while the current reference is kept constant. To keep the inductor current at the same level as before the load change, the output voltage (output of the inner current loop) decreases (see Fig. 3.66). This proves the controller is able to track any command provided by the outer voltage loop.

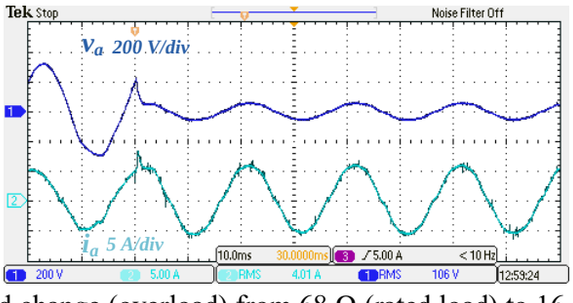

Fig. 3.66 Step load change (overload) from 68 Ω (rated load) to 16 ohm (4.25 times the rated load): capacitor voltage (output voltage) and inductor current in α-axis

3.7.2.3 Concluding considerations on the current loop

In the previous paragraphs, four regulators intended for the inner current loop of a three-phase VSI have been compared in terms of effect of the delay model, influence of the discretization method, sensitivity to frequency variation, effect of cross-coupling

decoupling, and influence of the integrator gain. The tools used for the analysis were the frequency response, root locus, and steady-state error. The regulators analysed were the proportional, the ideal PR, nonideal PR and Complex Vector PR. The comparisons were organised as follow:

- without voltage decoupling**;**
- with voltage decoupling**;**
- with nonideal voltage decoupling.

The following conclusions can be stated:

- Independently of the regulator used the delay model affects the design of the regulators. The resulting system can have a completely different bandwidth with respect to the one previously designed if the system delays have not been taken into account. For a wide bandwidth design, the first order Padè approximation with a non-minimal phase zero would be preferable.
- If no output voltage cross-coupling decoupling is used:
    - Independently of the regulator used, the capacitor voltage coupling produces load dependent dynamics**;**
    - As expected the **P** regulator is unable to produce zero steady-state error at 50 Hz. Indeed, the error is very large**;**
    - The **nonideal PR** regulator ability to produce zero steady- state error at the desired resonant frequency is highly dependent of the integrator gain. The smaller is the integrator gain, the bigger will be the error**;**
    - The **ideal PR** controller is able to produce zero steady-state error at the desired resonant frequency (50 Hz). However, the system frequency response is very sensitive to frequency variations around the fundamental frequency. This sensitivity is bigger than for the case of the nonideal PR controller**;**
    - The **complex vector PR** controller is unstable. From the frequency response analysis, if it could be used it would be able to produce zero steady-state error at the desired resonant frequency with low sensitivity to frequency and integrator gain variations. This regulator would be preferred, based on the steady-state analysis. However, from the stability (and transient) analysis the dominant poles are in the right half plane, which makes the system unstable. Because of the low sensitivity to the integrator gain (k_{il}) variation, the use of this regulator would give flexibility in this gain choice (if it could be used).
- If output voltage cross-coupling decoupling is used:

- The voltage cross-coupling decoupling has interesting features in the frequency response. For any of the controllers analysed it decreases the steady-state error, the sensitivity to frequency variations, and the sensitivity to the integrator gain (k_{iI}) values variation. Indeed, the benefits of the output voltage decoupling are larger than those caused by the additional resonator part in the regulators**;**
- Whenever voltage cross-coupling decoupling is performed, the resulting closed loop dynamics have better behaviour with more damping even if nonideal decoupling is performed**;**
- It is better to use just a **P** controller for the inner loop if its bandwidth is widened enough and there is an outer voltage loop as is the case in standalone microgrids/UPS applications. It is a simpler controller that leads to less stability problems**;**
- For the cases where there is no voltage loop, resonant regulators are preferred. Among the regulators analysed the **complex vector PR** would be preferred due to its low sensitivity to frequency variations around the resonant frequency.

It must be noted that the equivalent series resistor of the inductor will affect the results. The bigger its value, the bigger will be the steady-state error. In addition, the benefits of the PR regulators over the P regulator will be bigger.

3.7.3 Voltage and Current Loops

3.7.3.1 One VSI in standalone mode

The performance of the proposed current control in combination with the PR voltage loop is analysed in this section. It is experimentally verified that the proposed system solution fulfils the requirements imposed to UPS systems. In Fig. 3.67(a) a 100% linear (resistive) step load change is shown. The results obtained are compared to the envelope of the voltage deviation for linear loads, as reported in the IEC 62040 standard for UPS systems [Fig. 3.67(b)].

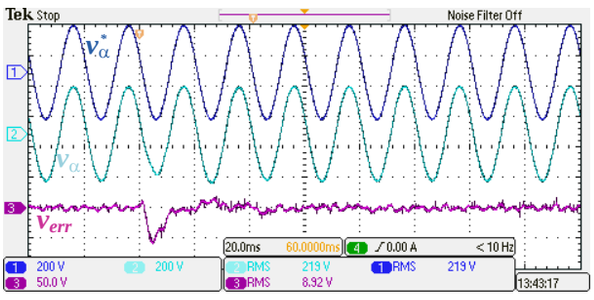

(a)

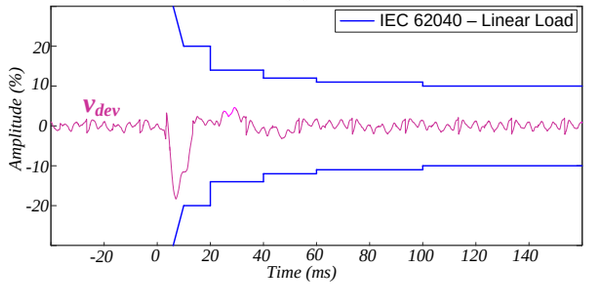

(b)

Fig. 3.67 Linear step load changing (0 – 100%): (a) reference (200 V/div), real (200 V/div), and capacitor voltage error (50 V/div) (α-axis); (b) Dynamic characteristics according to IEC 62040 standard for linear loads

This normative sets the dynamic characteristics of the output voltage for standardized linear and nonlinear loads (diode bridge rectifiers with output capacitor). According to the sign of the reference and real capacitor voltage, their difference (voltage deviation v_{dev}) belongs to the under-voltage ($v_{dev} < 0$) or over-voltage ($v_{dev} > 0$) region. It should be noted that the capacitor voltage error can differ from v_{dev} depending on the sign of the reference and real voltage. The values are normalized to the peak voltage. It can be seen that the system reaches steady-state in less than half a cycle after the load step change. The dynamic response is well damped, as predicted by the design, and within the normative limits.

A diode bridge rectifier with capacitor output filter (parameters in Table 3.1) is used as nonlinear load. A 100% nonlinear step load change is performed without and with the harmonic compensators tuned at the 5th and 7th harmonics [see Fig. 3.68(a) and Fig. 3.69(a)]. From the FFT analysis in Fig. 3.68(b) and Fig. 3.69(b) it can be seen the compensation of the harmonics to which the resonant controllers have been tuned. In Fig. 3.69(c) the results in terms of voltage deviations are compared with the standards set by IEC 62040. It should be noted the dynamic response is even within the limits imposed to linear loads.

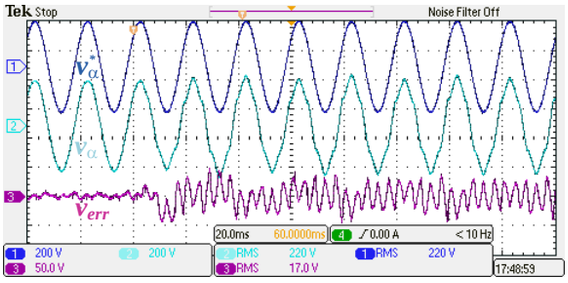

(a)

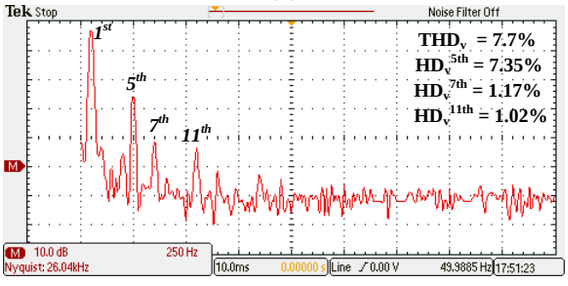

(b)

Fig. 3.68 Voltage loop without the 5th 7th HC and nonlinear load: (a) 100% Step load change, reference (200 V/div), real (200 V/div), and capacitor voltage error (50 V/div) (α-axis); (b) FFT of the capacitor voltage (250 Hz/div)

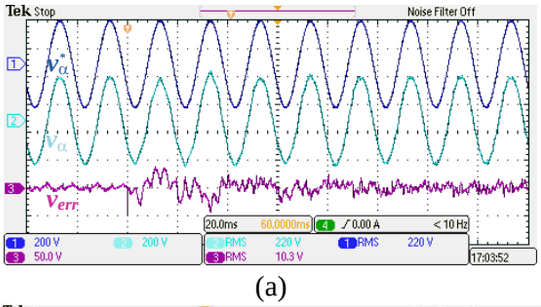

(a)

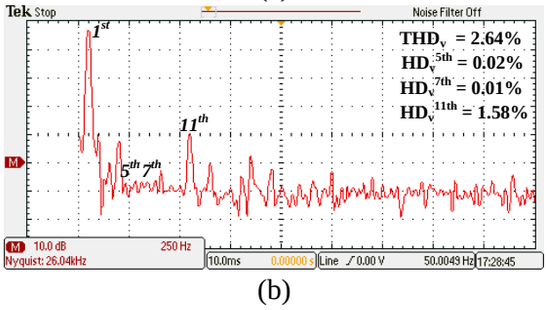

(b)

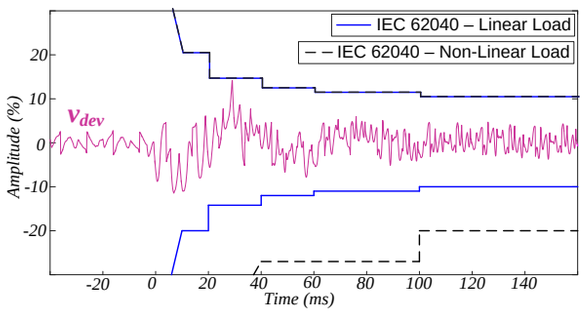

(c)

Fig. 3.69 Voltage loop with 5th 7th HC and nonlinear load: (a) 100% Step load change, reference (200 V/div), real (200 V/div), and capacitor voltage error (50 V/div) (α-axis); (b) FFT of the capacitor voltage (250 Hz/div); (c) Dynamic characteristics according to IEC 62040 standard for nonlinear loads

3.7.3.2 Two VSIs in parallel in standalone mode

The benefits of applying state feedback cross-coupling voltage decoupling are also experimentally verified with two converters in parallel. The physical system considered is shown in Fig. 3.70. In particular, control loops with reduced bandwidth are needed. An important point in standalone grids is the load sharing among distributed generators, especially when the distribution lines are not symmetric [171], [172], [173]. By including virtual impedance at fundamental frequency, the effect of the line impedances can be mitigated [30], [174], [175]. Furthermore, the virtual impedance can improve the sharing of nonlinear and unbalanced loads [172], [176], [177], [178], [179].

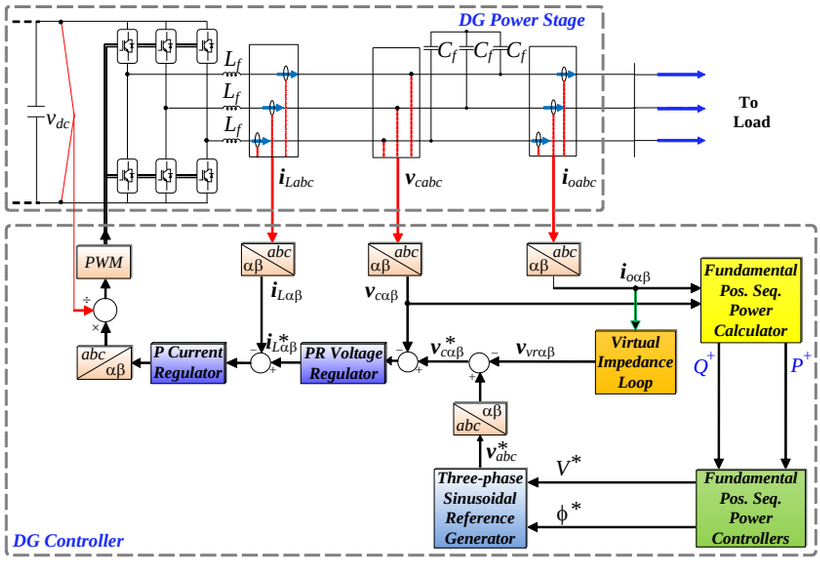

Fig. 3.70 DG power stage and control system

The power calculation and droop control methods are based on [26], [171], [180], [181]. The instantaneous values of active and reactive power in the stationary reference frame are defined as

$$p = v_{c\alpha} i_{o\alpha} + v_{c\beta} i_{o\beta}, \tag{3.39}$$

$$q = v_{c\beta} i_{o\alpha} - v_{c\alpha} i_{o\beta}. \tag{3.40}$$

A first order low-pass filter of 0.7 Hz cut-off frequency is used to extract the fundamental positive sequence component of active and reactive power (Fundamental Positive Sequence Power Calculator block in Fig. 3.70). Specifically

$$P^{+} = \frac{s}{s^2 + \omega_0^2} p, \tag{3.41}$$

$$Q^{+} = \frac{s}{s^2 + \omega_0^2} q. \tag{3.42}$$

Subsequently, a power droop control scheme is applied (Fundamental Positive Sequence Power Controllers block in Fig. 3.70). Droop control allows active and reactive power sharing among parallel connected VSIs without the need of using any critical low-bandwidth communication network [178]. The basic idea is to mimic the behaviour of a synchronous generator, which decreases the frequency as the active power is increased [178]. A similar relationship applies to reactive power and output voltage. As a result, the equations implemented are

$$\phi^{*} = \frac{1}{s}\omega_0 - G_P(s)(P^{+} - P_0^{+}), \tag{3.43}$$

$$V^{*} = V_0 - G_Q(s)(Q^{+} - Q_0^{+}). \tag{3.44}$$

The subscript $'0'$ denotes reference values, while $G_P(s)$ and $G_Q(s)$ are the transfer functions associated to active and reactive power respectively. In this work the following droop coefficients are applied [171]

$$G_P(s) = k_{pP} + \frac{k_{iP}}{s}, \tag{3.45}$$

$$G_Q(s) = k_{pQ}. \tag{3.46}$$

The proportional gain for active power droop control k_{pP} is designed to achieve a maximum frequency deviation of around $\Delta f_{max} = 0.01\%$ at steady-state according to

$$k_{pP} = \frac{\Delta f_{max}\omega_0}{2P_{max}}, \tag{3.47}$$

being P_{max} the maximum active power which can be provided by the converter [178]. On the other hand, k_{pQ} is selected for a maximum voltage deviation of $\Delta V_{max} = 0.1\%$ at steady-state according to

$$k_{pQ} = \frac{\Delta V_{max}\omega_0}{2Q_{max}}. \tag{3.48}$$

The values of the coefficients here defined are reported in Table 3.10 along with k_{iP}, designed to improve command tracking performance.

The structure of the virtual impedance block is depicted in Fig. 3.71 where the components of the inverter output current are extracted and then fed to a selective structure.

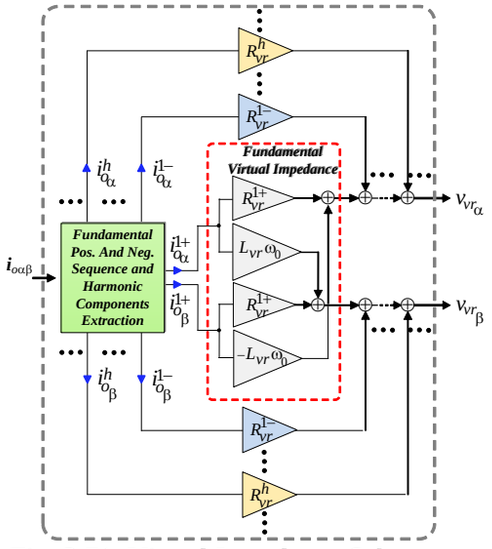

Fig. 3.71 Virtual Impedance Scheme

Specifically, fundamental positive sequence components are fed to an RL impedance block and other components (fundamental negative sequence as well as harmonic components, here the 3rd, 5th and 7th) pass through the virtual resistances [172]. This structure corresponds to

$$V_{vr\alpha} = R_{vr}^1 i_{o\alpha}^1 - L_{vr}\omega_0 i_{o\beta}^{1+} + \sum_{h=3,5,7} R_{vr}^h i_{o\alpha}^h, \tag{3.49}$$

$$V_{vr\beta} = R_{vr}^{1} i_{o\beta}^{1} + L_{vr}\omega_0 i_{o\alpha}^{1+} + \sum_{h=3,5,7} R_{vr}^{h} i_{o\beta}^{h}. \tag{3.50}$$

To extract the harmonic components $i_{o\alpha\beta}^{h}$, the sum of positive and negative sequence components $i_{o\alpha\beta}^{m}$ with $m \neq h$ is subtracted to $i_{o\alpha\beta}$.

Similarly to the previous laboratory tests, a low scale test bed made of two Danfoss power converters of 2.2 kVA each has been used. The control platform is based on the dSpace DS1006. An A/D DS2004 board is used to digitalize the analog signals sensed via LEM current and voltage transducers. A D/A conversion 16-bit high resolution board DS2102 has been used to record the data on two oscilloscopes.

A photo and schematic of the experimental setup are shown in Fig. 3.72 and Fig. 3.73. The PWM signals for each VSI are sent from dSpace DS1006 platform, based on the implemented control law. Three-phase inductor current, capacitor voltage and output current are measured for each VSI, as well as the voltage at the Point of Common Coupling (PCC). The measured variables are sent to the A/D board DS2004. Only the reference, real and capacitor voltage error in α-axis from each VSI are sent to the D/A board DS2102 and then to the oscilloscopes.

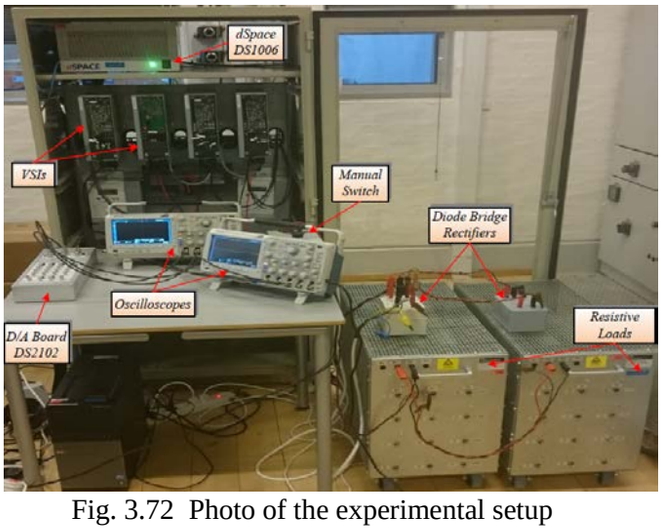

Fig. 3.72 Photo of the experimental setup

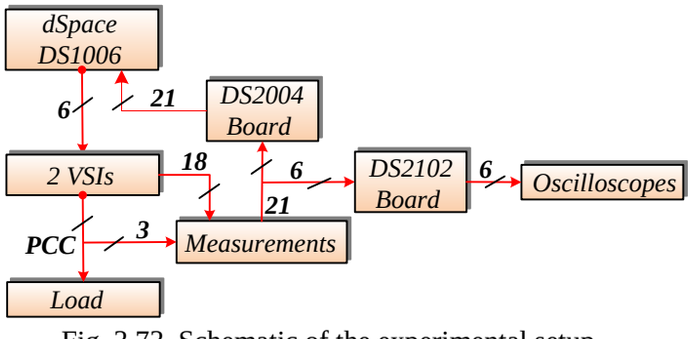

Fig. 3.73 Schematic of the experimental setup

All the following experimental results are performed using a proportional controller as current regulator and with state feedback decoupling of the capacitor voltage. Resonant regulators tuned at specific harmonic orders are used in the outer voltage loop. The two parallel power converters are droop-controlled and operate in voltage control mode. Two diode bridge rectifiers are used as nonlinear loads, with unbalance created opening one phase on the AC side of the loads.

Table 3.9 Voltage regulator parameters for two VSIs in parallel

Parameter	Symbol
Proportional gain	$k_{pV} = 0.05$
Integral gain	$k_{iV} = 100$
Integral gain 3rd HC	$k_{iV,h3} = 10$
Integral gain 5th HC	$k_{iV,h5} = 10$
Integral gain 7th HC	$k_{iV,h7} = 10$

Table 3.10 Droop control parameters

Parameter	Symbol
Proportional gain (active power)	$k_{pP} = 1 \times 10^{-6}$
Integral gain (active power)	$k_{iP} = 1 \times 10^{-4}$
Proportional gain (reactive power)	$k_{pQ} = 5 \times 10^{-4}$

Table 3.11 Virtual impedance parameters

Parameter	Symbol
Virtual inductance	$L_{vr} = 2.5$ mH
Fund. pos. sequence	$R_{vr}^{1+} = 0.3\ \Omega$
Fund. neg. sequence	$R_{vr}^{1-} = 1.5\ \Omega$
Pos. and neg. sequence 3rd H	$R_{vr}^{3} = 2\ \Omega$
Pos. and neg. sequence 5th H	$R_{vr}^{5} = 4\ \Omega$
Pos. and neg. sequence 7th H	$R_{vr}^{7} = 4\ \Omega$

The integral gain value k_{iI} has been increased to 100 to achieve a faster synchronization between the power converters. The voltage regulator control parameters are shown in Table 3.9. The same system and current control parameters in Table 3.1 and Table 3.8 are used. The droop control and virtual impedance parameters are reported in Table 3.10 and Table 3.11. In particular, their design is based on [171], [172].

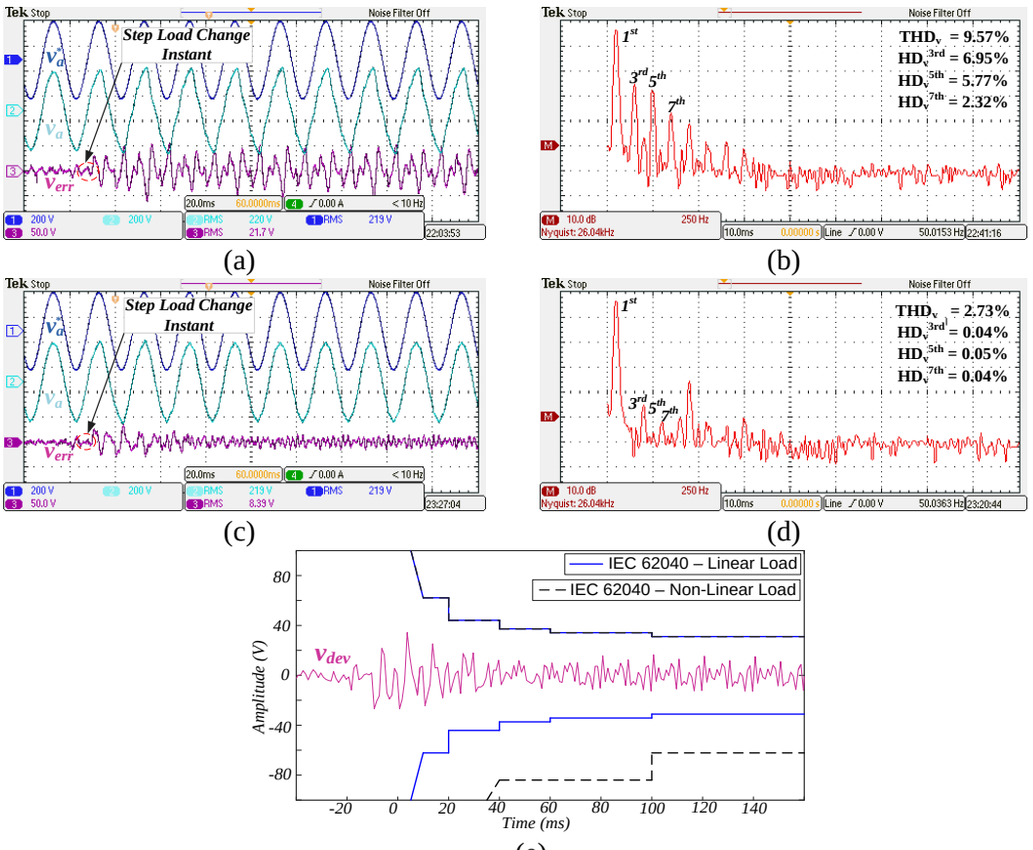

Fig. 3.74 Unbalanced nonlinear step load change with DGs in parallel: DG_1 with output impedance of L_1 = 1.8 mH; DG_2 with output impedance of L_2 = 1.8 mH - (a) Transient response without HC, reference (200 V/div), real (200 V/div) and capacitor voltage error (50 V/div) (α-axis); (b) FFT of the capacitor voltage (250 Hz/div); (c) Transient response with 3rd, 5th, 7th HC, reference (200 V/div), real (200 V/div) and capacitor voltage error (50 V/div) (α-axis); (d) FFT of the capacitor voltage (250 Hz/div); (e) 100% Step load change, Dynamic characteristics according to IEC 62040 standard for linear loads

In Fig. 3.74(a) a 100% unbalanced (one phase open) nonlinear step load change (from open circuit to full rated load) is performed, without activating the harmonic compensators (HC) in the voltage loop for both power converters. As expected from the FFT analysis [see Fig. 3.74(b)], harmonics are present in the capacitor voltage, mainly a 3rd harmonic component due to unbalanced load.

Performing the step load change with HC activated at the 3rd, 5th and 7th harmonic orders [see Fig. 3.74(c)] reduces significantly the THDv, without interfering the transient response. Still the system reaches steady-state in less than one cycle and a half after the load step change. Since the bandwidth of the voltage loop has been set to 100 Hz, a 3rd HC is needed. The transient response complies with the standards imposed by IEC 62040 for UPS systems, as shown in Fig. 3.74(e). Similar results are obtained for the other power converter, referred to as DG_2.

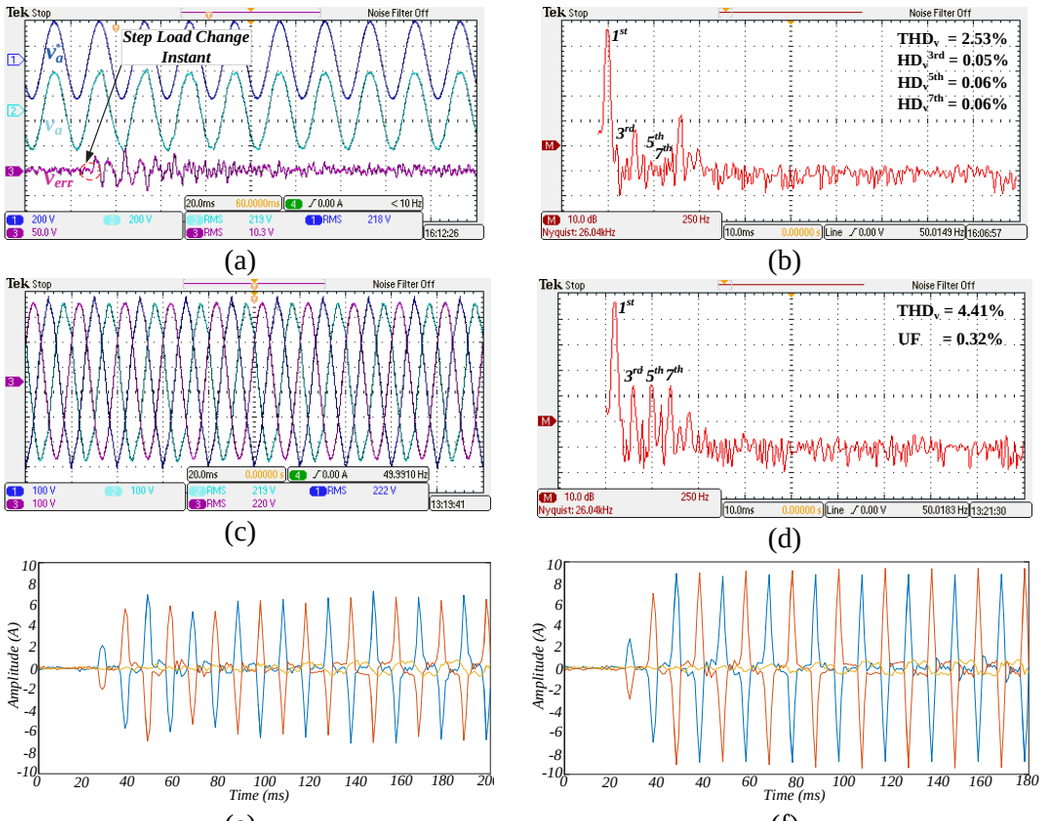

Fig. 3.75 Unbalanced nonlinear step load change with DGs in parallel: DG_1 with output impedance of L_1 = 3.6 mH; DG_2 with output impedance of L_2 = 1.8 mH; **virtual impedance not activated** - (a) Transient response, reference (200 V/div), real (200 V/div) and capacitor voltage error (50 V/div) (α-axis); (b) FFT of the capacitor voltage (250 Hz/div); (c) Voltage at PCC; (d) FFT of voltage at PCC (250 Hz/div); (e) Transient conditions, output current from DG_1; (f) Transient conditions, output current from DG_2

Unbalance between the two lines supplying the loads is created doubling the line impedance at the output of DG_1. Again, a 100% unbalanced nonlinear step load change is performed [see Fig. 3.75(a)]. Both power converters have the HC at 3rd, 5th and 7th harmonic activated. The steady-state voltage at PCC between the two VSIs is shown in Fig. 3.75(b), which results in an Unbalance Factor (UF) of 0.32%, in compliance with the standards which set the upper limit to 2% [182], [183]. The UF is defined as the ratio between the negative and the positive sequence voltage components. However, the load is not equally shared between the DGs as can be seen comparing Fig. 3.75(e) and Fig. 3.75(f). These last data have been plotted in Matlab after have been recorded in dSpace ControlDesk scopes.

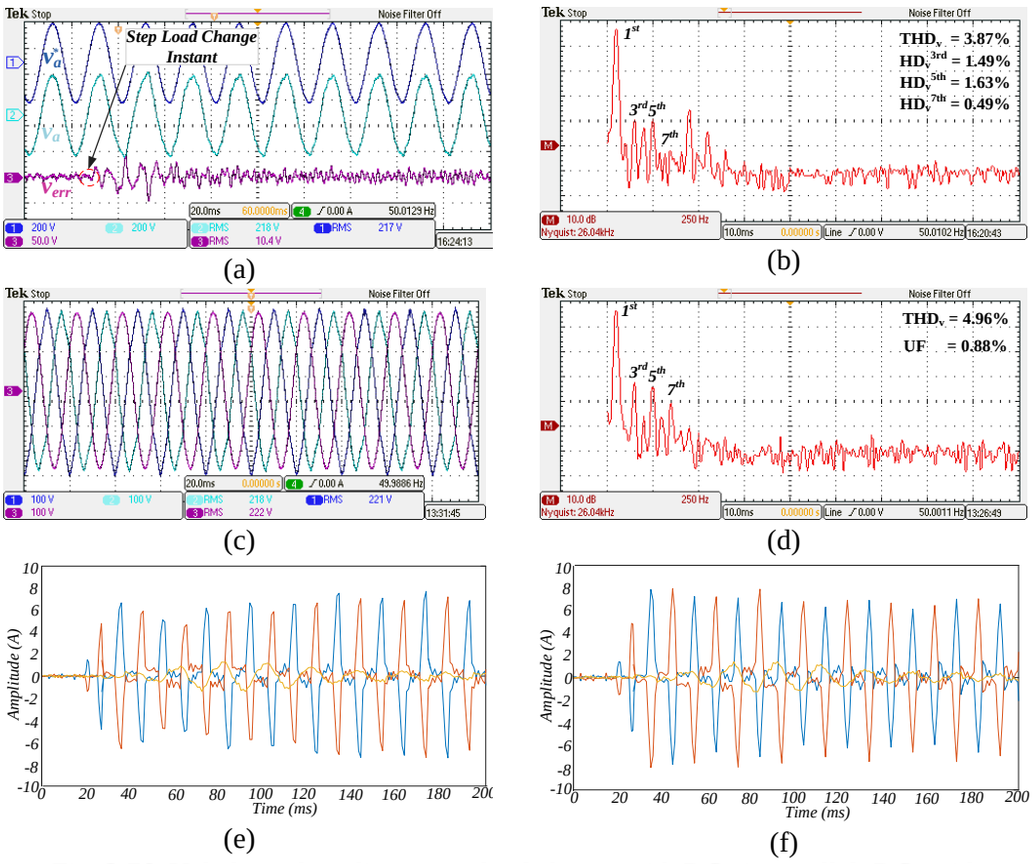

Fig. 3.76 Unbalanced nonlinear step load change with DGs in parallel: DG_1 with output impedance of L_1 = 3.6 mH; DG_2 with output impedance of L_2 = 1.8 mH; **virtual impedance activated** - (a) Transient response, reference (200 V/div), real (200 V/div) and capacitor voltage error (50 V/div) (α-axis); (b) FFT of the capacitor voltage (250 Hz/div); (c) Voltage at PCC; (d) FFT of voltage at PCC (250 Hz/div); (e) Transient conditions, output current from DG_1; (f) Transient conditions, output current from DG_2

When the Virtual Impedance outer loop is activated, the current sharing improves noticeably [see Fig. 3.76(e) and Fig. 3.76(f)]. This improvement is achieved by decrease the DG_2 current components and increase the DG_1 current components. In addition, fundamental positive sequence component of load current is still shared properly. However, it can be seen the current sharing improvement is achieved at the expense of increasing all voltage distortions: the THD and the UF at PCC slightly increase [see Fig. 3.76(c) and Fig. 3.76(d)] as well the harmonic distortion at DGs level [see Fig. 3.76(a) and Fig. 3.76(b)].

3.8 Continuous-Time Modelling - Conclusive Considerations

The effect of state feedback coupling on the dynamics performance of current and voltage regulators for islanded microgrids/UPS systems has been investigated. The benefits of applying capacitor voltage decoupling are motivated by the higher damping of the system, and almost zero steady-state error when a P controller is used for the current loop. The computation and PWM delays are the main responsible to limit the bandwidth that can be achieved by the current regulator. Even if the system delays are not compensated on the decoupling path (nonideal voltage decoupling), the system shows a higher damping than without decoupling. Further improvement can be obtained by introducing a lead-lag filter in the decoupling path.

Three different PR current regulators structures are analysed and compared. As the frequency harmonic order of the resonant regulator is increased, the mapping from the continuous-time domain to the discrete-time domain using the structure with two integrators and forward and backward Euler as discretization methods produces some discrepancy and higher steady-state error is observed. On the other hand, impulse invariant and Tustin with frequency prewarping allow the harmonic components to be perfectly represented. The sensitivity of the regulators to frequency and integral gain deviations is investigated. Complex Vector PR, which is stable only if voltage decoupling is performed, shows the lowest sensitivity to both frequency and integral gain value variations.

A design methodology for PR voltage regulators based on a lead compensator structure is provided, according to the proposed P inner current controller. Its effect is reflected in the Nyquist trajectories calculated for the voltage loop, and hence affects the selection of controller gains. A practical design methodology to select the minimum value of the fundamental resonant gain is proposed. The overall solution provides good performance both in steady-state and transients. More specifically, the requirements during transient imposed by the UPS standard IEC 62040 are verified according to the design proposed for the current and voltage regulators. The dynamic response is even within the standards for linear loads in case the 5^{th} and 7^{th} harmonic compensators are activated together with the fundamental gains, when a diode bridge rectifier is supplied. The analysis is extended to two droop-controlled voltage source inverters in parallel. Unbalance between the two lines is considered with the virtual impedance allowing proper load current sharing.

Chapter IV

4 Physical System Modelling in the Discrete-Time Domain

4.1 Discrete-Time Domain Design Benefits

Part of the work described in this chapter has been previously published in [2], [19], [21], [22].

A possible approach for physical system analysis is based on frequency and Laplace-domain models, which are useful as they improve the general perception of the dynamic behaviour of pulse-width modulators [63]. This analysis has been performed extensively in Chapter 3. As already explained, the *s*-domain design of the regulators is followed by their discretization, based on Euler, Trapezoidal discretization or similar methods. However, the mapping from the *s*-domain to the *z*-domain can introduce some discrepancy depending on the discretization method used [66], [184], in particular for discretization of high-frequency harmonic compensators. On the other hand, the direct design of digital compensators in the discrete-time domain provides more accuracy, being able to capture the sampling effects. In fact, the transformation of the system in the discrete-time domain by means of the z-transform or the discrete-time small-signal modelling in state-space form allows the sample-and-hold effect and time lag to be treated accurately [64], [185], [186], without the need of using the approximated rational transfer functions of the delay [37]. Moreover, the methodology presented in [187] allows the Cross-Coupled State Equations of a system with coupled variables and multiple feedback paths to be derived, following an exact discretization approach. This is the approach to be used in order to correctly represent the coupling between the controlled states. In general, other advantages can be identified for direct design in the *z*-domain:

- design for direct discrete-time pole-placement [188], [57], [189]**;**
- improved dynamic performance and robustness of the regulators [48], especially if the ratio of the sampling frequency to the fundamental frequency is low [188] or the current regulator is tuned for a very wide bandwidth [32];

- ease of implementation to track commanded arbitrary trajectories at each sampling instant.

Accordingly, *z*-domain design can be considered convenient.

As proved in Chapter 3 - Paragraph 3.4.1.5, the state feedback decoupling action can be improved by leading the capacitor voltage on the state feedback decoupling path. However, the analysis is performed in the continuous-time domain. Moreover, the possibility to widen the current loop bandwidth either by means of a lead compensator on the forward path or a Smith Predictor structure has not been investigated. As will be shown in this Chapter, both structures allow good dynamics properties to be achieved as the controller bandwidth is widened. However, the way these techniques aim at compensating for system delays is different. Specifically, the lead compensator adds an additional degree of freedom to the system in order to directly locate the poles of the closed loop controller transfer function. On the other hand, the Smith predictor structure permits the design of the controller based on the un-delayed model of the physical plant by building a parallel model which cancels the system delay. As the current regulator dynamics are enhanced, the voltage loop dynamics are widened as well.

In this Chapter it is shown how an accurate modelling of the delay effects in decoupling leads to a better control design and dynamics assessment.

A model in the discrete-time domain which takes into account the coupling of the capacitor voltage with the inductor current, even if voltage decoupling is performed, is derived analytically. This model is shown to better represent the physical system being addressed. It is important to note that even without the one sample delay introduced by computation, the sample-and-hold effect is still present and limits the achievable bandwidth, thus reducing the benefits introduced by the decoupling. The effect of widening the inner current loop bandwidth by means of two techniques based on a lead compensator structure and Smith Predictor is proposed. Finally, the results obtained for the current loop analysis are applied to design the voltage loop, based on the Nyquist criterion.

This Chapter is organized as follows.

In Section 4.2 the model in the discrete-time domain which takes into account the coupling of the controlled states is derived. The devised model is compared to the simplified formulation based on an RL load and the main differences are discussed.

In Section 4.3 the inner loop current control with state feedback voltage decoupling is analyzed. Two techniques aimed at widening the bandwidth of the current regulator, based on a lead compensator structure and Smith Predictor, are proposed and compared.

Subsequently, in Section 4.4, a PR voltage controller design is proposed based on the design of the current regulator with wide bandwidth. Detailed design and tuning are provided according to the Nyquist criterion.

Moreover, in Section 4.5 discretization issues of an anti-wind up scheme for the voltage regulator are analyzed.

In Section 4.6 the theoretical solution is supported by experimental results, verifying their compliance with the IEC 62040 normative for UPS systems.

4.2 Discrete-Time Domain Modelling

The physical system in Fig. 2.1 is represented in the discrete-time domain in Fig. 4.1. Compared to Fig. 3.1, $G_i(z)$ and $G_v(z)$ represent the current and voltage regulators transfer functions in the discrete-time domain. There is one sample computation delay associated to the implemented regular sample symmetrical PWM strategy, i.e. the time required to compute the duty-cycle control signal [82], [185]. $G_{dec}(z)$ is the transfer function related to the decoupling of the cross-coupling states in the z-domain.

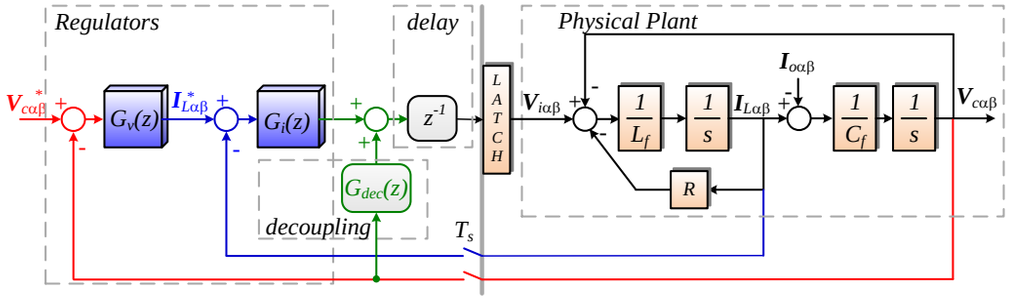

Fig. 4.1. Simplified block diagram of the closed loop system

According to the discussion in Chapter 3, as voltage decoupling is performed, higher damping is achieved with less overshoot for a given bandwidth. If it were possible to exactly decouple (cancel) the capacitor coupling, the system would become not dependent on the load impedance and the physical plant could be represented by an RL load. In this case, the modelling in the discrete-time domain is based on the z-transform of the part of the plant related to the inductor current $G_p(s)$ along with the latch effect [48], leading to

$$G_p(z) = \frac{\boldsymbol{I}_{L\alpha\beta}(z)}{\boldsymbol{V}_{i\alpha\beta}(z)} = \boldsymbol{Z}\{\boldsymbol{L}\{\text{Latch}\}G_p(s)\} =$$

$$= (1 - z^{-1})\boldsymbol{Z}\left\{\frac{G_p(s)}{s}\right\} = \frac{1}{R}\frac{\left(1 - e^{-T_s/\tau_p}\right)z^{-1}}{1 - e^{-T_s/\tau_p}z^{-1}}, \tag{4.1}$$

where $\boldsymbol{I}_{L\alpha\beta}(z)$ and $\boldsymbol{V}_{i\alpha\beta}(z)$ are the inductor current and input voltage in the z-domain, respectively; $\tau_p = L_f/R$ is the plant time-constant. However, the coupling

effect introduced by the second-order LC filter cannot be neglected, because of computation and PWM delays that are not compensated for on the state feedback decoupling path. Even without the one sample delay introduced by computation, the latch interface is still present, not allowing the exactly decoupling of the controlled states. The effect of the capacitor voltage in the dynamics should be considered in the design stage [190]. For this reason, an accurate model that clearly reflects this effect has been developed. The general methodology is similarly applied in [187], [191]:

1. Model and derive the Ordinary Differential Equations (ODE) of the system;
2. Form the Laplace transform of the ODE including the effects of initial conditions;
3. Form a step input for the latched manipulated input;
4. Find the continuous-time step response solution;
5. Find the response at the next sampling instant;
6. Substitute for the B-operator ($B = z^{-1}$);
7. Generalize the solution for arbitrary sampling instants (kT);
8. Form eventually the correspondent transfer function in the discrete-time domain.

The differential equations of the system are the same as in (3.1). The disturbance $i_o(t)$ is neglected in this analysis.

$$\begin{cases} \dfrac{d}{dt}v_c(t) = \dfrac{1}{C_f}i_L(t) \\ \dfrac{d}{dt}i_L(t) = \dfrac{1}{L_f}[v_i(t) - Ri_L(t) - v_c(t)]. \end{cases} \tag{4.2}$$

The system in (4.2) is transformed in the Laplace domain including the effects of initial conditions, fundamental to derive the Cross-Coupled State Equations. The complete derivation of the following equations is reported in Appendix - A.

The sample-and-hold effect is modelled as $V_i(s) = v_i(t = 0)/s$ (input modelled as a step). In particular the relationships between the states are

$$V_c(s) = \frac{\omega_n^2}{s^2 + 2\xi\omega_n s + \omega_n^2}\left\{v_i(t=0)\frac{1}{s} + \frac{1}{\omega_n^2}[sv_c(t=0) + \dot{v}_c(t=0)] + \frac{2\xi}{\omega_n}v_c(t=0)\right\}. \tag{4.3}$$

$$I_L(s) = \frac{\omega_n^2}{s^2 + 2\xi\omega_n s + \omega_n^2}\left[C_f v_i(t=0) + L_f C_f s i_L(t=0) - C_f v_c(t=0)\right], \quad (4.4)$$

where

$$\omega_n^2 = \frac{1}{L_f C_f}; \quad \xi = \frac{1}{2\omega_n}\frac{R}{L_f} = \frac{R}{2}\sqrt{\frac{C_f}{L_f}}. \quad (4.5)$$

ω_n is the natural frequency of the plant and ξ is the damping factor. Then the inverse Laplace transform is applied to (4.3) and (4.4). The continuous-time step response is generalized for arbitrary sampling instants, followed by the transformations to the *z*-domain and $\alpha\beta$-stationary reference frame. The Cross-Coupled State Equations are thus obtained

$$\begin{aligned} \boldsymbol{V}_{c\alpha\beta}(z)\left[1 + \frac{\omega_n}{\omega_d}e^{-\xi\omega_n T}\sin(\omega_d T - \phi)z^{-1} - \frac{2\xi\omega_n}{\omega_d}e^{-\xi\omega_n T}\sin(\omega_d T)z^{-1}\right] \\ = \left[1 - \frac{\omega_n}{\omega_d}e^{-\xi\omega_n T}\,sin(\omega_d T + \phi)\right]\boldsymbol{V}_{i\alpha\beta}(z)z^{-1} \\ + \frac{1}{C_f\omega_d}e^{-\xi\omega_n T}\,sin(\omega_d T)\,\boldsymbol{I}_{L\alpha\beta}(z)z^{-1}. \end{aligned} \quad (4.6)$$

$$\frac{\boldsymbol{I}_{L\alpha\beta}(z)}{\boldsymbol{V}^*_{i\alpha\beta}(z)} = \frac{1}{1 + \frac{\omega_n}{\omega_d}e^{-\xi\omega_n T}\sin(\omega_d T - \phi)\,z^{-1}}\,C_f\frac{\omega_n^2}{\omega_d}e^{-\xi\omega_n T}\sin(\omega_d T)\,z^{-1}, \quad (4.7)$$

where

$$\omega_d = \omega_n\sqrt{1-\xi^2}; \;\; \phi = tg^{-1}\left(\frac{\sqrt{1-\xi^2}}{\xi}\right). \quad (4.8)$$

Moreover, $\boldsymbol{V}^*_{i\alpha\beta}(z) = \boldsymbol{V}_{i\alpha\beta}(z) - \boldsymbol{V}_{c\alpha\beta}(z)$ is the applied voltage to the model after the voltage capacitor coupling effect in a block diagram representation. It can be clearly seen that the model of the RL load in (4.7) takes into account the effect of the coupling with the output capacitor by including C_f. Solving the coupling equations (4.6) and (4.7), yields to the independent transfer function

$$\frac{\boldsymbol{V}_{c\alpha\beta}(z)}{\boldsymbol{V}_{i\alpha\beta}(z)} = \frac{a_{num_1}z^{-1} + b_{num_1}z^{-2}}{1 - 2e^{-\xi\omega_n T}\cos(\omega_d T)\,z^{-1} + e^{-2\xi\omega_n T}z^{-2}}, \quad (4.9)$$

where

$$a_{num_1} = 1 - \frac{\xi\omega_n}{\omega_d} e^{-\xi\omega_n T} \sin(\omega_d T) - e^{-\xi\omega_n T} \cos(\omega_d T)$$

$$b_{num_1} = \frac{\xi\omega_n}{\omega_d} e^{-\xi\omega_n T} \sin(\omega_d T) - e^{-\xi\omega_n T} \cos(\omega_d T) + e^{-2\xi\omega_n T}$$

Similarly, starting from (4.6) we can achieve

$$\frac{\boldsymbol{I}_{L\alpha\beta}(z)}{\boldsymbol{V}_{i\alpha\beta}(z)} = \frac{\left[C_f \frac{\omega_n^2}{\omega_d} e^{-\xi\omega_n T} \sin(\omega_d T)\right](z^{-1} - z^{-2})}{1 - 2e^{-\xi\omega_n T} \cos(\omega_d T)\, z^{-1} + e^{-2\xi\omega_n T} z^{-2}}. \tag{4.10}$$

By considering (4.9) and (4.10), the relationship between $\boldsymbol{I}_{L\alpha\beta}(z)$ and $\boldsymbol{V}_{c\alpha\beta}(z)$ can be derived as

$$\frac{\boldsymbol{V}_{c\alpha\beta}(z)}{\boldsymbol{I}_{L\alpha\beta}(z)} = \frac{\boldsymbol{V}_{c\alpha\beta}(z)}{\boldsymbol{V}_{i\alpha\beta}(z)} \cdot \frac{\boldsymbol{V}_{i\alpha\beta}(z)}{\boldsymbol{I}_{L\alpha\beta}(z)}. \tag{4.11}$$

Leading to

$$\frac{\boldsymbol{V}_{c\alpha\beta}(z)}{\boldsymbol{I}_{L\alpha\beta}(z)} = \frac{a_{num_1} z^{-1} + b_{num_1} z^{-2}}{\left[C_f \frac{\omega_n^2}{\omega_d} e^{-\xi\omega_n T} \sin(\omega_d T)\right](1 - z^{-1})}. \tag{4.12}$$

The block diagram in Fig. 4.2 shows the complete system here derived, considering (4.7).

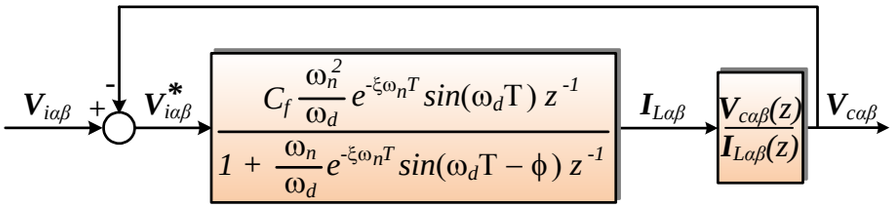

Fig. 4.2. Discrete-time block diagram of an LC filter neglecting the disturbance $I_{o\alpha\beta}(z)$.

The frequency responses of (4.1) and (4.7) are shown in Fig. 4.2, using the parameters in Table 3.1 and Table 3.2. The correspondent closed loop transfer function with a P controller as current regulator is represented in Fig. 4.4, considering voltage decoupling. The key point is that because of the coupling with the output capacitor, which is accurately modelled by (4.7), a lower gain is achieved at low frequencies. This model justifies the higher steady-state error observed in both simulation and experiments than with the continuous-time model and the discrete-time one based on (4.1). For this reason, the plant model in Fig. 4.2 is worth to be used to design and analyse the system.

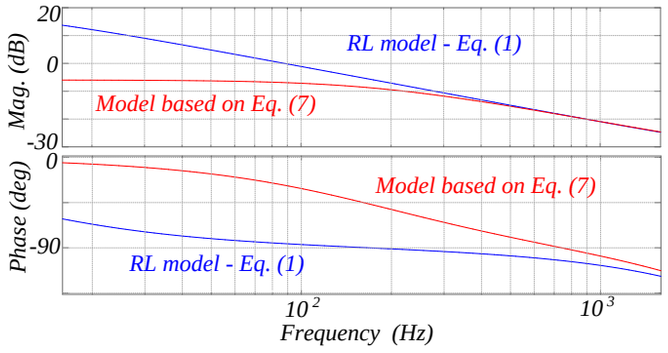

Fig. 4.3. Frequency response of the RL model in (4.1) and model based on (4.7)

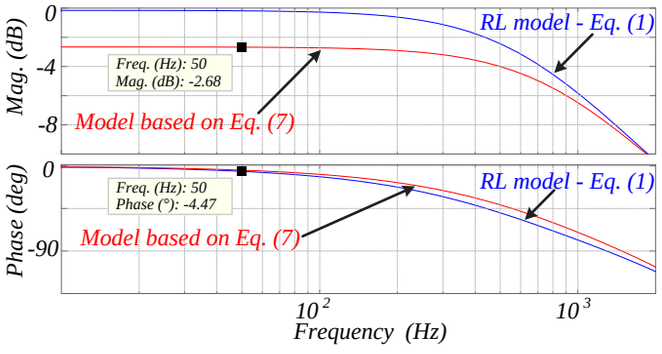

Fig. 4.4. Frequency response of the closed loop system of the RL model in (4.1) and model based on (4.7), and a P controller with $k_{pI} = 5.54$, neglecting the one sample delay

4.2.1 Validation of the Plant Model by Simulation

The derived model is validated by simulation. With reference to Fig. 4.1, the block diagram representation of an LC filter, without the current controller, is considered (see Fig. 4.5), using the system parameters in Table 3.1. A discrete-time sinusoidal input voltage is provided as input to the LC filter via a latch interface. For a better understanding, the one sample delay is neglected in this test. The simulation is performed at no load condition. To effectively validate (4.7) and (4.12), the LC filter in Fig. 4.5 is modelled in two different ways:

1. by using elementary transfer functions Simulink blocks for L_f, R, the integrator terms $1/s$ and C_f. The latch interface is modelled using a Zero-Order Hold block**;**
2. by replacing $1/(L_f\, s + R)$ along with the latch interface with (4.7). Additionally, $1/(C_f s)$ is replaced by (4.12). This is equivalent to test the block diagram in Fig. 4.2.

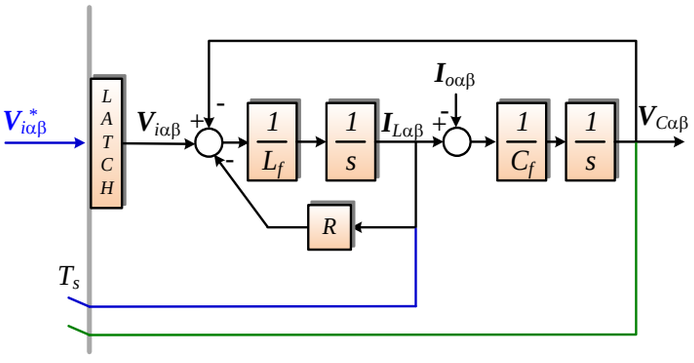

Fig. 4.5. Block diagram of the physical system

The inductor current and capacitor voltage provided by the two modelling are compared. With reference to Fig. 4.6, there is a perfect match at the sampling instants between the inductor current provided by the two modelling. It must be remarked only the second modelling provides access to the inductor current as an internal state. This is a key issue for design purposes. With reference to Fig. 4.7, the capacitor voltage simulated using the discrete-time model (see Fig. 4.2) is equal (at the sampling instants) to the capacitor voltage simulated using the continuous-time model. These results demonstrate the correctness of the devised model, which can be used for design purposes.

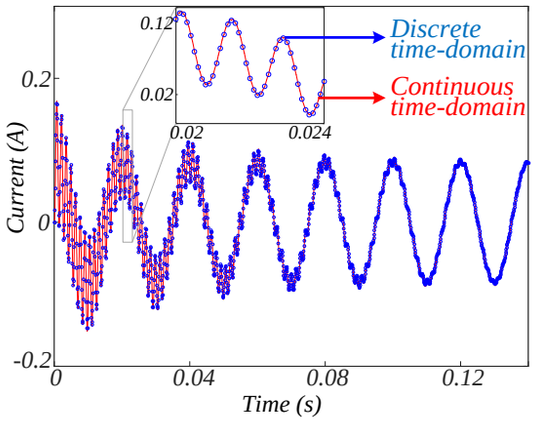

Fig. 4.6. Inductor current (α-axis) - Comparison of modelling: transfer function Simulink blocks (plant modelling in the continuous-time domain)**;** current simulated by using the derived model (block diagram shown in Fig. 4.2)

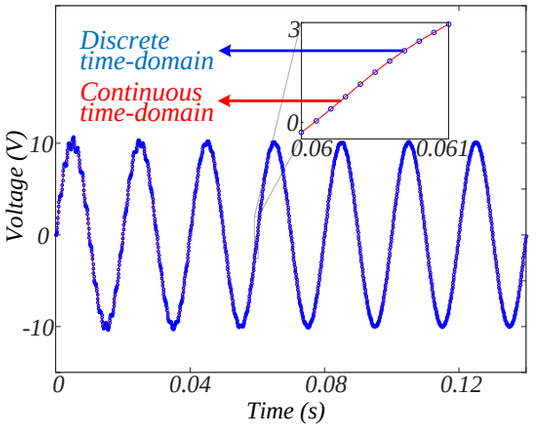

Fig. 4.7. Capacitor voltage (α-axis) - Comparison of modelling: transfer function Simulink blocks (plant modelling in the continuous-time domain)**;** voltage simulated by using the derived model (block diagram shown in Fig. 4.2)

A more rigorous validation is based on applying, in open loop, the actual pulse-width modulated voltage provided by a three-phase power converter to an LC filter at no load conditions. Again, the one sample delay is not included in the analysis. In order to mitigate non-linearity effects introduced by PWM, the physical parameters in Table 4.1 are used to perform the simulation. The results are compared with those provided by the model based on (4.7) and (4.12). With reference to Fig. 4.8 and Fig. 4.9, it can be seen the average value of the controlled states provided by the two models are equivalent. In fact, by using synchronous sampling, the average value, mainly of the inductor current, is used for control purposes [see Fig. 4.8(b)]. All these results demonstrate the correctness of the devised model, which can be used for design purposes.

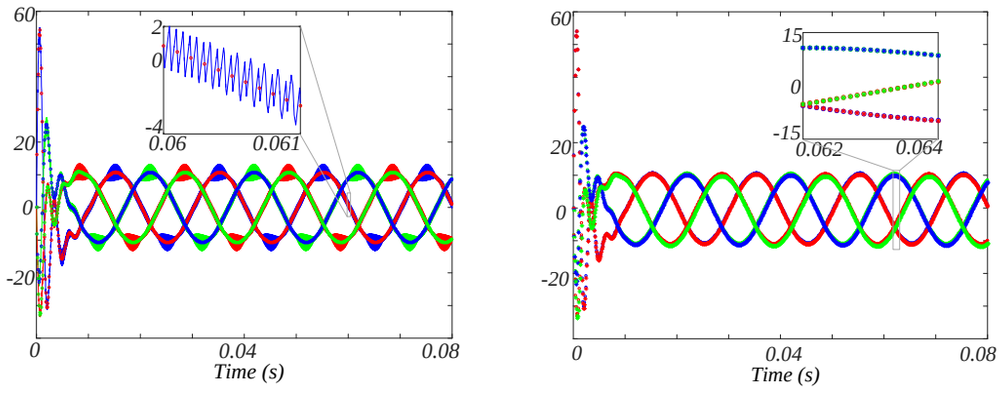

Fig. 4.8. Inductor current - Comparison of modelling: (a) PWM simulation with switch ripple, three-phase current from (4.7) (in dots)**;** (b) PWM simulation with synchronous sampling (in asterisks), three-phase current from (4.7) (in dots)

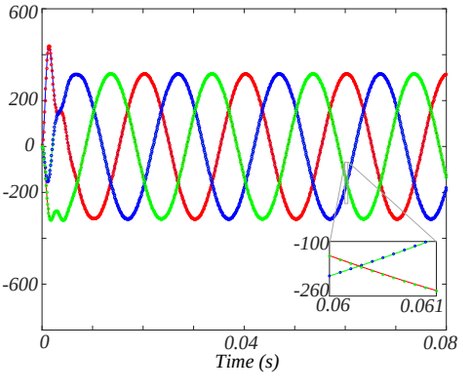

Fig. 4.9. Capacitor voltage - Comparison of modelling: pulse-width modulated simulation**;** current simulated by using the derived model in the natural reference frame (block diagram showed in Fig. 4.4)

Table 4.1 System parameters for simulation purposes

Parameter	**Value**
Switching frequency	$f_{sw} = 10\ kHz$
Filter inductance	$L_f = 1.8\ mH$
Filter capacitor	$C_f = 108\ \mu F$
Inductor ESR	$R = 10\ \Omega$

To investigate the effect of the latch interface and one sample delay on the closed loop transfer function, three different models with the inner current loop only and a P controller as regulator are considered (see Fig. 4.10, Fig. 4.12 and Fig. 4.14). The parameters in Table 3.1 and Table 4.2 are used for analysis. As the latch interface and one sample delay are neglected [see Fig. 4.10(a)], the physical system as seen from the controller simplifies as an RL load [see Fig. 4.10(b)]. This means the state feedback decoupling path perfectly cancels out the physical coupling of the capacitor voltage.

As a consequence, the reference current is properly tracked with almost zero steady-state error (see Fig. 4.11).

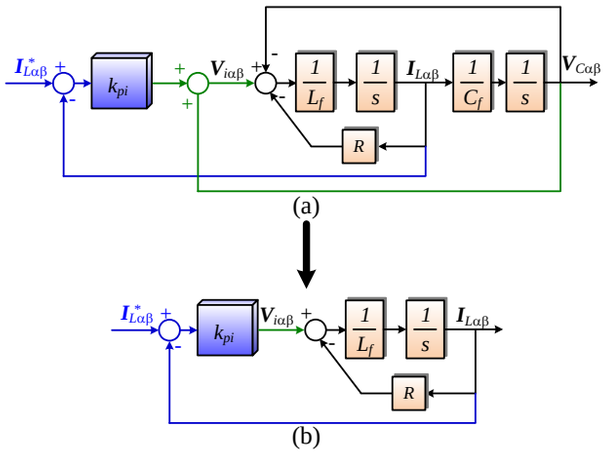

Fig. 4.10. Block diagram of the physical system with current loop only: (a) Plant modelling in the continuous-time domain; (b) Simplification of (a)

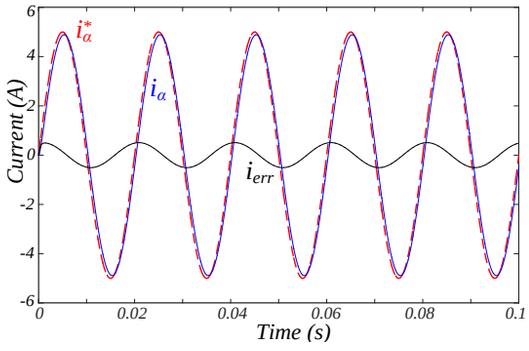

Fig. 4.11. Command tracking of the inductor current with $k_{pI} = 5.54$: (a) reference, real and inductor current error of the system (α-axis) in Fig. 4.10

On the other hand, as the latch interface is included (see Fig. 4.12) the steady-error between the reference and real inductor current increases (see Fig. 4.13). Given the reference current at f=50 Hz in α-axis $i^*_\alpha = 5\ A$, the real inductor current is $i_\alpha = 3.68\ A$. This means $i_\alpha = 0.736 i^*_\alpha$, which corresponds to -2.68 dB, in accordance with the frequency response analysis at 50 Hz of Fig. 4.4.

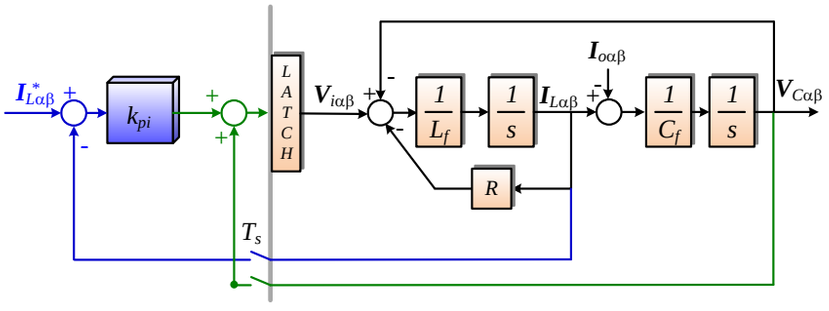

Fig. 4.12. Block diagram of the physical system with current loop only and latch interface

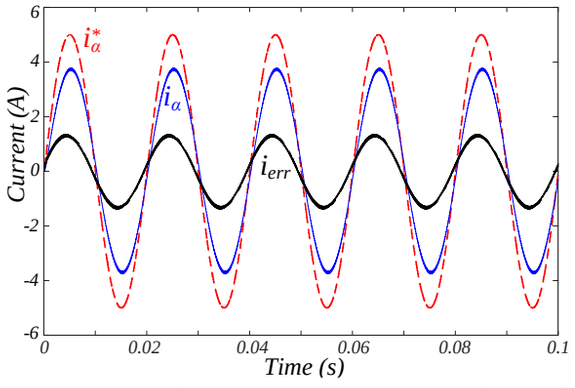

Fig. 4.13. Command tracking of the inductor current with $k_{pI} = 5.54$: (a) reference, real and inductor current error of the system (α-axis) in Fig. 4.12

Additionally, with reference to Fig. 4.14, it can be seen the combined effect of the one sample delay and latch interface. An even higher steady-state error is observed (see Fig. 4.15), limiting the current loop control bandwidth. As Fig. 4.12 and Fig. 4.14 implement an accurate plant modelling, previously verified in Fig. 4.6 and Fig. 4.7, it can be concluded that state feedback decoupling is far from being ideal. Thus, a design procedure based on (4.7) and (4.12) provides a more accurate pole placement.

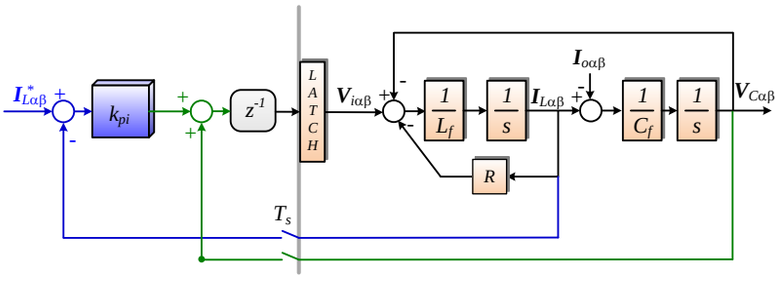

Fig. 4.14. Block diagram of the physical system with current loop only, latch interface and one sample delay

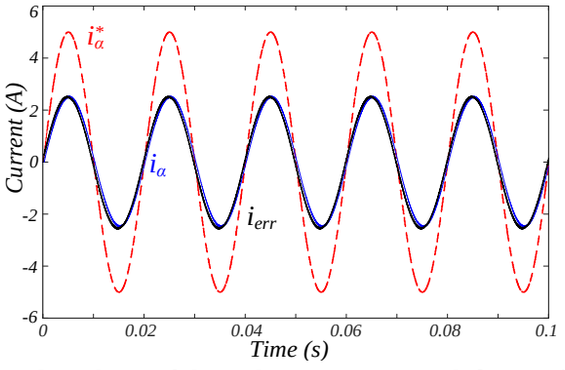

Fig. 4.15. Command tracking of the inductor current with $k_{pI} = 5.54$: (a) reference, real and inductor current error of the system (α-axis) in Fig. 4.14

4.3 Current Regulator Design

The closed loop controller bandwidth is mainly limited by computation and PWM delays [52]. This limitation is overcome by implementing techniques aimed at compensating for the system delays. In this Chapter, it is shown how the current control bandwidth can be designed for a third of the sampling frequency with wide stability margins, by means of a P controller + Smith predictor or a P controller along with a lead compensator structure. The physical and control parameters for the current loop used both in simulation and in laboratory tests are presented in Table 3.1 and Table 4.2.

Table 4.2 Current Regulator Parameters

Parameter	Value
Proportional gain w/o lead	$k_{pI} = 5.54$
Proportional and lead gains @$\boldsymbol{\omega_{nCL} = 2\pi 2400}$ rad/s, $\boldsymbol{\xi_{CL} = 0.707}$, $\boldsymbol{f_{bw} = 3.1}$ kHz	$\begin{cases} k_{pI} = 11.58 \\ k_L = 0.561 \end{cases}$
Proportional gain with Smith Predictor @$\boldsymbol{f_{bw} = 3.1}$ kHz	$k_{pI} = 12.6$

A simple P controller for the inner current loop, with decoupling transfer function $G_{dec}(z) = 1$ (see Fig. 4.1) and the discrete-time model based on (4.7) are considered, as shown in the block diagram of Fig. 4.16.

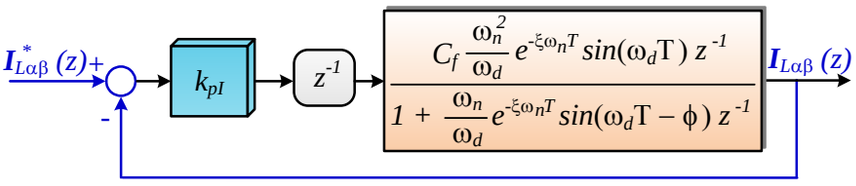

Fig. 4.16. Block diagram for design the inner current loop, including the lag introduced by computational delay

The closed loop transfer function of the inner current loop in Fig. 4.16 is

$$\frac{\boldsymbol{I}_{L\alpha\beta}(z)}{\boldsymbol{I}^*_{L\alpha\beta}(z)} = \frac{k_{pI} b}{z^2 - az + k_{pI} b}. \tag{4.13}$$

where $b = C_f \frac{\omega_n^2}{\omega_d} e^{-\xi\omega_n T} sin(\omega_d T)$; $a = -\frac{\omega_n}{\omega_d} e^{-\xi\omega_n T} sin(\omega_d T - \phi)$.

For the system parameters in Table 3.1, the root locus is shown in Fig. 4.17. It can be stated that, because of the delay, there is a limitation in the gain to achieve system dynamics with enough damping. There are two poles and just one variable (k_{pI}) that can change their locations. It is clear that it is not possible to place the roots at any desired location. The designed gain to achieve a damping of $\xi = 0.707$ is $k_{pI} = 5.54$, as presented in Table 4.2.

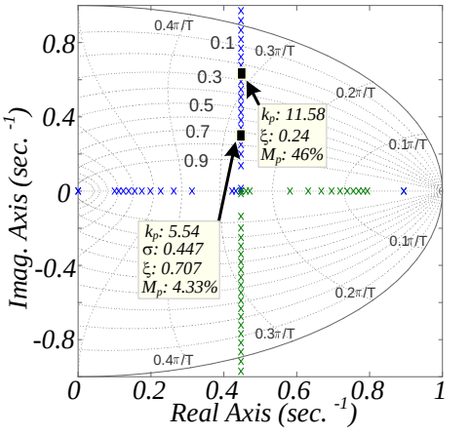

Fig. 4.17. Root locus of open loop transfer function in Fig. 4.16 including the lag introduced by PWM update

To widen the system bandwidth and still achieve a reasonable damped closed loop response, it is possible to design a lead compensator as shown in Fig. 4.18, also referred to as 'Delay prediction and Feedback' [52].

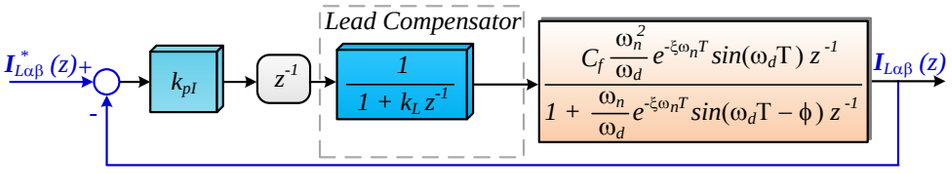

Fig. 4.18. Block diagram for design the inner current loop, including the lag introduced by computational delay, and the model of the lead compensator

The closed loop transfer function becomes

$$\frac{\boldsymbol{I}_{L\alpha\beta}(z)}{\boldsymbol{I}^*_{L\alpha\beta}(z)} = \frac{k_{pI} b}{(z + k_L)(z - a) + k_{pI} b}, \tag{4.14}$$

where k_L is the lead compensator gain. The poles of this transfer function must satisfy the relationship

$$z^2 - (p_1 + p_2)z + p_1 p_2 = z^2 + (k_L - a)z - k_L a + k_{pI} b, \tag{4.15}$$

where p_1, p_2 are the desired pole locations, defined as

$$p_{1,2} = e^{-\xi\omega_{nCL} T_s}[\cos(\omega_{dCL} T_s) \pm j \sin(\omega_{dCL} T_s)], \quad \omega_{dCL} = \omega_{nCL}\sqrt{1 - \xi_{CL}^2}. \tag{4.16}$$

Solving the system leads to

$$\begin{cases} k_L = a - (p_1 + p_2) \\ k_{pI} = (p_1 p_2 + k_L a)/b \end{cases}. \tag{4.17}$$

For the case $\omega_{nCL} = 2\pi 2400\, rad/s$ and $\xi_{CL} = 0.707$, the poles are located at $p_{1,2} = 0.166 \pm j0.301$ and the bandwidth of the system is $f_{bw} = 3.1\, kHz$. The controller and lead compensator gains are presented in Table 4.2. The resulting root locus with the lead compensator is shown in Fig. 4.19. The poles locations are more on the left compared to the previous case in Fig. 4.17, which means the system is faster [37]. Therefore, the proposed technique provides a wider bandwidth for the same damping factor.

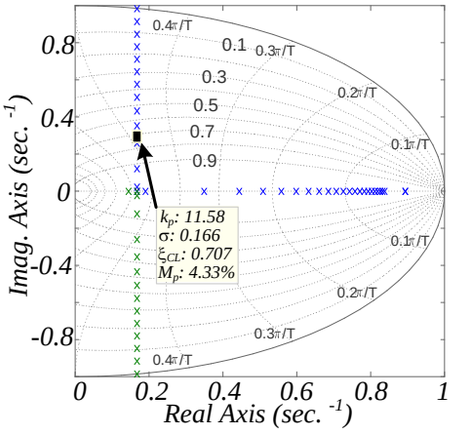

Fig. 4.19. Root locus of the open loop transfer function in Fig. 4.18 including the lag introduced by PWM update, with the lead compensator: $k_L = 0.561$

As shown in Fig. 4.20, the system with the lead compensator is much more damped around the desired bandwidth.

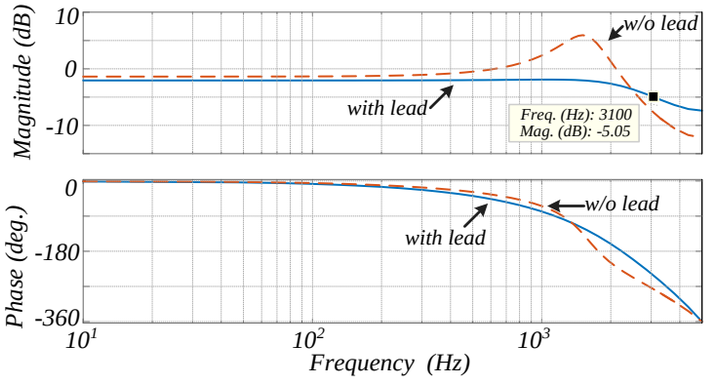

Fig. 4.20. Frequency response analysis with/without lead compensator, $k_L = 0.561$

The sensitivity to changes in the plant parameters is investigated. The system is less sensitive to variations of the Equivalent Series Resistance (ESR) of the inductor (see Fig. 4.21) than to changes in the inductance value. The eigenvalue migration as the inductance value changes is shown in Fig. 4.22.

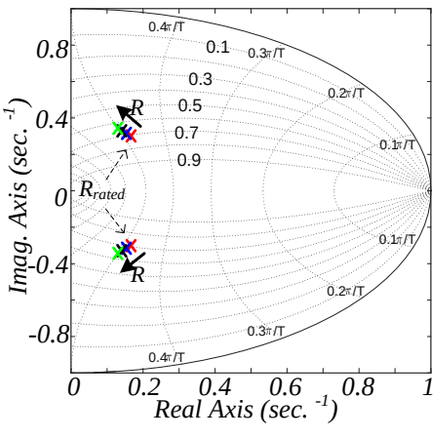

Fig. 4.21. Eigenvalue migration as a function of variation in $R_{rated} = 0.1\ \Omega \rightarrow R = 2\ \Omega$

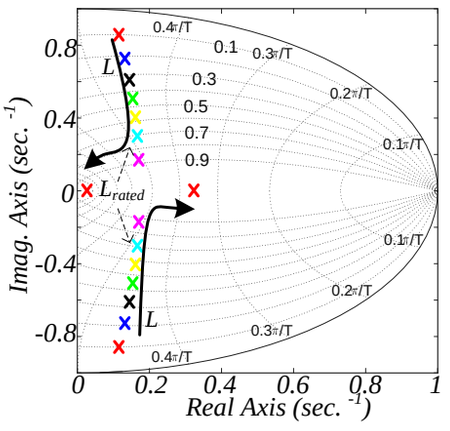

Fig. 4.22. Eigenvalue migration as a function of variation in $L = 0.9\ mH \rightarrow 2L_{rated} = 3.6\ mH$

Another technique aimed at widening the bandwidth of the current regulator while still achieving good dynamic properties is based on the Smith Predictor structure [145]. The basic idea is to build a parallel model which cancels the system delay (see Fig. 4.23). In this way, the design of the controller can be performed using the un-delayed model of the plant. Robustness issues must be considered with this method. If there is any model error, especially in the delay itself, the Smith predictor can degrade the system performance. These aspects are verified in the experiments by changing the predicted values of the plant and computation delay.

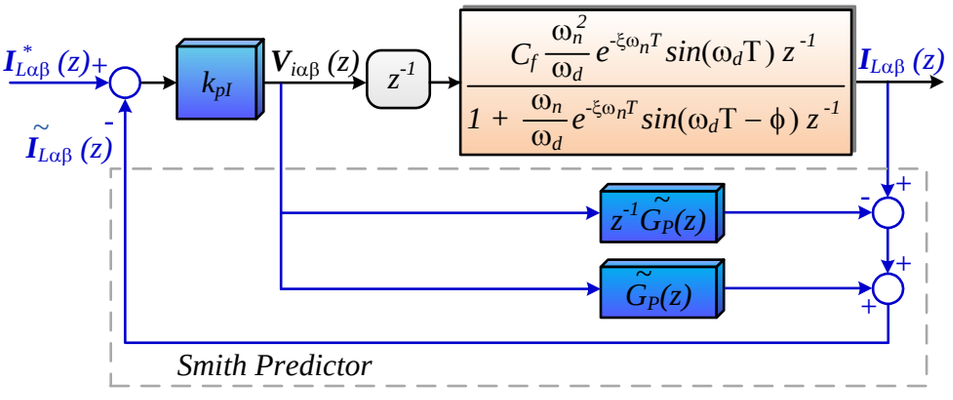

Fig. 4.23. Block diagram for design the inner current loop, including the lag introduced by PWM update, and the model of the Smith Predictor

According to Fig. 4.23, the following relationship can be derived

$$\left[\boldsymbol{V}_{i\alpha\beta}(z)z^{-1}G_P(z) - \boldsymbol{V}_{i\alpha\beta}(z)z^{-1}\tilde{G}_P(z)\right] + \boldsymbol{V}_{i\alpha\beta}(z)\tilde{G}_P(z) = \tilde{\boldsymbol{I}}_{L\alpha\beta}(z) \rightarrow$$

$$\boldsymbol{V}_{i\alpha\beta}(z)\left[z^{-1}G_P(z) + \tilde{G}_P(z)(1 - z^{-1})\right] = \tilde{\boldsymbol{I}}_{L\alpha\beta}(z). \qquad (4.18)$$

Since

$$\boldsymbol{V}_{i\alpha\beta}(z) = \left[\boldsymbol{I}^{*}_{L\alpha\beta}(z) - \tilde{\boldsymbol{I}}_{L\alpha\beta}(z)\right]k_{pI}. \tag{4.19}$$

Substituting (4.19) in (4.18) leads to

$$\left[\boldsymbol{I}^{*}_{L\alpha\beta}(z) - \tilde{\boldsymbol{I}}_{L\alpha\beta}(z)\right]\left[z^{-1}G_P(z) + \tilde{G}_P(z)(1 - z^{-1})\right]k_{pI} = \tilde{\boldsymbol{I}}_{L\alpha\beta}(z). \tag{4.20}$$

By rearranging

$$\frac{\tilde{\boldsymbol{I}}_{L\alpha\beta}(z)}{\boldsymbol{I}^{*}_{L\alpha\beta}(z)} = \frac{k_{pI}G_P(z)z^{-1} + k_{pI}\tilde{G}_P(z) - k_{pI}\tilde{G}_P(z)z^{-1}}{1 + k_{pI}G_P(z)z^{-1} + k_{pI}\tilde{G}_P(z) - k_{pI}\tilde{G}_P(z)z^{-1}}. \tag{4.21}$$

If $G_P(z) = \tilde{G}_P(z)$, (4.21) simplifies to

$$\frac{\boldsymbol{I}_{L\alpha\beta}(z)}{\boldsymbol{I}^{*}_{L\alpha\beta}(z)} = \frac{k_{pI}G_P(z)}{1 + k_{pI}G_P(z)}. \tag{4.22}$$

As a consequence, the design of the controller can be performed using the un-delayed model of the plant.

The root locus of the system is shown in Fig. 4.24. In particular, the closed-loop pole corresponding to $f_{bw} = 3.1\ kHz$ is highlighted and the correspondent gain is reported also in Table 4.2.

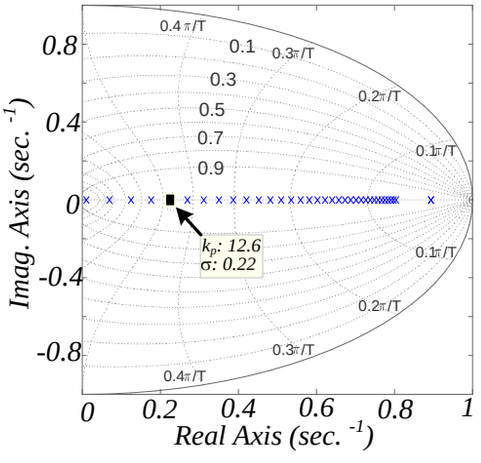

Fig. 4.24. Root locus of open loop transfer function in Fig. 4.23 including the lag introduced by PWM update, with the Smith Predictor

Since the un-delayed model of the plant is considered, the design is made for a first-order system. For the same damping the system response can be made faster than the model with the lead compensator, as can be seen by the step response in Fig. 4.25.

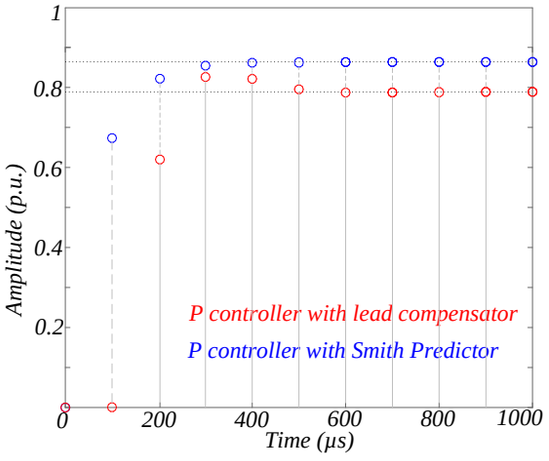

Fig. 4.25. Step response with the lead compensator ($k_L = 0.561$) and the Smith predictor for $f_{bw} = 3.1\ kHz$

4.4 Voltage Regulator Design

The same methodology discussed in Section 3.6 is applied to design the voltage loop. However, as the effects of the delays are well compensated with the proposed P + Smith predictor for the inner controller, a wide bandwidth with wide stability margins is achieved. This allows the selection of a low outer over inner bandwidth ratio. According to [192] the minimum ratio is chosen and thus the voltage regulator is designed for around 700 Hz of bandwidth. Accordingly, the voltage regulator control parameters are shown in Table 4.3.

Table 4.3 Voltage Regulator Control Parameters

Parameter		Value	
Proportional gain		$k_{pV} = 0.2$	
Integral gains and lead angles	@50Hz	$k_{iV,1} = 126$	$\varphi_1 = 3.3°$
	@250Hz	$k_{iV,5} = 15$	$\varphi_5 = 37°$
	@350Hz	$k_{iV,7} = 15$	$\varphi_7 = 44°$

In Fig. 4.26 the Nyquist diagram of the system in Fig. 4.1 with the parameters of Table 4.2 is shown. The inverse of the sensitivity peak, i.e. η, is almost equal to 0.8 at no-load condition with all the harmonic resonators activated. It must be noted the harmonic resonators at 5th and 7th do not intersect the unit circle since the voltage loop bandwidth is set much higher than the highest harmonic order resonant filter.

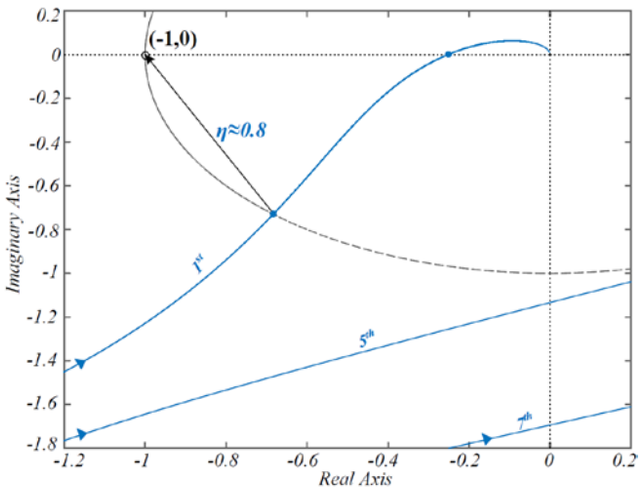

Fig. 4.26. Nyquist diagram of the system at no-load condition (command tracking of the reference voltage)

4.5 Anti-Wind Up Scheme

A discrete anti-wind up scheme must be implemented to avoid the saturation of the integral term in the voltage regulator. No anti-wind up scheme is needed for the current loop since a P controller is used as regulator. The anti-wind up scheme, which is based on a feedback implementation of inverse dynamics [193], is shown in Fig. 4.27 [145]. With this technique, the bounded signals can drive the states in any condition, i.e. also during demanding transients and saturation of the integral term. This represents a major advantage compared to usual anti-wind up implementations [194], e.g. the 'frozen' scheme [52].

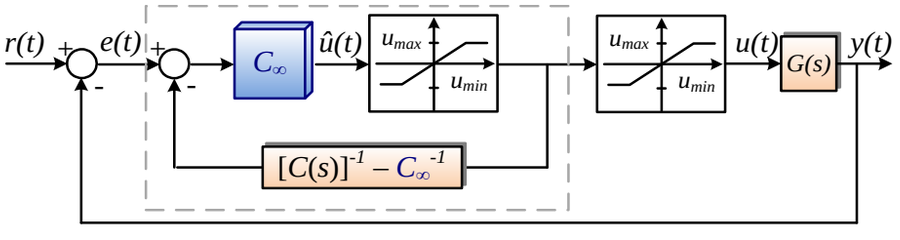

Fig. 4.27. Anti-wind up scheme based on a feedback implementation of inverse dynamics

According to [145], the controller $C(s)$ should be: i) biproper, i.e. zero relative degree between the transfer function numerator and denominator, and ii) minimum phase. If this is the case, the controller can be split into a direct feedthrough term (C_∞) and a strictly proper transfer function $\bar{C}(s)$

$$C(s) = C_\infty + \bar{C}(s). \tag{4.23}$$

For the particular case of an ideal PR controller

$$C_\infty = k_{pV}; \qquad \bar{C}(s) = k_{iV,1}\frac{s}{s^2+\omega_o^2} \tag{4.24}$$

$$C(s) = k_{pV} + k_{iV,1}\frac{s}{s^2+\omega_o^2}. \tag{4.25}$$

In normal operation ($u_{min} < \hat{u}(t) < u_{max}$), the closed loop transfer function (within the dotted line in Fig. 4.27) is equal to $C(s)$. During saturation, the input to the controller states is bounded.

As the anti-wind up scheme is implemented in the discrete-time domain, the following implementation issue, not recognizable in the s-domain, must be considered. In general, the discrete-time implementation of the feedback path in normal operation (without the saturation block) takes the form in Fig. 4.28.

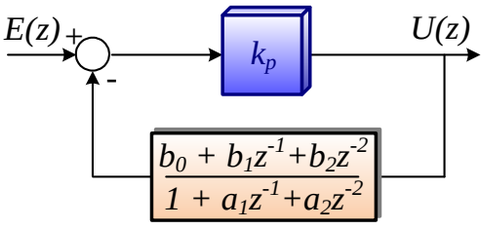

Fig. 4.28. Anti-wind up scheme based on inverse state feedback dynamics: discrete-time representation

If $b_0 \neq 0$, an algebraic loop arises, which means that this anti-wind up strategy cannot be implemented in real time. This is directly related to the discretization method used for $\bar{C}(s)$.

A possibility to avoid the algebraic loop can be to use as discretization methods Zero-Order Hold (ZOH), Forward Euler (FE) or Zero-Pole Matching (ZPM), which assure $b_0 = 0$. As an example, the transfer function in the feedback path in Fig. 4.27, takes the form in Table 4.4 for ZPM and Impulse Invariant. This latter cannot be used otherwise an algebraic loop arises, even though it is usually recommended for direct implementations [184]. In fact, the term $-k_{iV,1}/k_{pV}T_s cos(\varphi_1)$ in Table 4.4 implies $y(k) = f[x(k)]$, being $y(k)$ and $x(k)$ the output and the input at the generic sampling instant kT_s, respectively.

Table 4.4 Discretization of the feedback path in the anti-wind up scheme of Fig. 4.27

Discretization method	$\{[\boldsymbol{C(z)}]^{-1} - \boldsymbol{k_{pV}^{-1}}\}$
Impulse Invariant	$\dfrac{-\frac{k_{iV,1}}{k_{pV}}T_s\cos(\varphi_1) + \frac{k_{iV,1}}{k_{pV}}T_s\cos(\varphi_1 - \omega_1 T_s)z^{-1}}{[k_{pV} + k_{iV,1}T_s\cos(\varphi_1)] - [2k_{pV}\cos(\omega_1 T_s) + k_{iV,1}T_s\cos(\varphi_1 - \omega_1 T_s)]z^{-1} + k_{pV}z^{-2}}$
Zero-Pole Matching	$\dfrac{-\frac{k_{iV,1}}{k_{pV}}K_d z^{-1} + \frac{k_{iV,1}}{k_{pV}}K_d e^{\tan(\varphi_1)\omega_1 T_s}z^{-2}}{k_{pV} - [2k_{pV}\cos(\omega_1 T_s) - k_{iV,1}K_d]z^{-1} + [k_{pV} - k_{iV,1}K_d e^{\tan(\varphi_1)\omega_1 T_s}]z^{-2}}$

In case FE is used as discretization method, the performance of the voltage controller is degraded since zero steady-state error is not achieved [184]. This can be seen in Fig. 4.29, where the frequency response of the controller discretized with these methods is shown. The gain at the resonant frequency is no more infinite if FE is used as discretization method.

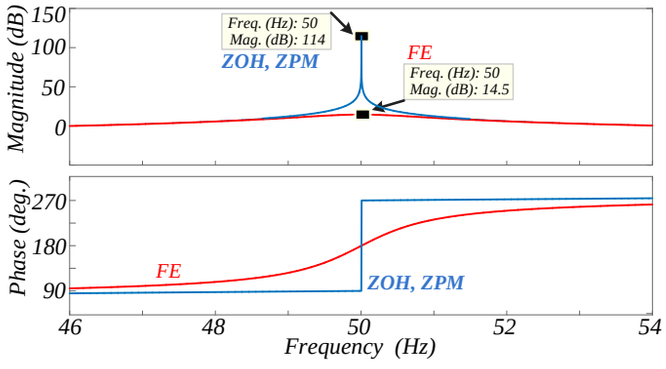

Fig. 4.29. Frequency response of the resonant controller using ZOH, ZPM and FE

The resulting implementation with ZOH or ZPM avoids wind up after saturation, and algebraic loops without losing any basic feature of the PR control during normal operation.

Moreover, in order to get an even more damped step response during transients [66], which corresponds to a lower gain at the resonant frequency, the following implementation is proposed. Firstly, the coefficients a_1 and a_2 are determined by discretization of $\left[C(s)^{-1} - k_p^{-1}\right]$, using ZOH for discretization in order to get an implementation that avoids algebraic loop. With reference to Fig. 4.28, the following is derived

$$\left[E(z) - U(z)\frac{b_1 z^{-1} + b_2 z^{-2}}{1 + a_1 z^{-1} + a_2 z^{-2}}\right] k_p = U(z) \rightarrow$$

$$E(z)k_p(1 + a_1 z^{-1} + a_2 z^{-2}) - U(z)k_p(b_1 z^{-1} + b_2 z^{-2}) = U(z)(1 + a_1 z^{-1} + a_2 z^{-2}) \rightarrow$$

$$E(z)k_p(1 + a_1 z^{-1} + a_2 z^{-2}) = U(z)\left[1 + \left(a_1 + b_1 k_p\right)z^{-1} + \left(a_2 + b_2 k_p\right)z^{-2}\right] \rightarrow$$

$$\frac{U(z)}{E(z)} = \frac{k_{pV}(1 + a_1 z^{-1} + a_2 z^{-2})}{1 + \left(a_1 + b_1 k_{pV}\right)z^{-1} + \left(a_2 + b_2 k_{pV}\right)z^{-2}} \equiv K(z). \quad (4.26)$$

After discretization, some errors arise at the placement of the resonant frequency. For this reason, the b_1 and b_2 coefficients should be re-calculated such that the inverse dynamics implementation matches the desired resonant frequency. $K(z)$ has an ideal resonance at the resonant frequency ω_1 if

$$\begin{cases} a_1 + b_1 k_p = -2\cos(\omega_1 T_s) \\ a_2 + b_2 k_p = 1 \end{cases}. \tag{4.27}$$

Solving the system of equations, the new coefficients b_1' and b_2' to be used instead of b_1 and b_2 coefficients are derived

$$b_1' = \frac{-2\,cos(\omega_1 T_s) - a_1}{k_p}. \tag{4.28}$$

$$b_2' = \frac{1 - a_2}{k_p}. \tag{4.29}$$

This implementation provides zero steady-state error and a damped response after transients. This little elaborated alternative has been found to provide more damped responses.

In the next section, the robustness of the controllers designed is verified via extensive experimental results performing step responses and step load changes with resistive and nonlinear loads.

4.6 Experimental Results

4.6.1 Current Loop Only

The same test bed used for testing the architecture in Fig. 2.1 is used to validate the theoretical analysis presented in the previous paragraphs. The LC filter parameters and operational information are shown in Table 3.1 in Chapter 3. In all the tests voltage decoupling is performed as shown in Fig. 4.1.

In order to compare the current loop performance with/without lead compensator schemes and Smith Predictor in terms of dynamic response, a step change of the inductor current is performed. As already explained with reference to P controller in Section 3.7.2.2, in order to achieve approximately zero steady-state error with different control structures, the reference is multiplied by a constant, which is equivalent to multiply by a gain the closed-loop transfer function of the inductor current. The dynamics of the system with the current loop only, i.e. voltage loop disabled and current reference generated manually, are not affected by this gain, which is also significantly lower as the bandwidth is widen.

For the case with the proportional gain only (see Fig. 4.16), the step response is degraded as k_{pI} is increased [see Fig. 4.30(a) and Fig. 4.30(b)].

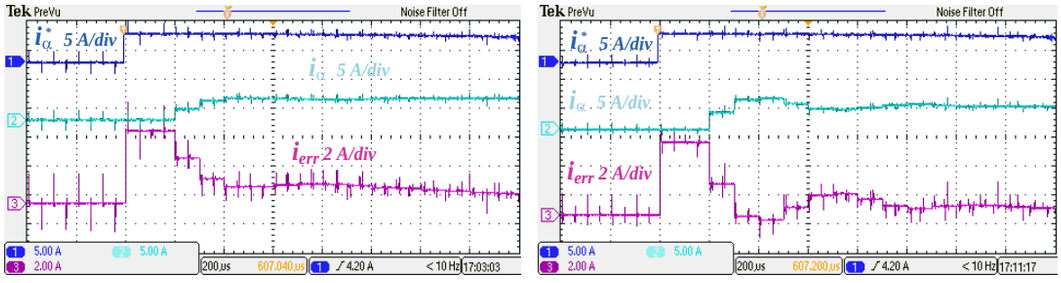

(a) (b)

Fig. 4.30. Step response, reference (5 A/div), real (5 A/div) and inductor current error (2 A/div) (α-axis), time scale (200 µs/div): (a) P controller, $k_{pI} = 5.54$; (b) P controller, $k_{pI} = 11.58$

This result also shows that due to additional losses the setup has more damping than expected. In Fig. 4.30(b) the step response is even less damped and more oscillatory for $k_{pI} = 11.58$. It is clear that there is a limitation in the achievable bandwidth due to the system delays.

If the control structure with a lead compensator is used (see Fig. 4.18), the bandwidth can be increased in comparison to the case with just a P controller for the same k_{pI} value, without degrading the dynamic performance.

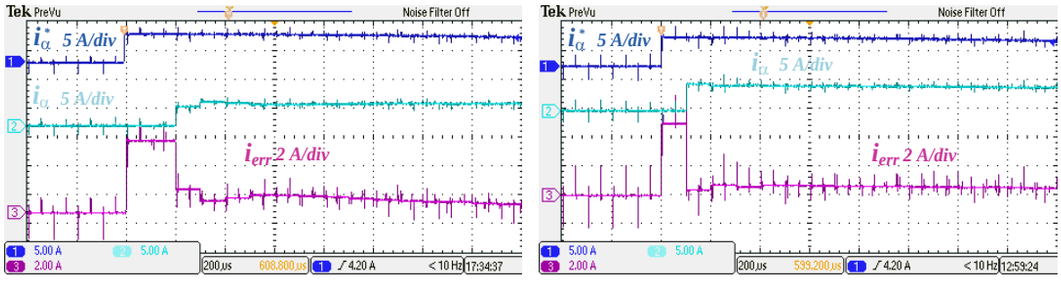

(a) (b)

Fig. 4.31. Step response, reference (5 A/div), real (5 A/div) and inductor current error (2 A/div) (α-axis) , time scale (200 µs/div): (a) P controller + lead compensator, $k_{pI} = 11.58$, $k_L = 0.561$; (b) P controller + Smith Predictor, $k_{pI} = 12.6$

The step response for $f_{bw} = 3.1$ kHz, to which corresponds $k_{pI} = 11.58$, is less oscillatory than the result in Fig. 4.30(b), as shown in Fig. 4.31(a). The step response is even faster if the Smith predictor, designed for the same bandwidth, is used to perform the test [see Fig. 4.31(b)]. The main reason is due to the fact that the Smith predictor produces a system similar to a first order one. These results are in accordance with the step responses shown in Section 4.4 in Fig. 4.25.

The sensitivity to changes in the predicted parameters values is verified. For this purpose, the predicted inductor value L_{SP} is set twice the rated value [see Fig. 4.32(a)]. The predicted ESR of the inductor R_{SP} is increased by ten times [see Fig. 4.32(b)]. The Smith Predictor is almost insensitive to changes in R_{SP}, while is more dependent on

L_{SP}. Nevertheless, even with huge variations in these parameters, the step response has an acceptable behaviour. The predicted computation delay T_{dSP} is changed to $0.5T_s$ and $2T_s$, as can be seen in Fig. 4.32(c) and Fig. 4.32(d). The system becomes more oscillatory during transients, in particular if T_{dSP} is higher than the real computation delay. Anyway, the sensitivity to system delays is a quite an artificial test, since in practice computation and PWM delays are well-known parameters.

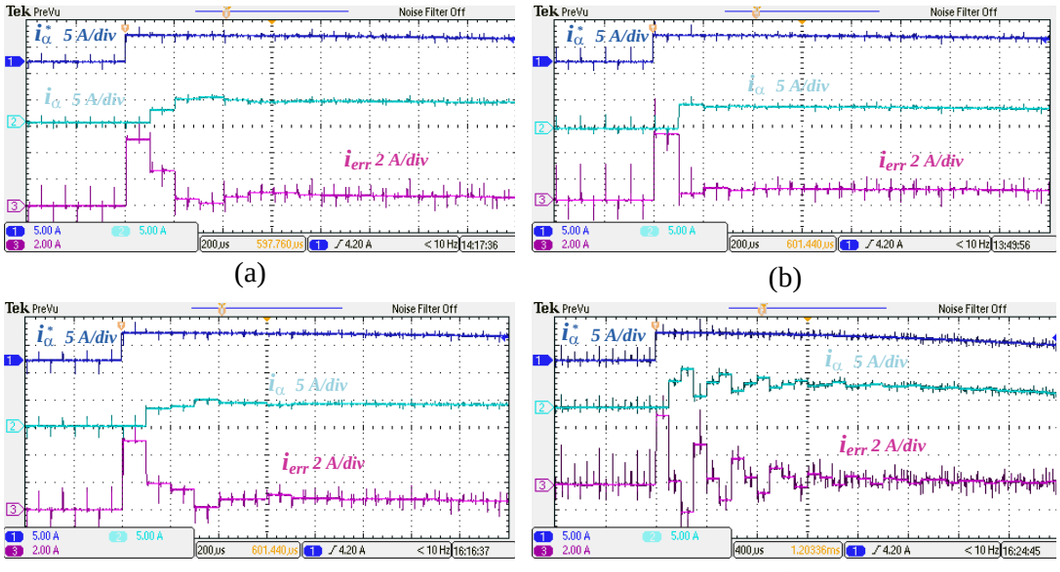

Fig. 4.32. Sensitivity analysis on predicted plant values for the Smith predictor - reference (5 A/div), real (5 A/div) and inductor current error (2 A/div) (α-axis) , time scale (200 µs/div): (a) $L_{SP} = 1.2L_{SP,rated}$; (b) $R_{SP} = 10R_{SP,rated}$; (c) $T_{d,SP} = 0.5T_{d,SP,rated}$; (d) $T_{d,SP} = 2T_{d,SP,rated}$

4.6.2 Voltage and Current Loops

A P controller with Smith Predictor is chosen as current regulator because computation and PWM delays are well-known deterministic parameters in this application and hence, this current controller is suitable to be used as inner current loop. For this reason all the following results (from Fig. 4.33 to Fig. 4.37) regarding the voltage loop are obtained with voltage decoupling, P + Smith Predictor as current regulator and the anti-wind up scheme proposed in the previous section. The parameters of the system are presented in Table 3.1.

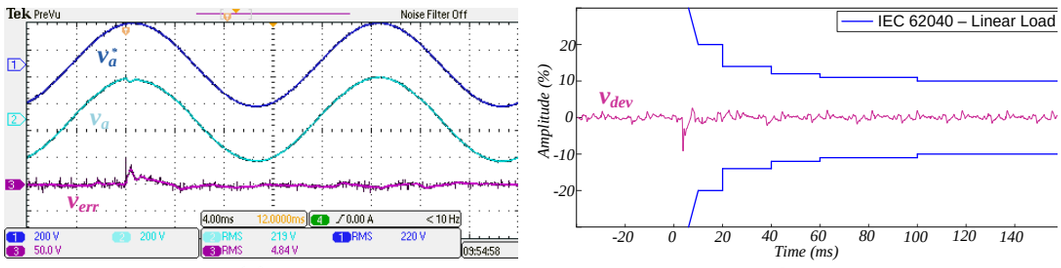

(a) (b)

Fig. 4.33 Linear step load changing (0 – 100%): (a) reference (200 V/div), real (200 V/div) and capacitor voltage error (50 V/div) (α-axis), time scale (4 ms/div); (b) Dynamic characteristics according to IEC 62040 standard for linear loads: overvoltage ($\boldsymbol{v_{dev} > 0}$) and undervoltage ($\boldsymbol{v_{dev} < 0}$)

In Fig. 4.33(a) a 100% linear step load change is shown, using just the regulator at fundamental. The results obtained are compared to the envelope of the voltage deviation v_{dev} as reported in the IEC 62040 standard for UPS systems [see Fig. 4.33(b)]. It can be seen that the system reaches steady-state in less than half a cycle after the load step change. The dynamic response is within the limits imposed by the standard.

A diode bridge rectifier with an LC output filter supplying a resistive load is used as nonlinear load. Its parameters are presented in Table 3.1. A 100% nonlinear step load change is performed with and without the harmonic compensators (HC) tuned at 5th and 7th harmonics. The results are in accordance with the standard IEC 62040 even for linear loads, as can be seen in Fig. 4.34(b) and Fig. 4.35(b). It is clear in Fig. 4.35(b) the benefits of using HCs in decreasing the steady-state error.

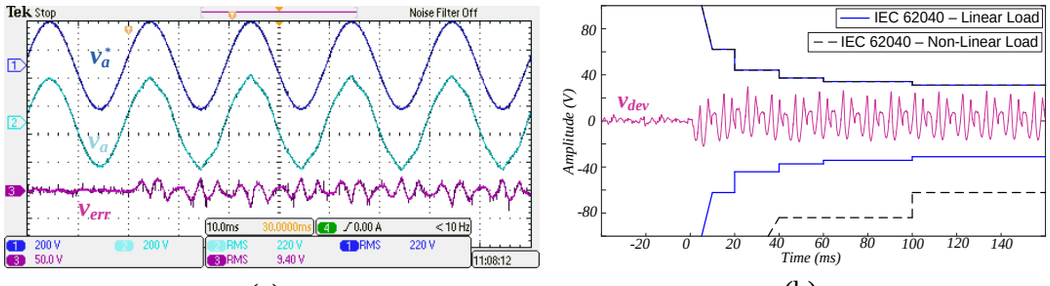

(a) (b)

Fig. 4.34 Nonlinear step load changing (0 – 100%) without HC: (a) reference (200 V/div), real (200 V/div) and capacitor voltage error (50 V/div) (α-axis), time scale (10 ms/div); (b) Dynamic characteristics according to IEC 62040 standard for linear and nonlinear loads: overvoltage ($\boldsymbol{v_{dev} > 0}$) and undervoltage ($\boldsymbol{v_{dev} < 0}$)

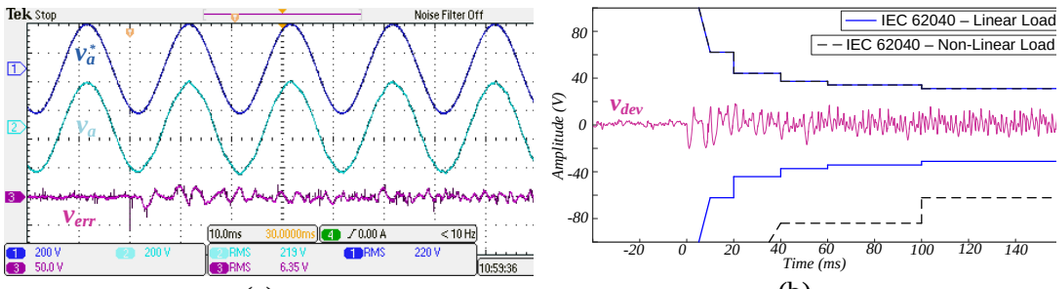

(a) (b)

Fig. 4.35. Nonlinear step load changing (0 – 100%) with HC at 5th and 7th harmonics: (a) reference (200 V/div), real (200 V/div) and capacitor voltage error (50 V/div) (α-axis), time scale (10 ms/div)**;** (b) Dynamic characteristics according to IEC 62040 standard for linear and nonlinear loads: overvoltage ($v_{dev} > 0$) and undervoltage ($v_{dev} < 0$)

To verify the attenuation of tripled harmonics, a 100% nonlinear unbalance (one phase open) step load change is performed, using the harmonic compensator at fundamental only. The response is again still in the boundaries imposed by linear loads [see Fig. 4.36(a)]. The FFT results in Fig. 4.36(b) show the mitigation of the 3rd harmonic component by a large extent, even with just the fundamental resonator. These results show the benefits of wide bandwidth for the voltage loop, possible to achieve with the design of the inner current loop based on Smith predictor.

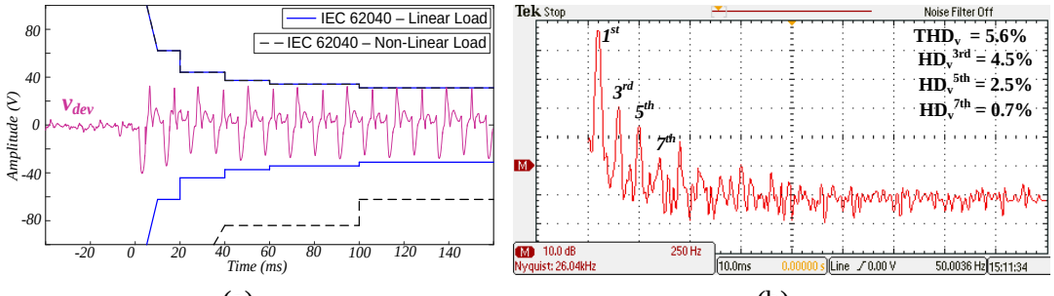

(a) (b)

Fig. 4.36. Unbalance nonlinear step load changing (0 – 100%): (a) Dynamic characteristics according to IEC 62040 standard for linear and nonlinear loads: overvoltage ($v_{dev} > 0$) and undervoltage ($v_{dev} < 0$) without HC**;** (b) FFT of the capacitor voltage

In order to show the performance of the anti-wind up implementation, a saturated control action (current reference) along with results of a step change from rated load to overload conditions and vice versa are shown in Fig. 4.37(a) and Fig. 4.37(b). The current limiter is set at 8 A as well as the saturation blocks in the anti-wind up scheme. It can be noted the output of the integral is bounded because of the anti-wind up scheme implemented.

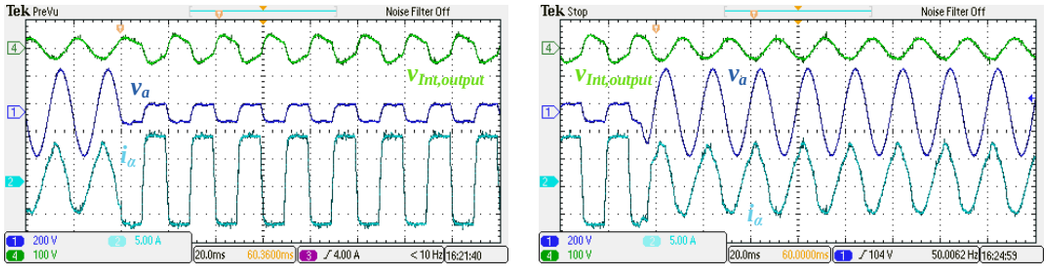

(a) (b)

Fig. 4.37. Linear step load changing (100% - 950% and viceversa) - integral output (100 V/div), real capacitor voltage (200 V/div) and real inductor current (5 A/div) (α-axis), time scale (20 ms/div): (a) from rated load (68 Ω) to overload conditions (7.2 Ω); (b) from overload conditions (7.2 Ω) to rated load (68 Ω)

4.7 Discrete-Time Domain Modelling – Conclusive Considerations

For what concerns the control of power converters working in standalone applications, state-feedback decoupling permits better dynamic response to be achieved. In this context, the model derived directly in the discrete-time domain allows a clear representation of the limitations introduced by computation and PWM delays when state feedback voltage decoupling is performed.

The simulation results validate the discrete-time model developed, which allows access to the internal states of the system. In order to enhance the current controller dynamics, a P controller with a lead compensator and Smith Predictor are implemented and compared. The implementation based on Smith Predictor has been shown to provide the fastest response to changes in the reference inductor current, allowing the current loop bandwidth to be widened while still preserving good dynamic properties. The wider inner current control bandwidth permits the bandwidth of the voltage loop to be widened as well.

As the dynamics of the voltage loop are enhanced, an anti-wind up scheme becomes even more important. The proposed design in the discrete-time domain of the anti-wind up scheme based on a feedback implementation of inverse dynamics avoids algebraic loops, which could arise depending on the discretization method employed.

The overall design provides good performance both in steady-state and transient conditions. More specifically, the requirements during transient imposed by the UPS standard IEC 62040 are verified according to the design proposed for the current and voltage regulators. Moreover, when a balanced or even unbalanced nonlinear load is supplied, the dynamic response is within the standards imposed to linear loads with just the compensator tuned at fundamental frequency.

5 Conclusions and Future Research Activities

5.1 Conclusions

The effect of state feedback coupling on the dynamics performance of current and voltage regulators for standalone microgrids/UPS systems has been investigated. The benefits of applying capacitor voltage decoupling are motivated by the higher damping of the system, almost zero steady-state error, when a P controller is used for the current loop and independence from the load impedance.

The computation and PWM delays are the main responsible to limit the bandwidth that can be achieved by the current regulator. Even if the system delays are not compensated on the decoupling path (nonideal voltage decoupling), the system shows a higher damping than without decoupling. Further improvements can be obtained by introducing a lead-lag filter in the decoupling path.

Among the PR regulator structures investigated, Complex vector PR controller, which is stable only if voltage decoupling is performed, shows the lowest sensitivity to integral gain and frequency deviations, thus it should be preferred in microgrid applications.

A design methodology for PR voltage regulators based on a lead compensator structure is provided, according to the proposed inner current controller. Its effect is reflected in the Nyquist trajectories calculated for the voltage loop, and hence affects the selection of controller gains.

A practical design methodology to select the minimum value of the fundamental resonant gain is also proposed. The solution devised provides good performance both in steady-state and transients. More specifically, the requirements during transient imposed by the UPS standard IEC 62040 are verified according to the design proposed for the current and voltage regulators. The dynamic response is even within the standards for linear loads in case the 5^{th} and 7^{th} harmonic compensators are activated together with the fundamental gains, when a diode bridge rectifier is supplied. The design is validated even in case of parallel droop-controlled power converters with unbalance in supply and virtual impedance for proper current sharing.

The exact model derived in the discrete-time domain of an LC filter allows a better representation of the limitations introduced by computation and PWM delays when state feedback voltage decoupling is performed.

In order to enhance the current controller dynamics, a P controller with a lead compensator and Smith Predictor are implemented and compared. The implementation based on Smith Predictor has been shown to provide the fastest response to changes in the reference inductor current, allowing the current loop bandwidth to be widened while still preserving good dynamic properties. The wider inner current control bandwidth permits, in particular, the increase of the voltage loop bandwidth. The systematic design methodology based on Nyquist criterion allows the identification of the phase-leading angles values as well as the gains at each harmonic frequency.

As the dynamics of the voltage loop are faster, an anti-wind up scheme becomes even more important. The proposed design in the discrete-time domain of the anti-wind up scheme avoids algebraic loops, which could arise depending on the discretization method.

The overall solution provides good performance both in steady-state and transients. Again, the requirements during transient imposed by the UPS standard IEC 62040 are verified according to the design proposed for the current and voltage regulators. The dynamic response is even within the standards imposed to linear loads with just the compensator tuned at the fundamental frequency, when a balanced or unbalanced diode bridge rectifier is supplied.

5.2 Future Research Activities

Further analysis can be performed starting from the system architecture addressed in this thesis. Specifically, the following activities could be of interest for future research activities:

- In the present work only state feedback cross-coupling decoupling has been considered as active control action. Disturbance input decoupling represents a valid alternative to achieve better dynamics performance of the regulators. Further research activities aimed at the comparison of these two control techniques, taking into account the limitation introduced by computation and PWM delays, would represent a step ahead in present research.

- Further techniques aimed at widening the current loop while preserving good dynamic performance can be proposed based on the exact model of the LC filter in the discrete-time domain.

- Further analysis on the voltage loop design can be performed using as reference the Nyquist criterion. In this sense, the effect on the dynamic performance of setting the trajectories of the resonant regulators parallel to the imaginary axis can be investigated. This technique has already been implemented with success for the current loop design of grid-connected VSIs.

Appendix

Section A

In this section the difference equations using the forward and backward Euler, the impulse invariant, and the Tustin with frequency prewarping discretization methods for nonideal PR, ideal PR and Complex Vector PR regulators of Chapter 3 are reported. The coefficients derived allow their implementation in C-code, e.g. via S-function in Simulink environment.

A.1 Ideal PR

The transfer function of ideal PR is

$$G(s) = k_{pI} + 2k_{iI}\frac{s}{s^2 + (hw_1)^2} = k_{pI} + 2k_{iI}R_1(s)$$

$$Y(z) = k_{pI}X(z) + 2k_{iI}R_1(z)X(z), \tag{A.1}$$

being X(z) and Y(z) the input and output of the transfer function in the discrete-time domain.

A.1.1 Structures with Two Integrators: Forward and Backward Euler

This structure is characterized by the following transfer function in the z-domain

$$G(z) = k_{ph} + \frac{2k_{Ih}T_{sw}(z^{-1} - z^{-2})}{1 + z^{-1}(h^2w_1^2T_{sw}^2 - 2) + z^{-2}}.$$

This implies

$$Y(z) = \left[k_{ph} + \frac{2k_{Ih}T_{sw}(z^{-1} - z^{-2})}{1 + z^{-1}(h^2w_1^2T_{sw}^2 - 2) + z^{-2}}\right]X(z)$$

$$Y(z) = \left[\frac{k_{ph}[1 + z^{-1}(h^2w_1^2T_{sw}^2 - 2) + z^{-2}] + 2k_{Ih}T_{sw}(z^{-1} - z^{-2})}{1 + z^{-1}(h^2w_1^2T_{sw}^2 - 2) + z^{-2}}\right]X(z)$$

$$Y(z)[1 + z^{-1}(h^2w_1^2T_{sw}^2 - 2) + z^{-2}] = \left\{k_{ph}[1 + z^{-1}(h^2w_1^2T_{sw}^2 - 2) + z^{-2}] + 2k_{Ih}T_{sw}(z^{-1} - z^{-2})\right\}X(z)$$

$$Y(z) + (h^2 w_1^2 T_{sw}^2 - 2)Y(z)z^{-1} + Y(z)z^{-2} = \left[k_{ph} + k_{ph}z^{-1}(h^2 w_1^2 T_{sw}^2 - 2) + k_{ph}z^{-2} + 2k_{Ih}T_{sw}(z^{-1} - z^{-2})\right]X(z)$$

$$Y(z) + (h^2 w_1^2 T_{sw}^2 - 2)Y(z)z^{-1} + Y(z)z^{-2} = k_{ph}X(z) + k_{ph}(h^2 w_1^2 T_{sw}^2 - 2)X(z)z^{-1} + k_{ph}X(z)z^{-2} + 2k_{Ih}T_{sw}X(z)z^{-1} - 2k_{Ih}T_{sw}X(z)z^{-2}$$

$$Y(z) = -(h^2 w_1^2 T_{sw}^2 - 2)Y(z)z^{-1} - Y(z)z^{-2} + k_{ph}X(z) + \left[k_{ph}(h^2 w_1^2 T_{sw}^2 - 2) + 2k_{Ih}T_{sw}\right]X(z)z^{-1} + [k_{ph} - 2k_{Ih}T_{sw}]X(z)z^{-2}$$

Substituting for the k-th sampling instant

$$y(z) = -(h^2 w_1^2 T_{sw}^2 - 2)y(k-1) - y(k-2) + k_{ph}x(k) + \left[k_{ph}(h^2 w_1^2 T_{sw}^2 - 2) + 2k_{Ih}T_{sw}\right]x(k-1) + \left[k_{ph} - 2k_{Ih}T_{sw}\right]x(k-2)$$

$$y(k) = a_1 y(k-1) + a_2 y(k-2) + b_1 x(k) + b_2 x(k-1) + b_3 x(k-2)$$

Being

$$a_1 = -(h^2 w_1^2 T_{sw}^2 - 2)$$

$$a_2 = -1$$

$$b_1 = k_{ph}$$

$$b_2 = k_{ph}(h^2 w_1^2 T_{sw}^2 - 2) + 2k_{Ih}T_{sw}$$

$$b_3 = k_{ph} - 2k_{Ih}T_{sw}$$

A.1.2 Impulse Invariant

According to Table 3.4

$$R_1(z) = T_{sw}\frac{1 - z^{-1}\cos(hw_1 T_{sw})}{1 - 2z^{-1}\cos(hw_1 T_{sw}) + z^{-2}}$$

With reference to the integral part of (A.1)

$$Y(z) = k_{iI}R_1(z)X(z) = k_{iI}T_{sw}\frac{1 - z^{-1}\cos(hw_1T_{sw})}{1 - 2z^{-1}\cos(hw_1T_{sw}) + z^{-2}}X(z)$$

$$Y(z)[1 - 2z^{-1}\cos(hw_1T_{sw}) + z^{-2}] = k_{iI}T_{sw}[1 - z^{-1}\cos(hw_1T_{sw})]X(z)$$

$$Y(z) = 2\cos(hw_1T_{sw})Y(z)z^{-1} - Y(z)z^{-2} + k_{iI}T_{sw}X(z) - k_{iI}T_{sw}\cos(hw_1T_{sw})X(z)z^{-1}$$

Substituting for the k-th sampling instant

$$y(k) = 2\cos(hw_1T_{sw})y(k-1) - y(k-2) + k_{iI}T_{sw}x(k) - k_{iI}T_{sw}\cos(hw_1T_{sw})x(k-1)$$

$$y(k) = a_1y(k-1) + a_2y(k-2) + b_1x(k) + b_2x(k-1)$$

Being

$$a_1 = 2\cos(hw_1T_{sw})$$

$$a_2 = -1$$

$$b_1 = k_{iI}T_{sw}$$

$$b_2 = -k_{iI}T_{sw}\cos(hw_1T_{sw})$$

A.1.3 Tustin with Frequency Prewarping

According to Table 3.4

$$R_1(z) = \frac{\sin(hw_1T_{sw})}{2hw_1}\frac{1 - z^{-2}}{1 - 2z^{-1}\cos(hw_1T_{sw}) + z^{-2}}$$

With reference to the integral part of (A.1)

$$Y(z) = k_{iI}R_1(z)X(z) = k_{iI}\frac{\sin(hw_1T_{sw})}{2hw_1}\frac{1 - z^{-2}}{1 - 2z^{-1}\cos(hw_1T_{sw}) + z^{-2}}X(z)$$

$$Y(z)2hw_1[1 - 2z^{-1}\cos(hw_1T_{sw}) + z^{-2}] = k_{iI}\sin(hw_1T_{sw})[1 - z^{-2}]X(z)$$

$$2hw_1Y(z) - 2\cos(hw_1T_{sw})\,2hw_1Y(z)z^{-1} + 2hw_1Y(z)z^{-2} = k_{iI}\sin(hw_1T_{sw})X(z) - k_{iI}\sin(hw_1T_{sw})z^{-2}X(z)$$

$$Y(z) = \frac{2\cos(hw_1T_{sw})\,2hw_1}{2hw_1}Y(z)z^{-1} + \frac{-2hw_1}{2hw_1}Y(z)z^{-2} + \frac{k_{iI}\sin(hw_1T_{sw})}{2hw_1}X(z) + \frac{-k_{iI}\sin(hw_1T_{sw})}{2hw_1}z^{-2}X(z)$$

Substituting for the k-th sampling instant

$$y(k) = \frac{2\cos(hw_1T_{sw})\,2hw_1}{2hw_1}y(k-1) + \frac{-2hw_1}{2hw_1}y(k-2) + \frac{k_{iI}\sin(hw_1T_{sw})}{2hw_1}x(k) + \frac{-k_{iI}\sin(hw_1T_{sw})}{2hw_1}x(k-2)$$

$$y(k) = a_1y(k-1) + a_2y(k-2) + b_1x(k) + b_2x(k-2)$$

Being

$$a_1 = 2\cos(hw_1T_{sw})$$

$$a_2 = -1$$

$$b_1 = 2k_{iI}T_{sw}$$

$$b_2 = -2k_{iI}T_{sw}\cos(hw_1T_{sw})$$

A.2 Nonideal PR

The transfer function of nonideal PR is

$$G(s) = k_{pI} + \frac{2k_{iI}w_cs}{s^2 + 2w_cs + (hw_1)^2} = k_{pI} + 2k_{iI}w_cR_1(s)$$

$$Y(z) = k_{pI}X(z) + 2k_{iI}w_cR_1(z)X(z) \quad \text{(A.2)}$$

A.1.2 Structures with Two Integrators: Forward and Backward Euler

Starting from G(s), by multiplying and dividing by $1/s^2$ the resonant term

$$G(s) = k_{ph} + \frac{2k_{ih}w_c\frac{1}{s}}{1 + 2w_c\frac{1}{s} + h^2w_1^2\frac{1}{s^2}}$$

By definition, it occurs to substitute s with the following expressions

$$\text{Forward Euler: } s = \frac{1-z^{-1}}{z^{-1}T_{sw}}$$

Backward Euler: $s = \frac{1-z^{-1}}{T_{sw}}$

$$G(z) = k_{ph} + \frac{2k_{ih}w_c \frac{z^{-1}T_{sw}}{1-z^{-1}}}{1 + 2w_c \frac{z^{-1}T_{sw}}{1-z^{-1}} + h^2 w_1^2 \frac{T_{sw}}{1-z^{-1}} \frac{z^{-1}T_{sw}}{1-z^{-1}}}$$

$$G(z) = k_{ph} + \frac{2k_{ih}w_c z^{-1}T_{sw}(1-z^{-1})}{(1-z^{-1})^2 + 2w_c z^{-1}T_{sw}(1-z^{-1}) + z^{-1}h^2 w_1^2 T_{sw}^2}$$

$$G(z) = k_{ph} + \frac{2k_{ih}w_c T_{sw}(z^{-1}-z^{-2})}{1 - 2z^{-1} + z^{-2} + 2w_c T_{sw}(z^{-1}-z^{-2}) + z^{-1}h^2 w_1^2 T_{sw}^2}$$

$$G(z) = k_{ph} + \frac{2k_{ih}w_c T_{sw}(z^{-1}-z^{-2})}{1 + z^{-1}(h^2 w_1^2 T_{sw}^2 - 2 + 2w_c T_{sw}) + z^{-2}(1 - 2w_c T_{sw})}$$

Substituting in (A.2)

$$Y(z) = \left[k_{ph} + \frac{2k_{ih}w_c T_{sw}(z^{-1}-z^{-2})}{1 + z^{-1}(h^2 w_1^2 T_{sw}^2 - 2 + 2w_c T_{sw}) + z^{-2}(1 - 2w_c T_{sw})}\right] X(z)$$

$$\begin{aligned} Y(z)[1 + z^{-1}(h^2 w_1^2 T_{sw}^2 - 2 + 2w_c T_{sw}) + z^{-2}(1 - 2w_c T_{sw})] \\ = \left[k_{ph} + k_{ph}z^{-1}(h^2 w_1^2 T_{sw}^2 - 2 + 2w_c T_{sw}) + k_{ph}z^{-2}(1 - 2w_c T_{sw})\right. \\ \left. + 2k_{ih}w_c T_{sw}(z^{-1} - z^{-2})\right] X(z) \end{aligned}$$

$$\begin{aligned} Y(z) + (h^2 w_1^2 T_{sw}^2 - 2 + 2w_c T_{sw})Y(z)z^{-1} + (1 - 2w_c T_{sw})Y(z)z^{-2} \\ = k_{ph}X(z) + k_{ph}(h^2 w_1^2 T_{sw}^2 - 2 + 2w_c T_{sw})X(z)z^{-1} \\ + k_{ph}(1 - 2w_c T_{sw})X(z)z^{-2} + 2k_{ih}w_c T_{sw}X(z)z^{-1} \\ - 2k_{ih}w_c T_{sw}X(z)z^{-2} \end{aligned}$$

$$\begin{aligned} Y(z) = -(h^2 w_1^2 T_{sw}^2 - 2 + 2w_c T_{sw})Y(z)z^{-1} - (1 - 2w_c T_{sw})Y(z)z^{-2} + k_{ph}X(z) \\ + \left[k_{ph}(h^2 w_1^2 T_{sw}^2 - 2 + 2w_c T_{sw}) + 2k_{ih}w_c T_{sw}\right] X(z)z^{-1} \\ + \left[k_{ph}(1 - 2w_c T_{sw}) - 2k_{ih}w_c T_{sw}\right] X(z)z^{-2} \end{aligned}$$

Substituting for the k-th sampling instant, the difference equation is

$$y(k) = a_1 y(k-1) + a_2 y(k-2) + b_1 x(k) + b_2 x(k-1) + b_3 x(k-2)$$

Being

$$a_1 = -(h^2 w_1^2 T_{sw}^2 - 2 + 2w_c T_{sw})$$

$$a_2 = -(1 - 2w_c T_{sw})$$

$$b_1 = k_{ph}$$

$$b_2 = k_{ph}(h^2 w_1^2 T_{sw}^2 - 2 + 2w_c T_{sw}) + 2k_{ih} w_c T_{sw}$$

$$b_3 = k_{ph}(1 - 2w_c T_{sw}) - 2k_{ih} w_c T_{sw}$$

A.2.2 Tustin with Frequency Prewarping

By definition, it occurs to substitute the variable s in $R_1(s)$

$$R_1(z) = \left[\frac{s}{s^2 + 2w_c s + h^2 w_1^2}\right]_{s=\frac{hw_1}{\tan\left(\frac{hw_1 T_s}{2}\right)}\frac{(1-z^{-1})}{(1+z^{-1})}}$$

$$R_1(z) = \frac{\frac{hw_1}{\tan\left(\frac{w_1 T_s}{2}\right)}\frac{(1-z^{-1})}{(1+z^{-1})}}{\left(\frac{hw_1}{\tan\left(\frac{hw_1 T_s}{2}\right)}\frac{(1-z^{-1})}{(1+z^{-1})}\right)^2 + 2w_c\frac{hw_1}{\tan\left(\frac{hw_1 T_s}{2}\right)}\frac{(1-z^{-1})}{(1+z^{-1})} + h^2 w_1^2}$$

Rearranging

$$R_1(z) = \frac{1}{hw_1}\frac{\tan\left(\frac{hw_1 T_s}{2}\right)\frac{(1-z^{-1})}{(1+z^{-1})}}{\left[\frac{(1-z^{-1})^2}{(1+z^{-1})^2} + \tan\left(\frac{hw_1 T_s}{2}\right)\frac{2w_c(1-z^{-1})}{hw_1(1+z^{-1})} + \tan^2\left(\frac{hw_1 T_s}{2}\right)\right]}$$

By multiplying and dividing by $(1 + z^{-1})^2$

$$R_1(z) = \frac{1}{hw_1}\frac{\tan\left(\frac{hw_1 T_s}{2}\right)(1-z^{-1})(1+z^{-1})}{\left[(1-z^{-1})^2 + \tan\left(\frac{hw_1 T_s}{2}\right)\frac{2w_c(1-z^{-1})(1+z^{-1})}{hw_1} + \tan^2\left(\frac{hw_1 T_s}{2}\right)(1+z^{-1})^2\right]}$$

After some mathematical passages

$$R_1(z) = \frac{\sin(hw_1 T_s)}{2hw_1}\frac{1 - z^{-2}}{\left[\sin(hw_1 T_s)\frac{w_c(1-z^{-2})}{hw_1} + 1 + 2z^{-1}\left(1 - 2\cos^2\left(\frac{hw_1 T_s}{2}\right)\right) + z^{-2}\right]}$$

Since $\cos\left(\frac{a}{2}\right) = \sqrt{\frac{1+\cos(a)}{2}}$, it comes: $-\cos(a) = 1 - 2\cos^2(\frac{a}{2})$

$$R_1(z) = \frac{\sin(hw_1T_s)}{2hw_1} \frac{1 - z^{-2}}{\left[\sin(hw_1T_s)\frac{w_c(1-z^{-2})}{hw_1} + 1 - 2z^{-1}\cos(hw_1T_s) + z^{-2}\right]}$$

$$R_1(z) = \frac{\sin(hw_1T_s)}{2hw_1} \frac{1 - z^{-2}}{\left[\left(1 + \sin(hw_1T_s)\frac{w_c}{hw_1}\right) - 2\cos(hw_1T_s)z^{-1} + \left(1 - \sin(hw_1T_s)\frac{w_c}{hw_1}\right)z^{-2}\right]}$$

This implies

$$Y(z) = 2k_{iI}w_cR_1(z)X(z) =$$

$$Y(z) = k_{iI}w_c\frac{\sin(hw_1T_s)}{hw_1} \frac{1 - z^{-2}}{\left[\left(1 + \sin(hw_1T_s)\frac{w_c}{hw_1}\right) - 2\cos(hw_1T_s)z^{-1} + \left(1 - \sin(hw_1T_s)\frac{w_c}{hw_1}\right)z^{-2}\right]}X(z)$$

$$Y(z)hw_1\left[\left(1 + \sin(hw_1T_s)\frac{w_c}{hw_1}\right) - 2\cos(hw_1T_s)z^{-1} + \left(1 - \sin(hw_1T_s)\frac{w_c}{hw_1}\right)z^{-2}\right] = k_{iI}w_c sin(hw_1T_s)(1 - z^{-2})X(z)$$

$$Y(z)hw_1\left(1 + \sin(hw_1T_s)\frac{w_c}{hw_1}\right) - 2\cos(hw_1T_s)hw_1Y(z)z^{-1} + \left(1 - \sin(hw_1T_s)\frac{w_c}{hw_1}\right)hw_1Y(z)z^{-2} = k_{iI}w_c sin(hw_1T_s)X(z) - k_{iI}w_c sin(hw_1T_s)X(z)z^{-2}$$

$$Y(z) = \frac{2\cos(hw_1T_s)hw_1}{hw_1\left(1 + \sin(hw_1T_s)\frac{w_c}{hw_1}\right)}Y(z)z^{-1} - \frac{\left(1 - \sin(hw_1T_s)\frac{w_c}{hw_1}\right)hw_1}{hw_1\left(1 + \sin(hw_1T_s)\frac{w_c}{hw_1}\right)}Y(z)z^{-2} + \frac{k_{iI}w_c sin(hw_1T_s)}{hw_1\left(1 + \sin(hw_1T_s)\frac{w_c}{hw_1}\right)}X(z) - \frac{k_{iI}w_c sin(hw_1T_s)}{hw_1\left(1 + \sin(hw_1T_s)\frac{w_c}{hw_1}\right)}X(z)z^{-2}$$

Substituting for the k-th sampling instant

$$y(k) = a_1y(k-1) + a_2y(k-2) + b_1x(k) + b_2x(k-2)$$

Being

$$a_1 = \frac{2cos(hw_1T_s)hw_1}{hw_1\left(1 + sin(hw_1T_s)\frac{w_c}{hw_1}\right)}$$

$$a_2 = -\frac{hw_1\left(1 - sin(hw_1T_s)\frac{w_c}{hw_1}\right)}{hw_1\left(1 + sin(hw_1T_s)\frac{w_c}{hw_1}\right)}$$

$$b_1 = \frac{k_{iI}w_c sin(hw_1T_s)}{hw_1\left(1 + sin(hw_1T_s)\frac{w_c}{hw_1}\right)}$$

$$b_2 = -b_1$$

A.3 Complex Vector PR

The transfer function of Complex Vector PR is

$$G(s) = k_{pI}\frac{s^2}{s^2 + (hw_1)^2} + 2k_{iI}\frac{s}{s^2 + (hw_1)^2} = k_{pI}R_2(s) + 2k_{iI}R_1(s)$$

$$Y(z) = k_{pI}R_2(z)X(z) + 2k_{iI}R_1(z)X(z) \quad \text{(A.3)}$$

A.3.1 Structures with Two Integrators: Forward and Backward Euler

This structure is characterized by the following transfer function in the z-domain

$$Y(z) = G(z)X(z)$$

$$G(z) = \frac{k_{ph} + z^{-1}\left(2k_{Ih}T_{sw} - 2k_{ph}\right) - z^{-2}(2k_{Ih}T_{sw} - k_{ph})}{1 + z^{-1}(h^2w_1^2T_{sw}^2 - 2) + z^{-2}}$$

$$Y(z) = \frac{k_{ph} + z^{-1}\left(2k_{Ih}T_{sw} - 2k_{ph}\right) - z^{-2}(2k_{Ih}T_{sw} - k_{ph})}{1 + z^{-1}(h^2w_1^2T_{sw}^2 - 2) + z^{-2}}X(z)$$

$$Y(z)[1 + z^{-1}(h^2w_1^2T_{sw}^2 - 2) + z^{-2}] = \left[k_{ph} + z^{-1}\left(2k_{Ih}T_{sw} - 2k_{ph}\right) - z^{-2}(2k_{Ih}T_{sw} - k_{ph})\right]X(z)$$

$$Y(z) + (h^2w_1^2T_{sw}^2 - 2)Y(z)z^{-1} + Y(z)z^{-2} = k_{ph}X(z) + \left(2k_{Ih}T_{sw} - 2k_{ph}\right)X(z)z^{-1} - (2k_{Ih}T_{sw} - k_{ph})X(z)z^{-2}$$

$$Y(z) = -(h^2 w_1^2 T_{sw}^2 - 2)Y(z)z^{-1} - Y(z)z^{-2} + k_{ph}X(z) + \left(2k_{Ih}T_{sw} - 2k_{ph}\right)X(z)z^{-1} - (2k_{Ih}T_{sw} - k_{ph})X(z)z^{-2}$$

The difference equation is

$$y(k) = a_1 y(k-1) + a_2 y(k-2) + b_1 x(k) + b_2 x(k-1) + b_3 x(k-2)$$

Being

$$a_1 = -(h^2 w_1^2 T_{sw}^2 - 2)$$

$$a_2 = -1$$

$$b_1 = k_{ph}$$

$$b_2 = \left(2k_{Ih}T_{sw} - 2k_{ph}\right)$$

$$b_3 = -(2k_{Ih}T_{sw} - k_{ph})$$

A.3.2 Tustin with Frequency Prewarping

With reference to the proportional part of (A.3)

$$R_2(z) = \cos^2\left(\frac{hw_1T_{sw}}{2}\right)\frac{1 - 2z^{-1} + z^{-2}}{1 - 2z^{-1}\cos(hw_1T_s) + z^{-2}}$$

$$Y(z) = k_{ph}R_2(z)X(z)$$

$$Y(z) = k_{ph}\cos^2\left(\frac{hw_1T_{sw}}{2}\right)\frac{1 - 2z^{-1} + z^{-2}}{1 - 2z^{-1}\cos(hw_1T_s) + z^{-2}}X(z)$$

$$Y(z)[1 - 2z^{-1}\cos(hw_1T_s) + z^{-2}] = k_{ph}\cos^2\left(\frac{hw_1T_{sw}}{2}\right)(1 - 2z^{-1} + z^{-2})X(z)$$

$$Y(z) - 2\cos(hw_1T_s)Y(z)z^{-1} + Y(z)z^{-2} = k_{ph}\cos^2\left(\frac{hw_1T_{sw}}{2}\right)X(z) - 2k_{ph}\cos^2\left(\frac{hw_1T_{sw}}{2}\right)X(z)z^{-1} + k_{ph}\cos^2\left(\frac{hw_1T_{sw}}{2}\right)X(z)z^{-2}$$

Since $cos\left(\frac{a}{2}\right) = \sqrt{\frac{1+cos(a)}{2}}$, it comes: $cos^2(\frac{a}{2}) = \frac{1+cos(a)}{2}$

$$Y(z) = 2\cos(hw_1T_s)Y(z)z^{-1} - Y(z)z^{-2} + k_{ph}\left[\frac{1+cos(hw_1T_{sw})}{2}\right]X(z) - 2k_{ph}\left[\frac{1+cos(hw_1T_{sw})}{2}\right]X(z)z^{-1} + k_{ph}\left[\frac{1+cos(hw_1T_{sw})}{2}\right]X(z)z^{-2}$$

$$y(k) = a_1y(k-1) + a_2y(k-2) + b_1x(k) + b_2x(k-1) + b_3x(k-2)$$

Being

$$a_1 = 2\,cos(hw_1T_s)$$

$$a_2 = -1$$

$$b_1 = k_{ph}\left[\frac{1+cos(hw_1T_{sw})}{2}\right]$$

$$b_2 = -2b_1$$

$$b_3 = b_1$$

With reference to the integral part of (A.3)

$$R_1(z) = \frac{\sin(hw_1T_{sw})}{2hw_1}\frac{1-z^{-2}}{1-2z^{-1}\cos(hw_1T_{sw})+z^{-2}}$$

This implies

$$Y(z) = 2k_{il}R_1(z)X(z) = 2k_{il}\frac{\sin(hw_1T_{sw})}{2hw_1}\frac{1-z^{-2}}{1-2z^{-1}\cos(hw_1T_{sw})+z^{-2}}X(z)$$

$$Y(z)2hw_1[1-2z^{-1}\cos(hw_1T_{sw})+z^{-2}] = 2k_{il}\sin(hw_1T_{sw})[1-z^{-2}]X(z)$$

$$2hw_1Y(z) - 2\cos(hw_1T_{sw})\,2hw_1Y(z)z^{-1} + 2hw_1Y(z)z^{-2} = 2k_{il}\sin(hw_1T_{sw})X(z) - 2k_{il}\sin(hw_1T_{sw})z^{-2}X(z)$$

$$Y(z) = \frac{2\cos(hw_1T_{sw})\,2hw_1}{2hw_1}Y(z)z^{-1} - \frac{2hw_1}{2hw_1}Y(z)z^{-2} + \frac{2k_{il}\sin(hw_1T_{sw})}{2hw_1}X(z) - \frac{2k_{il}\sin(hw_1T_{sw})}{2hw_1}z^{-2}X(z)$$

$$y(k) = a_1y(k-1) + a_2y(k-2) + b_1x(k) + b_2x(k-2)$$

Being

$$a_1 = \frac{2\cos(hw_1 T_{sw})\, 2hw_1}{2hw_1}$$

$$a_2 = -\frac{2hw_1}{2hw_1}$$

$$b_1 = \frac{2k_{il}\sin(hw_1 T_{sw})}{2hw_1}$$

$$b_2 = -b1$$

Section B

In this section the complete derivation of the discrete-time model for an LC filter with manipulated inputs via latched interface is reported. In particular, the methodology explained in Chapter 4 is applied to derive the system shown in Fig. 4.2. The main equations are highlighted in red colour.

1a. Ordinary Differential Equations of the system

The differential equations of the system are here reported as in (4.2), neglecting the disturbance $i_o(t)$

$$\begin{cases} \dfrac{d}{dt}v_c(t) = \dfrac{1}{C_f}i_L(t) \\ \dfrac{d}{dt}i_L(t) = \dfrac{1}{L_f}[v_i(t) - Ri_L(t) - v_c(t)]. \end{cases} \tag{B.1}$$

The following parameters are defined, as reported in (4.5) and (4.8)

$$\omega_n^2 = \frac{1}{L_f C_f}; \quad \xi = \frac{1}{2\omega_n}\frac{R}{L_f} = \frac{R}{2}\sqrt{\frac{C_f}{L_f}} \tag{B.2}$$

$$\omega_d = \omega_n\sqrt{1-\xi^2}; \;\; \phi = tg^{-1}\left(\frac{\sqrt{1-\xi^2}}{\xi}\right) \tag{B.3}$$

Substituting the first ODE in the second one and solving for $v_i = f(v_c)$ leads to

$$v_i(t) = C_f L_f \frac{dv_c^2(t)}{d^2 t} + RC_f\frac{dv_c(t)}{dt} + v_c(t) \tag{B.4}$$

2a. Laplace Transform of differential equations

Firstly, solve (B.4) for $V_c(s) = f(V_i, I_L)$ to derive

$$V_i(s) = L_f C_f[s^2 V_c(s) - s v_c(t=0) - \dot{v}_c(t=0)] + RC_f[sV_c(s) - v_c(t=0)] + V_c(s) \rightarrow$$

$$V_i(s) = \left[L_f C_f s^2 + RC_f s + 1\right] V_c(s) - L_f C_f[s v_c(t=0) + \dot{v}_c(t=0)] - RC_f v_c(t=0) \rightarrow$$

$$V_i(s) = L_f C_f \left[s^2 + \frac{R}{L_f} s + \frac{1}{L_f C_f}\right] V_c(s) - L_f C_f[s v_c(t=0) + \dot{v}_c(t=0)] - RC_f v_c(t=0) \rightarrow$$

$$V_i(s) = \left[\frac{s^2 + 2\xi\omega_n s + \omega_n^2}{\omega_n^2}\right] V_c(s) - \frac{1}{\omega_n^2}[s v_c(t=0) + \dot{v}_c(t=0)] - \frac{2\xi}{\omega_n} v_c(t=0) \rightarrow$$

$$\left[\frac{s^2 + 2\xi\omega_n s + \omega_n^2}{\omega_n^2}\right] V_c(s) = V_i(s) + \frac{1}{\omega_n^2}[s v_c(t=0) + \dot{v}_c(t=0)] + \frac{2\xi}{\omega_n} v_c(t=0) \rightarrow$$

$$V_c(s) = \frac{\omega_n^2}{s^2 + 2\xi\omega_n s + \omega_n^2}\left\{V_i(s) + \frac{1}{\omega_n^2}[s v_c(t=0) + \dot{v}_c(t=0)] + \frac{2\xi}{\omega_n} v_c(t=0)\right\} \quad \text{(B.5)}$$

3a. Substituting $V_i(s) = v_i(t=0)/s$ (latch effect) in (B.5):

Equation (4.3) is derived

$$V_c(s) = \frac{\omega_n^2}{s^2 + 2\xi\omega_n s + \omega_n^2}\left\{v_i(t=0)\frac{1}{s} + \frac{1}{\omega_n^2}[s v_c(t=0) + \dot{v}_c(t=0)] + \frac{2\xi}{\omega_n} v_c(t=0)\right\} \quad \text{(B.6)}$$

4a. Inverse Laplace Transform of (B.6):

$$v_c(t) = \left[1 - \frac{1}{\sqrt{1-\xi^2}} e^{-\xi\omega_n t} \sin\left(\sqrt{1-\xi^2}\omega_n t + \phi\right)\right] v_i(t=0) + \frac{v_c(t=0)}{\omega_n^2} \frac{-\omega_n^2}{\sqrt{1-\xi^2}} e^{-\xi\omega_n t} \sin\left(\sqrt{1-\xi^2}\omega_n t - \phi\right) + \frac{2\xi}{\omega_n} v_c(t=0) \frac{\omega_n}{\sqrt{1-\xi^2}} e^{-\xi\omega_n t} \sin\left(\sqrt{1-\xi^2}\omega_n t\right) + \frac{\dot{v}_c(t=0)}{\omega_n^2} \frac{\omega_n}{\sqrt{1-\xi^2}} e^{-\xi\omega_n t} \sin\left(\sqrt{1-\xi^2}\omega_n t\right) \rightarrow$$

$$
\begin{aligned}
v_c(t) = &\left[1 - \frac{1}{\sqrt{1-\xi^2}} e^{-\xi\omega_n t} \sin(\omega_d t + \phi)\right] v_i(t=0) \\
&+ \frac{v_c(t=0)}{\omega_n^2} \frac{-\omega_n^2}{\sqrt{1-\xi^2}} e^{-\xi\omega_n t} \sin(\omega_d t - \phi) \\
&+ \frac{2\xi}{\omega_n} v_c(t=0) \frac{\omega_n}{\sqrt{1-\xi^2}} e^{-\xi\omega_n t} \sin(\omega_d t) \\
&+ \frac{\dot{v}_c(t=0)}{\omega_n^2} \frac{\omega_n}{\sqrt{1-\xi^2}} e^{-\xi\omega_n t} \sin(\omega_d t)
\end{aligned}
\tag{B.7}
$$

5a. Response in the next sample time:

$$
\begin{aligned}
v_c(T) = &\left[1 - \frac{1}{\sqrt{1-\xi^2}} e^{-\xi\omega_n T} \sin(\omega_d T + \phi)\right] v_i(t=0) \\
&+ \frac{v_c(t=0)}{\omega_n^2} \frac{-\omega_n^2}{\sqrt{1-\xi^2}} e^{-\xi\omega_n T} \sin(\omega_d T - \phi) \\
&+ \frac{2\xi}{\omega_n} v_c(t=0) \frac{\omega_n}{\sqrt{1-\xi^2}} e^{-\xi\omega_n T} \sin(\omega_d T) \\
&+ \frac{\dot{v}_c(t=0)}{\omega_n^2} \frac{\omega_n}{\sqrt{1-\xi^2}} e^{-\xi\omega_n T} \sin(\omega_d T)
\end{aligned}
\tag{B.8}
$$

6a. Generalization of the solution (difference equation)

$$
\begin{aligned}
v_c(kT) = &\left[1 - \frac{1}{\sqrt{1-\xi^2}} e^{-\xi\omega_n T} \sin(\omega_d T + \phi)\right] v_i\big((k-1)T\big) \\
&+ \frac{v_c\big((k-1)T\big)}{\omega_n^2} \frac{-\omega_n^2}{\sqrt{1-\xi^2}} e^{-\xi\omega_n T} \sin(\omega_d T - \phi) \\
&+ \frac{2\xi}{\omega_n} v_c\big((k-1)T\big) \frac{\omega_n}{\sqrt{1-\xi^2}} e^{-\xi\omega_n T} \sin(\omega_d T) \\
&+ \frac{\dot{v}_c\big((k-1)T\big)}{\omega_n^2} \frac{\omega_n}{\sqrt{1-\xi^2}} e^{-\xi\omega_n T} \sin(\omega_d T)
\end{aligned}
\tag{B.9}
$$

7a. Model in B operator

$$
\begin{aligned}
V_c(B) = &\left[1 - \frac{1}{\sqrt{1-\xi^2}} e^{-\xi\omega_n T} \sin(\omega_d T + \phi)\right] BV_i(B) \\
&+ \frac{BV_c(B)}{\omega_n^2} \frac{-\omega_n^2}{\sqrt{1-\xi^2}} e^{-\xi\omega_n T} \sin(\omega_d T - \phi) \\
&+ \frac{2\xi}{\omega_n} BV_c(B) \frac{\omega_n}{\sqrt{1-\xi^2}} e^{-\xi\omega_n T} \sin(\omega_d T) \\
&+ \frac{B\dot{V}_c(B)}{\omega_n^2} \frac{\omega_n}{\sqrt{1-\xi^2}} e^{-\xi\omega_n T} \sin(\omega_d T)
\end{aligned}
\tag{B.10}
$$

Equation (B.10) cannot be written in transfer function format due to the term $\dot{V}_c(B)$. However, remember that $\dot{V}_c(B) = (1/C_f) I_L(B)$. Therefore, this model with cross-coupling can be written as:

$$
\begin{aligned}
V_c(B) = &\left[1 - \frac{1}{\sqrt{1-\xi^2}} e^{-\xi\omega_n T} \sin(\omega_d T + \phi)\right] BV_i(B) \\
&+ \frac{1}{\omega_n^2} \frac{-\omega_n^2}{\sqrt{1-\xi^2}} e^{-\xi\omega_n T} \sin(\omega_d T - \phi)\, BV_c(B) \\
&+ \frac{2\xi}{\omega_n} \frac{\omega_n}{\sqrt{1-\xi^2}} e^{-\xi\omega_n T} \sin(\omega_d T)\, BV_c(B) \\
&+ \frac{1}{C_f \omega_n^2} \frac{\omega_n}{\sqrt{1-\xi^2}} e^{-\xi\omega_n T} \sin(\omega_d T)\, BI_L(B) \rightarrow \\
&\left[1 + \frac{\omega_n}{\omega_d} e^{-\xi\omega_n T} \sin(\omega_d T - \phi)\, B - \frac{2\xi\omega_n}{\omega_d} e^{-\xi\omega_n T} \sin(\omega_d T)\, B\right] V_c(B) \\
&= \left[1 - \frac{\omega_n}{\omega_d} e^{-\xi\omega_n T} \sin(\omega_d T + \phi)\right] BV_i(B) \\
&+ \frac{1}{C_f \omega_d} e^{-\xi\omega_n T} \sin(\omega_d T)\, BI_L(B)
\end{aligned}
\tag{B.11}
$$

Solving (B.12) **for $i_L = f(V_i, V_c)$**

Substituting $v_c(t) = \frac{1}{C_f}\int_0^t i_L(t)dt + v_c(t=0)$ in the second ODE of (B.1)

$$
v_i(t) = L_f \frac{di_L(t)}{dt} + Ri_L(t) + \frac{1}{C_f}\int_0^t i_L(t)dt + v_c(t=0) \tag{B.12}
$$

2b. Laplace transform of differential equations

It is correct to model the output initial voltage as $v_c(t=0)1/s$, since this is a quantity higher than zero. So $L(v_c(t=0)1/s) = v_c(t=0)$

$$V_i(s) = L_f[sI_L(s) - i_L(t=0)] + RI_L(s) + \frac{1}{C_f}\frac{1}{s}I_L(s) + v_c(t=0)\frac{1}{s} \rightarrow$$

$$V_i(s) = \left[L_f s + R + \frac{1}{C_f}\frac{1}{s}\right]I_L(s) - L_f i_L(t=0) + v_c(t=0)\frac{1}{s} \rightarrow$$

$$V_i(s) = L_f\left[s + \frac{R_f}{L_f} + \frac{1}{L_f C_f}\frac{1}{s}\right]I_L(s) - L_f i_L(t=0) + v_c(t=0)\frac{1}{s} \rightarrow$$

$$V_i(s) = L_f\left[\frac{s^2 + 2\xi\omega_n s + \omega_n^2}{s}\right]I_L(s) - L_f i_L(t=0) + v_c(t=0)\frac{1}{s} \qquad \text{(B.13)}$$

3b. Substituting $V_i(s) = v_i(t=0)/s$ (latch effect), it gives

$$\frac{v_i(t=0)}{s} = L_f\left[\frac{s^2 + 2\xi\omega_n s + \omega_n^2}{s}\right]I_L(s) - L_f i_L(t=0) + v_c(t=0)\frac{1}{s} \rightarrow$$

$$v_i(t=0) = L_f[s^2 + 2\xi\omega_n s + \omega_n^2]I_L(s) - L_f s i_L(t=0) + v_c(t=0) \rightarrow$$

$$L_f[s^2 + 2\xi\omega_n s + \omega_n^2]I_L(s) = v_i(t=0) + L_f s i_L(t=0) - v_c(t=0) \rightarrow$$

$$I_L(s) = \frac{1}{L_f(s^2 + 2\xi\omega_n s + \omega_n^2)}\left[v_i(t=0) + L_f s i_L(t=0) - v_c(t=0)\right] \rightarrow$$

$$I_L(s) = \frac{C_f}{L_f C_f(s^2 + 2\xi\omega_n s + \omega_n^2)}\left[v_i(t=0) + L_f s i_L(t=0) - v_c(t=0)\right] \rightarrow$$

$$I_L(s) = \frac{\omega_n^2}{s^2 + 2\xi\omega_n s + \omega_n^2}\left[C_f v_i(t=0) + L_f C_f s i_L(t=0) - C_f v_c(t=0)\right] \qquad \text{(B.14)}$$

4b. Inverse Laplace transform

$$i_L(t) = C_f\frac{\omega_n}{\sqrt{1-\xi^2}}e^{-\xi\omega_n t}\sin\left(\sqrt{1-\xi^2}\omega_n t\right)v_i(t=0)$$
$$+ L_f C_f\frac{-\omega_n^2}{\sqrt{1-\xi^2}}e^{-\xi\omega_n t}\sin\left(\sqrt{1-\xi^2}\omega_n t - \phi\right)i_L(t=0)$$
$$- C_f\frac{\omega_n}{\sqrt{1-\xi^2}}e^{-\xi\omega_n t}\sin\left(\sqrt{1-\xi^2}\omega_n t\right)v_c(t=0) \rightarrow$$

$$i_L(t) = C_f \frac{\omega_n}{\sqrt{1-\xi^2}} e^{-\xi\omega_n t} \sin(\omega_d t)\, v_i(t=0) + \frac{1}{\omega_n^2} \frac{-\omega_n^2}{\sqrt{1-\xi^2}} e^{-\xi\omega_n t} \sin(\omega_d t - \phi)\, i_L(t=0) - C_f \frac{\omega_n}{\sqrt{1-\xi^2}} e^{-\xi\omega_n t} \sin(\omega_d t)\, v_c(t=0) \quad \text{(B.15)}$$

5b. Response in the next sample instant

$$i_L(T) = C_f \frac{\omega_n^2}{\omega_n\sqrt{1-\xi^2}} e^{-\xi\omega_n T} \sin(\omega_d T)\, v_i(t=0) - \frac{\omega_n}{\omega_d} e^{-\xi\omega_n T} \sin(\omega_d T - \phi)\, i_L(t=0) - C_f \frac{\omega_n^2}{\omega_n\sqrt{1-\xi^2}} e^{-\xi\omega_n T} \sin(\omega_d T)\, v_c(t=0) \rightarrow$$

$$i_L(T) = C_f \frac{\omega_n^2}{\omega_d} e^{-\xi\omega_n T} \sin(\omega_d T)\, v_i(t=0) - \frac{\omega_n}{\omega_d} e^{-\xi\omega_n T} \sin(\omega_d T - \phi)\, i_L(t=0) - C_f \frac{\omega_n^2}{\omega_d} e^{-\xi\omega_n T} \sin(\omega_d T)\, v_c(t=0) \quad \text{(B.16)}$$

6b. Generalization of the solution (difference equation)

$$i_L(kT) = C_f \frac{\omega_n^2}{\omega_d} e^{-\xi\omega_n T} \sin(\omega_d T)\, v_i\big((k-1)T\big) - \frac{\omega_n}{\omega_d} e^{-\xi\omega_n T} \sin(\omega_d T - \phi)\, i_L\big((k-1)T\big) - C_f \frac{\omega_n^2}{\omega_d} e^{-\xi\omega_n T} \sin(\omega_d T)\, v_c\big((k-1)T\big) \quad \text{(B.17)}$$

7b. Model in B operator

$$I_L(B) = C_f \frac{\omega_n^2}{\omega_d} e^{-\xi\omega_n T} \sin(\omega_d T)\, BV_i(B) - \frac{\omega_n}{\omega_d} e^{-\xi\omega_n T} \sin(\omega_d T - \phi)\, BI_L(B) - C_f \frac{\omega_n^2}{\omega_d} e^{-\xi\omega_n T} \sin(\omega_d T)\, BV_c(B) \rightarrow$$

$$\left[1+\frac{\omega_n}{\omega_d}e^{-\xi\omega_n T}\sin(\omega_d T-\phi)\,B\right]I_L(B)$$
$$=C_f\frac{\omega_n^2}{\omega_d}e^{-\xi\omega_n T}\sin(\omega_d T)\,BV_i(B)-C_f\frac{\omega_n^2}{\omega_d}e^{-\xi\omega_n T}\sin(\omega_d T)\,BV_c(B)$$
$$\rightarrow$$
$$I_L(B)=\frac{1}{1+\frac{\omega_n}{\omega_d}e^{-\xi\omega_n T}\sin(\omega_d T-\phi)\,B}C_f\frac{\omega_n^2}{\omega_d}e^{-\xi\omega_n T}\sin(\omega_d T)\,B[V_i(B)-V_c(B)] \quad \text{(B.18)}$$

8. Solving the coupling equations (B.11) **and** (B.18)**, here reported, to obtain the independent transfer functions yields to**

$$\left[1+\frac{\omega_n}{\omega_d}e^{-\xi\omega_n T}\sin(\omega_d T-\phi)\,B-\frac{2\xi\omega_n}{\omega_d}e^{-\xi\omega_n T}\sin(\omega_d T)\,B\right]V_c(B) \quad \text{(B.19)}$$
$$=\left[1-\frac{\omega_n}{\omega_d}e^{-\xi\omega_n T}\sin(\omega_d T+\phi)\right]BV_i(B)$$
$$+\frac{1}{C_f\omega_d}e^{-\xi\omega_n T}\sin(\omega_d T)\,BI_L(B)$$

$$I_L(B)=\frac{1}{1+\frac{\omega_n}{\omega_d}e^{-\xi\omega_n T}\sin(\omega_d T-\phi)\,B}C_f\frac{\omega_n^2}{\omega_d}e^{-\xi\omega_n T}\sin(\omega_d T)\,B[V_i(B)-V_c(B)] \quad \text{(B.20)}$$

$$\left[1+\frac{\omega_n}{\omega_d}e^{-\xi\omega_n T}\sin(\omega_d T-\phi)\,B-\frac{2\xi\omega_n}{\omega_d}e^{-\xi\omega_n T}\sin(\omega_d T)\,B\right]V_c(B)$$
$$=\left[1-\frac{\omega_n}{\omega_d}e^{-\xi\omega_n T}\sin(\omega_d T+\phi)\right]BV_i(B)$$
$$+\frac{1}{C_f\omega_d}e^{-\xi\omega_n T}\sin(\omega_d T)\frac{B^2}{1+\frac{\omega_n}{\omega_d}e^{-\xi\omega_n T}\sin(\omega_d T-\phi)\,B}C_f\frac{\omega_n^2}{\omega_d}e^{-\xi\omega_n T}\sin(\omega_d T)\,[V_i(B)-V_c(B)]\rightarrow$$

$$\left[1+\frac{\omega_n}{\omega_d}e^{-\xi\omega_n T}\sin(\omega_d T-\phi)\,B-\frac{2\xi\omega_n}{\omega_d}e^{-\xi\omega_n T}\sin(\omega_d T)\,B\right]V_c(B)$$
$$=\left[1-\frac{\omega_n}{\omega_d}e^{-\xi\omega_n T}\sin(\omega_d T+\phi)\right]BV_i(B)$$
$$+\frac{B^2}{1+\frac{\omega_n}{\omega_d}e^{-\xi\omega_n T}\sin(\omega_d T-\phi)\,B}\left[\frac{\omega_n^2}{\omega_d^2}e^{-2\xi\omega_n T}\sin^2(\omega_d T)\,V_i(B)-\frac{\omega_n^2}{\omega_d^2}e^{-2\xi\omega_n T}\sin^2(\omega_d T)\,V_c(B)\right]\rightarrow$$

$$\left[1+\frac{\omega_n}{\omega_d}e^{-\xi\omega_n T}\sin(\omega_d T-\phi)\,B-\frac{2\xi\omega_n}{\omega_d}e^{-\xi\omega_n T}\sin(\omega_d T)\,B\right.$$
$$\left.+\frac{B^2}{1+\frac{\omega_n}{\omega_d}e^{-\xi\omega_n T}\sin(\omega_d T-\phi)\,B}\frac{\omega_n^2}{\omega_d^2}e^{-2\xi\omega_n T}\sin^2(\omega_d T)\right]V_c(B)$$
$$=\left[1-\frac{\omega_n}{\omega_d}e^{-\xi\omega_n T}\sin(\omega_d T+\phi)\right]BV_i(B)$$
$$+\frac{B^2}{1+\frac{\omega_n}{\omega_d}e^{-\xi\omega_n T}\sin(\omega_d T-\phi)\,B}\frac{\omega_n^2}{\omega_d^2}e^{-2\xi\omega_n T}\sin^2(\omega_d T)\,V_i(B)\rightarrow$$

- **Terms of $V_c(B)$ (numerator)**

$$\left[1+\frac{\omega_n}{\omega_d}e^{-\xi\omega_n T}\sin(\omega_d T-\phi)\,B-\frac{2\xi\omega_n}{\omega_d}e^{-\xi\omega_n T}\sin(\omega_d T)\,B\right]\left[1\right.$$
$$\left.+\frac{\omega_n}{\omega_d}e^{-\xi\omega_n T}\sin(\omega_d T-\phi)\,B\right]+(\omega_n^2/\omega_d^2)e^{-2\xi\omega_n T}\sin^2(\omega_d T)\,B^2\rightarrow$$

$$1+\frac{\omega_n}{\omega_d}e^{-\xi\omega_n T}\sin(\omega_d T-\phi)\,B+\frac{\omega_n}{\omega_d}e^{-\xi\omega_n T}\sin(\omega_d T-\phi)\,B$$
$$+\left(\frac{\omega_n^2}{\omega_d^2}\right)e^{-2\xi\omega_n T}\sin^2(\omega_d T-\phi)\,B^2-\frac{2\xi\omega_n}{\omega_d}e^{-\xi\omega_n T}\sin(\omega_d T)\,B$$
$$-2\xi(\omega_n^2/\omega_d^2)e^{-2\xi\omega_n T}\sin(\omega_d T)\sin(\omega_d T-\phi)\,B^2$$
$$+(\omega_n^2/\omega_d^2)e^{-2\xi\omega_n T}\sin^2(\omega_d T)\,B^2\rightarrow$$

$$1+\left[2\frac{\omega_n}{\omega_d}e^{-\xi\omega_n T}\sin(\omega_d T-\phi)-\frac{2\xi\omega_n}{\omega_d}e^{-\xi\omega_n T}\sin(\omega_d T)\right]B$$
$$+\left[\frac{\omega_n^2}{\omega_d^2}e^{-2\xi\omega_n T}\sin^2(\omega_d T-\phi)\right.$$
$$-2\xi(\omega_n^2/\omega_d^2)e^{-2\xi\omega_n T}\sin(\omega_d T)\sin(\omega_d T-\phi)$$
$$\left.+(\omega_n^2/\omega_d^2)e^{-2\xi\omega_n T}\sin^2(\omega_d T)\right]B^2\rightarrow$$

- ✓ **Terms of $V_c(B)$ (numerator) – B terms**

$$2\frac{\omega_n}{\omega_d}e^{-\xi\omega_n T}\sin(\omega_d T-\phi)-\frac{2\xi\omega_n}{\omega_d}e^{-\xi\omega_n T}\sin(\omega_d T)$$
$$=2\frac{\omega_n}{\omega_d}e^{-\xi\omega_n T}[\sin(\omega_d T)\cos(\phi)-\sin(\phi)\cos(\omega_d T)]$$
$$-\frac{2\xi\omega_n}{\omega_d}e^{-\xi\omega_n T}\sin(\omega_d T)\rightarrow$$

Grouping the 1st term with the 3rd yields to

$$2\frac{\omega_n}{\omega_d}e^{-\xi\omega_n T}[\sin(\omega_d T)\cos(\phi)-\xi\sin(\omega_d T)]-2\frac{\omega_n}{\omega_d}e^{-\xi\omega_n T}\sin(\phi)\cos(\omega_d T)$$

Since $\cos(\phi)=\xi$,$\sin(\phi)=\sqrt{1-\xi^2}$ and $\omega_d=\omega_n\sqrt{1-\xi^2}$, it implies

$$2\frac{\omega_n}{\omega_d}e^{-\xi\omega_n T}[\sin(\omega_d T)\cos(\phi)-\xi\sin(\omega_d T)]-2\frac{\omega_n}{\omega_d}e^{-\xi\omega_n T}\sin(\phi)\cos(\omega_d T)$$
$$=2\frac{\omega_n}{\omega_d}e^{-\xi\omega_n T}\underbrace{[\sin(\omega_d T)\,\xi-\xi\sin(\omega_d T)]}_{=0}$$
$$-2\frac{\omega_n}{\omega_n\sqrt{1-\xi^2}}e^{-\xi\omega_n T}\sqrt{1-\xi^2}\cos(\omega_d T)$$

$$2\frac{\omega_n}{\omega_d}e^{-\xi\omega_n T}[\sin(\omega_d T)\cos(\phi)-\xi\sin(\omega_d T)]-2\frac{\omega_n}{\omega_d}e^{-\xi\omega_n T}\sin(\phi)\cos(\omega_d T)$$
$$=-2e^{-\xi\omega_n T}\cos(\omega_d T)$$

✓ **Terms of $V_c(B)$ (numerator) – B^2 terms**

$$\frac{\omega_n^2}{\omega_d^2}e^{-2\xi\omega_n T}\sin^2(\omega_d T-\phi)-2\xi(\omega_n^2/\omega_d^2)e^{-2\xi\omega_n T}\sin(\omega_d T)\sin(\omega_d T-\phi)$$
$$+(\omega_n^2/\omega_d^2)e^{-2\xi\omega_n T}\sin^2(\omega_d T)$$

$$\underbrace{\frac{\omega_n^2}{\omega_d^2}[\sin^2(\omega_d T-\phi)-2\xi\sin(\omega_d T)\sin(\omega_d T-\phi)+\sin^2(\omega_d T)]}_{=1}e^{-2\xi\omega_n T}=e^{-2\xi\omega_n T}$$

- **Terms of $V_i(B)$ (numerator)**

$$\left[1-\frac{\omega_n}{\omega_d}e^{-\xi\omega_n T}\sin(\omega_d T+\phi)\right]BV_i(B)$$
$$+\frac{B^2}{1+\frac{\omega_n}{\omega_d}e^{-\xi\omega_n T}\sin(\omega_d T-\phi)\,B}\frac{\omega_n^2}{\omega_d^2}e^{-2\xi\omega_n T}\sin^2(\omega_d T)\,V_i(B)\rightarrow$$
$$\left[1-\frac{\omega_n}{\omega_d}e^{-\xi\omega_n T}\sin(\omega_d T+\phi)\right]\left[1+\frac{\omega_n}{\omega_d}e^{-\xi\omega_n T}\sin(\omega_d T-\phi)\,B\right]BV_i(B)$$
$$+\frac{\omega_n^2}{\omega_d^2}e^{-2\xi\omega_n T}\sin^2(\omega_d T)\,B^2V_i(B)\rightarrow$$

$$\left[1+\frac{\omega_n}{\omega_d}e^{-\xi\omega_n T}\sin(\omega_d T-\phi)\,B-\frac{\omega_n}{\omega_d}e^{-\xi\omega_n T}\sin(\omega_d T+\phi)\right.$$
$$\left.-\frac{\omega_n^2}{\omega_d^2}e^{-2\xi\omega_n T}\sin(\omega_d T+\phi)\sin(\omega_d T-\phi)\,B\right]BV_i(B)$$
$$+\frac{\omega_n^2}{\omega_d^2}e^{-2\xi\omega_n T}\sin^2(\omega_d T)\,B^2E_i(B)\rightarrow$$

$$\left[1-\frac{\omega_n}{\omega_d}e^{-\xi\omega_n T}\sin(\omega_d T+\phi)\right]BV_i(B)$$
$$+\left[\frac{\omega_n}{\omega_d}e^{-\xi\omega_n T}\sin(\omega_d T-\phi)-\frac{\omega_n^2}{\omega_d^2}e^{-2\xi\omega_n T}\sin(\omega_d T+\phi)\sin(\omega_d T-\phi)\right.$$
$$\left.+\frac{\omega_n^2}{\omega_d^2}e^{-2\xi\omega_n T}\sin^2(\omega_d T)\right]B^2V_i(B)$$

- ✓ **Terms of $V_i(B)$ (numerator) – B terms**

$$1-\frac{\omega_n}{\omega_d}e^{-\xi\omega_n T}\sin(\omega_d T+\phi)$$
$$=1-\frac{\omega_n}{\omega_d}e^{-\xi\omega_n T}\sin(\omega_d T)\cos(\phi)-\frac{\omega_n}{\omega_d}e^{-\xi\omega_n T}\sin(\phi)\cos(\omega_d T)\rightarrow$$
$$1-\frac{\omega_n}{\omega_d}e^{-\xi\omega_n T}\sin(\omega_d T)\cos(\phi)-\frac{\omega_n}{\omega_d}e^{-\xi\omega_n T}\sin(\phi)\cos(\omega_d T)$$
$$=1-\frac{\omega_n}{\omega_d}e^{-\xi\omega_n T}\sin(\omega_d T)\,\xi-\frac{\omega_n}{\omega_d}e^{-\xi\omega_n T}\sqrt{1-\xi^2}\cos(\omega_d T)\rightarrow$$

$$1-\frac{\omega_n}{\omega_d}e^{-\xi\omega_n T}\sin(\omega_d T)\,\xi-\frac{\omega_n}{\omega_d}e^{-\xi\omega_n T}\sqrt{1-\xi^2}\cos(\omega_d T)$$
$$=1-\frac{\xi\omega_n}{\omega_d}e^{-\xi\omega_n T}\sin(\omega_d T)-e^{-\xi\omega_n T}\cos(\omega_d T)$$

- ✓ **Terms of $V_i(B)$ (numerator) – B^2 terms**

$$\frac{\omega_n}{\omega_d}e^{-\xi\omega_n T}\sin(\omega_d T-\phi)-\frac{\omega_n^2}{\omega_d^2}e^{-2\xi\omega_n T}\sin(\omega_d T+\phi)\sin(\omega_d T-\phi)$$
$$+\frac{\omega_n^2}{\omega_d^2}e^{-2\xi\omega_n T}\sin^2(\omega_d T)=$$

$$\frac{\omega_n}{\omega_d}e^{-\xi\omega_n T}[\sin(\omega_d T)\cos(\phi)-\sin(\phi)\cos(\omega_d T)]$$
$$+\underbrace{\frac{\omega_n^2}{\omega_d^2}[\sin^2(\omega_d T)-\sin(\omega_d T+\phi)\sin(\omega_d T-\phi)]}_{=1}e^{-2\xi\omega_n T}\rightarrow$$

$$\frac{\omega_n}{\omega_d}e^{-\xi\omega_n T}[\sin(\omega_d T)\cos(\phi)-\sin(\phi)\cos(\omega_d T)]+e^{-2\xi\omega_n T}$$
$$=\frac{\xi\omega_n}{\omega_d}e^{-\xi\omega_n T}\sin(\omega_d T)-e^{-\xi\omega_n T}\cos(\omega_d T)+e^{-2\xi\omega_n T}$$

Therefore

$$\left[1-2e^{-\xi\omega_n T}\cos(\omega_d T)\,B+e^{-2\xi\omega_n T}B^2\right]V_c(B)$$
$$=\left\{\left[1-\frac{\xi\omega_n}{\omega_d}e^{-\xi\omega_n T}\sin(\omega_d T)-e^{-\xi\omega_n T}\cos(\omega_d T)\right]B\right.$$
$$\left.+\left[\frac{\xi\omega_n}{\omega_d}e^{-\xi\omega_n T}\sin(\omega_d T)-e^{-\xi\omega_n T}\cos(\omega_d T)+e^{-2\xi\omega_n T}\right]B^2\right\}V_i(B)\rightarrow$$

$$\frac{V_c(B)}{V_i(B)}=\frac{a_{num_1}B+b_{num_1}B^2}{1-2e^{-\xi\omega_n T}\cos(\omega_d T)\,B+e^{-2\xi\omega_n T}B^2} \quad \text{(B.21)}$$

where

$$a_{num_1}=1-\frac{\xi\omega_n}{\omega_d}e^{-\xi\omega_n T}\sin(\omega_d T)-e^{-\xi\omega_n T}\cos(\omega_d T)$$

$$b_{num_1}=\frac{\xi\omega_n}{\omega_d}e^{-\xi\omega_n T}\sin(\omega_d T)-e^{-\xi\omega_n T}\cos(\omega_d T)+e^{-2\xi\omega_n T}$$

By considering that $\boldsymbol{B=z^{-1}}$, the single-phase form of (4.9) is derived

$$\frac{V_c(B)}{V_i(B)}=\frac{a_{num_1}z^{-1}+b_{num_1}z^{-2}}{1-2e^{-\xi\omega_n T}cos(\omega_d T)\,z^{-1}+e^{-2\xi\omega_n T}z^{-2}}. \quad \text{(B.22)}$$

Using similar development, from (B.11) **we can achieve**

$$\left[1+\frac{\omega_n}{\omega_d}e^{-\xi\omega_n T}\sin(\omega_d T-\phi)\,B-\frac{2\xi\omega_n}{\omega_d}e^{-\xi\omega_n T}\sin(\omega_d T)\,B\right]V_c(B)$$
$$=\left[1-\frac{\omega_n}{\omega_d}e^{-\xi\omega_n T}\sin(\omega_d T+\phi)\right]BV_i(B)$$
$$+\frac{1}{C_f\omega_d}e^{-\xi\omega_n T}\sin(\omega_d T)\,BI_L(B)\rightarrow$$

$$V_c(B)$$
$$=\frac{\left[1-\frac{\omega_n}{\omega_d}e^{-\xi\omega_n T}\sin(\omega_d T+\phi)\right]BV_i(B)+\frac{1}{C_f\omega_d}e^{-\xi\omega_n T}\sin(\omega_d T)\,B}{\left[1+\frac{\omega_n}{\omega_d}e^{-\xi\omega_n T}\sin(\omega_d T-\phi)\,B-\frac{2\xi\omega_n}{\omega_d}e^{-\xi\omega_n T}\sin(\omega_d T)\,B\right]}I_L(B)$$

Substituting $V_c(B)$ in (B.18)

$$I_L(B) = \frac{1}{1 + \frac{\omega_n}{\omega_d} e^{-\xi\omega_n T} \sin(\omega_d T - \phi)\, B} C_f \frac{\omega_n^2}{\omega_d} e^{-\xi\omega_n T} \sin(\omega_d T)\, B[V_i(B) - V_c(B)]$$

$$\rightarrow$$

$$I_L(B)$$
$$= \frac{1}{1 + \frac{\omega_n}{\omega_d} e^{-\xi\omega_n T} \sin(\omega_d T - \phi)\, B} C_f \frac{\omega_n^2}{\omega_d} e^{-\xi\omega_n T} \sin(\omega_d T)\, BV_i(B)$$
$$- \frac{1}{1 + \frac{\omega_n}{\omega_d} e^{-\xi\omega_n T} \sin(\omega_d T - \phi)\, B} C_f \frac{\omega_n^2}{\omega_d} e^{-\xi\omega_n T} \sin(\omega_d T)\, B \frac{\left[1 - \frac{\omega_n}{\omega_d} e^{-\xi\omega_n T} \sin(\omega_d T + \phi)\right] BV_i(B) + \frac{1}{C_f \omega_d} e^{-\xi\omega_n T} \sin(\omega_d T)\, BI_L(B)}{\left[1 + \frac{\omega_n}{\omega_d} e^{-\xi\omega_n T} \sin(\omega_d T - \phi)\, B - \frac{2\xi\omega_n}{\omega_d} e^{-\xi\omega_n T} \sin(\omega_d T)\, B\right]}$$
$$\rightarrow$$

$$I_L(B)$$
$$= \frac{1}{\left[1 + \frac{\omega_n}{\omega_d} e^{-\xi\omega_n T} \sin(\omega_d T - \phi)\, B\right]} C_f \frac{\omega_n^2}{\omega_d} e^{-\xi\omega_n T} \sin(\omega_d T)\, BV_i(B)$$
$$- \frac{\left[1 - \frac{\omega_n}{\omega_d} e^{-\xi\omega_n T} \sin(\omega_d T + \phi)\right]}{\left[1 + \frac{\omega_n}{\omega_d} e^{-\xi\omega_n T} \sin(\omega_d T - \phi)\, B\right]\left[1 + \frac{\omega_n}{\omega_d} e^{-\xi\omega_n T} \sin(\omega_d T - \phi)\, B - \frac{2\xi\omega_n}{\omega_d} e^{-\xi\omega_n T} \sin(\omega_d T)\, B\right]} C_f \frac{\omega_n^2}{\omega_d} e^{-\xi\omega_n T} \sin(\omega_d T)\, B^2 V_i(B)$$
$$- \frac{1}{\left[1 + \frac{\omega_n}{\omega_d} e^{-\xi\omega_n T} \sin(\omega_d T - \phi)\, B\right]\left[1 + \frac{\omega_n}{\omega_d} e^{-\xi\omega_n T} \sin(\omega_d T - \phi)\, B - \frac{2\xi\omega_n}{\omega_d} e^{-\xi\omega_n T} \sin(\omega_d T)\, B\right]} \frac{\omega_n^2}{\omega_d^2} e^{-2\xi\omega_n T} \sin^2(\omega_d T)\, B^2 I_L(B)$$

$$\rightarrow$$

$$I_L(B)$$
$$+ \frac{1}{\left[1 + \frac{\omega_n}{\omega_d} e^{-\xi\omega_n T} \sin(\omega_d T - \phi)\, B\right]\left[1 + \frac{\omega_n}{\omega_d} e^{-\xi\omega_n T} \sin(\omega_d T - \phi)\, B - \frac{2\xi\omega_n}{\omega_d} e^{-\xi\omega_n T} \sin(\omega_d T)\, B\right]} \frac{\omega_n^2}{\omega_d^2} e^{-2\xi\omega_n T} \sin^2(\omega_d T)\, B^2 I_L(B)$$
$$= \frac{1}{\left[1 + \frac{\omega_n}{\omega_d} e^{-\xi\omega_n T} \sin(\omega_d T - \phi)\, B\right]} C_f \frac{\omega_n^2}{\omega_d} e^{-\xi\omega_n T} \sin(\omega_d T)\, BV_i(B)$$
$$- \frac{\left[1 - \frac{\omega_n}{\omega_d} e^{-\xi\omega_n T} \sin(\omega_d T + \phi)\right]}{\left[1 + \frac{\omega_n}{\omega_d} e^{-\xi\omega_n T} \sin(\omega_d T - \phi)\, B\right]\left[1 + \frac{\omega_n}{\omega_d} e^{-\xi\omega_n T} \sin(\omega_d T - \phi)\, B - \frac{2\xi\omega_n}{\omega_d} e^{-\xi\omega_n T} \sin(\omega_d T)\, B\right]} C_f \frac{\omega_n^2}{\omega_d} e^{-\xi\omega_n T} \sin(\omega_d T)\, B^2 V_i(B)$$
$$\rightarrow$$

$$\left[1+\frac{\omega_n}{\omega_d}e^{-\xi\omega_n T}\sin(\omega_d T-\phi)\,B\right]\left[1+\frac{\omega_n}{\omega_d}e^{-\xi\omega_n T}\sin(\omega_d T-\phi)\,B\right.$$
$$\left.-\frac{2\xi\omega_n}{\omega_d}e^{-\xi\omega_n T}\sin(\omega_d T)\,B\right]I_L(B)+\frac{\omega_n^2}{\omega_d^2}e^{-2\xi\omega_n T}\sin^2(\omega_d T)\,B^2 I_L(B)$$
$$=\left[1+\frac{\omega_n}{\omega_d}e^{-\xi\omega_n T}\sin(\omega_d T-\phi)\,B\right.$$
$$\left.-\frac{2\xi\omega_n}{\omega_d}e^{-\xi\omega_n T}\sin(\omega_d T)\,B\right]C_f\frac{\omega_n^2}{\omega_d}e^{-\xi\omega_n T}\sin(\omega_d T)\,BV_i(B)$$
$$-\left[1-\frac{\omega_n}{\omega_d}e^{-\xi\omega_n T}\sin(\omega_d T+\phi)\right]C_f\frac{\omega_n^2}{\omega_d}e^{-\xi\omega_n T}\sin(\omega_d T)\,B^2V_i(B)\rightarrow$$

$$\left[1+\frac{\omega_n}{\omega_d}e^{-\xi\omega_n T}\sin(\omega_d T-\phi)\,B\right]\left[1+\frac{\omega_n}{\omega_d}e^{-\xi\omega_n T}\sin(\omega_d T-\phi)\,B\right.$$
$$\left.-\frac{2\xi\omega_n}{\omega_d}e^{-\xi\omega_n T}\sin(\omega_d T)\,B\right]I_L(B)+\frac{\omega_n^2}{\omega_d^2}e^{-2\xi\omega_n T}\sin^2(\omega_d T)\,B^2 I_L(B)$$
$$=(B-B^2)C_f\frac{\omega_n^2}{\omega_d}e^{-\xi\omega_n T}\sin(\omega_d T)\,V_i(B)$$
$$+\frac{\omega_n}{\omega_d}e^{-\xi\omega_n T}\underbrace{[\sin(\omega_d T-\phi)-2\xi\sin(\omega_d T)+\sin(\omega_d T+\phi)]}_{=0}C_f\frac{\omega_n^2}{\omega_d}e^{-\xi\omega_n T}\sin(\omega_d T)\,B^2V_i(B)\rightarrow$$

$$\left\{1+\frac{\omega_n}{\omega_d}e^{-\xi\omega_n T}\sin(\omega_d T-\phi)\,B+\frac{\omega_n}{\omega_d}e^{-\xi\omega_n T}\sin(\omega_d T-\phi)\,B\right.$$
$$+\left(\frac{\omega_n^2}{\omega_d^2}\right)e^{-2\xi\omega_n T}\sin^2(\omega_d T-\phi)\,B^2-\frac{2\xi\omega_n}{\omega_d}e^{-\xi\omega_n T}\sin(\omega_d T)\,B$$
$$-2\xi\left(\frac{\omega_n^2}{\omega_d^2}\right)e^{-2\xi\omega_n T}\sin(\omega_d T)\sin(\omega_d T-\phi)\,B^2$$
$$\left.+\frac{\omega_n^2}{\omega_d^2}e^{-2\xi\omega_n T}\sin^2(\omega_d T)\,B^2\right\}I_L(B)=(B-B^2)C_f\frac{\omega_n^2}{\omega_d}e^{-\xi\omega_n T}\sin(\omega_d T)\,V_i(B)\rightarrow$$

$$\left\{1+\left[2\frac{\omega_n}{\omega_d}e^{-\xi\omega_n T}\sin(\omega_d T-\phi)-\frac{2\xi\omega_n}{\omega_d}e^{-\xi\omega_n T}\sin(\omega_d T)\right]B\right.$$
$$+\frac{\omega_n^2}{\omega_d^2}e^{-2\xi\omega_n T}[\sin^2(\omega_d T-\phi)-2\xi\sin(\omega_d T)\sin(\omega_d T-\phi)$$
$$\left.+\sin^2(\omega_d T)]B^2\right\}I_L(B)=(B-B^2)C_f\frac{\omega_n^2}{\omega_d}e^{-\xi\omega_n T}\sin(\omega_d T)\,V_i(B)\rightarrow$$

$$\left\{1-2e^{-\xi\omega_n T}\cos(\omega_d T)B+e^{-2\xi\omega_n T}B^2\right\}I_L(B)=(B-B^2)C_f\frac{\omega_n^2}{\omega_d}e^{-\xi\omega_n T}\sin(\omega_d T)\,V_i(B)\rightarrow$$

$$\frac{I_L(B)}{V_i(B)} = \frac{\left[C_f \frac{\omega_n^2}{\omega_d} e^{-\xi\omega_n T} \sin(\omega_d T)\right](B - B^2)}{1 - 2e^{-\xi\omega_n T}\cos(\omega_d T)B + e^{-2\xi\omega_n T}B^2}$$

By considering that $B = z^{-1}$, the single-phase form of (4.10) is derived. This is the overall transfer function $I_L(z)/V_i(z)$ including output voltage feedback, i.e. V_c

$$\frac{I_L(z)}{V_i(z)} = \frac{\left[C_f \frac{\omega_n^2}{\omega_d} e^{-\xi\omega_n T} \sin(\omega_d T)\right](z^{-1} - z^{-2})}{1 - 2e^{-\xi\omega_n T}\cos(\omega_d T)\, z^{-1} + e^{-2\xi\omega_n T} z^{-2}}. \tag{B.23}$$

The transfer function between the inductor current and capacitor voltage is derived according to (B.22) **and** (B.23)

$$\frac{V_c(z)}{I_L(z)} = \frac{V_c(z)}{V_i(z)} \cdot \frac{V_i(z)}{I_L(z)} \rightarrow$$

$$\frac{V_c(z)}{I_L(z)} = \frac{a_{num_1} z^{-1} + b_{num_1} z^{-2}}{1 - 2e^{-\xi\omega_n T}\cos(\omega_d T)\, z^{-1} + e^{-2\xi\omega_n T} z^{-2}}$$

$$\cdot \frac{1 - 2e^{-\xi\omega_n T}\cos(\omega_d T)\, z^{-1} + e^{-2\xi\omega_n T} z^{-2}}{\left[C_f \frac{\omega_n^2}{\omega_d} e^{-\xi\omega_n T} \sin(\omega_d T)\right](z^{-1} - z^{-2})} \rightarrow$$

$$\frac{V_c(z)}{I_L(z)} = \frac{a_{num_1} z^{-1} + b_{num_1} z^{-2} z^{-2}}{\left[C_f \frac{\omega_n^2}{\omega_d} e^{-\xi\omega_n T} \sin(\omega_d T)\right](z^{-1} - z^{-2})}$$

The single-phase form of (4.12) is derived

$$\frac{V_c(z)}{I_L(z)} = \frac{a_{num_1} + b_{num_1} z^{-1}}{\left[C_f \frac{\omega_n^2}{\omega_d} e^{-\xi\omega_n T} \sin(\omega_d T)\right](1 - z^{-1})}. \tag{B.24}$$

Repeating (B.18)

$$I_L(B) = \frac{1}{1 + \frac{\omega_n}{\omega_d} e^{-\xi\omega_n T} \sin(\omega_d T - \phi)\, B} C_f \frac{\omega_n^2}{\omega_d} e^{-\xi\omega_n T} \sin(\omega_d T)\, B[V_i(B) - V_c(B)] \tag{B.25}$$

By considering that $B = z^{-1}$, the single-phase form of (4.7) is derived

$$I_L(z) = \frac{1}{1 + \frac{\omega_n}{\omega_d} e^{-\xi \omega_n T} \sin(\omega_d T - \phi)\, z^{-1}} C_f \frac{\omega_n^2}{\omega_d} e^{-\xi \omega_n T} \sin(\omega_d T)\, z^{-1} [V_i(z) - V_c(z)] \quad \text{(B.26)}$$

The single-phase representation of Fig. 4.2 is shown below.

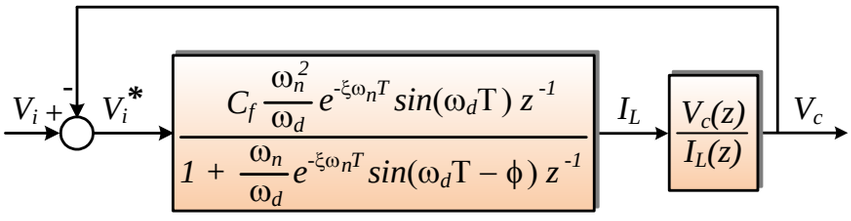

Fig. B.1. Discrete-time block diagram of an LC filter - single-phase representation of Fig. 4.2

References

[1] F. de Bosio, L. A. d. S. Ribeiro, F. D. Freijedo, M. Pastorelli and J. M. Guerrero, "Effect of state feedback coupling and system delays on the transient performance of stand-alone VSI with LC output filter," *IEEE Trans. Ind. Electron.*, vol. 63, no. 8, pp. 4909-4918, 2016.

[2] F. de Bosio, L. A. d. S. Ribeiro, F. D. Freijedo, M. Pastorelli and J. M. Guerrero, "Discrete-Time Domain Modelling of Voltage Source Inverters in Standalone Applications: Enhancement of Regulators Performance by Means of Smith Predictor," *IEEE Trans. Power Electron.*, pp. 1-15, Early Access.

[3] F. de Bosio and V. Verda, "Thermoeconomic analysis of a Compressed Air Energy Storage (CAES) system integrated with a wind power plant in the framework of the IPEX Market," *Applied Energy*, vol. 152, pp. 173-182, 2015.

[4] C. Li, F. de Bosio, S. K. Chaudhary, J. C. Vasquez and J. M. Guerrero, "Economic Dispatch for Operation Cost Minimization under Real Time Pricing in Droop Controlled DC Microgrid," *IEEE Trans. Emerg. Sel. Topics Power Electron.*, In Printing.

[5] F. de Bosio, M. Pastorelli and M. Fantino, "Sistemi di accumulo: tipologie e applicazioni," *AEIT journal*, vol. 10, 2014.

[6] F. de Bosio, M. Pastorelli, A. Mazza, G. Chicco, G. Bracco, E. Giorcelli, G. Mattiazzo and M. Raffero, "Sea-wave power converter modeling for fault conditions analysis," in *Conf. Proc. IEEE PowerTech*, Eindhoven, NL, Jun./Jul. 2015.

[7] F. de Bosio, M. Pastorelli, L. A. d. S. Ribeiro, M. S. Lima, F. D. Freijedo and J. M. Guerrero, "Current control loop design and analysis based on resonant regulators for microgrid applications," in *Conf. Proc. IEEE Ind. Electron. Soc. (IECON)*, Yokohama, JP, Nov. 2015.

[8] F. de Bosio, L. A. d. S. Ribeiro, M. S. Lima, F. D. Freijedo, J. M. Guerrero and M. Pastorelli, "Inner current loop analysis and design based on resonant regulators for isolated microgrid applications," in *Proc. IEEE Braz./South. Power Electron. Conf.(COBEP/SPEC)*, Fortaleza, BR, Nov. 2015.

[9] C. Li, F. de Bosio, S. K. Chaudhary, J. C. Vasquez and J. M. J. M. Guerrero, "Operation Cost Minimization of Droop-Controlled DC Microgrids Based on Real-Time Pricing and Optimal Power Flow," in *Conf. Proc. IEEE Ind. Electron. Soc. (IECON)*, Yokohama, JP, Nov. 2015.

[10] E. Riva Sanseverino, N. Q. Nguyen, M. L. Di Silvestre, G. Zizzo, F. de Bosio and Q. Tran, "Frequency constrained optimal Power Flow based on Glow-worm Swarm Optimization in Islanded Microgrids," in *Conf. IEEE AEIT Int. Annu.*, Naples, IT, Oct. 2015.

[11] G. Chicco, F. de Bosio, M. Pastorelli and M. Fantino, "Clustering-based Performance Assessment of Thermal Energy Management in Buildings," in *IEEE Int. Telecom. Energy Conf. (INTELEC)*, Osaka, JP, Oct. 2015.

[12] M. Pastorelli, G. Mutani and F. de Bosio, "A model for the evaluation of thermal and electric energy consumptions in residential buildings," in *Proc. IEEE Int. Conf. on Ren. Energy Res. And Appl. (ICRERA)*, Palermo, IT, Nov. 2015.

[13] M. Martino, M. Pastorelli and F. de Bosio, "Towards Smart Energy Users by Adopting an Innovative Billing System," in *Optimisation of Community Scale Renewables*, Turin, IT, Sep. 2015.

[14] F. de Bosio, L. A. d. S. Ribeiro, F. D. Freijedo, J. M. Guerrero and M. Pastorelli, "Effect of state feedback coupling on the transient performance of voltage source inverters with LC filter," in *Conf. Proc. IEEE Power Electron. and Appl. (EPE)*, Karlsruhe, DEU, Sep. 2016.

[15] F. de Bosio, L. A. d. S. Ribeiro, F. D. Freijedo and J. M. Guerrero, "Implementation issues on the design of current loops based on resonant regulators for isolated microgrids," in *Conf. Proc. IEEE Power Electron. and Appl. (EPE)*, Karlsruhe, DEU, Sep. 2016.

[16] F. de Bosio, L. A. d. S. Ribeiro, F. D. Freijedo, M. Pastorelli and J. M. Guerrero, "Control Design of VSIs to Enhance Transient Performance in Microgrids," in *Conf. Proc. IEEE Power Electron. and Appl. (EPE)*, Karlsruhe, DEU, Sep. 2016.

[17] R. Tisseur, F. de Bosio, G. Chicco, M. Fantino and M. Pastorelli, "Ant Colony for Storage Optimization," in *Proc. IEEE Int. Univ. Power Eng. Conf. (UPEC)*, Coimbra, PT, Sep. 2016.

[18] F. de Bosio, A. Luna, L. A. d. S. Ribeiro, M. Graells, O. R. Saavedra and J. M. Guerrero, "Analysis and Improvement of the Energy Management of an Isolated

Microgrid in Lencois Island based on a Linear Optimization Approach," in *Conf. Proc. IEEE Energy Conv. Congr. and Exp. (ECCE)*, Milwaukee, USA, Sep. 2016.

[19] F. de Bosio, L. A. d. S. Ribeiro, F. D. Freijedo, J. M. Guerrero and M. Pastorelli, "Enhancement of Current and Voltage Controllers Performance by Means of Lead Compensation and Anti-Windup for Islanded Microgrids," in *Conf. Proc. IEEE Energy Conv. Congr. and Exp. (ECCE)*, Milwaukee, USA, Sep. 2016.

[20] F. de Bosio, L. A. d. S. Ribeiro, F. D. Freijedo, J. M. Guerrero and M. Pastorelli, "Voltage and Current Regulators Design of Power Converters in Islanded Microgrids based on State Feedback Decoupling," in *Conf. Proc. IEEE Energy Conv. Congr. and Exp. (ECCE)*, Milwaukee, USA, Sep. 2016.

[21] F. de Bosio, L. A. d. S. Ribeiro, F. D. Freijedo, M. Pastorelli and J. M. Guerrero, "State Feedback Decoupling with In-Loop Lead Compensator in Stand-Alone VSIs," in *Conf. Proc. IEEE Ind. Electron. Soc. (IECON)*, Florence, IT, Nov. 2016.

[22] F. de Bosio, L. A. d. S. Ribeiro, F. D. Freijedo, J. M. Guerrero and M. Pastorelli, "Enhanced current and voltage regulators for stand-alone applications," in *IEEE Int. Telecom. Energy Conf. (INTELEC)*, Austin, Texas, USA, Oct. 2016.

[23] F. de Bosio, V. Verda, M. Masoero and M. Pastorelli, "Unit cost of electrical energy of a hybrid CAES-wind power plant by means of exergoeconomic analysis," in *Conf. Smart Int. and Green Energy (SINERGREEN)*, Rome, IT, May 2016.

[24] G. J. M. Smit, "Efficient ICT for efficient Smart Grids," in *Conf. Proc. IEEE Innov. Smart Grid Techn. (ISGT)*, Washington, DC, 2012.

[25] Organization for Economic Cooperation Development, "Environmental Outlook to 2030," OECD publishing, Danver, 2008.

[26] J. C. Vasquez, J. M. Guerrero, M. Savaghebi, J. Eloy-Garcia and R. Teodorescu, "Modeling, Analysis, and Design of Stationary-Reference-Frame Droop-Controlled Parallel Three-Phase Voltage Source Inverters," *IEEE Trans. Ind. Electron.*, vol. 60, no. 4, pp. 1271-1280, 2013.

[27] M. N. Arafat, A. Elrayyah and Y. Sozer, "An Effective Smooth Transition Control Strategy Using Droop-Based Synchronization for Parallel Inverters," *IEEE Trans. Ind. Appl.*, vol. 51, no. 3, pp. 2443-2454, 2015.

[28] X. Lu, J. M. Guerrero, K. Sun and J. C. Vasquez, "An Improved Droop Control Method for DC Microgrids Based on Low Bandwidth Communication With DC Bus Voltage

Restoration and Enhanced Current Sharing Accuracy," *IEEE Trans. Power Electron.,* vol. 29, no. 4, pp. 1800-1812, 2014.

[29] J. Rocabert, A. Luna, F. Blaabjerg and P. Rodriguez, "Control of Power Converters in AC Microgrids," *IEEE Trans. Power Electron.,* vol. 27, no. 11, pp. 4734-4749, 2012.

[30] J. M. Guerrero, J. C. Vasquez, J. Matas, L. G. d. Vicuña and M. Castilla, "Hierarchical Control of Droop-Controlled AC and DC Microgrids—A General Approach Toward Standardization," *IEEE Trans. Ind. Electron.,* vol. 58, no. 1, pp. 158 - 172, 2011.

[31] V. Nasirian, Q. Shafiee, J. M. Guerrero, F. L. Lewis and A. Davoudi, "Droop-Free Distributed Control for AC Microgrids," *IEEE Trans. Power Electron.,* vol. 31, no. 2, pp. 1600-1617, 2016.

[32] K. Hongrae, M. W. Degner, J. M. Guerrero, F. Briz and R. D. Lorenz, "Discrete-Time Current Regulator Design for AC Machine Drives," *IEEE Trans. Ind. Appl.,* vol. 46, no. 4, pp. 1425-1435, 2010.

[33] F. B. del Blanco, M. W. Degner and R. D. Lorenz, "Dynamic analysis of current regulators for AC motors using complex vectors," *IEEE Trans. Ind. Appl.,* vol. 35, no. 6, pp. 1424-1432, 1999.

[34] T. M. Rowan and R. J. Kerkman, "A New Synchronous Current Regulator and an Analysis of Current-Regulated PWM Inverters," *IEEE Trans. Ind. Appl.,* Vols. IA-22, no. 4, pp. 678-690, 1986.

[35] M. P. Kazmierkowski and L. Malesani, "Current control techniques for three-phase voltage-source PWM converters: a survey," *IEEE Trans. Ind. Electron.,* vol. 45, no. 5, pp. 691-703, 1998.

[36] R. Teodorescu, M. Liserre and P. Rodriguez, Grid Converters for Photovoltaic and Wind Power Systems, New York, NY, USA: Wiley-IEEE Press, 2011.

[37] F. D. Freijedo, A. Vidal, A. G. Yepes, J. M. Guerrero, Ó. López, J. Malvar and J. Doval-Gandoy, "Tuning of Synchronous-Frame PI Current Controllers in Grid-Connected Converters Operating at a Low Sampling Rate by MIMO Root Locus," *IEEE Trans. Ind. Electron.,* vol. 62, no. 8, pp. 5006-5017, 2015.

[38] M. J. Newman and D. G. Holmes, "A universal custom power conditioner (UCPC) with selective harmonic voltage compensation," in *Conf. Proc. IEEE Ind. Electron. Soc. (IECON),* Sevilla, ESP, 2002.

[39] M. Ciobotaru, R. Teodorescu and F. Blaabjerg, "Control of single-stage single-phase PV inverter," in *Conf. Proc. IEEE Power Electron. and Appl. (EPE)*, Dresden, DEU, 2005.

[40] E. Twining and D. G. Holmes, "Grid current regulation of a three-phase voltage source inverter with an LCL input filter," *IEEE Trans. Power Electron.*, vol. 18, no. 3, pp. 888-895, 2003.

[41] N. Zhang, H. Tang and C. Yao, "A Systematic Method for Designing a PR Controller and Active Damping of the LCL Filter for Single-Phase Grid-Connected PV Inverters," *Energies*, vol. 7, pp. 3934-3954, 2014.

[42] X. Mingyu, Z. Yu, K. Yong, Y. Yongxian, L. Shuming and L. Fangrui, "Full Feedforward of Grid Voltage for Discrete State Feedback Controlled Grid-Connected Inverter With LCL Filter," *IEEE Trans. Power Electron.*, vol. 27, no. 10, pp. 4234-4247, 2012.

[43] J. Yaoqin, Z. Jiqian and F. Xiaowei, "Direct Grid Current Control of LCL-Filtered Grid-Connected Inverter Mitigating Grid Voltage Disturbance," *IEEE Trans. Power Electron.*, vol. 29, no. 3, pp. 1532-1541, 2014.

[44] A. M. Hava, T. A. Lipo and W. L. Erdman, "Utility interface issues for line connected PWM voltage source converters: a comparative study," in *Proc. IEEE Appl. Power Electron. Conf. and Exp. (APEC)*, Dallas, TX, 1995.

[45] A. V. Stankovic and T. A. Lipo, "A generalized control method for input-output harmonic elimination for the PWM boost rectifier under simultaneous unbalanced input voltages and input impedances," in *Proc. IEEE Power Electron. Spec. Conf. (PESC)*, Vancouver, BC, 2001.

[46] F. D. Freijedo, A. G. Yepes, J. Malvar, O. Lopez, P. Fernandez-Comesana, A. Vidal and J. Doval-Gandoy, "Frequency tracking of digital resonant filters for control of power converters connected to public distribution systems," *IET Power Electron.*, vol. 4, no. 4, pp. 454-462, 2011.

[47] A. Vidal, F. D. Freijedo, A. G. Yepes, J. Malvar, Ó. López and J. Doval-Gandoy, "Transient response evaluation of stationary-frame resonant current controllers for grid-connected applications," *IET Power Electron.*, vol. 7, no. 7, pp. 1714-1724, 2014.

[48] H. Kum-Kang and R. D. Lorenz, "Discrete-Time Domain Modeling and Design for AC Machine Current Regulation," in *Proc. IEEE Ind. Appl. Soc. (IAS) Annu. Meeting*, New Orleans, LA, USA, 2007.

[49] T. M. Jahns, "Motion control with permanent-magnet AC machines," *Proc. IEEE,* vol. 82, no. 8, pp. 1241-1252, 1994.

[50] S.-H. Song, J.-W. Choi and S.-K. Sul, "Current measurement of digital field oriented control," in *Proc. IEEE Ind. Appl. Soc. (IAS) Annu. Meeting*, San Diego, CA, 1996.

[51] G. Ellis and R. D. Lorenz, "Comparison of motion control loops for industrial applications," in *Proc. IEEE Ind. Appl. Soc. (IAS) Annu. Meeting*, Phoenix, AZ, 1999.

[52] D. G. Holmes, T. A. Lipo, B. P. McGrath and W. Y. Kong, "Optimized Design of Stationary Frame Three Phase AC Current Regulators," *IEEE Trans. Power Electron.,* vol. 24, no. 11, pp. 2417-2426, 2009.

[53] P. C. Loh and D. G. Holmes, "Analysis of multiloop control strategies for LC/CL/LCL-filtered voltage-source and current-source inverters," *IEEE Trans. Ind. Appl.,* vol. 41, no. 2, pp. 644-654, 2005.

[54] M. J. Ryan, W. E. Brumsickle and R. D. Lorenz, "Control topology options for single-phase UPS inverters," *IEEE Trans. Ind. Appl.,* vol. 33, no. 2, pp. 493-501, 1997.

[55] L. P. Chiang, M. J. Newman, D. N. Zmood and D. G. Holmes, "A comparative analysis of multiloop voltage regulation strategies for single and three-phase UPS systems," *IEEE Trans. Power Electron.,* vol. 18, no. 5, pp. 1176-1185, 2003.

[56] M. J. Ryan and R. D. Lorenz, "A synchronous-frame controller for a single-phase sine wave inverter," in *Proceedings of APEC 97 - Applied Power Electronics Conference*, Atlanta, GA, 1997.

[57] B. P. McGrath, S. G. Parker and D. G. Holmes, "High Performance Stationary Frame AC Current Regulation Incorporating Transport Delay Compensation," *EPE Journal,* vol. 22, no. 4, pp. 17-24, 2012.

[58] S. S. H. Bukhari, T. A. Lipo and B. Kwon, "An on-line UPS system that eliminates the inrush current phenomenon while feeding multiple load transformers," in *Conf. Proc. IEEE Energy Conv. Congr. and Exp. (ECCE-ICPE) Asia*, Seoul, Korea, 2015.

[59] R. Teodorescu, F. Blaabjerg, M. Liserre and P. C. Loh, "Proportional-resonant controllers and filters for grid-connected voltage-source converters," *IEE Proceedings - Electric Power Applications,* vol. 153, no. 5, pp. 750-762, 2006.

[60] R. Bojoi, L. R. Limongi, D. Roiu and A. Tenconi, "Frequency-domain analysis of resonant current controllers for active power conditioners," in *Conf. Proc. IEEE Ind. Electron. Soc. (IECON)*, Orlando, FL, USA, 2008.

[61] A. Vidal, F. D. Freijedo, A. G. Yepes, P. Fernández-Comesaña, J. Malvar, Ó. López and J. Doval-Gandoy, "Assessment and Optimization of the Transient Response of Proportional-Resonant Current Controllers for Distributed Power Generation Systems," *IEEE Trans. Ind. Electron.,* vol. 60, no. 4, pp. 1367-1383, 2013.

[62] S. Zhou and J. Liu, "Analysis and comparison of resonant-based current controllers implemented in stationary reference frame: A complex pole-zero placement perspective," in *IEEE Energy Conversion Congress and Exposition (ECCE)*, Montreal, QC, 2015.

[63] D. M. V. d. Sype, K. D. Gussemé, F. M. L. L. D. Belie, A. P. V. d. Bossche and J. A. Melkebeek, "Small-Signal z-Domain Analysis of Digitally Controlled Converters," *IEEE Trans. Power Electron.,* vol. 21, no. 2, pp. 470-478, 2006.

[64] Y. Ito and S. Kawauchi, "Microprocessor based robust digital control for UPS with three-phase PWM inverter," *IEEE Trans. Power Electron.,* vol. 10, no. 2, pp. 196-204, 1995.

[65] H. Zhongyi, L. Mingzhu and X. Yan, "Core techniques of digital control for UPS," in *IEEE Conf. Rec. ICIT*, Hong Kong, China, 2005.

[66] S. Buso and P. Mattavelli, Digital Control in Power Electronics, 1st ed., San Rafael, CA, USA: Morgan & Claypool, 2006.

[67] R. D. Lorenz, D. B. Lawson and M. O. Lucas, "Synthesis of State Variable Controllers for Industrial Servo Drives," WEMPEC – University of Wisconsin, May 1986.

[68] R. D. Lorenz, T. A. Lipo and D. W. Novotny, "Motion Control with induction motor drives," *Proc. of the IEEE,* vol. 82, no. 8, p. 1215 – 1240, 1994.

[69] E. d. C. Gomes, L. A. d. S. Ribeiro, J. V. M. Caracas, S. Y. C. Catunda and R. D. Lorenz, "State Space Decoupling Control Design Methodology for Switching Converters," in *Conf. Rec. ECCE*, Atlanta, US, 2010.

[70] P. C. Loh, M. J. Newman, D. N. Zmood and D. G. Holmes, "A Comparative Analysis of Multiloop Voltage Regulation Strategies for Single and Three-Phase UPS Systems," *IEEE Trans. on Power Electron.,* vol. 18, no. 5, p. 1176 – 1185, 2003.

[71] H. Wu, D. Lin, D. Zhang, K. Yao and J. Zhang, "A current-mode control technique with instantaneous inductor-current feedback for UPS inverters," in *Proc. IEEE Appl. Power Electron. COnf. and Exp. (APEC)*, Dallas, TX, 1999.

[72] G. Escobar, P. Mattavelli, A. M. Stankovic, A. A. Valdez and J. Leyva-Ramos, "An Adaptive Control for UPS to Compensate Unbalance and Harmonic Distortion Using a Combined Capacitor/Load Current Sensing," *IEEE Trans. Ind. Electron.*, vol. 54, no. 2, pp. 839-847, 2007.

[73] W. C. Duesterhoeft, M. W. Schulz and E. Clarke, "Determination of Instantaneous Currents and Voltages by Means of Alpha, Beta, and Zero Components," *Transactions of the American Institute of Electrical Engineers*, vol. 70, no. 2, pp. 1248-1255, 1951.

[74] B. Bose, Modern Power Electronics, Upper Saddle River, NJ, USA, 736p: 1st ed. Prentice-Hall, 2001.

[75] S. Buso, P. Mattavelli, L. Rossetto and G. Spiazzi, "Simple digital control improving dynamic performance of power factor preregulators," *IEEE Trans. Power Electron.*, vol. 13, no. 5, pp. 814-823, 1998.

[76] A. Costabeber, L. Corradini, P. Mattavelli and S. Saggini, "Time optimal, parameters-insensitive digital controller for DC-DC buck converters," in *Proc. IEEE Power Electron. Spec. Conf. (PESC)*, Rhodes, GR, 2008.

[77] H. Peng, D. Maksimovic, A. Prodic and E. Alarcon, "Modeling of quantization effects in digitally controlled DC-DC converters," in *Proc. IEEE Power Electron. Spec. Conf. (PESC)*, Aachen, DEU, 2004.

[78] D. Trevisan, P. Mattavelli, S. Saggini, G. Garcea and M. Ghioni, "High-performance synchronous-asynchronous digital voltage-mode control for dc-dc converters," in *Proc. IEEE Appl. Power Electron. Conf. and Exp. (APEC)*, Dallas, TX, 2006.

[79] H. Hanselmann, "Implementation of Digital Controllers—A Survey," *Automatica*, vol. 23, no. 1, pp. 7-32, 1987.

[80] S.-H. Song, J.-W. Choi and S.-K. Sul, "Current measurement in digitally controlled AC drives," *IEEE Ind. Appl. Magazine*, vol. 6, no. 4, pp. 51-62, 2000.

[81] J.-H. Jang, S.-K. Sul and Y.-C. Son, "Current Measurement Issues in Sensorless Control Algorithm using High Frequency Signal Injection Method," in *Proc. IEEE Ind. Appl. Soc. (IAS) Annu. Meeting*, Salt Lake City, UT, USA, 2003.

[82] D. G. Holmes and T. A. Lipo, Pulse Width Modulation for Power Converters: Principles and Practice, NJ, USA: Wiley-IEEE Press, 2003.

[83] T. M. Rowan, R. J. Kerkman and T. A. Lipo, "Operation of Naturally Sampled Current Regulators in the Transition Mode," *IEEE Trans. Ind. Appl.,* Vols. IA-23, no. 4, pp. 586-596, 1987.

[84] P. Stumpf, R. K. Járdán and I. Nagy, "Comparison of Naturally Sampled PWM Techniques in Ultrahigh Speed Drives," in *Proc. IEEE Int. Symp. on Ind. Electron. (ISIE)*, Hangzhou, CHN, 2012.

[85] G. R. Walker, "Digitally-Implemented Naturally Sampled PWM Suitable for Multilevel Converter Control," *IEEE Trans. Power Electron.,* vol. 18, no. 6, pp. 1322-1329, 2003.

[86] B.-H. Bae and S.-K. Sul, "A compensation method for time delay of full-digital synchronous frame current regulator of PWM AC drives," *IEEE Trans. Ind. Appl.,* vol. 39, no. 3, pp. 802-810, 2003.

[87] J. Richardson and O. T. Kukrer, "Implementation of a PWM Regular Sampling Strategy for AC Drives," *IEEE Trans. Power Electron.,* vol. 6, no. 4, pp. 645-655, 1991.

[88] Y. Suh and T. A. Lipo, "Control scheme in hybrid synchronous stationary frame for PWM AC/DC converter under generalized unbalanced operating conditions," *IEEE Trans. Ind. Appl.,* vol. 42, no. 3, pp. 825-835, 2006.

[89] J. Holtz, J. Quan, J. Pontt, J. Rodriguez, P. Newman and H. Miranda, "Design of fast and robust current regulators for high-power drives based on complex state variables," *IEEE Trans. Ind. Appl.,* vol. 40, no. 5, pp. 1388-1397, 2004.

[90] F. B. del Blanco, M. W. Degner, A. Diez and R. Lorenz, "Generalization of linear control tools for complex vectors," in *Proc. 15th IFAC World Congress*, 2002.

[91] D. Novotny and T. Lipo, Vector Control and Dynamics of AC Drives, New York, USA: Oxford University Press, 1996.

[92] S. Zhou, J. Liu, L. Zhou and H. She, "Cross-coupling and decoupling techniques in the current control of grid-connected voltage source converter," in *IEEE Appl. Power Electron. Conf. and Exp. (APEC)*, Charlotte, NC, 2015.

[93] R. B. Sepe and J. H. Lang, "Implementation of discrete-time field-oriented current control," *IEEE Trans. Ind. Appl.,* vol. 30, no. 3, pp. 723-728, 1994.

[94] W. Y. Kong, D. G. Holmes and B. P. McGrath, "Improved Stationary Frame AC Current Regulation using Feedforward Compensation of the Load EMF," in *Proc. IEEE Appl. Power Electron. Conf. and Exp. (APEC)*, Washington, DC, 2009.

[95] D. N. Zmood and D. G. Holmes, "Improved voltage regulation for current-source inverters," *IEEE Trans. Ind. Appl.*, vol. 37, no. 4, pp. 1028-1036, 2001.

[96] D. N. Zmood and D. G. Holmes, "Stationary frame current regulation of PWM inverters with zero steady-state error," *IEEE Trans. Power Electron.*, vol. 18, no. 3, pp. 814-822, 2003.

[97] W. Y. Kong, D. G. Holmes and B. P. McGrath, "Enhanced three phase ac stationary frame PI current regulators," in *Conf. Proc. IEEE Energy Conv. Congr. and Exp. (ECCE)*, San Jose, CA, 2009.

[98] D. N. Zmood, D. G. Holmes and G. H. Bode, "Frequency-domain analysis of three-phase linear current regulators," *IEEE Trans. Ind. Appl.*, vol. 37, no. 2, pp. 601-610, 2001.

[99] B. A. Francis and W. M. Wonham, "The internal model principle for linear multivariable regulators," *Appl. Math. Optimization*, vol. 2, no. 2, pp. 170-194, 1975.

[100] G. Escobar, A. A. Valdez, J. Leyva-Ramos and P. Mattavelli, "Repetitive-Based Controller for a UPS Inverter to Compensate Unbalance and Harmonic Distortion," *IEEE Trans. Ind. Electron.*, vol. 54, no. 1, pp. 504-510, 2007.

[101] Y. Sato, T. Ishizuka, K. Nezu and T. Kataoka, "A new control strategy for voltage-type PWM rectifiers to realize zero steady-state control error in input current," *IEEE Trans. Ind. Appl.*, vol. 34, no. 3, pp. 480-486, 1998.

[102] L. R. Limongi, R. Bojoi, G. Griva and A. Tenconi, "New Control Strategy for Hybrid Power Filters Using Sinusoidal Signal Integrators for Current Reference Generation," in *Proc. IEEE Ind. Appl. Conf.*, New Orleans, Louisiana, 2007.

[103] C. Lascu, L. Asiminoaei, I. Boldea and F. Blaabjerg, "High Performance Current Controller for Selective Harmonic Compensation in Active Power Filters," *IEEE Trans. Power Electron.*, vol. 22, no. 5, pp. 1826-1835, 2007.

[104] A. G. Yepes, F. D. Freijedo, Ó. Lopez and J. Doval-Gandoy, "High-Performance Digital Resonant Controllers Implemented With Two Integrators," *IEEE Trans. Power Electron.*, vol. 26, no. 2, pp. 563-576, 2011.

[105] R. Teodorescu, F. Blaabjerg, U. Borup and M. Liserre, "A new control structure for grid-connected LCL PV inverters with zero steady-state error and selective harmonic compensation," in *Conf. Proc. in IEEE Appl. Power Electron. Conf. and Exp. (APEC)*, Anaheim, CA, 2004.

[106] X. Yuan, W. Merk, H. Stemmler and J. Allmeling, "Stationary-frame generalized integrators for current control of active power filters with zero steady-state error for current harmonics of concern under unbalanced and distorted operating conditions," *IEEE Trans. Ind. Appl.*, vol. 38, no. 2, pp. 523-532, 2002.

[107] W. Lenwari, "Review of a high performance control of AC signals based on a proportional plus resonant compensator," *Suranaree J. Sci. Technol.*, vol. 15, no. 4, pp. 333-344, 2008.

[108] H. Zheng, C. Lv, X. Xu and J. Ye, "An Improved Proportional Resonant Control Strategy for Three Phase Three Level Grid-connected Inverter," *Journ. of Comp. Inform. Systems*, vol. 10, no. 23, p. 10345–10354, 2014.

[109] R. I. Bojoi, G. Griva, V. Bostan, M. Guerriero, F. Farina and F. Profumo, "Current control strategy for power conditioners using sinusoidal signal integrators in synchronous reference frame," *IEEE Trans. Power Electron.*, vol. 20, no. 6, pp. 1402-1412, 2005.

[110] C. B. Jacobina, M. B. R. Correa, T. M. Oliveira, A. M. N. Lima and E. R. C. d. Silva, "Vector modeling and control of unbalanced electrical systems," in *Proc. IEEE Ind. Appl. Soc. (IAS) Annu. Meeting*, Phoenix, AZ, USA, 1999.

[111] P. Mattavelli, "A closed-loop selective harmonic compensation for active filters," *IEEE Trans. Ind. Appl.*, vol. 37, no. 1, pp. 81-89, 2001.

[112] V. Blasko, L. Arnedo, P. Kshirsagar and S. Dwari, "Control and elimination of sinusoidal harmonics in power electronics equipment: A system approach," in *Conf. Proc. IEEE Energy Conv. Congr. and Exp. (ECCE)*, Phoenix, AZ, 2011.

[113] F. B. del Blanco, M. W. Degner and R. D. Lorenz, "Analysis and design of current regulators using complex vectors," *IEEE Trans. Ind. Appl.*, vol. 36, no. 3, pp. 817-825, 2000.

[114] R. Wu, S. B. Dewan and G. R. Slemon, "Analysis of a PWM AC to DC voltage source converter under the predicted current control with a fixed switching frequency," *IEEE Trans. Ind. Appl.*, vol. 27, no. 4, pp. 756-764, 1991.

[115] G. Mirzaeva, G. Goodwin and B. McGrath, "Optimal design of VSI current controllers based on MPC approach," in *IEEE 24th International Symposium on Industrial Electronics (ISIE)*, 2015.

[116] S. Buso, L. Malesani and P. Mattavelli, "Comparison of current control techniques for active filter applications," *IEEE Trans. Ind. Electron.*, vol. 45, no. 5, pp. 722-729, 1998.

[117] D. G. Holmes and D. A. Martin, "Implementation of a direct digital predictive current controller for single and three phase voltage source inverters," in *Proc. IEEE Ind. Appl. Soc. (IAS) Annu. Meeting*, San Diego, CA, 1996.

[118] Y. Yan, F. C. Lee, P. Mattavelli and S. Tian, "Small-signal Laplace-domain model for digital predictive current mode controls," in *Conf. Proc. IEEE Energy Conv. Congr. and Exp. (ECCE)*, Raleigh, NC, 2012.

[119] O. Kukrer, "Deadbeat control of a three-phase inverter with an output LC filter," *IEEE Trans. Power Electron.*, vol. 11, no. 1, pp. 16-23, 1996.

[120] R. D. Lorenz and N. T. West, "Implementation and Evaluation of a Stator and Rotor Flux Linkage-Based Dead-Beat, Direct Torque Control of Induction Machines at the Operational Voltage Limits," in *Proc. IEEE Ind. Appl. Soc. (IAS) Annu. Meeting*, New Orleans, LA, USA, 2007.

[121] P. Mattavelli, "An Improved Deadbeat Control for UPS Using Disturbance Observers," *IEEE Trans. Ind. Electron.*, vol. 52, no. 1, pp. 206-212, 2005.

[122] S. Buso, S. Fasolo and P. Mattavelli, "Uninterruptible power supply multiloop control employing digital predictive voltage and current regulators," *IEEE Trans. Ind. Appl.*, vol. 37, no. 6, pp. 1846-1854, 2001.

[123] G. E. Valderrama, A. M. Stankovic and P. Mattavelli, "Dissipativity-based adaptive and robust control of UPS in unbalanced operation," *IEEE Trans. Power Electron.*, vol. 18, no. 4, pp. 1056-1062, 2003.

[124] T. Kawabata, T. Miyashita and Y. Yamamoto, "Digital control of three-phase PWM inverter with LC filter," *IEEE Trans. Power Electron.*, vol. 6, no. 1, pp. 62-72, 1991.

[125] P. Mattavelli, G. Spiazzi and P. Tenti, "Predictive digital control of power factor preregulators with input voltage estimation using disturbance observers," *IEEE Trans. Power Electron.*, vol. 20, no. 1, pp. 140-147, 2005.

[126] G. E. Valderrama, A. M. Stankovic and P. Mattavelli, "Dissipativity-based adaptive and robust control of UPS in unbalanced operation," *IEEE Trans. Power Electron.*, vol. 18, no. 4, pp. 1056-1062, 2003.

[127] P. Mattavelli, "An improved deadbeat control for UPS using disturbance observers," *IEEE Trans. Ind. Electron.*, vol. 52, no. 1, pp. 206-212, 2005.

[128] J. S. Lim, C. Park, J. Han and Y. I. Lee, "Robust Tracking Control of a Three-Phase DC–AC Inverter for UPS Applications," *IEEE Trans. Ind. Electron.*, vol. 61, no. 8, pp. 4142-4151, 2014.

[129] S. Kim and S. J. K., "Finite-Settling-Steps Direct Torque and Flux Control for Torque-Controlled Interior PM Motors at Voltage Limits," *IEEE Trans. Ind. Appl.*, vol. 50, no. 5, pp. 3374-3381, 2014.

[130] M. Cannon, "Step response and pole locations - Lecture 4," University of Oxford, Oxford, US, 2016.

[131] D. M. Brod and D. W. Novotny, "Current Control of VSI-PWM Inverters," *IEEE Trans. Ind. Appl.*, Vols. IA-21, no. 3, pp. 562-570, 1985.

[132] Q. Yao and D. G. Holmes, "A simple, novel method for variable-hysteresis-band current control of a three phase inverter with constant switching frequency," in *Proc. IEEE Ind. Appl. Soc. (IAS) Annu. Meeting*, St. Louis, MO, USA, 1993.

[133] L. Malesani, P. Mattavelli and P. Tomasin, "Improved constant-frequency hysteresis current control of VSI inverters with simple feedforward banswidth prediction," *IEEE Trans. Ind. Appl.*, vol. 33, no. 5, pp. 1194-1202, 1997.

[134] P. S. Ninkovic, "A novel constant-frequency hysteresis current control of PFC converters," in *Conf. Proc. IEEE Int. Symp. Ind. Electron. (ISIE)*, L'Aquila, ABR, Italy, 2002.

[135] C. N. M. Ho, V. S. P. Cheung and H. S. H. Chung, "Constant-Frequency Hysteresis Current Control of Grid-Connected VSI Without Bandwidth Control," *IEEE Trans. on Power Electron.*, vol. 24, no. 11, pp. 2484-2495, 2009.

[136] R. Ramchand, K. Gopakumar, C. Patel, K. Sivakumar, A. Das and H. Abu-Rub, "Online Computation of Hysteresis Boundary for Constant Switching Frequency Current-Error Space-Vector-Based Hysteresis Controller for VSI-Fed IM Drives," *IEEE Trans. Power Electron.*, vol. 27, no. 3, pp. 1521-1529, 2012.

[137] H. I. Okumus and M. Aktas, "Direct Torque Control of Induction Machine Drives Using Adaptive Hysteresis Band for Constant Switching Frequency," in *Proc. IEEE Int. Electric Machines Drives Conf. (IEMDC)*, Antalya, TR, 2007.

[138] S. Buso, S. Fasolo, L. Malesani and P. Mattavelli, "A Dead-Beat Adaptive Hysteresis Current Control," *IEEE Trans. Ind. Appl.*, vol. 36, no. 4, pp. 1174-1180, 2000.

[139] J. W. Kimball, P. T. Krein and Y. Chen, "Hysteresis and delta modulation control of converters using sensorless current mode," *IEEE Trans. Power Electron.,* vol. 21, no. 4, pp. 1154-1158, 2006.

[140] T. C. Green and B. W. Williams, "Spectra of delta-sigma modulated inverters: an analytical treatment," *IEEE Trans. Power Electron.,* vol. 7, no. 4, pp. 644-654, 1992.

[141] P. Wipasuramonton, Z. Zi Qiang and D. Howe, "Improved current-regulated delta Modulator for reducing switching frequency and low-frequency current error in permanent magnet brushless AC drives," *IEEE Trans. Power Electron.,* vol. 20, no. 2, pp. 475-484, 2005.

[142] R. D. Lorenz and D. M. Divan, "Dynamic analysis and experimental evaluation of delta modulators for field-oriented AC machine current regulators," *IEEE Trans. Ind. Appl.,* vol. 26, no. 2, pp. 296-301, 1990.

[143] D. Ciscato, L. Malesani, L. Rossetto, P. Tenti, G. L. Basile, M. Pasti and F. Voelker, "PWM rectifier with low DC voltage ripple for magnet supply," *IEEE Trans. Ind. Appl.,* vol. 28, no. 2, pp. 414-420, 1992.

[144] A. Mertens, "Performance analysis of three-phase inverters controlled by synchronous delta-modulation systems," in *Proc. IEEE Ind. Appl. Soc. (IAS) Annu. Meeting,* Houston, TX, USA, 1994.

[145] G. C. Goodwin, S. F. Graebe and M. E. Salgado, Control System Design, 1st ed., Valparáıso, Chile: Pearson, 2000.

[146] P. Y. Li, "Notes of the course ME 8281: Advanced Control Systems," Spring, University of Minnesota, 2016.

[147] T. Inoue, M. Nakano, T. Kubo, S. Matsumoto and H. Baba, "High accuracy control of a proton synchrotron magnet power supply," *Unknown Host Publication Title,* pp. 3137-3142, 1982.

[148] L. Cuiyan, Z. Dongchun and Z. Xianyi, "Theory and applications of the repetitive control," in *Conf. Proc. IEEE Soc. of Instr. and Control Eng. (SICE),* Sapporo, JP, 2004.

[149] B. F. Chen, J. W. Gong, L. Xiong, L. Qin and X. M. Zha, "Analysis and realization of a novel repetitive controller in active power filter system," in *Conf. Proc. IEEE Power Electron. and Drive Syst. (PEDS),* Taipei, TWN, 2009.

[150] H. A. Gründling, E. G. Carati and J. R. Pifheiro, "Analysis and implementation of a modified robust model reference adaptive control with repetitive controller for UPS applications," in *Conf. Proc. IEEE Ind. Electron. Soc. (IECON)*, Aachen, Germany, 1998.

[151] T. Ying-Yu, O. Rong-Shyang, J. Shih-Liang and C. Meng-Yueh, "High-performance programmable AC power source with low harmonic distortion using DSP-based repetitive control technique," *IEEE Trans. Power Electron.*, vol. 12, no. 4, pp. 715-725, 1997.

[152] B. Widrow, J. R. Glover, J. M. McCool, J. Kaunitz, C. S. Williams, R. H. Hearn, J. R. Zeidler, J. E. Dong and R. C. Goodlin, "Adaptive noise cancelling: Principles and applications," *Proc. IEEE*, vol. 63, no. 12, pp. 1692-1716, 1975.

[153] S. M. Kuo and D. R. Morgan, "Active noise control: a tutorial review," *Proc. IEEE*, vol. 87, no. 6, pp. 943-973, 1999.

[154] V. Blasko, "Adaptive filtering for selective elimination of higher harmonics from line currents of a voltage source converter," in *Proc. IEEE Ind. Appl. Soc. (IAS) Annu. Meeting*, St. Louis, MO, USA, 1998.

[155] V. K. Sood, N. Kandil, R. V. Patel and K. Khorasani, "Comparative evaluation of neural-network-based and PI current controllers for HVDC transmission," *IEEE Trans. Power Electron.*, vol. 9, no. 3, pp. 288-296, 1994.

[156] S. Kaitwanidvilai and P. Piyarungsan, "Low-cost microprocessor-based alternating current voltage controller using genetic algorithms and neural network," *IET Power Electron.*, vol. 3, no. 4, pp. 490-499, 2010.

[157] X. Fu and S. Li, "A Novel Neural Network Vector Control Technique for Induction Motor Drive," *IEEE Trans. Energy Convers.*, vol. 30, no. 4, pp. 1428-1437, 2015.

[158] A. Rubaai, R. Kotaru and M. D. Kankam, "A continually online-trained neural network controller for brushless DC motor drives," *IEEE Trans. Ind. Appl.*, vol. 36, no. 2, pp. 475-483, 2000.

[159] F. Piglione, "Lecture Notes - Electrical load management, forecasting and control," Politecnico di Torino, 2014.

[160] S. A. Mir, D. S. Zinger and M. E. Elbuluk, "Fuzzy controller for inverter fed induction machines," *IEEE Trans. Ind. Appl.*, vol. 30, no. 1, pp. 78-84, 1994.

[161] M. Nasir Uddin and J. Khastoo, "Fuzzy Logic-Based Efficiency Optimization and High Dynamic Performance of IPMSM Drive System in Both Transient and Steady-State Conditions," *IEEE Trans. Ind. Appl.*, vol. 50, no. 6, pp. 4251-4259, 2014.

[162] P. Kirawanich and R. M. O'Connell, "Fuzzy logic control of an active power line conditioner," *IEEE Trans. Power Electron.*, vol. 19, no. 6, pp. 1574-1585, 2004.

[163] H. Cai, W. Wei, Y. Peng and H. Hu, "Fuzzy proportional-resonant control strategy for three-phase inverters in islanded micro-grid with nonlinear loads," in *Proc. IEEE Int. Conf. on Fuzzy Syst. (FUZZ)*, Beijing, CHN, 2014.

[164] X. Yuan, I. Brown, R. D. Lorenz and A. Qui, "Observer-based inverter disturbance compensation," in *Proc. IEEE Energy Conv. Congr. and Exp. (ECCE)*, San Jose, CA, 2009.

[165] K. Lee, T. M. Jahns, T. A. Lipo, V. Blasko and R. D. Lorenz, "Observer-Based Control Methods for Combined Source-Voltage Harmonics and Unbalance Disturbances in PWM Voltage-Source Converters," *IEEE Trans. Ind. Appl.*, vol. 45, no. 6, pp. 2010-2021, 2009.

[166] K. Lee, T. M. Jahns, T. A. Lipo and V. Blasko, "New Control Method Including State Observer of Voltage Unbalance for Grid Voltage-Source Converters," *IEEE Trans. Ind. Electron.*, vol. 57, no. 6, pp. 2054-2065, 2010.

[167] "IEC EN 62040-3," Feb. 2015.

[168] K. J. Aström and T. Hägglung, PID Controllers: Theory, Designing, and Tuning, 2nd ed., Research Triangle Park, NC, USA: Instrum. Soc. Amer., 2006.

[169] P. C. Loh, M. J. Newman, D. N. Zmood and D. G. Holmes, "Improved transient and steady state voltage regulation for single and three phase uninterruptible power supplies," in *Proc. IEEE Power Electron. Spec. Conf. (PESC)*, 2001.

[170] A. G. Yepes, F. D. Freijedo, Ó. López and J. Doval-Gandoy, "Analysis and Design of Resonant Current Controllers for Voltage-Source Converters by Means of Nyquist Diagrams and Sensitivity Function," *IEEE Trans. Ind. Electron.*, vol. 58, no. 11, pp. 5231-5250, 2011.

[171] M. M. Hashempour, M. Savaghebi, J. C. Vasquez and J. M. Guerrero, "A Control Architecture to Coordinate Distributed Generators and Active Power Filters Coexisting in a Microgrid," *IEEE Trans. Smart Grid*, vol. 7, no. 5, pp. 2325 - 2336, 2016.

[172] M. Savaghebi, A. Jalilian, J. C. Vasquez and J. M. Guerrero, "Secondary control for voltage quality enhancement in microgrids," *IEEE Trans. Smart Grid,* vol. 3, no. 4, pp. 1893-1902, 2012.

[173] J. He, Y. W. Li and M. S. Munir, "A Flexible Harmonic Control Approach Through Voltage-Controlled DG-Grid Interfacing Converters," *IEEE Trans. Ind. Electron.*, vol. 59, no. 1, pp. 444-455, 2012.

[174] J. He and Y. W. Li, "Analysis, Design, and Implementation of Virtual Impedance for Power Electronics Interfaced Distributed Generation," *IEEE Trans. Ind. Appl.*, vol. 47, no. 6, pp. 2525-2538, 2011.

[175] Y. Guan, J. C. Vasquez and J. M. Guerrero, "A simple autonomous current-sharing control strategy for fast dynamic response of parallel inverters in islanded microgrids," in *Proc. IEEE Int. Energy Conf. (ENERGYCON)*, Cavtat, DBV, HR, 2014.

[176] D. De and V. Ramanarayanan, "Decentralized Parallel Operation of Inverters Sharing Unbalanced and Nonlinear Loads," *IEEE Trans. Power Electron.*, vol. 25, no. 12, pp. 3015-3025, 2010.

[177] J. M. Guerrero, J. Matas, L. G. d. Vicuna, M. Castilla and J. Miret, "Decentralized Control for Parallel Operation of Distributed Generation Inverters Using Resistive Output Impedance," *IEEE Trans. Ind. Electron.*, vol. 54, no. 2, pp. 994-1004, 2007.

[178] J. M. Guerrero, P. C. Loh, M. Chandorkar and T.-L. Lee, "Advanced Control Architectures for Intelligent Microgrids—Part I Decentralized and Hierarchical Control," *IEEE Trans. Ind. Electron.*, vol. 60, no. 4, pp. 1254-1262, 2013.

[179] Y. Guan, J. C. Vasquez, J. M. Guerrero and E. A. A. Coelho, "Small-signal modeling, analysis and testing of parallel three-phase-inverters with a novel autonomous current sharing controller," in *Proc. IEEE Appl. Power Electron. Conf. and Exp. (APEC)*, Charlotte, NC, 2015.

[180] N. L. Díaz, E. A. Coelho, J. C. Vasquez and J. M. Guerrero, "Stability analysis for isolated AC microgrids based on PV-active generators," in *Conf. Proc. IEEE Energy Conv. Congr. and Exp. (ECCE)*, Montreal, QC, 2015.

[181] J. M. Guerrero, L. G. de Vicuna, J. Matas, M. Castilla and J. Miret, "Output Impedance Design of Parallel-Connected UPS Inverters With Wireless Load-Sharing Control," *IEEE Trans. Ind. Electron.*, vol. 52, no. 4, pp. 1126-1135, 2005.

[182] R. Dugan, M. McGranaghan and H. Beaty, "Electrical Power Systems Quality," New York, McGraw-Hill, 1996.

[183] M. El-Hawary, "Definitions of Voltage Unbalance," *IEEE Power Engineering Review,* vol. 21, no. 5, pp. 49-51, 2011.

[184] A. G. Yepes, F. D. Freijedo, J. Doval-Gandoy, Ó. L. J. Malvar and P. Fernandez-Comesaña, "Effects of Discretization Methods on the Performance of Resonant Controllers," *IEEE Trans. Power Electron.,* vol. 25, no. 7, pp. 1692-1712, 2010.

[185] D. Maksimovic and R. Zane, "Small-Signal Discrete-Time Modeling of Digitally Controlled PWM Converters," *IEEE Trans. Power Electron.,* vol. 22, no. 6, pp. 2552-2556, 2007.

[186] R. D. Middlebrook, "Predicting modulator phase lag in PWM converter feedback loops," in *Proc. of the Adv. in Swit. mode Power Conver. (ASPC)*, 1981.

[187] Y. Shi, Y. Wang and R. D. Lorenz, "A Low-Switching-Frequency Flux Observer and Torque Model of Deadbeat–Direct Torque and Flux Control on Induction Machine Drives," *IEEE Trans. Ind. Appl.,* vol. 51, no. 3, pp. 2255-2267, 2015.

[188] M. Hinkkanen, H. Awan, Z. Qu, T. Tuovinen and F. Briz, "Current Control for Synchronous Motor Drives: Direct Discrete-Time Pole-Placement Design," *IEEE Trans. Ind. Appl.,* vol. PP, no. 99, pp. 1-1, 2015.

[189] M. Hinkkanen, Z. Qu, H. A. A. Awan, T. Tuovinen and F. B. d. Blanco, "Current control for IPMSM drives: Direct discrete-time pole-placement design," in *Proc. IEEE Workshop on Electric. Mach. Design, Contr. and Diagn. (WEMDCD)*, Turin, IT, 2015.

[190] P. Mattavelli, F. Polo, F. D. Lago and S. Saggini, "Analysis of Control-Delay Reduction for the Improvement of UPS Voltage-Loop Bandwidth," *IEEE Trans. Ind. Electron.,* vol. 55, no. 8, pp. 2903-2911, 2008.

[191] Y. Shi, Y. Wang and R. D. Lorenz, "Loss minimization for dynamic load trajectories on induction machine drives without torque performance degradation," in *Proc. IEEE Int. Conf. on Power Electron. and Drive Syst. (PEDS)*, Sydney, NSW, 2015.

[192] F. G. Shinskey, B. G. Liptak, R. Bars and J. Hetthéssy, Control Systems - Cascade Loops, vol. 2, C. Press: Instrument Engineers' Handbook: Process Control and Optimization, 2006.

[193] G. C. Goodwin, S. F. Graebe and W. S. Levine, "Internal model control of linear systems with saturating actuators," in *Proc. ECC*, Groningen, NL, 1993.

[194] S. A. Richter and R. W. D. Doncker, "Digital proportional-resonant (PR) control with anti-windup applied to a voltage-source inverter," in *Conf. Proc. IEEE Power Electron. and Appl. (EPE)*, Birmingham, UK, 2011.